Actinide Interactions with Minerals Relevant to Geological Disposal and Contaminated Land Management

A thesis submitted to the University of Manchester for the degree of Doctor of Philosophy in the Faculty of Science and Engineering

2017

Rosemary Hibberd

School of Chemistry

Contents

List of Figures

Chapter 4.

Chapter 5.

Chapter 6.

Chapter 7.

List of Tables

Chapter 4.

Chapter 5.

Chapter 6.

Chapter 7.

List of Abbreviations

AGR	Advanced Gas-cooled Reactor
ANDRA	*Agence nationale pour la gestion des déchets radioactifs* (National Agency for Radioactive Waste Management, France)
BET	Brunauer–Emmett–Teller method of specific surface area analysis
BIGRAD	Biogeochemical Gradients and Radionuclide Transport
BOC	British Oxygen Company
BWR	Boiling Water Reactor
CDZ	Chemical Disturbed Zone
CoRWM	Committee on Radioactive Waste Management
COSHH	Control Of Substances Hazardous to Health
C-S-H	Calcium-Silicate-Hydrate
DECC	Department of Energy and Climate Change
DEFRA	Department for Environment, Food and Rural Affairs
DU	Depleted Uranium
EBS	Engineered Barrier System
EDF	Électricité de France
EDX	Energy Dispersive X-ray Spectroscopy
ESEM	Environmental Scanning Electron Microscope
ESEM-FEG	ESEM – Field Emission Gun
ETDA	Ethylenediaminetetraacetic Acid
EXAFS	Extended X-ray Absorption Fine Structure
GDF	Geological Disposal Facility
GLEEP	Graphite Low Energy Experimental Pile
HAW	Higher Activity Waste
HLW	High Level Waste
HR-TEM	High Resolution – Transmission Electron Microscope
IAP	Ion Activity Product
ICDD	The International Centre for Diffraction Data
ICP-AES	Inductively Coupled Plasma – Atomic Emission Spectrometry
ICP-MS	Inductively Coupled Plasma – Mass Spectrometry

ILW	Intermediate Level Waste
IPA	Isopropanol
IUPAC	International Union of Pure and Applied Chemistry
LLNL	Lawrence Livermore National Laboratory
LLW	Low Level Waste
LO-RISE	Long-Lived Radionuclides In the Surface Environment
LSC	Liquid Scintillation Counting
MOX	Mixed Oxide Fuel
MQ	18.2 MΩ Milli-Q deionised water
NDA	Nuclear Decommissioning Authority
NEA	Nuclear Energy Agency
NERC	Natural Environment Research Council
NNL	National Nuclear Lab
NRVB	Nirex Reference Vault Backfill
OECD	Organisation for Economic Co-operation and Development
OPC	Ordinary Portland Cement
PCA	The Portland Cement Association
PES	Polyethersulfone
PHREEQC	pH-Redox-Equilibrium in C
POST	Parliamentary Office of Science and Technology
PUREX	Plutonium Uranium Redox Extraction
PVDF	Polyvinylidene fluoride
PWR	Pressured Water Reactor
PZC	Point of Zero Charge
RATE	Radioactivity and the Environment
RWM	Radioactive Waste Management Limited
SAED	Selected Area Electron Diffraction
SAXS	Small Angle X-ray Scattering
SDD-EDX	Silicon Drift Detector - EDX
SEM	Scanning Electron Microscopy
SIT	Specific ion Interaction Theory

TEM	Transmission Electron Microscope
THORP	Thermal Oxide Reprocessing Plant
UK	United Kingdom
UNSCEAR	United Nations Scientific Committee on the Effects of Atomic Radiation
USNRC	United State Nuclear Regulatory Commission
UV-Vis-nIR	Ultraviolet-Visible-Near Infrared
VLLW	Very Low Level Waste
XANES	X-ray Absorption Near Edge Spectroscopy
XAS	X-ray Absorption Spectroscopy
XPS	X-ray Photoelectron Spectroscopy
XRD	X-ray Diffraction

Abstract

The University of Manchester
Rosemary Hibberd
Doctor of Philosophy
Actinide Interactions with Minerals Relevant to Geological Disposal and Contaminated Land Management
2017

Many countries intend to achieve the safe management of their radioactive wastes through geological disposal. In addition, radioactively contaminated land is of global concern. To address both of these technical challenges it is imperative to understand the behaviour and subsequent migration of radionuclides in the subsurface. This thesis addresses uncertainties in the behaviour of the long-lived, risk-driving radionuclides U and Np in their most mobile and environmentally relevant oxidation states, U(VI) and Np(V).

The formation the U(VI) colloidal nanoparticles is identified under the high pH, low carbonate conditions expected within the near field of a cementitious Geological Disposal Facility (GDF). XAS, SAXS, and TEM have been used to characterise these U(VI) colloids as 60 – 80 nm clusters of 1 – 2 nm clarkeite-like (Na uranate) nanoparticles, which are stable in cement leachate for a period of at least 5 years. The reactivity of these U(VI) colloids towards a range of mineral phases was investigated. In the presence of the common rock-forming minerals biotite, orthoclase, and quartz, only limited reactivity was observed with > 80 % of the U(VI) remaining in the filtered fraction after up to 5 years of reaction. In contact with cement, > 97 % of the U(VI) was removed from solution within 1 month. Reversibility studies, luminescence spectroscopy, and XAS suggest that a large portion of the cement associated U(VI) is in a uranophane-like coordination environment, likely incorporated into the C-S-H interlayers or as a stable surface precipitate. Together, this suggests that while U(VI) colloids could form in high pH (> 13) cement leachate, providing an additional pathway for migration, many of them are likely to be removed from suspension by the presence of solid cement, although 2.4 % (1.0 μM) U(VI) remained in the filtered fraction even after 21 months of reaction.

The interaction of aqueous U(VI) and Np(V) with a range of environmentally relevant Mn minerals has also been studied under circumneutral to alkaline conditions. Here, extensive (up to 99 %) uptake of U(VI) and Np(V) was observed in systems containing δ-$Mn(IV)O_2$, triclinic (Na)-birnessite [$Na_{0.5}Mn(IV/III)_2O_4 \cdot 1.5H_2O$], hausmannite [$Mn(III/II)_3O_4$], and rhodochrosite [$Mn(II)CO_3$]. The uptake of U(VI) by δ-MnO_2 and hausmannite was found to be partially irreversible, suggesting that these minerals could be particularly important in determining radionuclide migration. XAS indicated that both U(VI) and Np(V) formed edge-sharing bidentate adsorption complexes on the surface of δ-MnO_2 and hausmannite, implying that these complexes are responsible for the observed reversibility. These complexes were also identified on triclinic (Na)-birnessite; however, after 1 month of reaction U(VI) was found to have migrated into the triclinic (Na)-birnessite interlayer, replacing Na^+. Reaction with all three investigated Mn oxide phases was rapid, with equilibrium being reached within at least 2 weeks. However, whilst U(VI) and Np(V) were both extensively removed from solution in systems containing rhodochrosite, these reactions were much slower, with equilibrium taking up to 4 months to be established. XAS suggested that this was due to the formation of a U(VI) or Np(V) containing precipitate on the rhodochrosite surface.

Declaration

No portion of this work referred to in this thesis has been submitted in support of an application for another degree or qualification of this or any other institute of learning.

Copyright Statement

i. The author of this thesis (including any appendices and/or schedules to this thesis) owns certain copyright or related rights in it (the "Copyright") and s/he has given The University of Manchester certain rights to use such Copyright, including for administrative purposes.

ii. Copies of this thesis, either in full or in extracts and whether in hard or electronic copy, may be made **only** in accordance with the Copyright, Designs and Patents Act 1988 (as amended) and regulations issued under it or, where appropriate, in accordance with licensing agreements which the University has from time to time. This page must form part of any such copies made.

iii. The ownership of certain Copyright, patents, designs, trademarks and other intellectual property (the "Intellectual Property") and any reproductions of copyright works in the thesis, for example graphs and tables ("Reproductions"), which may be described in this thesis, may not be owned by the author and may be owned by third parties. Such Intellectual Property and Reproductions cannot and must not be made available for use without the prior written permission of the owner(s) of the relevant Intellectual Property and/or Reproductions.

iv. Further information on the conditions under which disclosure, publication and commercialisation of this thesis, the Copyright and any Intellectual Property and/or Reproductions described in it may take place is available in the University IP Policy (see http://documents.manchester.ac.uk/DocuInfo.aspx?DocID=2442 0), in any relevant Thesis restriction declarations deposited in the University Library, The University Library's regulations (see http://www.library.manchester.ac.uk/about/regulations/) and in The University's policy on Presentation of Theses.

Acknowledgements

Firstly, I would like to thank Nick Bryan for agreeing to let me to begin this project in the first place and for his guidance throughout this process; the science contained in this thesis has been much improved by your sound advice and patient discussion. Thank you to Kath Morris for pushing me to be the best scientist I could be, and for the hours spent attempting to teach me to write, both are very much appreciated. And thank you to Gareth Law for being a great supervisor: your expertise, support, and advice have been invaluable, as well as the many opportunities you have afford to me. Thanks also to Katie Law, Hamza Al-Qasmi, John Waters, Heath Bagshaw, Paul Lythgoe, Fred Mosselmans, Chris Boothman, Laura Newsome, Carolyn Pearce, and especially Sam Shaw for their technical and analytical assistance, and willingness to help. I would also like to thank the Nuclear First Doctoral Training Centre (EP/G037140/1) for the funding and training opportunities which have made this thesis possible.

For letting me follow them around various labs and sharing their wisdom, and for their friendship, I would like to thank Nick Sherriff and Pieter Bots. Thank you to Adam Fuller (yes, I've finally written it!) for your support, both technical and otherwise, over the last few years – it wouldn't have been half as much fun without you. And to my many friends across RCRD and CRR who have made my time here a pleasure (particularly Graham, Matt, Daisy, Debbie, and Kurt), and especially those of you who have brightened many an hour in a glovebox or beamline hutch (Will, Hannah, Tom Neill, Adam F, NMW). Thanks to NMW for answering my many 'quick' questions, Hollie for tending to my glove box, and NJ for dragging me out for beer.

Particular congratulations also go to Hannah and Fabiola for never failing to make me smile – thank you. And Chloe: for 4 years of sharing wine, and 4+ years of coffee (and some wine) – long may it continue!

To Mum, Dad, F, and my family, I can't even begin to thank you enough for everything you've done over the years. I couldn't have done it without you; thank you for entertaining me while I walk home (at whatever time it happened to be) and for pretending not to mind that you haven't actually seen me in… too long.

And finally, to Matt, for listening to incomprehensible descriptions of red and blue lines for years now and for your unwavering belief in me: thank you and I'm back in the room.

Author

The Author attended The University of Manchester graduating with an undergraduate degree in Chemistry with Industrial Experience (MChem) in 2012. After which, she joined the Centre for Radiochemistry Research group at The University of Manchester where, to date, she has been conducting the research presented in this thesis.

1. Thesis Content

1.1. Thesis Structure

The thesis is divided into 8 chapters. In Chapter 1, the background and rationale for the PhD are described, placing my research in the context of the UK nuclear legacy and the safe management of its radioactive wastes. Chapter 2 provides a comprehensive review of the literature related to the geodisposal of uranium and neptunium and the management of radioactively contaminated land. It is split into broad topics such as: mineral phases, radionuclide migration, and radionuclide geochemistry. Chapter 2 also details the aims of this thesis and the hypotheses addressed. Chapter 3 discusses the materials and methods used throughout this thesis. Chapters 4-7 present the key, novel, research outputs from this thesis, specifically concerning the behaviour of uranium and neptunium in environmental systems (see below for further details). Finally, in Chapter 8 the main conclusions from this thesis are summarised and discussed in the context of the aims and hypotheses. Details on individual experimental chapters are as follows:

Chapter 4 is a reproduction of a paper published in *Langmuir* entitled "Formation of Stable Uranium(VI) Colloidal Nanoparticles in Conditions Relevant to Radioactive Waste Disposal". This work investigates the formation of U(VI) colloids in high pH cement leachate. The experiments described in this chapter were designed by P. Bots, G. Law, R. Hibberd, K. Morris, and S. Shaw. Experiments and analysis were conducted by P. Bots (SAXS, XAS, TEM, geochemical modelling) and R. Hibberd (filtration experiments, TEM). The manuscript was prepared by P. Bots and R. Hibberd under the guidance of S. Shaw and the PhD supervisors. Analytical assistance was provided by F. Mosselmans, A. Brown, J. Doutch, and A. Smith. Additional assistance was provided by G. Law, K. Morris, and S. Shaw through editorial advice on an advanced draft of manuscript.

Chapter 5 is a manuscript prepared for submission to *Applied Geochemistry* entitled "U(VI) Nanoparticle Stability in the Presence of Minerals Under Alkaline Conditions". This work investigates the stability of U(VI) colloids formed in high pH cement leachate in the presence of cement, biotite, quartz, and orthoclase. The experiments conducted for this chapter were designed by R. Hibberd, G. Law, N. Bryan, T. Marshall, R. Telchadder, S. Shaw, and K. Morris. Experiments were prepared, executed, and analysed by R. Hibberd (cement, and selected quartz and orthoclase filtration experiments, XAS, SEM, geochemical modelling), G. Law (quartz and orthoclase filtration experiments), T. Marshall (biotite filtration experiments, TEM), and R. Telchadder (^{232}U experiments, luminescence spectroscopy). The manuscript was written by R. Hibberd under the guidance of G. Law, K. Morris, N. Bryan, and S. Shaw. Analytical assistance was provided by P. Bots, K. Smith, A. Swinbourne, and L. Natrajan. An advanced draft of the manuscript was edited by K. Morris and G. Law, and RWM Ltd. provided advice and comments on the final draft.

Chapter 6 is a manuscript prepared for submission to *Environmental Science and Technology* entitled "Interaction of U(VI) with Mn-Minerals: An EXAFS and reversibility study". The study investigates the interaction of U(VI) with a range of Mn-minerals under conditions relevant to the geological disposal of radioactive waste and contaminated land. The experiments described in this chapter were designed by R. Hibberd, N. Bryan, K. Morris, and G. Law. All experiments were conducted and the resulting data analysed by R. Hibberd. The manuscript was written by R. Hibberd under the guidance of G. Law, K. Morris, and N. Bryan. Analytical assistance was provided by S. Shaw and A. Fuller. An advanced draft of the manuscript was edited by G. Law and K. Morris.

Chapter 7 is a manuscript prepared for submission to *Applied Geochemistry* entitled "Interaction of Np(V) with Mn-minerals". The study concentrates on the interaction of Np(V) with δ-MnO_2, triclinic (Na)-birnessite, hausmannite, and rhodochrosite. The

experiments described in this chapter were designed by R. Hibberd, C. Thorpe, K. Morris, and G. Law. Experiments were conducted by R. Hibberd (5.24 μM sorption experiments, XAS) and C. Thorpe (0.162 μM sorption experiments, XAS) and the resulting data were analysed by R. Hibberd. The manuscript was written by R. Hibberd under the guidance of G. Law and K. Morris. An advanced draft of the manuscript was edited by G. Law and K. Morris.

1.2. Thesis Overview

The long-term management of radioactive waste, and contaminated land at legacy nuclear sites, is of national and global concern (DECC, 2010; Morris et al., 2011; NDA, 2013; Ministry of the Environment Sweden, 2014). In the UK, the cost of decommissioning and cleaning up our nuclear legacy is expected to exceed £ 115 billion and take 120 years to complete (NDA, 2015).

Currently, the UK has 400, 000 m^3 of Higher Activity radioactive Wastes (HAWs) (NDA, 2014a) which our Government intends to place in a Geological Disposal Facility (GDF), 200 – 1000 m underground (DECC, 2015). This GDF will utilise a multi-barrier concept, including specially designed waste-forms, containers, and backfills, to retard the migration of radionuclides back to the biosphere. Further, the host rock will provide the final barrier to the release of radionuclides to the Earth's surface. Due to the long half-lives of many radionuclides present in HAW it is important to ensure these radionuclides remain isolated from the biosphere until the threat they pose is negligible. It is therefore necessary to understand how they will behave and migrate over the $1000 – 1 \times 10^6$ year time scale required for radioactive decay to render isolation redundant (Morris et al., 2011), so that an appropriate GDF can be designed and constructed.

The migration of radionuclides through the geosphere is predominantly controlled by their solution concentration. Interaction of radionuclides with minerals can reduce the aqueous

concentration through sorption, incorporation, and surface-mediated precipitation. The formation of colloids can also facilitate the transport of non-aqueous radionuclides with groundwater flow (Renshaw et al., 2011).

Cement will be abundant within a GDF environment as it is one of the proposed backfill materials for the geodisposal of Intermediate Level Wastes (ILW). In addition cement, as a common construction material, will be used as a structural material in the GDF. Therefore, it is likely that the interaction of radionuclides with cement and cement leachate will exert significant influence and control over their migration and mobility through the Engineered Barrier Systems (EBS). In geological settings, Fe and Mn oxide minerals are ubiquitous and have been identified as potentially important reactive phases (Roy, 1981; Dixon et al., 1990; Post, 1999; NDA, 2010d). Iron oxides are known to be important sinks for immobilising risk-driving, cationic actinides such as U and Np. However, their interactions with Mn-minerals are poorly constrained. This thesis aims to begin addressing this knowledge gap by investigating U(VI) and Np(V) interactions with a range of Mn-minerals under conditions relevant to geological disposal. The formation of colloids is also known to exert significant control over radionuclide mobility (Parry et al., 2011; Vines and Beard, 2012; Walther and Denecke, 2013). Therefore, the formation and stability of intrinsic U(VI) colloids in high pH cement leachate is also investigated in order to determine their potential to increase U(VI) mobility.

2. Literature Review

2.1. The UK Nuclear Industry

The United Kingdom has a long history of civil nuclear power with the first nuclear reactor in Western Europe, GLEEP (the Graphite Low Energy Experimental Pile, sited at Harwell, Oxfordshire), achieving criticality in 1947 (Walls, 2011). In 1956 this was followed by the first of the Calder Hall reactors (the first full-scale civilian reactor to provide electricity to a national grid), then a fleet of Magnox reactors and later, Advanced Gas-cooled Reactors (AGR) (Walls, 2011). In 1995, the Magnox and AGR fleet were joined by the UK's only Pressurised Water Reactor (PWR), Sizewell B, which was the last reactor to come online in the UK (Walls, 2011). Recently, The UK Government has announced its decision to proceed with a deal with EDF to build a new nuclear power station at Hinkley Point (Clark, 2016); representing the first new nuclear build in the UK since Sizewell B which began supplying electricity to the national grid in 1995 (EDF Energy, 2017).

2.1.1. Radioactively Contaminated Ground

Over time nuclear licensed sites and the wider environment can become contaminated as a result of accidental and/or authorised release of radioactivity (Cochran et al., 1993; Wu et al., 2006; Dounreay Site Restoration Ltd., 2009; Luo et al., 2009; NDA, 2010b; Kimber et al., 2011). Contamination can occur as a result of serious accidents such as Fukushima (World Nuclear Association, 2016b), Chernobyl (UNSCEAR, 2000), and Three Mile Island (USNRC, 2014), but is often caused by leakages and spills that result in the contamination of ground and groundwater. It can therefore be necessary to remediate these sites (Hunter, 2004; McKinley et al., 2006). In order to achieve this, it is important to understand the solubility of radionuclides in groundwater and their interactions with minerals and microbes present in soil and rock. This allows their behaviour to be predicted and a suitable remediation / management strategy to be developed (Kimber et al., 2011).

2.1.1.1. The Sellafield Site

The Sellafield site is the UK's largest nuclear site. Its operations encompass a wide range of activities including reprocessing spent nuclear fuel, fabricating mixed oxide fuel, and the management and storage of nuclear waste (Kimber et al., 2011; Sellafield Ltd, 2016a). Both accidental and authorised discharges have occurred from the site and led to the radioactive contamination of the subsurface, both within the site boundary and beyond the boundary in the Irish Sea, and in groundwater outside of the site (MacKenzie et al., 1999). Groundwater monitoring shows the highest areas of activity on site are in the vicinity of the separation area (Sellafield Ltd., 2014). This area has been used for reprocessing spent nuclear fuel and was subject to significant leaks throughout the 1970s (Hunter, 2004).

2.1.2. The Nuclear Fuel Cycle

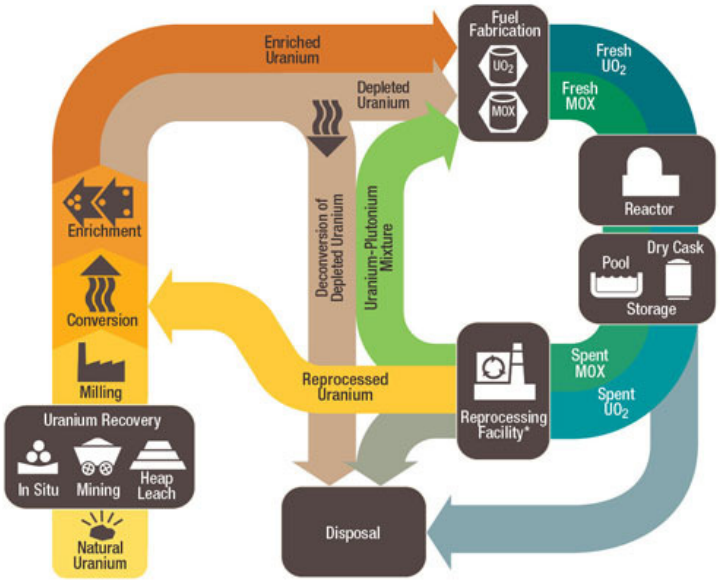

Figure 2.1: The nuclear fuel cycle (from USNRC (2016c)).

The first step in the nuclear fuel cycle (Figure 2.1) is mining the uranium ore from which the fuel is created. This predominantly occurs in Canada, Australia, Kazakhstan, Niger, Russia, and Namibia (Wilson, 1996; Sharrad et al., 2011). Conventional open pit or underground mines are often used to extract the ore which is then milled and acid leached

in order to dissolve the uranium. This method generates significant waste ("tailings") which still contain significant amounts of U and also daughter radionuclides from the ^{238}U decay chain and can therefore contain significant radioactivity and require careful management to prevent the spread of contamination (Abdelouas, 2006; World Nuclear Association, 2016a). Alternatively, *in situ* leaching can sometimes be utilised to extract uranium from loosely packed deposits. Here a leachate solution, often acidic or basic groundwater containing an oxidant, is pumped through a uranium containing aquifer before being recovered (World Nuclear Association, 2016a).

Once the uranium containing leachate has been generated it is converted into "yellowcake" (U_3O_8), *via* a process of solvent extraction and precipitation. The uranium can be enriched, if required, and converted into UO_2 (by reaction with H_2) which is then pressed into fuel pellets (USNRC, 2016b). Enrichment is the process by which the relative proportion of fissile ^{235}U in the fuel is increased, to power civil light water reactors (*e.g.* PWRs and BWRs) this is generally done to ~ 3 – 5 % ^{235}U (Sharrad et al., 2011; USNRC, 2016b), although some reactor designs can use natural uranium (~ 0.78 % ^{235}U; *e.g.* CANDU) (Canadian Nuclear Association, 2016). To enrich the U the yellowcake is first converted to UF_6, as F only has one stable isotope, ^{19}F. A series of centrifuges are then used to steadily concentrate the ^{235}U based on the differing molecular weights of $^{235}UF_6$, $^{238}UF_6$, and $^{234}UF_6$ (Sharrad et al., 2011; USNRC, 2016a). The enriched U is then used to make fuel pellets that are commonly stacked into fuel rods and clad in a heat conductive material to provide primary containment of the radioactive material while the fuel is in the reactor core. Once the irradiated fuel is removed from a reactor core it can either be reprocessed or enter long-term be storage until it can be disposed of as spent nuclear fuel.

2.1.2.1. Radioactive Waste Reprocessing

The primary purpose of early nuclear reactors was the generation of fissile ^{239}Pu for atomic weapons programmes (Walls, 2011). The irradiated nuclear fuel therefore underwent a

chemical separation process in order to separate out the desired plutonium. Today the UK still performs chemical separations on spent nuclear fuel to remove the potentially useful plutonium and uranium from the long-lived fission products and the highly radioactive activation products (Sharrad et al., 2011). This is achieved using the PUREX (Plutonium URanium EXtraction) process performed by Sellafield Ltd. at THORP (THermal Oxide Reprocessing Plant), although this is set to close in 2018 halting the UK's reprocessing of spent nuclear fuel (Sellafield Ltd, 2016b). The PUREX process is, in principle, a solvent extraction, and the uranium and plutonium it recovers can then be used to make Mixed Oxide (MOX) fuel which can be re-used in nuclear reactors (NDA, 2011; Sharrad et al., 2011). By recycling the uranium and plutonium the volume of the waste is significantly reduced, however, since the remaining waste is largely activation and fission products, the waste produced by the PUREX process is of very high specific activity (Morris et al., 2011; Sharrad et al., 2011). As the UK is one of only a handful of countries to attempt to close the nuclear fuel cycle by reprocessing its spent nuclear fuel, its radioactive waste inventory differs from that of many "once through" countries (Morris et al., 2011; World Nuclear Association, 2016c).

2.1.3. UK Radioactive Waste Inventory

Radioactive waste is split into three categories, Low Level Waste (LLW), Intermediate Level Waste (ILW), and High Level Waste (HLW) depending on the radioactivity of the waste and the heat it generates. To be classified as LLW, the waste must contain < 4 GBq / tonne of α or 12 GBq / tonne of β/γ (DECC, 2012). ILW is more radioactive than LLW, but does not generate sufficient heat to require this to be taken into account when considering its storage and disposal. In contrast, HLW is heat generating and its temperature may rise significantly due to its isotopic composition. This must be accounted for in the design of HLW storage and disposal facilities (NDA, 2013). There is also a sub-category of LLW, known as Very Low Level Waste (VLLW), which contains very little

radioactivity (< 400 kBq / 0.1 m^3) and principally originates from hospitals and universities. It is sometimes appropriate for this waste to be disposed of with municipal, commercial, or industrial waste (either directly or after incineration) since it does not require the same treatment as LLW (NDA, 2009).

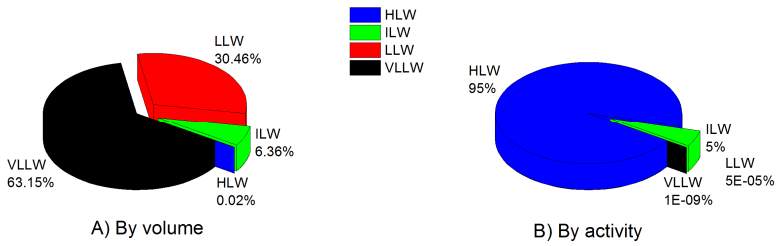

Figure 2.2: The UK radioactive waste inventory by a) volume and b) activity (NDA, 2014a).

By volume, the UK radioactive waste inventory is predominately LLW and VLLW. However, the ~ 6 % by volume of the inventory which represents the ILW and HLW (HAW) is responsible for almost all of the activity (Figure 2.2) (NDA, 2013). Uranium and plutonium recovered *via* the PUREX process, as well as spent nuclear fuels, are not contained within the waste inventory since these materials may be used to fabricate fuel in the future and are therefore not considered to be waste. Currently, these materials are designated "zero value assets" (NDA, 2011; POST, 2016).

2.1.4. Disposal Routes for Radioactive Wastes

2.1.4.1. The Low Level Waste Repository at Drigg

Currently the UK only has a disposal route for LLW, which is provided by LLW Repository Ltd., at Drigg, Cumbria (LLW Repository Ltd., 2014). This facility accepts solid LLW from the nuclear industry, the Ministry of Defence, and other industrial, educational, medical, and research establishments. The waste is packaged into metal containers which are then filled with a cement based grout to minimise the void space

within the containers. Since 1988 these containers have then been placed into low permeability, concrete lined vaults, which are capped when filled. The design is intended to reduce the ingress of water, in order to maintain the containment of radionuclides by increasing the lifetime of the containers and decreasing the flow of water through the facility and therefore the transport of radionuclides away from it (LLW Repository Ltd., 2014). Due to the low level nature of the waste disposed of in this facility, the period of isolation, and therefore the requirements of the engineered barrier, are substantially lower that of a GDF.

2.1.4.2. Higher Activity Wastes

Due to their high radioactivity, HAWs must be isolated from the biosphere to allow radioactive decay to reduce the activity until the risk posed is negligible, which will take hundreds of thousands of years (Morris et al., 2011). The UK Government and devolved administrations for Wales and Northern Ireland intend to achieve the safe disposal of the UK's HAW *via* a GDF (DECC, 2015). The safety case for a GDF must demonstrate that no further intervention would be required to prevent the transport of radionuclides back to the biosphere until the risk they pose is negligible. The Scottish policy on the long-term management of HAW differs from that of England and Wales and favours a near-surface facility as near to the site where the waste was produced as possible (The Scottish Government, 2011). As part of this policy it is also necessary for the developers to demonstrate how facilities will be monitored and how the waste, or the waste packages, could be retrieved (NDA, 2013). The UK Government's advisory Committee on Radioactive Waste Management defines geological disposal as the "burial underground (200 – 1000 m) of radioactive waste in a purpose built facility with no intention to retrieve the waste once the facility is closed" (CoRWM, 2006; Morris et al., 2011; NDA, 2014b; DECC, 2015).

The generic design for a UK GDF (Figure 2.3) is based on a multi-barrier concept consisting of a wasteform, waste container, buffer or backfill, and the geosphere (Morris et al., 2011; NDA, 2014b). The wasteform is designed to provide a stable, durable, and low solubility matrix which minimises the release of radionuclides into the groundwater (NDA, 2010d). The majority of the ILW currently in existence has already been packaged for interim storage and eventual disposal (NDA, 2014a). This packaging involves encapsulating the waste in steel drums and filling the void space with a cementitious grout (NDA, 2010d). This provides mechanical stability and will generate reducing conditions, as a result of steel corrosion, retarding radionuclide migration (NDA, 2013). However, UK HLW is vitrified, meaning that the radionuclides are an intrinsic part of the wasteform and therefore can only be released as the glass is dissolved, even once the container has been breached (NDA, 2010d).

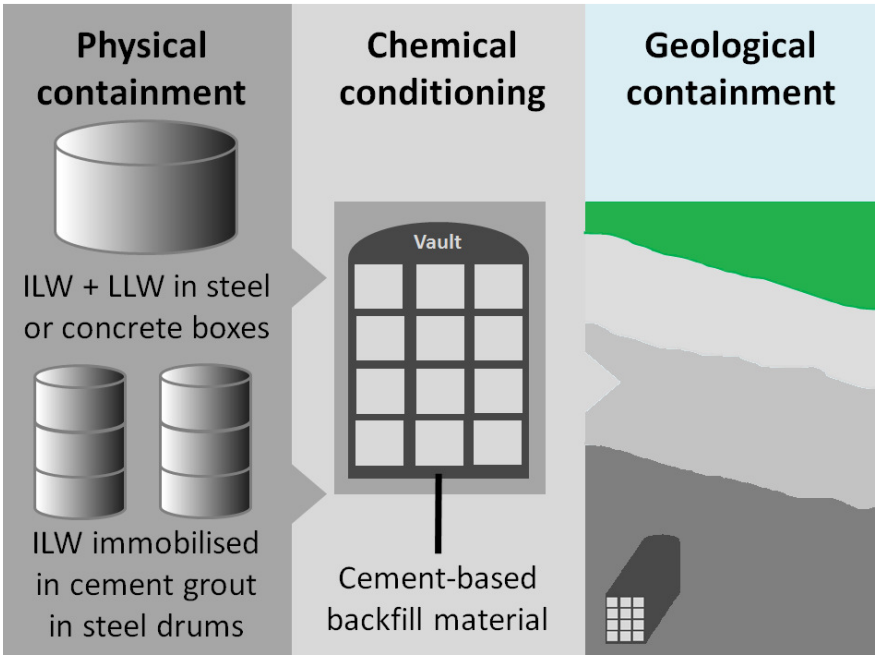

Figure 2.3: Schematic illustration of a generic GDF design for UK ILW (from NDA (2014b)).

The primary function of all radioactive waste containers is to provide physical containment of the wasteform and isolate it from groundwater. However, the different wastes

necessitate different containers. For example, HLW containers are designed to remain sealed for as long as possible and are considered to have failed once the container is breached (NDA, 2010e), while, ILW has the potential to generate gas meaning the waste containers have vents to prevent the build-up of pressure (NDA, 2010e). Therefore ILW is not isolated from groundwater even whilst the container remains intact. However, groundwater incursion through the vents would be slow meaning flow through the container will remain minimal whilst it remains intact. The concept for the disposal of spent nuclear fuel is less well developed than that than for other types of waste since the decision to stop reprocessing and to dispose of waste as spent nuclear fuel was only taken relatively recently (NDA, 2010f; Sellafield Ltd, 2016b).

A GDF will be constructed underground by creating a series of tunnels and caverns within the host rock, leaving voids in the host rock after the waste has been emplaced (Morris et al., 2011; NDA, 2014b). Therefore, a backfill (or buffer) material will be used to surround the waste containers and to fill tunnels and access shafts. The role of the backfill is two-fold; firstly it should support the host rock and protect the wasteform, and its container, from any geological events. Secondly, the backfill should provide a barrier to both the ingress of water to both the wasteform and its container, and to the transport of radionuclides and gases out into the geosphere (NDA, 2010e; NDA, 2010d; Morris et al., 2011; Vines and Beard, 2012). The UK Government has postponed the decision on whether the waste must be retrievable (DEFRA et al., 2008; DECC, 2015). Therefore, the GDF must be designed so that this option is not excluded, meaning any cementitious backfill would also need to be friable.

The function of a backfill can be fulfilled by using either a low-permeability backfill which provides containment due to the substantial time required for both water and radionuclides to migrate across the barrier *via* diffusion, or a porous backfill which controls the chemical environment surrounding the waste (NDA, 2010d; NDA, 2010e). The most suitable

backfill will depend on the overall GDF design and the type of waste being disposed of (NDA, 2010a). For example, the current UK design uses a cementitious backfill to surround ILW as this provides a hyper-alkaline environment which encourages the precipitation of hydroxides, thereby limiting the solubility and transport of many cationic radionuclides (NDA, 2010d). This backfill is particularly suited to ILW since the wasteform is also cementitious.

The host rock of a GDF has several functions. It must provide a stable chemical and geological environment which optimises the effectiveness of the EBS, as well as limiting the flow of groundwater through the GDF since the majority of processes by which the EBS will be degraded are water mediated (NDA, 2010e; NDA, 2014b). The chemistry of the groundwater to which the waste packages become exposed is therefore an important factor in determining the rate of radionuclide release (NDA, 2010e). However, it is inevitable that eventually some radionuclides will breach the backfill, and once this occurs the geosphere becomes the final barrier preventing the release of radionuclides to the surface (Morris et al., 2011). The migration of radionuclides through the geosphere will vary with rock type. This is predominantly controlled by the hydrology of the area, although the reaction of radionuclides with minerals will also exert significant control (NDA, 2010d). Therefore, in order to understand the migration of radionuclides it is essential to understand their reactions with the mineral phases which constitute the host rock (Vines and Beard, 2012).

2.1.5. Conditions within a Cementitious GDF

Under the current generic safety case for ILW, the majority of the cement within a GDF is likely to be the Nirex Reference Vault Backfill (NRVB). This consists of Ordinary Portland Cement (OPC), limestone flour, and hydrated lime in a 256:291:100 ratio, mixed with water in a 1.8:1 ratio (NDA, 2010e; Butcher et al., 2012; Telchadder et al., 2012). After closure a GDF will become re-saturated by groundwater (NDA, 2010e). In a GDF

utilising NRVB this will lead to high pH and the formation of C-S-H (Calcium-Silica-Hydrate) gels ($xCaO{\cdot}SiO_2{\cdot}yH_2O$) with a Ca : Si ratio of 0.7 – 1.7 (Pointeau et al., 2001; Pointeau et al., 2004; Grive et al., 2011). As C-S-H phases have large surface areas and a high affinity for both cations and anions (Schlegel et al., 2004), their formation is expected to increase the sorption of radionuclides, thereby reducing their mobility (NDA, 2010e). The dissolution of NRVB in groundwater creates a hyperalkaline environment, which in turn causes the hydrolysis and precipitation of metal ions, thereby limiting the transport of cationic radionuclides (NDA, 2010d; Morris et al., 2011). Chambers et al. (2003) have investigated the evolution of pH within a GDF by modelling the dissolution of portlandite ($Ca(OH)_2$) and C-S-H gel in pure water. It is accepted that the pH of the cement leachate will initially be ~ 13 falling to ~ 10.5, 100 000 years after closure, and will contain elevated levels of Na, K, and Ca (Small and Thompson, 2009; Butcher et al., 2012). It is expected that an alkaline environment will also promote the sorption of cationic radionuclides by generating negatively charged surfaces on minerals (NDA, 2010d).

An abundance of iron metal within the repository, from the wasteform and structural materials, is expected to lead to chemically reducing conditions post-closure, as a result of iron corrosion (Butcher et al., 2012). These conditions are intended to further decrease the mobility of redox sensitive actinides such as U, Np and Pu which tend to form less densely charged '–yl' species in their higher oxidation states and are therefore most susceptible to hydrolysis (and precipitation) in their reduced states (Morris et al., 2011).

2.1.6. Conditions in the Far-Field of a Cementitious GDF

The cement leachate generated by the EBS of a cementitious GDF will create an alkaline plume extending out into the far-field known as the Chemical Disturbed Zone (CDZ) (NDA, 2010d). The pH of the leachate in the CDZ is expected to gradually fall back to that typical of the local groundwater with both time since re-saturation, and distance from the facility. Therefore, alkaline to circumneutral pH, as well as reducing, low carbonate

conditions are still expected in the far-field of a cementitious GDF (Moyce et al., 2014). The behaviour and mobility of radionuclides in this area will be predominantly controlled by their interactions with the mineral phases which comprise the host rock in which the GDF has been sited (NDA, 2010d).

2.2. Minerals Phases

The mineral phases with which a radionuclide containing groundwater comes into contact often significantly impact its migration (NDA, 2010d). Radionuclide interactions with biotite, quartz, orthoclase, cement, δ-MnO_2, triclinic (Na)-birnessite, hausmannite, and rhodochrosite have been investigated in this thesis; as such their mineralogy is discussed here.

2.2.1. Biotite, Quartz, and Orthoclase (mineralogy and behaviour at high pH)

Biotite, quartz, and orthoclase are common, rock-forming, silicate minerals. They are ubiquitous in the environment and would be expected to be major constituent phases of the host rock of a GDF sited in hard rock (Deer et al., 1992; NDA, 2010a).

2.2.1.1. Biotite

Biotite is a layered, iron-bearing, silicate mineral with a 2:1 sheet silicate structure (monoclinic, space group C2/m) (Deer et al., 1992). Two layers of Si^{4+} and Al^{3+} tetrahedra (T) sandwich a layer of Mg^{+} and Fe^{2+} octahedra (O) to form T-O-T layers with a negative charge (due to the Al^{3+}), which is balanced by interlayer K^{+} (Bailey, 1984). The Mg : Fe ratio of the octahedral layer can be varied to create a series of minerals, including phlogopite, siderophyllite, annite, and eastonite, which are collectively known as biotite (Rieder et al., 1999). However, annite, the pure Fe end-member, does not occur naturally (Deer et al., 1992). Substitution of Al into both the octahedral and tetrahedral sites is commonly observed in natural biotite, leading to the formation of siderophyllite $[K_2Fe_4Al_2(Si_4Al_4O_{20})(OH)_4]$ and eastonite $[K_2Mg_4Al_2(Si_4Al_4O_{20})(OH)_4]$ end-members.

Ideally the octahedral sites in biotite are completely filled but vacancies do occur. The distribution of octahedral sites occupied by Mg or Fe, as well as the tetrahedral sites by Si or Al, is unexplained and appears random, although there is some indication the Fe^{3+} prefers the smaller octahedral sites (Deer et al., 1992).

The weathering of biotite under environmental conditions always produces kaolinite; however, a number of different intermediates can be observed when the conditions, chemical environments, and fluid compositions are varied (Gilkes and Suddhiprakarn, 1979; Meunier and Velde, 1979; Banfield and Eggleton, 1988; Dong et al., 1998). Under alkaline conditions biotite dissolution releases both K^+ from the interlayer, and Al, Si, Mg, and Fe from the framework, into solution. This increase in the solution concentration of Al, Mg, and Fe leads to the formation of vermiculite ($(Mg(Mg,Fe^{3+},Al^{3+})_6[Si_4Al_4O_{20}](OH)_4 \cdot nH_2O$) a sheet silicate mineral with hydrated cations in the interlayer (Murakami et al., 2004; Samson et al., 2005; Sugimori et al., 2008). This transformation has been shown to occur *via* a direct modification of the biotite structure, continuous 2:1 layers can be observed by transmission electron microscopy (TEM) with both 10 Å and 14 Å layers, indicative of biotite and vermiculite, respectively (Banfield and Eggleton, 1988). Vermiculitisation is limited by the rate of Al dissolution and leads to an overall release of Si and K into solution.

2.2.1.2. Quartz

Quartz is a common rock-forming silicate mineral, comprised of Si^{4+} tetrahedra arranged into hexagonal or trigonal helices (trigonal, space group $P3_121$) with the chemical formula SiO_2 (Deer et al., 1992). Pure quartz is colourless, transparent, and very hard but inclusions of other minerals or trace impurities can form a wide variety of colours. Along with its chemical durability, the hardness of quartz leads to its abundance in a wide range of environments (Deer et al., 1992). Under alkaline conditions the deprotonation of surface Si tetrahedra to form $\equiv Si - O^-$ is thought to lead to the polarisation and subsequent weakening

of the Si – O bonds and dissolution of silica. The formation of surface ≡Si – O^- species at alkaline pH is therefore considered to be a precursor to quartz dissolution; thus quartz dissolution is expected at hyperalkaline pH (Brady and Walther, 1989).

2.2.1.3. Orthoclase

Orthoclase is a type of K-feldspar with the chemical formula $KAlSi_3O_8$. Its crystals have monoclinic morphology, although a 'tweed' texture can often be observed under a microscope which results from fine twinning with strands of triclinic geometry. Once formed the very finely twinned lamellae are relatively stable and so remain as pseudo-monoclinic orthoclase, rather than reordering to form the fully triclinic microcline (Deer et al., 2001). Natural orthoclase can contain relatively small amounts of $CaAl_2Si_2O_8$, although this is more common in Na-feldspars, as well as limited amounts of Ba, Ti, Fe^{2+}, Fe^{3+}, Mg, Sr, and Mn (Deer et al., 1992). Under the hyperalkaline conditions relevant to this thesis, mild stoichiometric dissolution of orthoclase is expected (Deer et al., 2001; Teng et al., 2001).

2.2.2. Cement

One cementitious material currently being considered as a backfill is Nirex Reference Vault Backfill (NRVB) (NDA, 2010e; Vines and Beard, 2012). This material has been shown to be fluid enough to flow across the vault to reach and surround the waste containers and can also be cut using a water jet, aiding the ease of retrieval if required (McCall et al., 1997; Crossland, 2007). The NRVB will also undergo partial dissolution and create a hyperalkaline environment in which the solubility, and consequently mobility, of cationic radionuclides is minimised, as well as providing a mineral surface for sorption (Braney et al., 1993; NDA, 2010e).

Cement generally consist of OPC mixed with an aggregate (typically gravel, sand, or crushed rock) and hydrated using water; however, small amounts of chemical admixtures

can be added to modify the properties of the final cement (PCA, 2016). Ordinary Portland Cement is predominantly a mixture of calcium, silica, alumina, and iron oxides, but will normally include other oxide impurities (comprising < 5 %) including Mn, Ti, Mg, K, and Na (PCA, 2016). One cubic metre of NRVB contains: 450 kg OPC, 170 kg limestone flour, 495 kg hydrated lime, and 615 kg water (Crossland, 2007). Once set, X-ray diffraction (XRD) of NRVB has shown it to be predominantly comprised of calcite, with significant amounts of calcium hydroxide and portlandite, minor quantities of $Ca_4Al_2O_6CO_3 \cdot 11H_2O$ and $Mg_6Al_2CO_3(OH)_{16} \cdot 4H_2O$ (hydrotalcite), and trace amounts of ettringite and quartz (Baston et al., 2010). However, this is misleading since cement phases, including NRVB, contain large amounts of Calcium-Silicate-Hydrate (C-S-H) phases which lack long range order and therefore do not contribute to the XRD pattern. The cement phase used throughout this thesis has been chosen to be representative of NRVB.

The cement setting process typically takes place over a period of weeks or months, although a viscoelastic skeletal solid capable of supporting applied stress generally forms within 24 hours of water addition. When OPC is mixed with water, the very soluble phases, such as the aluminates, dissolve. This is rapidly followed by the precipitation of much less soluble phases such as ettringite, often leading to the formation of an ettringite coating on the aggregate particles. Calcium and silica containing phases are also dissolved and the ions re-precipitated as C-S-H phases. These phases covert the concentrated suspension of flocculated particles into the viscoelastic skeleton responsible for the initial strength and then continue to precipitate in the pore spaces until there is no water, OPC, or space remaining. During this time the cement will continue to harden and gain strength as the pore spaces become filled, a process known as hardening (Gartner et al., 2001; Nonat, 2004; Richardson, 2004).

C-S-H phases are important in determining radionuclide interactions with cement, and have been found to control U(VI) behaviour in systems containing hardened cement paste (Macé et al., 2013). The structure of C-S-H phases is related to that of 14 Å tobermorite and jennite, and consists of layers of Ca-O flanked by chains of silicate tetrahedra with Ca and water in the interlayer (Chen et al., 2004; Bonaccorsi et al., 2005). However, C-S-H phases, particularly the C-S-H gels formed upon hydration of OPC, contain a substantial concentration of defects leading to a disordered structure (Nonat, 2004). This means C-S-H gels can accommodate a range of Ca/Si ratios, which can range from 0.67 to ~ 2 (Chen et al., 2004), creating a variety of different C-S-H phases.

2.2.3. Mn-Minerals

Mn-minerals, like Fe minerals, are ubiquitous in the environment and Mn oxides often occur as coatings or fine grain aggregates (Dixon et al., 1990; Post, 1999). Therefore, they will be ubiquitous within the host rock of a GDF sited in higher strength or lower strength sedimentary rock, which comprises the final barrier to radionuclide release to the biosphere (NDA, 2010c; 2010d). However, while many studies have shown Fe minerals to immobilise radionuclides (Brookshaw et al., 2012 and references therein), Mn-minerals have received comparatively little attention despite the co-location of radionuclides with Mn-minerals (section 2.4.1.1.3) (Means et al., 1978; Duff et al., 1999; Powell et al., 2006).

2.2.3.1. δ-MnO_2

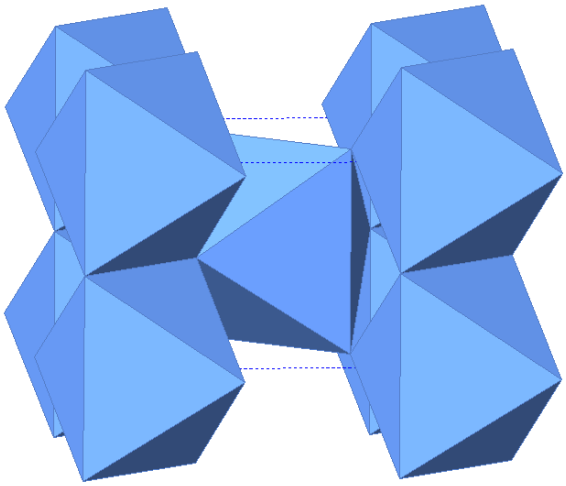

Figure 2.4: δ-MnO_2 structure, MnO_6 octahedra.

δ-MnO_2, along with birnessite, is one of the most common Mn-minerals and is ubiquitous in soils and sediments (Burns and Burns, 1977; Chukhrov and Gorshkov, 1981; Post, 1999; Dixon and White, 2002; Schulze, 2002). It is a fine-grained poorly crystalline Mn(IV) oxide (Roy, 1981; Post, 1999) and is generally considered to have the same structure as vernadite (Figure 2.4), but is often denoted δ-MnO_2 when produced synthetically (Burns and Burns, 1977; Chukhrov et al., 1980; Chukhrov and Gorshkov, 1981; Roy, 1981; McKenzie, 1989; Dixon and White, 2002). Biogenic-MnO_2 is a common form of Mn oxide in the environment (Tebo et al., 1984; Nealson et al., 1988; Tebo, 1991; Tebo et al., 1997; Marble et al., 1999; Tebo et al., 2004; Spiro et al., 2010). Some bacterial strains have been shown to produce biogenic-MnO_2 with a structure very similar to that of δ-MnO_2, although the crystallinity of the biogenic version is often lower (Bargar et al., 2000; Villalobos et al., 2003; Webb et al., 2005). Some studies suggest a discrepancy between the affinity of δ-MnO_2 and biogenic-MnO_2 for cationic contaminants (Nelson et al., 1999; Nelson et al., 2002; Villalobos et al., 2003; Tani et al., 2004; Villalobos et al., 2005; Tanaka et al., 2011; Wang et al., 2013), although some authors found δ-MnO_2 to be more reactive (Tanaka et al., 2011; Wang et al., 2013), while others found the opposite (Nelson et al., 1999; Nelson

et al., 2002; Tani et al., 2004; Villalobos et al., 2005). This could be due to variation in washing of the biogenic-MnO_2 prior to sorption experiments since the presence of organic ligands released by the parent bacteria could hinder reactivity, although this hypothesis has not yet been tested (Tanaka et al., 2011).

Some authors view δ-MnO_2 as a disordered variety of birnessite (Giovanoli, 1970; Giovanoli and Brutsch, 1979), where disorder in the stacking order of the layers leads to the loss of the basal planes in the XRD pattern. However, treatment of δ-MnO_2 in water at high pressure produced additional lines in the diffractions pattern (at approximately 0.96 and 0.48 nm), while no change was observed in the diffraction pattern of synthetic birnessite after comparable treatment (Burns et al., 1974), suggesting these phases are not identical. The authors instead related δ-MnO_2 to todorokite rather than to birnessite and concluded that it should be regarded as a discrete phase. It is now thought that δ-MnO_2 contains both edge-shared and corner-shared Mn octahedra (Manceau et al., 1992; Dixon and White, 2002).

Vernadite is found in nature (Tebo et al., 1984; Tebo, 1991), and δ-MnO_2 is synthesised (Villalobos et al., 2003), under circumneutral to mildly alkaline conditions and so stability under these conditions is expected. Since Mn(IV) is favoured under oxic conditions and at high pH (Tebo et al., 2004), δ-MnO_2 is also expected to be stable at high pH.

2.2.3.2. Triclinic (Na)-Birnessite

Birnessite refers to a group of Mn oxide minerals with the general formula $(Ca,Na,K,Mn,H)_x(Mn(IV/III))_2O_4 \cdot 1.5H_2O$, they are comprised of layers of edge-shared MnO_6 octahedra separated by water molecules and cations (McKenzie, 1989; Al-Attar and Budeir, 2011). Globally birnessites are the most commonly occurring Mn oxides found in soils and sediments (McKenzie, 1989; Post, 1999).

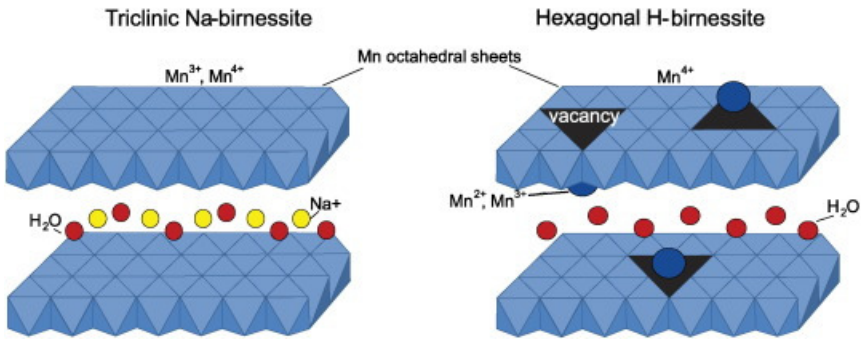

Figure 2.5: Schematic diagram (a) triclinic Na-birnessite and (b) hexagonal H-birnessite. Reproduced from (Ling et al., 2015).

Birnessite can contain a range of ions in the interlayer (*e.g.* K^+ and Ca^{2+}), leading to a group of layered minerals with similar structures (Post et al., 2008). The two major types of birnessite are hexagonal birnessite, which is formed under acidic conditions, and triclinic (Na)-birnessite, which is formed under alkaline conditions (Glover, 1977; Lanson et al., 2002; Fischer, 2011). Both of these birnessite types consist of layers of Mn(III/IV) in edge-sharing MnO_6 octahedra (Figure 2.5) (Post et al., 2002; Fleeger et al., 2013). However, triclinic (Na)-birnessite does not contain any cation vacancies and instead has a higher Mn(III):Mn(IV) ratio (~1:3) (Villalobos et al., 2005). However, a large number of vacancies are expected in hexagonal birnessite to compensate for the Mn^{2+}, Mn^{3+}, and H^+ which replace the hydrated Na+ in the interlayer (Lanson et al., 2002; Ling et al., 2015). Some of these vacancies are capped by Mn^{2+} which reduces the symmetry of the phase (Lanson et al., 2002; Ling et al., 2015). The presence of Mn(III) leads to a permanent negative charge on the layer, in triclinic (Na)-birnessite this is balanced by Na^+ contained in the single layer of water molecules present in the 7 Å interlayer. The acidification of triclinic (Na)-birnessite leads to its conversion to hexagonal H-birnessite (Fischer, 2011). Here, the interlayer cations are leached from the interlayer and replaced by H^+. Ling et al. (2015) suggest that hexagonal birnessite is favoured below pH 8.2, while triclinic (Na)-birnessite is favoured above this pH. The authors also observed that a portion of the Mn^{2+} in the interlayer of hexagonal birnessite was replaced by Na^+ when exposed to a high

pH solution containing Na^+ (Ling et al., 2015). Fleeger (2012) found that when hexagonal birnessite was added to a 0.1 M NaOH solution at pH 13, it was transformed into triclinic (Na)-birnessite within 20 minutes.

2.2.3.3. Hausmannite

Hausmannite has the formula $Mn(II)Mn(III)_2O_4$. It has a spinel-like structure with the Mn(II) located in tetrahedral sites while the Mn(III) is located in octahedral sites (Figure 2.6) (Goodenough and Loeb, 1955; Jarosch, 1987; McKenzie, 1989; Post, 1999; Dixon and White, 2002). However, while most spinels are cubic, hausmannite is tetragonal (McKenzie, 1989; Dixon and White, 2002).

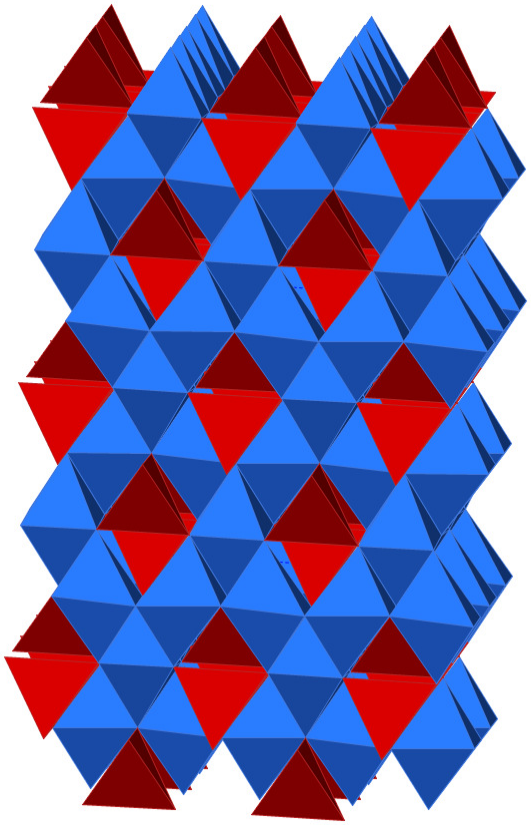

Figure 2.6: Hausmannite structure. Blue = Mn(III) octahedra; red = Mn(II) tetrahedra.

Hausmannite is susceptible to oxidation under alkaline conditions and is therefore less common in soils than δ-MnO_2 or birnessite (McKenzie, 1989). However, whilst the

formation of hausmannite in soils is improbable, it may persist in a physically protected, coated form (Dixon and White, 2002), or under reducing conditions. Chukhrov and Gorshkov (1981) examined 100 soils from a range of countries and found hausmannite to be the 5th most common Mn-mineral. In the presence of oxygen hausmannite undergoes slow oxidation to manganite (MnOOH) (Bricker, 1965; Kirillov et al., 2009). As a result, the hausmannite used in this thesis was formed and handled anaerobically and its stability was monitored periodically.

Cornell and Giovanoli (1988) found that at 70°C and under very high pH conditions, hausmannite underwent a slow conversion to birnessite, although this process was not complete after a period of several months. The conversion still occurred when KOH was replaced with NaOH, while decreasing the temperature to 25°C significantly decreased the rate. However, the transformation of hexagonal birnessite into hausmannite has been observed at mildly alkaline pH (8.0 – 8.5) in the presence of $Mn^{2+}_{(aq)}$ (Lefkowitz et al., 2013).

2.2.3.4. Rhodochrosite

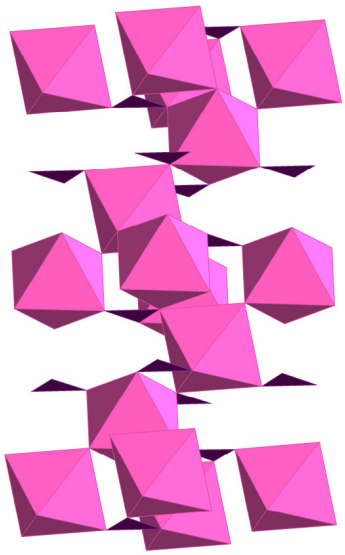

Figure 2.7: Rhodochrosite structure. Pink = Mn; purple = Carbonate.

Rhodochrosite ($MnCO_3$) is a Mn(II) carbonate mineral often found in hydrothermal veins (Roy, 1981). It crystallises in a trigonal system (Roy, 1981; Doner and Gossel, 2002), giving a crystal structure (Figure 2.7) similar to that of calcite (Roy, 1981) and siderite and is often found in solid solution with calcite (Roy, 1981). Rhodochrosite has low solubility (Doner and Gossel, 2002), and forms under alkaline reducing conditions with high CO_2 partial pressures (Hem, 1963).

2.3. Radionuclide Migration

When radionuclides are released into the geosphere their migration can be influenced by a number of abiotic process, including: the redox conditions, precipitation, sorption and incorporation reactions, and the presence or formation of colloids. In addition microbes and associated biogeochemical processes can also have an important impact on the migration of radionuclides (Konhauser et al., 2002; Lloyd and Macaskie, 2002; Lloyd, 2003; NDA, 2010d; West et al., 2010; Newsome et al., 2014). For example, microbes can couple the oxidation of carbon compounds to the reduction of radionuclides, which in turn leads to the formation of less soluble oxidation states (Lovley et al., 1991; Lovley and Phillips, 1992; Francis et al., 1994; Shelobolina et al., 2004; Wu et al., 2006). Further, some microorganisms can incorporate radionuclides into insoluble biominerals (Macaskie et al., 1992; Mondani et al., 2011), sorb them onto their cell structure (Beveridge and Murray, 1980; Suzuki and Banfield, 1999; Lloyd and Macaskie, 2000), or produce biofilms (Anderson et al., 2007). However, while these processes are important, this thesis focuses on the abiotic processes that influence radionuclide migration.

2.3.1. Precipitation

The purpose of creating a hyperalkaline environment is to encourage the precipitation of radionuclides (NDA, 2010d; Vines and Beard, 2012; NDA, 2014b). Under hyperalkaline conditions cationic radionuclides, especially those with high charge density, will hydrolyse

water leading to the formation of insoluble hydroxide phases. For example U(IV) exists in solution as $U^{4+}_{(aq)}$, with a high charge density. It is therefore strongly attracted to the $O^{\delta-}$ atom of a water molecules, to which it forms a bond, breaking one of the O-H bonds and releasing H^+ (as H_3O^+) into solution. This process forms U(IV) hydroxides which are then expected to precipitate out of solution, immobilising the U(IV). However, U(VI) exists in solution as the uranyl species, $[U(VI)O_2]^{2+}$, with a much lower charge density. This means that while $[U(VI)O_2]^{2+}$ is still attracted to the $O^{\delta-}$ of water molecules this interaction is no longer strong enough to break the O-H bonds. Hydroxides are therefore not as readily formed, hence the reduction of U(IV) to U(VI) is desirable within a GDF.

In addition to high pH, the proposed cementitious backfill for ILW (NRVB) will also form a leachate with high K^+ and Na^+, and later Ca^+, concentrations (Small and Thompson, 2009; Butcher et al., 2012). This is expected to lead to the oversaturation of a range of radionuclide-containing sodium and calcium phases, such as uranates, further limiting radionuclide solubility (Yamamura et al., 1998; Gorman-Lewis et al., 2008). Given this, it is critical to understand how U(VI) will behave at high pH and in the presence of the high alkali and alkaline earth concentrations (particularly, Na^+, K^+, Ca^{2+}) expected in cement leachates. This is particularly important as an unforeseen mechanism which allowed uranium to remain in the aqueous phase could lead to increased migration away from a GDF.

2.3.2. Sorption

The migration of radionuclides can be impeded by their sorption to a range of minerals in the geosphere (NDA, 2010c). Sorption is a general term and encompasses a number of ways in which ions can interact with mineral surfaces. These include the formation of both outer-sphere and inner-sphere adsorption surface complexes, as well as absorption *via* cation exchange and incorporation (Krauskopf and Bird, 1995; Sposito, 2004). During outer-sphere adsorption an ion retains its hydration sphere and is electrostatically bonded

to the surface through these water molecules. Alternatively, inner-sphere adsorption complexes can form where the ions hydration sphere is lost and a bond is formed directly with the mineral surface (Krauskopf and Bird, 1995; Sposito, 2004). Cation exchange is observed on minerals whose structural framework possesses a permanent negative charge due to isomeric substitution, which is then balanced by cations. It is common in layered minerals (such as birnessite; section 2.2.3.2) and clays (Al-Attar and Dyer, 2002; Beresford, 2005; Lopano et al., 2011; Seliman et al., 2014). Here, interlayer, or structural, cations are exchanged for absorbing contaminant cations. Since inner-sphere adsorption results in a stronger interaction with the surface than outer-sphere adsorption, it is important to determine the mechanism by which adsorption occurs in order to predict the impact on contaminant mobility as the extent and rate of desorption is expected to differ (Strawn and Sparks, 1999; Catalano et al., 2008).

Occasionally, generally at high adsorbate concentration, adsorption can also lead to the formation of a surface precipitate (Sposito, 2004). This can occur when there is a high density of ions adsorbed onto a surface (or in a particular area of a surface) and these are well organised on a lattice, which in turn can lead to the formation of a phase on top of the original surface.

The extent of the sorption of an ion to a mineral is often described using R_d and K_d values. Both of these represent the ratio of the ion concentration in solution to that on the solid ([solution]/[solid]), however, while K_d values must describe at system at equilibrium, R_d values can be used to describe the ratio at any given point. As well as the mineral present, the K_d value of a system is also dependent on the solid:solution ratio, ionic strength, and pH (OECD and NEA, 2012). However, by determining the K_d value under a range of conditions it is possible to determine thermodynamic logK values, for the reaction of a specific radionuclide with a specific mineral (Appelo and Postma, 2005). Thermodynamic logK values are independent of these parameters and can therefore be used in

thermodynamic models to predict the migration of radionuclides in various scenarios (Appelo and Postma, 2005).

In models used to predict radionuclide mobility, sorption to bulk mineral phases is generally assumed to be reversible (NDA, 2010d). In the case of outer-sphere complexes, which do not require the exchange of a ligand to become desorbed, this is generally a valid assumption. However, systems containing inner-sphere adsorption complexes, or where radionuclides are located in the interlayer of layered minerals, can exhibit irreversibility (Pan et al., 2004; Sajih et al., 2014; Sheng et al., 2014; Boggs et al., 2015; Fuller et al., 2015). For this reason it is important to understand the mechanism of sorption and to investigate desorption. In order to study the desorption of radionuclides from minerals the process is encouraged, usually by the addition of a competing ligand, surface, or metal (e.g. Sims et al., 1996; Park and Hahn, 1999; Rigol et al., 2000; Iijima et al., 2010; Sherriff et al., 2015), or by the removal of the residual radionuclide from the solution phase (e.g. Park and Hahn, 1999; Markai et al., 2003; Um et al., 2004; Savoye et al., 2006; Sajih et al., 2014). These experiments can then be used to generate R_d values (R_d = [solid (mol/g)] / [solution (mol/mL)]) which can be compared to K_d values to indicate irreversibility in a system (Sajih et al., 2014).

2.3.2.1. Incorporation

As well as adsorbing to the surface of a mineral, radionuclides can also become incorporated into mineral structures. This generally occurs when a mineral phase is formed in the presence of radionuclides which then become substituted into the mineral structure (NDA, 2010d). However, incorporation can also occur when a mineral phase is in dynamic equilibrium with a solution, *i.e.* it is constantly dissolving and re-precipitating. As this re-precipitation occurs radionuclides which have been adsorbed onto the mineral surface *via* inner-sphere sorption, can become 'buried' in the mineral structure, taking the place of chemically similar elements as the phase extends around them (Krauskopf and Bird, 1995;

NDA, 2010d). Generally, when radionuclides become incorporated into a mineral structure they take the place of an ion with a similar ionic radius (Krauskopf and Bird, 1995). A similar sized ion is required since a small distortion in the structure can usually be tolerated, while a large distortion is likely to lead to the disruption of the mineral structure. For example, the lattice of magnetite, which normally contains Fe(II) and Fe(III), is able to expand or contract in order to accommodate cations with different radii (Cornell and Schwertmann, 2003). As a result, magnetite is capable of incorporating a range of trace metals (*e.g.* Co^{2+}, Ni^{2+}, Zn^{2+}, Cu^{2+}, Mn^{2+}, and Cd^{2+}) into its structure (Sidhu et al., 1978). Substitution by ions with the same charge is ideal. However, similarly charged ions can often also be accommodated though this creates a charge imbalance. This can be addressed by further substitution, incorporation of an additional ion, or the creation of a vacancy site (Appelo and Postma, 1999). In the case of magnetite, Ti(IV) can be incorporated into structure in the place of Fe(III), which is then accompanied by the reduction of the remaining Fe(III) in the unit cell to Fe(II) to maintain the charge balance (Pearce et al., 2006). In birnessites cation vacancies (sometimes capped with Mn^{2+}) are a common mechanism of maintaining charge balance, although this can also be achieved by altering the Mn(III)/Mn(IV) ratio (Appelo and Postma, 1999). Once radionuclides have been incorporated into minerals they can only be released back into solution by the dissolution of the host phase. Given this, structurally incorporated radionuclides are much less accessible and their migration is likely to be significantly retarded (Vines and Beard, 2012; Marshall et al., 2014).

2.3.3. Colloids

Whilst adsorption of radionuclides to, and absorption into, bulk mineral phases decreases their mobility, this may not be the case if a radionuclide is associated with a nano-particulate colloidal phase. The term colloid is used to describe a particle 1 – 1000 nm in size, in at least one dimension, and implies that the particles are dispersed within a medium

(IUPAC, 1997). Due to their small size, Brownian motion can keep colloids suspended in solution over geological timescales making them relevant to geological disposal (Wold, 2010). Colloids formed within a GDF, or transported though it by groundwater flow, have the potential to promote the migration of radionuclides (Vines and Beard, 2012). This is particularly important for cationic radionuclides, which are expected to precipitate out as hydroxides or sorb to mineral phases, since the formation of colloids could allow them to remain in solution, facilitating transport by diffusion and advection.

There are two ways in which colloids can facilitate the transport of radionuclides. Firstly, radionuclides can sorb to pre-formed colloids. This is generally caused by the high negative charge density associated with colloid surfaces, which prevents aggregation, causing the electrostatic attraction of cationic radionuclides which then sorb to negatively charged binding sites. Secondly, radionuclides may form colloidal precipitates of which they are an intrinsic part.

Intrinsic colloids formed from a range of radionuclide oxides have been observed (Walther and Denecke, 2013) (*e.g.* $Pu(OH)_4$ (Parry et al., 2011) and ThO_2 (Walther and Denecke, 2013)). Studies showing radionuclides bound to a range of colloids (Swanton et al., 2009), including NRVB-derived colloids (Gardiner et al., 1998; Swanton et al., 2009) and colloids of iron oxides (Gardiner et al., 1990) have also been observed. At the Nevada Test Site, USA, plutonium and fission products such as Co, Cs, and Eu from nuclear weapons tests have been found to have migrated 1.3 km from the original detonation site over approximately 30 years. This is significantly faster than predicted by models which do not include a contribution from colloid-facilitated transport. Plutonium, for example, was found to be associated with the colloidal (7 – 1000 nm) fraction, suggesting that colloidal transport was responsible for its accelerated migration (Kersting et al., 1999). Further investigation of the site revealed U was also present in colloidal form, associated with Cs and silicates, and as an oxide hydrate (Utsunomiya et al., 2009). The migration of colloid

associated Pu over 3 km has also been observed at Mayak, a Russian nuclear waste reprocessing facility (Novikov et al., 2006). Here, migration was found to occur at a comparable rate to that observed at the Nevada Test Site. Nano–secondary ion mass spectrometry suggested that the mobile Pu was associated with iron oxides (Novikov et al., 2006).

Similarly to aqueous radionuclides, colloids can also be removed from solution by sorption to mineral surfaces (Arnold et al., 2006; Walther and Denecke, 2013), although this is not generally expected at high pH when many colloids and mineral surfaces would be expected to be negatively charged. Colloids can also aggregate and settle out of solution, particularly under changing geochemical conditions, although again this is not generally expected at high pH due to the electrostatic repulsion caused by the negative surface charges. However, it is important to determine the stability of any colloids which could form under conditions within a GDF due to their potentially large impact on radionuclide migration.

2.4. Radionuclide Geochemistry

2.4.1. Uranium

The nuclear industry has produced large quantities of waste uranium worldwide. Much of this is stored as spent nuclear fuel or ILW, and is destined for geological disposal. In addition many nuclear sites around the globe suffer from uranium contamination of the surface and/or subsurface. The two most abundant isotopes of uranium are ^{238}U and ^{235}U, which both undergo decay *via* emission of an alpha particle to ^{234}Th and ^{231}Th, respectively. Given its prevalence, and the long half-lives of both ^{238}U and ^{235}U ($t_{½} = 4.46 \times 10^{9}$ years and $t_{½} = 7.03 \times 10^{8}$ years, respectively), uranium behaviour will play an important role in any GDF safety case.

In ILW, uranium will be present in a range of redox states including, but not limited to, U(VI) and U(IV) (Health and Safety England et al., 2007). Under reducing conditions,

highly insoluble U(IV) (section 2.3.1) would normally be expected to dominate uranium behaviour. However, under alkaline, mildly reducing conditions U(VI) is expected to be relatively stable and is likely to be present for a significant time post-closure (Gaona et al., 2012). U(VI) exists in solution as the linear uranyl moiety UO_2^{2+}, the solubility of which is limited by equilibrium with the solid alkali/alkaline-earth "uranates" (*e.g.* $Na(UO_2)O(OH)\cdot(H_2O)_{0\text{-}1}$ and $CaUO_4$) which dominate speciation. Very low solution concentrations (~10^{-9} M) of U(VI) are therefore expected in solution (Yamamura et al., 1998; Gorman-Lewis et al., 2008).

$$CO_{2(g)} + H_2O_{(l)} \leftrightarrow H_2CO_{3(aq)} \leftrightarrow H^+_{(aq)} + HCO^-_{3(aq)} \leftrightarrow 2H^+_{(aq)} + CO^{2-}_{3(aq)} \quad (2.1)$$

Under atmospheric conditions, CO_2 dissolves in water to form carbonate (CO_3^{2-}) (Equation 2.1). In alkaline solutions $H^+_{(aq)}$ released when ($H_2CO_{3(aq)}$ splits into $H^+_{(aq)}$ and $HCO_3^-{}_{(aq)}$) is increasingly desired as the pH decreases, driving the equilibrium to the right. In turn this increases the carbonate concentration in solution and decreases the pH (Stumm and Morgan, 1996; White, 2013). The presence of carbonate and bicarbonate ligands in solution increases the solubility of UO_2^{2+} as these react to form very stable, soluble complexes (Barnett et al., 2000; Runde, 2000). This means that carbonate complexes generally control U(VI) solubility in alkaline systems containing carbonate. However, very low dissolved carbonate concentrations are expected within a GDF since this will be isolated from air after the initial emplacement period and calcite precipitation is expected to remove much of the residual carbonate from solution (Dow and Glasser, 2003; Smith et al., 2015). Therefore, for an experiment to be relevant to deep geological disposal, the dissolved carbonate concentration must be controlled. In the absence of carbonate, hydroxide species such as $UO_2(OH)_2$, $UO_2(OH)_3^-$, and $UO_2(OH)_4^{2-}$ dominate U(VI) speciation under hyperalkaline conditions. These complexes have low solubility with

aqueous U(VI) concentrations in the order of nM (Barnett et al., 2000; Runde, 2000; Choppin, 2006).

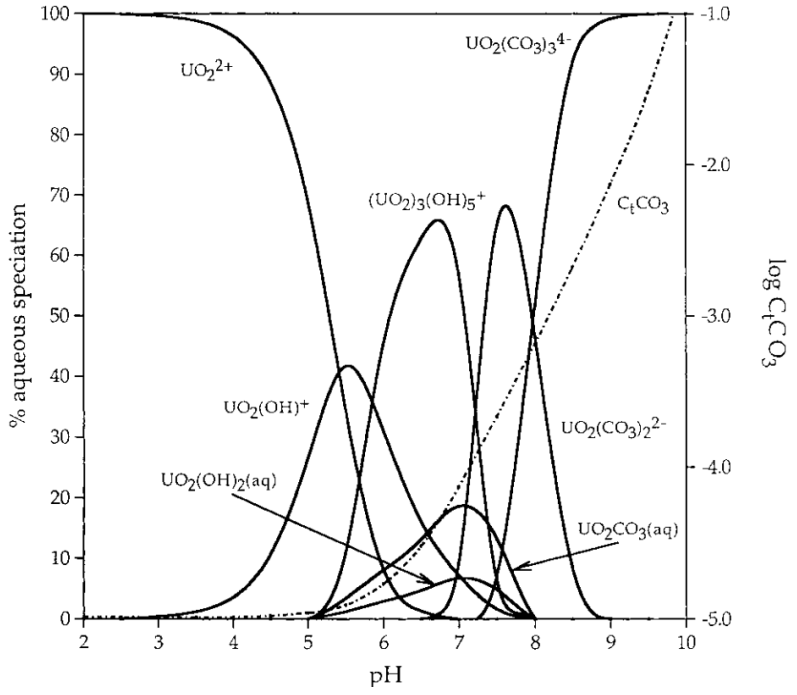

Figure 2.8: Speciation of 1 ppm U(VI) and log total dissolved carbonate (broken line) as a function of pH. Log P_{CO2} = -3.5 in 0.1 M $NaNO_3$. Taken from (Barnett et al., 2000).

As the pH decreases with both distance from the facility and time since closure, U(VI) speciation will become increasingly influenced by positively charged hydroxide species, such as $UO_2(OH)^+$ and $(UO_2)_3(OH)_5^+$, until they dominate at ~ pH 8 (Figure 2.8). Below pH 5, free UO_2^{2+} dominates U(VI) speciation (Kaplan et al., 1998).

2.4.1.1. Interactions of U(VI) with Minerals

2.4.1.1.1. Biotite, Quartz, and Orthoclase

The interaction of U(VI) with biotite at circumneutral pH has been observed in low carbonate systems (Brookshaw et al., 2015). However, much lower levels of sorption are observed in systems with elevated carbonate concentrations due to the formation of uranyl-carbonate species (Ames et al., 1983; Brookshaw et al., 2015). Modest reduction of U(VI)

to U(IV) has also been observed over extended periods of time in a low carbonate biotite system (Ilton et al., 2006). The uptake of U(VI) has not been as widely studied under high pH conditions; although the co-location of U and biotite has been seen under mildly alkaline (pH 8.9 – 9.2), reducing conditions at the Tono uranium deposit, Japan (Yoshida, 1994). More generally, the interaction of any cations with biotite under alkaline conditions has received little attention in the literature (alkaline alteration of biotite is discussed in section 2.2.1.1.).

The sorption of U(VI) to both orthoclase (Arnold et al., 1998; Walter et al., 2005; Nebelung and Brendler, 2010) and quartz (Arnold et al., 1998; Arnold et al., 2001; Ilton et al., 2012b) has been observed at circumneutral pH. Above pH 8.5 and in the presence of carbonate, the formation of soluble uranyl-carbonate species leads to U(VI) remaining in solution in the presence of both quartz (Schmeide et al., 2000; Fox et al., 2006; Nebelung and Brendler, 2010) and feldspars (Chardon et al., 2008; Ding et al., 2014; Richter et al., 2016). In contrast, in the absence of carbonate, and therefore under conditions relevant to this study, U(VI) has been found to sorb to quartz (Prikryl et al., 2001) at alkaline pHs of up to pH 9.5. In systems containing orthoclase, molecular dynamics simulations have predicted the formation of inner-sphere $UO_2(CO_3)_2^{2-}$ surface complexes at pHs above 9, albeit at low (0.1 µM) U(VI) concentrations (Kerisit and Liu, 2012; Kerisit and Liu, 2014), suggesting U(VI) sorption to feldspars under alkaline conditions.

Uptake of up to 60 % U(VI) from pH 6 and pH 10 solution by the feldspars microcline and plagioclase has been observed. However, this was reduced at pH 10 in contact with atmospheric CO_2 due to the formation of very stable uranyl carbonate complexes (Chardon et al., 2008). At pH 6 the authors found a threshold initial U(VI) concentration above which U(VI) uptake by plagioclase increased dramatically, suggesting the formation of a surface precipitate. This was supported by scanning electron microscopy (SEM) and atomic force microscopy (AFM), although these techniques found randomly orientated and

distributed becquerelite crystals on the plagioclase surface, suggesting the surface did not play a particularly important role in precipitation (Chardon et al., 2008). The adsorption of U(VI) to quartz at circumneutral pH was also suggested when columns packed with quartz were found to retard U(VI) migration through said columns (Mibus et al., 2007).

2.4.1.1.2. Cement

Numerous studies have observed that the introduction of hardened cement paste, or C-S-H phases, into a system containing aqueous U(VI), results in the removal of U(VI) from solution (Harfouche et al., 2006; Tits et al., 2008; Wieland et al., 2010; Tits et al., 2011; Macé et al., 2013). This uptake has been found to be particularly strong (with R_d values in the region of $10^5 – 10^6$ L kg^{-1}) and fast (equilibrium was reached within 10 days), suggesting and these phases may play an important role in controlling the solution U(VI) concentration (Tits et al., 2008). The authors also found that increasing pH decreased U(VI) uptake, meanwhile an increased aqueous Ca concentration, caused an increase in U(VI) uptake. This suggests that Ca must have a significant influence on U(VI) uptake. Luminescence spectroscopy of U(VI) associated with C-S-H phases identified the presence of four uranium coordination environments: aqueous $U(VI)O_2(OH)_4^{2-}$, a Ca uranate precipitate, and two uranyl silicate-like coordination environments – one of which was thought to be a surface complex and the other was thought to be incorporated into the C-S-H interlayer (Tits et al., 2008). Macé et al. (2013) and Harfouche et al. (2006) used extended X-ray absorption fine structure spectroscopy (EXAFS) to study the interaction of U(VI) with C-S-H phases at pH 13.3. At low loadings (< ~ 0.5 mM) a single uranyl silicate-like uranium coordination environment was identified which was consistent with the incorporation of a uranyl hydroxide species (*e.g.* $U(VI)O_2(OH)_4^{2-}$) into the C-S-H interlayer. In addition, at concentrations > ~ 0.5 mM U(VI), a Ca-uranate-like phase was also observed suggesting that precipitation of a Ca-uranate phase controls U(VI) solubility at elevated concentrations (Macé et al., 2013). The Ca-uranate-like environment has also

been observed by Moroni and Glasser (1995), Tits et al. (2008; 2011), and Smith et al. (2015) over a variety of U(VI) concentrations.

2.4.1.1.3. Mn-minerals

The interaction of U(VI) with iron oxide and hydroxide minerals has received significant attention in the literature and these minerals have been found to be particularly important in controlling the U(VI) concentration in groundwater (Li and Kaplan, 2012). The sorption of U(VI) to, or incorporation into, iron oxide or hydroxide minerals has been widely observed in the literature (Lenhart and Honeyman, 1999; Moyes et al., 2000; Sherman et al., 2008; Yusan and Akyil, 2008; Ilton et al., 2012a; Sun et al., 2012; Marshall et al., 2014). However, the impact of Mn-minerals on U(VI) migration has received comparatively little attention, despite their abundance.

Plutonium has been found sorbed to δ-MnO_2 and rancieite (a Ca-rich member of the birnessite group), under circumneutral pH conditions (McKenzie, 1989; Powell et al., 2006; Francis and Dodge, 2015). Micro-focus XRF mapping has also shown plutonium to be predominately associated with Mn oxides and smectites, as opposed to the Fe oxides which were found to be present in greater abundance (Duff et al., 1999). Mn-minerals therefore have the potential to significantly affect the migration of cations, including U(VI), through the subsurface. This is supported by the work of Al-Attar and Dyer (2002), Mukherjee et al. (2013), and Zou et al. (2010), who observed the removal of U(VI) from solution by birnessite, δ-MnO_2, and birnessite coated sand, respectively. All three studies found U(VI) removal decreased above ~ pH 6; however, all experiments were carried out under oxic conditions in the presence of atmospheric CO_2. Therefore, the observed decrease in sorption at alkaline pHs likely reflects the formation of soluble uranyl carbonate complexes, as frequently observed in studies of U(VI) to Fe oxides (Waite et al., 1994; Barnett et al., 2000; Stewart et al., 2010).

In a limited number of cases, EXAFS has been used to study the coordination environment of Mn oxide associated uranium. Webb et al. (2006) use the technique to study the influence of U(VI) concentration on the structure of Mn oxides formed biogenically in its presence, as well as the coordination of U(VI) within the solid phase. The authors found that low (< 1 μM) U(VI) concentrations had little effect on Mn oxide formation, with a hexagonal phyllomanganate formed with U(VI) adsorbed as a bidentate surface complex. However, at U(VI) concentrations < 4 μM, Mn oxide formation was visibly supressed and a Mn oxide with a poorly ordered tunnel structure, similar to that of todorokite, was formed. The U(VI) associated with the Mn phase was predominantly found in the tunnels as a tridentate complex.

Wang et al. (2013) investigated the adsorption of U(VI) to synthetic and biogenic MnO_2. Sorption to synthetic MnO_2 (δ-MnO_2) was near complete after 48 hours at neutral pH, but was inhibited at alkaline pH due to the formation of uranyl-carbonate complexes. Sorption to biogenic MnO_2 followed the same trends and was only marginally less extensive in the same timeframe. The U L_{III}–edge EXAFS of both minerals were best fit by a split equatorial O shell, indicative of inner-sphere surface complexation, and two U-Mn distances (3.3 – 3.4 and 4.0 – 4.4 Å), suggesting the presence of multiple surface complexes. In the presence of 5 mM carbonate the addition of a C at ~ 2.9 Å was required to model the data, suggesting the formation of a ternary uranyl carbonate complex.

The uptake of U(VI) by synthetic hexagonal birnessite has been studied under acidic conditions (Rihs et al., 2014). Here, the split equatorial O shell, required to reproduce the EXAFS, indicated formation of an inner sphere complex at pH 3 – 6. At pH 3 and 4 the fit included a Mn shell at ~ 3.4 Å suggesting the formation of a bidentate surface complex; this is absent at pH 6 which suggests a change in the coordination environment. However, the data lacks the resolution to determine whether there is an extended U-Mn distance. The uptake of U(VI) by K-birnessite has also been observed (Brennecka et al., 2011). EXAFS

of the U-L_{III} edge suggested the equatorial O shell could be split, although this could not be conclusively determined (Brennecka et al., 2011).

The majority of these studies investigate the interaction of U(VI) with Mn minerals at acidic or circumneutral pH conditions. Relatively few study the high pH, low carbonate conditions expected in the far-field of a GDF, and none of them investigates the reversibility of any of these interactions. In order to understand how the presence of these potentially important mineral phases could impact the migration of U(VI) through the far-field of a GDF, it is important to study the interaction of U(VI) with Mn minerals and their reversibility, under the relevant geochemical conditions.

2.4.1.1.3.1. Other Relevant Mn Oxide, Cation Interactions

Relatively few authors have studied the interaction of U(VI) with Mn-minerals, particularly under alkaline conditions. It is therefore important to consider the literature in which U(VI) interacts with structurally similar minerals, as well as the interaction of a range of cations with Mn-minerals – this section summarises the relevant literature.

The uptake of Tl(I) by hexagonal birnessite has been observed at pH 8, with EXAFS suggesting that this was most likely sorbed as an outer-sphere complex (Peacock and Moon, 2012). In contrast, Cs^+ exchanges for the interlayer Na^+ in a series of sequential steps (Lopano et al., 2009). Firstly, the octahedral sheets delaminate and all of the interlayer Na^+ ions in that layer are replaced by Cs^+, which is then followed by the rapid reassembly of the sheet structure. The authors found that this preferentially occurred in successive sheets of the same birnessite platelets, leading to localised areas of Cs-birnessite. This is in agreement with kinetic modelling of cation exchange in the system (Lopano et al., 2011). The removal of $CoCl^+$ and Sr^{2+} from pH 5 solution has also been observed *via* exchange with hydrogen ions in the interlayer hydroxyl groups of

K-birnessite, the layers of which alternate between that of hexagonal and triclinic birnessite (Ghaly et al., 2016).

The sorption on Pu(VI) to hausmannite in the presence of carbonate has been found to reach a maximum at pH 8, presumably due to the formation of soluble carbonate complexes above this pH (Shaughnessy et al., 2003). X-ray Absorption Spectroscopy (XAS) showed that the majority of the Pu adsorbed to the hausmannite surface had been reduced to Pu(IV) and the EXAFS were consistent with the formation of inner-sphere sorption complexes.

The sorption of As(III) and As(V) to hausmannite has been observed under acidic conditions (Parsons et al., 2009; Silva et al., 2012; Li et al., 2015). Some authors also found evidence suggesting sorbed As(III) had been oxidised to As(V) by hausmannite (Parsons et al., 2009). Li et al. (2015) also found that > 85 % sorption of As(V) at pH 11. Similar behaviour has been observed with Cr(III) and Cr(VI) sorption observed at acidic pH (Weaver and Hochella Jr, 2003; Cantu et al., 2014), with some evidence for the oxidation of Cr(III) (Weaver and Hochella Jr, 2003). The removal of Zn, Cu, Co, and Ni from solution at pH 3 – 6 has been observed upon the addition of hausmannite, although only 3.5, 10, 3.2, and 2 % removal of the cations from solution was observed, respectively, and precipitation of $Cu(OH)_2$ was observed in the Cu containing system (McKenzie, 1972).

There are no laboratory studies of the interaction of U(VI) with rhodochrosite in the published literature to date. However, U(VI) has been found to sorb to or be coprecipitated with siderite ($FeCO_3$) (Ithurbide et al., 2009; Ithurbide et al., 2010; O'Loughlin et al., 2010) and calcite ($CaCO_3$) (Geipel et al., 1997; Reeder et al., 2000; Reeder et al., 2001; Elzinga et al., 2004; Reeder et al., 2004; Rihs et al., 2004; Dong et al., 2005; Wang et al., 2005). These are both carbonate minerals, possessing the trigonal $R\bar{3}c$ space group. Trace concentrations of uranium are also often found incorporated into natural calcites (Sturchio et al., 1998; Kelly et al., 2003). Although XAS suggested that this uranium was substituted

into the Ca^{2+} sites as U(IV), with a further 2 Ca^{2+} ions replaced by Na^{+} ions to maintain charge balance (Ishikawa and Ichikuni, 1984; Sturchio et al., 1998). Kelly et al. (2003) found U(VI) was incorporated into the calcite lattice in place of a Ca^{2+} and 2 CO_3^{2-}, again the charge was balanced by the non-local substitution of Ca^{2+} by Na^{+}.

When calcite grows, steps are formed (Figure 2.9), creating a variety of potential sorption sites for cations with differing preferences. Elzinga et al. (2004) and Rihs et al. (2004) suggested that uranyl sorption to calcite is best explained by the formation of an inner-sphere surface calcium-uranyl-carbonate complex. While Rihs et al. (2004) goes on to suggest that uranyl can only sorb the calcite at an edge step, or adjacent to a Ca vacancy or pit due to steric hindrance (Figure 2.9).

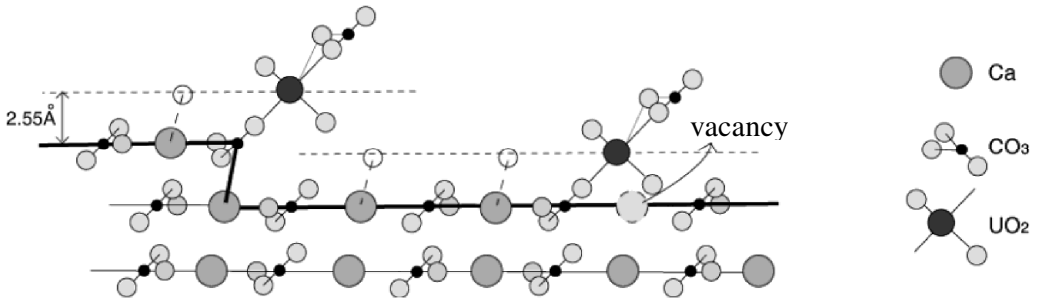

Figure 2.9: Ball and stick representation of calcite with uranyl complexed on the surface. Reproduced from (Rihs et al., 2004).

Uptake of U(VI) onto siderite has also been observed over the pH range 7 – 9 (Ithurbide et al., 2009). At pH 7 this was associated with minor reduction to U(IV) (O'Loughlin et al., 2010). At pH 9 X-ray Photoelectron Spectroscopy (XPS) showed the presence of two uranium oxidation states on the siderite surface, suggesting reduction of U(VI) to U(IV) by the siderite surface (Ithurbide et al., 2009). Uranyl retention on siderite decreased with increasing pH and carbonate concentration, pressumably due to the formation of soluble U(VI) carbonate species (Ithurbide et al., 2009). Ithurbide et al. (2010) suggest U(VI) removal occurs *via* two different mechanisms. At pH 7 siderite is thought to dissolve

releasing iron into solution, causing co-precipitation, followed by reduction. Whereas, at pH 9, the results are consistent with the uptake of U(VI) by the surface, reduction and precipitation of U_3O_8.

2.4.1.1.3.2. Reversibility of Cation Interactions with Mn-minerals

Assuming that U(VI) becomes associated with Mn-minerals, it is important to understand the reversibility of this interaction in order to predict the long-term stability of these U-Mn-mineral complexes and therefore their effect on uranium migration and subsurface behaviour. However, there are currently no studies investigating the reversibility of uranium uptake by Mn-minerals in the published literature. Although the desorption of Zn(II) from acid birnessite (Li et al., 2004) and manganite (γ-MnOOH) (Pan et al., 2004) has been studied. Zn(II) sorbed to acid birnessite at pH 5.5 was found in a corner-sharing octahedral interlayer complex. This was located above and below vacancies in the layers of MnO_6 octahedra, and was coordinated with interlayer H_2O molecules. Upon replacement of the solution phase with an identical Zn(II)-free version, sorption was found to be highly reversible (Li et al., 2004). Interestingly, the same treatment of Zn(II) sorbed to manganite found uptake to be largely irreversible at pH 7.5 (Pan et al., 2004). In this case the Zn(II) was sorbed in both edge-sharing and corner-sharing inner-sphere complexes. The authors hypothesise that observed irreversibility results from the formation of more energetically favourable edge-sharing complexes, while the Zn(II) sorbed as corner-sharing complexes is reversibly bound. Partial irreversibility has also been observed in the sorption of Eu(III) to β-MnO_2 at pH 6 (Sheng et al., 2014). Again, this has been attributed to a bidentate, edge-sharing, inner-sphere surface complex identified by EXAFS.

2.4.2. Neptunium

^{237}Np is produced in the cores of nuclear reactors when ^{235}U undergoes neutron capture, and by the alpha decay of ^{241}Am and ^{241}Pu. The half-life of ^{237}Np is long (2.144×10^6 years

(Nichols et al., 2008; Yoshida et al., 2011)) and it decays primarily to ^{233}Pa *via* the emission of an alpha particles. ^{237}Np contributes significantly to the activity of HLW (Figure 2.10), particularly as the waste ages due to its long half-life and ingrowth from ^{241}Am (Ojovan and Lee, 2014).

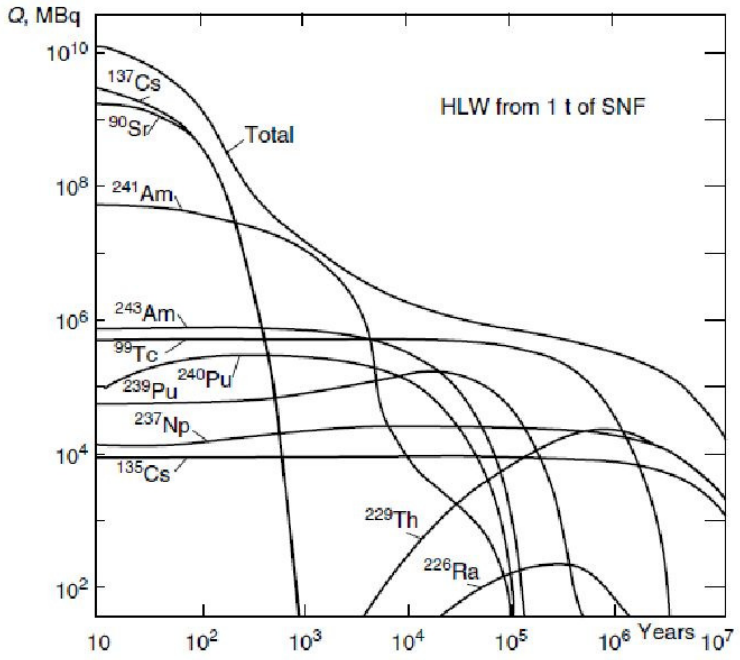

Figure 2.10: The change in activity of the HLW remaining after the processing of 1 ton of spent nuclear fuel with time (reproduced from (Ojovan and Lee, 2014)).

Neptunium has two oxidation states which are of environmental importance, Np(IV) and Np(V). Np(IV) dominates under reducing conditions (Choppin, 2006; Law et al., 2010) and behaves similarly to U(IV) (sections 2.4.1 and 2.3.1); it is expected to undergo hydrolysis resulting in relatively low solubility (Yoshida et al., 2011). Under oxidising conditions, Np(V) is expected to dominate (Hursthouse et al., 1991; Choppin, 2006). Much like U(VI), Np(V) exists as the neptunyl ion (NpO_2^+) (Keeney-Kennicutt and Morse, 1984; Hursthouse et al., 1991; Yamamoto et al., 1991; Kaszuba and Runde, 1999; Zavarin et al., 2012). However, the charge density of NpO_2^+ ion is lower than that of UO_2^{2+}, due to its lower overall charge, making NpO_2^+ less susceptible to hydrolysis and therefore more soluble (Runde, 2000; Choppin, 2006; Yoshida et al., 2011).

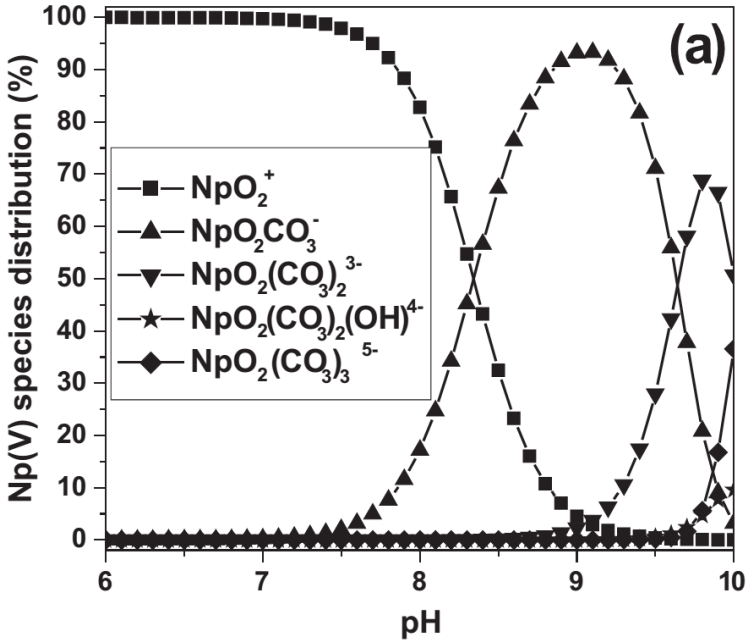

Figure 2.11: Speciation of Np(V) solution with a pCO_2 = -3.5 log [CO_2] (Np(V) = 1 x 10^{-5} M; I = 0.01 M). Reproduced from (Schmeide and Bernhard, 2010).

The comparative stability of NpO_2^+ means that it typically exists free in solution as $NpO_2^+{}_{(aq)}$ at pH < 10 (Schmeide and Bernhard, 2010), and that Np(V) is relatively soluble in circumneutral aqueous solutions compared to other actinides (Nitsche and Edelstein, 1985; Nitsche, 1987; Nitsche, 1991; Nitsche et al., 1993; Novak et al., 1996; Turner et al., 1998). Above pH 10 the formation of aqueous hydroxide complexes is observed (*e.g.* $NpO_2OH_{(aq)}$) (Schmeide and Bernhard, 2010). However, in the presence of CO_2, highly soluble carbonate complexes form meaning NpO_2^+ speciation (much like that of UO_2^{2+} (section 2.4.1)) is sensitive to carbonate concentration (Figure 2.11) (Heberling et al., 2008; Schmeide and Bernhard, 2010). Therefore, the presence of carbonate generally reduces Np(V) sorption to mineral surfaces (Turner et al., 1998; Arai et al., 2007; Schmeide and Bernhard, 2010). Together with the reduced charge density of NpO_2^+, this leads to Np being considered as potentially the most mobile transuranic (Runde et al., 1996; Kaszuba and Runde, 1999).

2.4.2.1. Interactions of Np(V) with Minerals

The sorption of Np(V) to the Mn(III) minerals hausmannite (Mn_3O_4) and manganite (γ-MnOOH) has been investigated as a function of Np(V) concentration and pH (Wilk et al., 2005). Uptake from solutions containing 10^{-6}, 10^{-5}, and 10^{-4} M Np(V) increased from ~ 20 % pH 4 to a maximum of ~ 80 % at pH 7, in the presence of both hausmannite and manganite. The authors suggested that the rapid kinetics of this uptake meant it could likely be attributed to a diffusion controlled surface reaction. At increasingly alkaline pH, sorption to both minerals decreased due to the formation of anionic carbonate species. The oxidation state of the mineral associated and solution phase Np was investigated using XANES. Significant (up to ~ 80 %) reduction of Np(V) to Np(IV) was observed in some of the mineral samples analysed. Analysis by optical absorption spectroscopy showed no reduction of Np(V) in solution samples contacted with manganite unless samples had been introduced to the X-ray beam in order to perform XAS. This implied that the observed reduction of Np(V) was occurring in the beam, either as a direct result of interaction with the beam, or at least that the beam catalysed reduction. This is an important finding since it throws into question the reduction of Np(V) in other systems characterised by XAS. For example, Np(IV) on the surface of iron oxides (Nakata et al., 2002) and iron sulphides (Moyes et al., 2002) has previously attributed to the reduction of Np(V) by the mineral, but this could in fact in an artefact of the XAS. The EXAFS collected of Np on hausmannite and manganite at pH 8 also suggest it is present as Np(IV) since no axial oxygens can be fitted, indcating the neptunyl moiety is no longer present. The presence of a Np backscatter at ~ 3.83 Å suggests the formation of a precipitate, and therefore also indicates to presence of Np(IV).

The investigation of the sorption of Np(V) to δ-MnO_2 (Tanaka et al., 2011), revealed greater than 95 % sorption of Np(V) to synthetic δ-MnO_2 at pH 6.1. However, when sorption to biogenic Mn oxide was investigated under the same conditions no sorption of

Np(V) was observed. This was attributed to complexation with organic ligands released from the fungal cells used to produce the biogenic Mn oxide, which was not washed prior to addition.

The association of Np with Mn oxides has also been suggested by Kenna (2009), who found Np to be predominantly associated with Mn and Fe oxides in sediment collected from the Ob River (Siberia). While Thorpe et al. (2015) found that under Mn-reducing conditions, extended by the addition of δ-MnO_2 to microcosms containing natural sediment, Np(V) was reduced to $Np(IV)_{(s)}$.

In general, the literature is lacking laboratory studies investigating Np interactions with mineral phases due to the specialised facilities, training, and experience required to study this challenging element safely. The literature is particularly lacking in studies investigating Mn minerals, with the four studies discussed above constituting the entirety of the literature. Given the risk-driving nature of Np-237 and the potential importance of Mn minerals, this is a significant knowledge gap, which is important for predicting Np behaviour in both geological disposal and contaminated land scenarios.

2.5. Thesis Aims

This project investigates the interaction of U(VI) and Np(V) with geological disposal / environmentally relevant mineral phases in order to better inform U and Np migration pathways in the geosphere. The project has two main aims: (1) to *examine the formation of U(VI) colloids and their stability in the presence of mineral phases representative of the near- and far-field of a GDF*; (2), to *examine the interaction of U(VI) and Np(V) with a range of Mn-minerals under conditions relevant to geological disposal and contaminated land.* Batch studies and X-ray absorption spectroscopy have been used throughout to determine the extent and nature of interaction.

The hypotheses tested in this thesis are:

- 4.2, 42, and 252 μM U(VI) will be removed from solution under high pH conditions representative of geological disposal.
- U(VI) nanoparticles formed in high pH cement leachate will be removed from solution by the addition of cement, biotite, quartz, and orthoclase.
- U(VI) is removed from high pH cement leachate by incorporation into the interlayer of the C-S-H phases in cement.
- U(VI) and Np(V) are removed from solution by sorption to δ-MnO_2, triclinic (Na)-birnessite, hausmannite, and rhodochrosite under circumneutral to high pH conditions relevant to geological disposal.
- The sorption of U(VI) to δ-MnO_2, triclinic (Na)-birnessite, hausmannite, and rhodochrosite is reversible.

2.6. References

Abdelouas, A. (2006). Uranium mill tailings: geochemistry, mineralogy, and environmental impact. *Elements,* 2**,** 335-341.

Al-Attar, L. and Budeir, Y. (2011). Thorium uptake on synthetic inorganic ion exchangers. *Separation Science and Technology,* 46(15)**,** 2313-2321.

Al-Attar, L. and Dyer, A. (2002). Sorption behaviour of uranium on birnessite, a layered manganese oxide. *Journal of Materials Chemistry,* 12(5)**,** 1381-1386.

Ames, L. L., McGarrah, J. E. and Walker, B. A. (1983). Sorption of uranium and radium by biotite, muscovite, and phlogopite. *Clays and Clay Minerals,* 31(5)**,** 343-351.

Anderson, C., Jakobsson, A.-M. and Pedersen, K. (2007). Influence of in situ Biofilm Coverage on the Radionuclide Adsorption Capacity of Subsurface Granite. *Environmental Science & Technology,* 41(3)**,** 830-836.

Appelo, C. A. J. and Postma, D. (1999). A consistent model for surface complexation on birnessite (-MnO_2) and its application to a column experiment. *Geochimica et Cosmochimica Acta,* 63(19/20)**,** 3039-3033-3048.

Appelo, C. A. J. and Postma, D. (2005). *Geochemistry groundwater and pollution*. Leiden: A.A. Balkema Publishers.

Arai, Y., Moran, P. B., Honeyman, B. D. and Davis, J. A. (2007). In situ spectroscopic evidence for neptunium(V)-carbonate inner-sphere and outer-sphere ternary surface complexes on hematite surfaces. *Environmental Science & Technology,* 41(11)**,** 3940-3944.

Arnold, T., Utsunomiya, S., Geipel, G., Ewing, R. C., Baumann, N. and Brendler, V. (2006). Adsorbed U(VI) Surface Species on Muscovite Identified by Laser Fluorescence Spectroscopy and Transmission Electron Microscopy. *Environmental Science & Technology,* 40(15)**,** 4646-4652.

Arnold, T., Zorn, T., Bernhard, G. and Nitsche, H. (1998). Sorption of uranium(VI) onto phyllite. *Chemical Geology,* 151(1-4)**,** 129-141.

Arnold, T., Zorn, T., Zänker, H., Bernhard, G. and Nitsche, H. (2001). Sorption behavior of U(VI) on phyllite: Experiments and modeling. *Journal of Contaminant Hydrology,* 47(2-4)**,** 219-231.

Bailey, S. W. (1984). Classification and Structures of the Micas. *Reviews in Mineralogy,* 13**,** 1-12.

Banfield, J. F. and Eggleton, R. A. (1988). Transmission Electron Microscopy Study of Biotite Weathering. *Clays and Clay Minerals,* 36**,** 47-60.

Bargar, J. R., Tebo, B. M. and Villinski, J. E. (2000). In situ characterization of Mn(II) oxidation by spores of the marine Bacillus sp. strain SG-1. *Geochimica et Cosmochimica Acta,* 64(16)**,** 2775-2778.

Barnett, M. O., Jardine, P. M., Brooks, S. C. and Selim, H. M. (2000). Adsorption and transport of uranium(VI) in subsurface media. *Soil Science Society of America Journal,* 64(3)**,** 908-917.

Baston, G. M. N., Cowper, M. M. and Marshall, T. A. (2010). *Sorption of U(VI) onto Leached and Hydrothermally aged NRVB* SA/ENV-0959.

Beresford, N. A. (2005). Land contaminated by radioactive materials. *Soil Use and Management,* 21**,** 468-474.

Beveridge, T. J. and Murray, R. G. E. (1980). Sites of metal deposition in the cell wall of Bacillus subtilis. *Journal of Bacteriology,* 141(2)**,** 876-887.

Boggs, M. A., Dai, Z. R., Kersting, A. B. and Zavarin, M. (2015). Plutonium(IV) sorption to montmorillonite in the presence of organic matter. *Journal of Environmental Radioactivity,* 141**,** 90-96.

Bonaccorsi, E., Merlino, S. and Kampf, A. R. (2005). The Crystal Structure of Tobermorite 14 Å (Plombierite), a C–S–H Phase. *Journal of the American Ceramic Society,* 88(3)**,** 505-512.

Brady, P. V. and Walther, J. V. (1989). Controls on silicate dissolution rates in neutral and basic pH solution at 25°C. *Geochimica et Cosmochimica Acta,* 53(11)**,** 2823-2830.

Braney, M. C., Haworth, A., Jefferies, N. L. and Smith, A. C. (1993). A study of the effects of an alkaline plume from a cementitious repositiory on geological materials. *Journal of Contaminant Hydrology,* 13**,** 379-402.

Brennecka, G. A., Wasylenki, L. E., Bargar, J. R., Weyer, S. and Anbar, A. D. (2011). Uranium Isotope Fractionation during Adsorption to Mn-Oxyhydroxides. *Environmental Science & Technology,* 45(4)**,** 1370-1375.

Bricker, O. (1965). Some Stability Relations in the System $Mn\text{-}O_2\text{-}H_2O$ at 25 and one atmosphere total pressure. *American Mineralogist,* 50**,** 1296-1354.

Brookshaw, D. R., Pattrick, R. A. D., Bots, P., Law, G. T. W., Lloyd, J. R., Mosselmans, J. F. W., Vaughan, D. J., Dardenne, K. and Morris, K. (2015). Redox Interactions of Tc(VII), U(VI), and Np(V) with Microbially Reduced Biotite and Chlorite. *Environmental Science & Technology,* 49(22)**,** 13139-13148.

Brookshaw, D. R., Pattrick, R. A. D., Lloyd, J. R. and Vaughan, D. J. (2012). Microbial effects on mineral-radionuclide interactions and radionuclide solid-phase capture processes. *Mineralogical Magazine,* 76(3)**,** 777-806.

Burns, R. G. and Burns, V. M. (1977). Mineralogy. *In:* Glassby, G. P. (ed.) *Marine Manganese Deposits.* Amsterdam: Elsevier Scientific Publishing Company.

Burns, R. G., Burns, V. M., Sung, W. and Brown, B. A. (1974). Ferromanganese mineralogy - Suggested terminology of the principle manganese oxide phases. *Geological Society of Americal Annual Meeting.* Miami.

Butcher, E. J., Borwick, J., Collier, N. and Williams, S. J. (2012). Long term leachate evolution during flow-through leaching of a vault backfill (NRVB). *Mineralogical Magazine,* 76(8)**,** 3023-3031.

Canadian Nuclear Association. (2016). *How Reactors Work* [Online]. Available: https://cna.ca/technology/energy/how-reactors-work/ [Accessed 26/09/2016 2016].

Cantu, Y., Remes, A., Reyna, A., Martinez, D., Villarreal, J., Ramos, H., Trevino, S., Tamez, C., Martinez, A., Eubanks, T. and Parsons, J. G. (2014). Thermodynamics, kinetics, and activation energy studies of the sorption of chromium(III) and chromium(VI) to a Mn3O4 nanomaterial. *Chemical Engineering Journal,* 254**,** 374-383.

Catalano, J. G., Park, C., Fenter, P. and Zhang, Z. (2008). Simultaneous inner- and outer-sphere arsenate adsorption on corundum and hematite. *Geochimica et Cosmochimica Acta,* 72(8)**,** 1986-2004.

Chambers, A., Gould, L., Harris, A., Pilkington, N. and Williams, S. (2003). *Evolution of the near field of Nirex disposal concept*.

Chardon, E. S., Bosbach, D., Bryan, N. D., Lyon, I. C., Marquardt, C., Römer, J., Schild, D., Vaughan, D. J., Wincott, P. L., Wogelius, R. A. and Livens, F. R. (2008). Reactions of the feldspar surface with metal ions: Sorption of Pb(II), U(VI) and Np(V), and surface analytical studies of reaction with Pb(II) and U(VI). *Geochimica et Cosmochimica Acta,* 72(2)**,** 288-297.

Chen, J. J., Thomas, J. J., Taylor, H. F. W. and Jennings, H. M. (2004). Solubility and structure of calcium silicate hydrate. *Cement and Concrete Research,* 34(9)**,** 1499-1519.

Choppin, G. R. (2006). Actinide speciation in aquatic systems. *Marine Chemistry,* 99(1-4)**,** 83-92.

Chukhrov, F. V. and Gorshkov, A. I. (1981). Iron and manganese oxide minerals in soils. *Earth and Environmental Science Transactions of the Royal Society of Edinbrugh,* 72(03)**,** 195-200.

Chukhrov, F. V., Gorshkov, A. I., Rudnitskaya, E. S., Beresovskaya, V. V. and Sivtsov, A. V. (1980). Manganese minerals in clay - A review. *Clays and Clay Minerals,* 28**,** 346-354.

Clark, G. (2016). *UK energy security and Low carbon technologies: Hinkley Point C*.

Cochran, T. B., Norris, R. S. and Suokko, K. L. (1993). Radioactive Contamination at Chelyabinsk-65, Russia. *Annual Review of Energy and the Environment,* 18(1)**,** 507-528.

Cornell, R. M. and Giovanoli, R. (1988). Transformation of Hausmannite into Birnessite in Alkaline Media. *Clays and Clay Minerals,* 36(3)**,** 249-257.

Cornell, R. M. and Schwertmann, U. (2003). *The Iron Oxides: Structure, Properties, Reacrions, Occurences and Uses* (2nd ed. ed.): Wiley-VCH: Weinham.

CoRWM. (2006). *Managing our Radioactive Waste Safely* CoRWM 700.

Crossland, I. (2007). *Cracking of the Nirex Reference Vault Backfill: A Review of its Likely Occurrence and Significance* CCL/2007/1.

DECC. (2010). *Government Response to the House of Lords Science and Technology Committee Report: Radioactive Waste Management: A Further Update*. ST/10-11/40.

DECC. (2012). *Strategy for the management of solid low level radioactive waste from the non-nuclear industry in the United Kingdom* 12D/026.

DECC. (2015). *Implementing Geological Disposal: Annual Report*. London. URN 15D/361.

Deer, W. A., Howie, R. A. and Zussman, J. (1992). *An Introduction to The Rock Forming Minerals* (Second Edition ed.). Essex: Pearson Eduction Limited.

Deer, W. A., Howie, R. A. and Zussman, J. (2001). Framework Silicates: Feldspars. *Rock-Forming Minerals.* 2nd ed. London: The Geological Society.

DEFRA, BERR and The devolved admistrations for Wales and Northern Ireland. (2008). *A Framework for Implementing Geological Disposal*. Edinburgh. Cm 7386.

Ding, D., Fu, P., Li, L., Xin, X., Hu, N. and Li, G. (2014). U(VI) ion adsorption thermodynamics and kinetics from aqueous solution onto raw sodium feldspar and acid-activated sodium feldspar. *Journal of Radioanalytical and Nuclear Chemistry,* 299(3)**,** 1903-1909.

Dixon, J. B., Golden, D. C., Uzochukwu, G. A. and Chen, C. C. (1990). Soil Manganese Oxides. *In:* De Boodt, M. F., Hayes, M. H. B., Herbillon, A., De Strooper, E. B. A. & Tuck, J. J. (eds.) *Soil Colloids and Their Associations in Aggregates.* Boston, MA: Springer US.

Dixon, J. B. and White, G. N. (2002). Manganese Oxides. *In:* Dick, W. A. (ed.) *Soil Mineralogy with Environmental Applications.* Madison, Wisconsin: Soil Science Society of America.

Doner, H. E. and Gossel, P. R. (2002). Carbonates and Evaporites. *In:* Dixon, J. B. & Schulze, D. G. (eds.) *Soil Mineralogy with Environmental Application.* Madision, Wisconsin: Soil Science Society of America, Inc.

Dong, H., Peacor, D. R. and Murphy, S. F. (1998). TEM study of progressive alteration of igneous biotite to kaolinite throughout a weathered soil profile. *Geochimica et Cosmochimica Acta,* 62(11)**,** 1881-1887.

Dong, W., Ball, W. P., Liu, C., Wang, Z., Stone, A. T., Bai, J. and Zachara, J. M. (2005). Influence of Calcite and Dissolved Calcium on Uranium(VI) Sorption to a Hanford Subsurface Sediment. *Environmental Science & Technology,* 39(20)**,** 7949-7955.

Dounreay Site Restoration Ltd. (2009). *Strategy for Contaminated Land Management and Restoration*.

Dow, C. and Glasser, F. P. (2003). Calcium carbonate efflorescence on Portland cement and building materials. *Cement and Concrete Research,* 33(1)**,** 147-154.

Duff, M. C., Hunter, D. B., Triay, I. R., Bertsch, P. M., Reed, D. T., Sutton, S. R., Shea-McCarthy, G., Kitten, J., Eng, P., Chipera, S. J. and Vaniman, D. T. (1999).

Mineral Associations and Average Oxidation States of Sorbed Pu on Tuff. *Environmental Science & Technology,* 33**,** 2163-2169.

EDF Energy. (2017). *Sizewell B Power Station* [Online]. Available: https://www.edfenergy.com/energy/power-stations/sizewell-b [Accessed 01/02/2017 2017].

Elzinga, E. J., Tait, C. D., Reeder, R. J., Rector, K. D., Donohoe, R. J. and Morris, D. E. (2004). Spectroscopic investigation of U(VI) sorption at the calcite-water interface. *Geochimica et Cosmochimica Acta,* 68(11)**,** 2437-2448.

Fischer, T. B. (2011). *Structural Transformations of Birnessite (δ-MnO2) During Biological and Abiological Reduction.* Doctor of Philosophy, The Pennsylvania State University.

Fleeger, C. R. (2012). *Contaminant sequestration and phase transformation properties of birnessite-like phases (δ-MnO2).* Doctor of Philosophy, The Pannsyvania State University.

Fleeger, C. R., Heaney, P. J. and Post, J. E. (2013). A time-resolved X-ray diffraction study of Cs exchange into hexagonal H-birnessite. *American Mineralogist,* 98(4)**,** 671.

Fox, P. M., Davis, J. A. and Zachara, J. M. (2006). The effect of calcium on aqueous uranium(VI) speciation and adsorption to ferrihydrite and quartz. *Geochimica et Cosmochimica Acta,* 70(6)**,** 1379-1387.

Francis, A. J. and Dodge, C. J. (2015). Microbial mobilization of plutonium and other actinides from contaminated soil. *Journal of Environmental Radioactivity,* 150**,** 277-285.

Francis, A. J., Dodge, C. J., Lu, F., Halada, G. P. and Clayton, C. R. (1994). XPS and XANES Studies of Uranium Reduction by Clostridium sp. *Environmental Science & Technology,* 28(4)**,** 636-639.

Fuller, A. J., Shaw, S., Ward, M. B., Haigh, S. J., Mosselmans, J. F. W., Peacock, C. L., Stackhouse, S., Dent, A. J., Trivedi, D. and Burke, I. T. (2015). Caesium incorporation and retention in illite interlayers. *Applied Clay Science,* 108**,** 128-134.

Gaona, X., Kulik, D. A., Macé, N. and Wieland, E. (2012). Aqueous–solid solution thermodynamic model of U(VI) uptake in C–S–H phases. *Applied Geochemistry,* 27(1)**,** 81-95.

Gardiner, M. P., Hotlom, G. J. and Swanton, S. W. (1998). Influence of Colloids, Microbes and Other Perturbations on the Near-field Source Term, Paper 3. *RSC/Nirex Symposium: The Chemistry of Deep Disposal of Radioactive Waste.* Loughborough.

Gardiner, M. P., Smith, A. J. and Williams, S. J. (1990). *Sorption on Inactive Repository Components* DoE/HMIP/RR/90/084.

Gartner, E. M., Young, J. F., Damidot, D. and Jawed, I. (2001). Hydration of Portland Cement. *In:* Bensted, J. & Barnes, P. (eds.) *Structure and Performance of Cements.* 2nd ed.: CRC Press.

Geipel, G., Reich, T., Brendler, V., Bernhard, G. and Nitsche, H. (1997). Laser and X-ray spectroscopic studies of uranium-calcite interface phenomena. *Journal of Nuclear Materials,* 248**,** 408-411.

Ghaly, M., El-Dars, F. M. S. E., Hegazy, M. M. and Abdel Rahman, R. O. (2016). Evaluation of synthetic Birnessite utilization as a sorbent for cobalt and strontium removal from aqueous solution. *Chemical Engineering Journal,* 284**,** 1373-1385.

Gilkes, R. J. and Suddhiprakarn, A. (1979). Biotite alteration in deeply weathered granite; I, Morphological, mineralogical, and chemical properties. *Clays and Clay Minerals,* 27(5)**,** 349.

Giovanoli, R. (1970). Vernadite is random-stacked birnessite. *Mineralium Deposita,* 15**,** 251-253.

Giovanoli, R. and Brutsch, R. (1979). Uber Oxidhydroxide des Mn(IV) mit Schichtengitte. *Chimia,* 33**,** 372-376.

Glover, E. D. (1977). Characterization of a marine birnessite. *American Mineralogist,* 62**,** 278-285.

Goodenough, J. B. and Loeb, A. L. (1955). Theory of Ionic Ordering, Crystal Distortion, and Magnetic Exchange Due to Covalent Forces in Spinels. *Physical Review,* 98(2)**,** 391-408.

Gorman-Lewis, D., Fein, J. B., Burns, P. C., Szymanowski, J. E. S. and Converse, J. (2008). Solubility measurements of the uranyl oxide hydrate phases metaschoepite, compreignacite, Na-compreignacite, becquerelite, and clarkeite. *Journal of Chemical Thermodynamics,* 40(6)**,** 980-990.

Grive, M., L., D., Domenech, C. and Salas, J. (2011). Redox Evolution of a Cementitous Geological Disposal Facility. *13th International High-Level Radioactive Waste Management Confenece.* Albuqueque, NM.

Harfouche, M., Wieland, E., Dahn, R., Fujita, T., Tits, J., Kunz, D. and Tsukamoto, M. (2006). EXAFS study of U(VI) uptake by calcium silicate hydrates. *Journal of Colloid and Interface Science,* 303(1)**,** 195-204.

Health and Safety England, Environment Agency and Scottish Environment Protection Agency. (2007). *Fundamental of the managment of radioactive waste: An introduction to the management of higher-level radioactive waste on nuclear licensed sites* NRW02.

Heberling, F., Denecke, M. A. and Bosbach, D. (2008). Neptunium(V) Coprecipitation with Calcite. *Environmental Science & Technology,* 42**,** 471-476.

Hem, J. D. (1963). *Chemical equilibria and rates of manganese oxidation*.

Hunter, J. (2004). *SCLS Phase 1 - Conceptual Model of Contamination Below Ground at Sellafield*. UK.

Hursthouse, A. S., Baxter, M. S., Livens, F. R. and Duncan, H. J. (1991). Transfer of Sellafield-derived Np-237 to and within the Terrestrial Environment. *Journal of Environmental Radioactivity,* 14(2)**,** 147-174.

Iijima, K., Tomura, T., Tobita, M. and Suzuki, Y. (2010). Distribution of Cs and Am in the solution-bentonite colloids-granite ternary system: effect of addition order and sorption reversibility. *Radiochimica Acta,* 98(9-11)**,** 729-736.

Ilton, E. S., Heald, S. M., Smith, S. C., Elbert, D. and Liu, C. (2006). Reduction of uranyl in the interlayer region of low iron micas under anoxic and aerobic conditions. *Environmental Science & Technology,* 40(16)**,** 5003-5009.

Ilton, E. S., Pacheco, J. S., Bargar, J. R., Shi, Z., Liu, J., Kovarik, L., Engelhard, M. H. and Felmy, A. R. (2012a). Reduction of U(VI) incorporated in the structure of hematite. *Environmental Science & Technology,* 46(17)**,** 9428-9436.

Ilton, E. S., Wang, Z., Boily, J. F., Qafoku, O., Rosso, K. M. and Smith, S. C. (2012b). The effect of pH and time on the extractability and speciation of uranium(VI) sorbed to SiO 2. *Environmental Science and Technology,* 46(12)**,** 6604-6611.

Ishikawa, M. and Ichikuni, M. (1984). Uptake of sodium and potassium by calcite. *Chemical Geology,* 42(1)**,** 137-146.

Ithurbide, A., Peulon, S., Miserque, F., Beaucaire, C. and Chaussé, A. (2009). Interaction between uranium(VI) and siderite (FeCO3) surfaces in carbonate solutions. *Radiochimica Acta,* 97(3)**,** 177-180.

Ithurbide, A., Peulon, S., Miserque, F., Beaucaire, C. and Chaussé, A. (2010). Retention and redox behaviour of uranium(VI) by siderite (FeCO3). *Radiochimica Acta,* 98(9-11)**,** 563-568.

IUPAC. (1997). *Compendium of Chemical Terminology* (2nd ed.). Oxford: Blackwell Scientific Publications.

Jarosch, D. (1987). Crystal structure refinement and reflectance measurements of hausmannite, Mn3O4. *Mineralogy and Petrology,* 37(1)**,** 15-23.

Kaplan, D. I., Gervals, T. L. and Krupka, K. M. (1998). Uranium(VI) Sorption to Sediments Under High pH and Ionic Strength Conditions. *Radiochimica Acta,* 80**,** 201-211.

Kaszuba, J. P. and Runde, W. H. (1999). The Aqueous Geochemistry of Neptunium: Dynamic Control of Soluble Concentrations with Applications to Nuclear Waste Disposal. *Environmental Science & Technology,* 33(24)**,** 4427-4433.

Keeney-Kennicutt, W. L. and Morse, J. W. (1984). The interaction of $Np(V)O_2^+$ with common mineral surfaces in dilute aqueous solutions and seawater. *Marine Chemistry,* 15(2)**,** 133-150.

Kelly, S. D., Newville, M. G., Cheng, L., Kemner, K. M., Sutton, S. R., Fenter, P., Sturchio, N. C. and Spötl, C. (2003). Uranyl Incorporation in Natural Calcite. *Environmental Science & Technology,* 37(7)**,** 1284-1287.

Kenna, T. C. (2009). Using sequential extraction techniques to assess the partitioning of plutonium and neptunium-237 from multiple sources in sediments from the Ob River (Siberia). *Journal of Environmental Radioactivity,* 100(7)**,** 547-557.

Kerisit, S. and Liu, C. (2012). Diffusion and adsorption of uranyl carbonate species in nanosized mineral fractures. *Environmental Science and Technology,* 46(3)**,** 1632-1640.

Kerisit, S. and Liu, C. (2014). Molecular Dynamics Simulations of Uranyl and Uranyl Carbonate Adsorption at Aluminosilicate Surfaces. *Environmental Science & Technology,* 48(7)**,** 3899-3907.

Kersting, A. B., Efurd, D. W., Finnegan, D. L., Rokop, D. J., Smith, D. K. and Thompson, J. L. (1999). Migration of plutonium in ground water at the Nevada Test Site. *Nature,* 397**,** 56-59.

Kimber, R., Livens, F. R. and Lloyd, J. R. (2011). Management of Land Contaminated by the Nuclear Legacy. *In:* Hester, R. E. & Harrison, R. M. (eds.) *Nuclear Power and the Environment.* Royal Society of Chemistry.

Kirillov, S. A., Aleksandrova, V. S., Lisnycha, T. V., Dzanashvili, D. I., Khainakov, S. A., García, J. R., Visloguzova, N. M. and Pendelyuk, O. I. (2009). Oxidation of synthetic hausmannite (Mn3O4) to manganite (MnOOH). *Journal of Molecular Structure,* 928(1-3)**,** 89-94.

Konhauser, K. O., Mortimer, R. J. G., Morris, K. and Dunn, V. (2002). The role of microorganisms during sediment diagenesis: implications for radionuclide mobility. *Interactions of Microorganisms with Radionuclides,* 2**,** 61-100.

Krauskopf, K. B. and Bird, D. K. (1995). *Introduction to Geochemistry*. New Jersey: McGraw-Hill.

Lanson, B., Drits, V. A., Feng, Q. and Manceau, A. (2002). Structure of synthetic Na-birnessite: Evidence for a triclinic one-layer unit cell. *American Mineralogist,* 87(11-12)**,** 1662-1671.

Law, G. T. W., Geissler, A., Lloyd, J. R., Livens, F. R., Boothman, C., Begg, J. D. C., Denecke, M. A., Rothe, J., Dardenne, K., Burke, I. T., Charnock, J. M. and Morris, K. (2010). Geomicrobiological Redox Cycling of the Transuranic Element Neptunium. *Environmental Science & Technology,* 44(23)**,** 8924-8929.

Lefkowitz, J. P., Rouff, A. A. and Elzinga, E. J. (2013). Influence of pH on the Reductive Transformation of Birnessite by Aqueous Mn(II). *Environmental Science & Technology,* 47(18)**,** 10364-10371.

Lenhart, J. J. and Honeyman, B. D. (1999). Uranium(VI) sorption to hematite in the presence of humic acid. *Geochimica et Cosmochimica Acta,* 63(19)**,** 2891-2901.

Li, D. and Kaplan, D. I. (2012). Sorption coefficients and molecular mechanisms of Pu, U, Np, Am and Tc to Fe (hydr)oxides: A review. *Journal of Hazardous Materials,* 243**,** 1-18.

Li, F., Geng, D. and Cao, Q. (2015). Adsorption of As(V) on aluminum-, iron-, and manganese-(oxyhydr)oxides: equilibrium and kinetics. *Desalination and Water Treatment,* 56(7)**,** 1829-1838.

Li, X. L., Pan, G., Qin, Y. W., Hu, T. D., Wu, Z. Y. and Xie, Y. N. (2004). EXAFS studies on adsorption-desorption reversibility at manganese oxide-water interfaces II. Reversible adsorption of zinc on delta-MnO2. *Journal of Colloid and Interface Science,* 271(1)**,** 35-40.

Ling, F. T., Heaney, P. J., Post, J. E. and Gao, X. (2015). Transformations from triclinic to hexagonal birnessite at circumneutral pH induced through pH control by common biological buffers. *Chemical Geology,* 416**,** 1-10.

Lloyd, J. R. (2003). Microbial reduction of metals and radionuclides. *FEMS Microbiology Reviews,* 27(2-3)**,** 411-425.

Lloyd, J. R. and Macaskie, L. E. (2000). Bioremediation of Radionuclide-Containing Wastewaters. *Environmental Microbe-Metal Interactions.* American Society of Microbiology.

Lloyd, J. R. and Macaskie, L. E. (2002). Biochemical Basis of Microbe-Radionuclide Interactions. *In:* Keith-Roach, M. J. & Livens, F. (eds.) *Radioactivity and the Environement.* Oxford: Elsevier.

LLW Repository Ltd. (2014). *www.llwrsite.com* [Online]. [Accessed 07/08/2014 2014].

Lopano, C. L., Heaney, P. J., Bandstra, J. Z., Post, J. E. and Brantley, S. L. (2011). Kinetic analysis of cation exchange in birnessite using time-resolved synchrotron X-ray diffraction. *Geochimica et Cosmochimica Acta,* 75(14)**,** 3973-3981.

Lopano, C. L., Heaney, P. J. and Post, J. E. (2009). Cs-exchange in birnessite: Reaction mechanisms inferred from time-resolved x-ray diffraction and transmission electron microscopy. *American Mineralogist,* 94(5-6)**,** 816-826.

Lovley, D. R. and Phillips, E. J. P. (1992). Reduction of Uranium by Desulfovibrio-desulfuricans. *Applied and Environmental Microbiology,* 58(3)**,** 850-856.

Lovley, D. R., Phillips, E. J. P., Gorby, Y. A. and Landa, E. R. (1991). Microbial reduction of uranium. *Nature,* 350(6317)**,** 413-416.

Luo, W., Kelly, S. D., Kemner, K. M., Watson, D., Zhou, J., Jardine, P. M. and Gu, B. (2009). Sequestering Uranium and Technetium through Co-Precipitation with Aluminum in a Contaminated Acidic Environment. *Environmental Science & Technology,* 43(19)**,** 7516-7522.

Macaskie, L. E., Empson, R. M., Cheetham, A. K., Grey, C. P. and Skarnulis, A. J. (1992). Uranium bioaccumulation by a citrobacter sp. as a result of enzymically mediated growth of polycrystalline HUO_2PO_4. *Science,* 257(5071)**,** 782-784.

Macé, N., Wieland, E., Dähn, R., Tits, J. and Scheinost, A. C. (2013). EXAFS investigation on U(VI) immobilization in hardened cement paste: influence of experimental conditions on speciation. *Radiochimica Acta,* 101(6)**,** 379-389.

MacKenzie, A. B., Cook, G. T. and McDonald, P. (1999). Radionuclide distributions and particles size associations in Irish Sea surface sediments: implications for actinide dispersion. *Journal of Environmental Radioactivity,* 44**,** 275-296.

Manceau, A., Gorshkov, A. I. and Drits, V. A. (1992). Structural chemistry of Mn, Fe, Co, and Ni in manganese hydrous oxides: Part 1. Information from XANES spectroscopy. *American Mineralogist,* 77**,** 1133-1143.

Marble, J. C., Corley, T. L., Conklin, M. H. and Fuller, C. C. (1999). Environmental factors affecting oxidation of manganese in Pinal Creek, Arizona. *In:* Morganwalp, D. W. & Buxton, H. T. (eds.) *Water-Resources Investigations Reports.* West Trenton, New Jersey: U.S. Geological Survey.

Markai, S., Andrès, Y., Montavon, G. and Grambow, B. (2003). Study of the interaction between europium (III) and Bacillus subtilis: Fixation sites, biosorption modeling and reversibility. *Journal of Colloid and Interface Science,* 262(2)**,** 351-361.

Marshall, T. A., Morris, K., Law, G. T., Livens, F. R., Mosselmans, J. F., Bots, P. and Shaw, S. (2014). Incorporation of Uranium into Hematite during crystallization from ferrihydrite. *Environmental Science & Technology,* 48(7)**,** 3724-3731.

McCall, A., Holmes, J., Harrison, M. and Francis, A. (1997). Backfill - Development and Placement of an Engineered Barrier. *6th Internation Conference on Radioactive Waste Management and Environmental Remediation ICEM'97.* Singapore.

McKenzie, R. M. (1972). The sorption of some heavy metals by the lower oxides of manganese. *Geoderma,* 8(1)**,** 29-35.

McKenzie, R. M. (1989). Manganese Oxides and Hydroxides. *In:* Dixon, J. B. & Weed, S. B. (eds.) *Minerals in Soil Environments.* 2nd ed. Madison, Wisconsin: Soil Science Society of America.

McKinley, J. P., Zachara, J. M., Liu, C., Heald, S. C., Prenitzer, B. I. and Kempshall, B. W. (2006). Microscale controls on the fate of contaminant uranium in the vadose zone, Hanford Site, Washington. *Geochimica et Cosmochimica Acta,* 70(8)**,** 1873-1887.

Means, J. L., Crerar, D. A., Borcsik, M. P. and Duguid, J. O. (1978). Adsorption of Co and selected actinides by Mn and Fe oxides in soils and sediments. *Geochimica et Cosmochimica Acta,* 42**,** 1763-1773.

Meunier, A. and Velde, B. (1979). Biotite Weathering in Granites of Western France. *In:* Mortland, M. M. & Farmer, V. C. (eds.) *Developments in Sedimentology.* Elsevier.

Mibus, J., Sachs, S., Pfingsten, W., Nebelung, C. and Bernhard, G. (2007). Migration of uranium(IV)/(VI) in the presence of humic acids in quartz sand: A laboratory column study. *Journal of Contaminant Hydrology,* 89(3-4)**,** 199-217.

Ministry of the Environment Sweden. (2014). *Sweden's implementation of the obligations of the Joint Convention*. Ds 2014:32.

Mondani, L., Benzerara, K., Carrière, M., Christen, R., Mamindy-Pajany, Y., Février, L., Marmier, N., Achouak, W., Nardoux, P., Berthomieu, C. and Chapon, V. (2011). Influence of Uranium on Bacterial Communities: A Comparison of Natural Uranium-Rich Soils with Controls. *PLoS ONE,* 6(10)**,** e25771.

Moroni, L. P. and Glasser, F. P. (1995). Reactions between cement components and U(VI) oxide. *Waste Management,* 15(3)**,** 243-254.

Morris, K., Law, G. T. W. and Bryan, N. D. (2011). Geodisposal of Higher Activity Wastes. *In:* Hester, R. E. & Harrison, R. M. (eds.) *Nuclear Power and the Environment.* Royal Society of Chemistry.

Moyce, E. B. A., Rochelle, C., Morris, K., Milodowski, A. E., Chen, X., Thornton, S., Small, J. S. and Shaw, S. (2014). Rock alteration in alkaline cement waters over 15 years and its relevance to the geological disposal of nuclear waste. *Applied Geochemistry,* 50**,** 91-105.

Moyes, L. N., Jones, M. J., Reed, W. A., Livens, F. R., Charnock, J. M., Mosselmans, J. F. W., Hennig, C., Vaughan, D. J. and Pattrick, R. A. D. (2002). An X-ray Absorption Spectroscopy Study of Neptunium(V) Reactions with Mackinawite (FeS). *Environmental Science & Technology,* 36(2)**,** 179-183.

Moyes, L. N., Parkman, R. H., Charnock, J. M., Vaughan, D. J., Livens, F. R., Hughes, C. R. and Braithwaite, A. (2000). Uranium Uptake from Aqueous Solution by Interaction with Goethite, Lepidocrocite, Muscovite, and Mackinawite: An X-ray Absorption Spectroscopy Study. *Environmental Science & Technology,* 34(6)**,** 1062-1068.

Mukherjee, J., Ramkumar, J., Chandramouleeswaran, S., Shukla, R. and Tyagi, A. K. (2013). Sorption characteristics of nano manganese oxide: efficient sorbent for removal of metal ions from aqueous streams. *Journal of Radioanalytical and Nuclear Chemistry,* 297(1)**,** 49-57.

Murakami, T., Ito, J. I., Utsunomiya, S., Kasama, T., Kozai, N. and Ohnuki, T. (2004). Anoxic dissolution processes of biotite: Implications for Fe behavior during Archean weathering. *Earth and Planetary Science Letters,* 224(1-2)**,** 117-129.

Nakata, K., Nagasaki, S., Tanaka, S., Sakamoto, Y., Tanaka, T. and Ogawa, H. (2002). Sorption and reduction of neptunium(V) on the surface of iron oxides. *Radiochimica Acta,* 90**,** 665-669.

NDA. (2009). *UK Strategy for the Management of Soild Low Level Radioactive Waste from the Nuclear Industry: UK Nuclear Industry LLW Strategy*. Harwell. 21585-07.

NDA. (2010a). *Geological Disposal: Generic Post-closure Safety Assessment*. Harwell. NDA/RWMD/030.

NDA. (2010b). *Site Specific Baselines - Capenhurst*. Harwell. 21585-02.

NDA. (2010c). *Geosphere status report*. Harwell. NDA/RWMD/035.

NDA. (2010d). *Geological Disposal: Radionuclide behaviour status report.* Harwell. NDA/RWMD/034.

NDA. (2010e). *Near-field evolution status report*. Harwell. NDA/RWMD/033.

NDA. (2010f). *Geological Disposal: Steps Towards Implimentation*. Harwell. NDA/RWMD/013.

NDA. (2011). *Plutonium Strategy: Current Position Paper*. Harwell. SMS/TS/B1-PLUT/001/A.

NDA. (2013). *Radioactive Wastes in the UK: A Summary of the 2013 Inventory*. Harwell. NDA/ST/STY (14) 0006.

NDA. (2014a). *The 2013 UK Radioactive Waste Inventory: Radioactive Waste Composition*. NDA/ST/STY(14)0011.

NDA. (2014b). *Geological Disposal: Generic disposal facility designs*. Harwell. NDA/RWMD/048.

NDA. (2015). *Nuclear Provision: explaining the cost of cleaning up Britain's nuclear legacy*. Harwell.

Nealson, K. H., Tebo, B. M. and Rosson, R. A. (1988). Occurrence and Mechanisms of Microbial Oxidation of Manganese. *In:* Allen, I. L. (ed.) *Advances in Applied Microbiology.* Academic Press.

Nebelung, C. and Brendler, V. (2010). U(VI) sorption on granite: Prediction and experiments. *Radiochimica Acta,* 98(9-11)**,** 621-625.

Nelson, Y. M., Lion, L. W., Ghiorse, W. C. and Shuler, M. L. (1999). Production of biogenic Mn oxides by Leprothrix discophora SS-1 in a chemically defined growth medium and evaluation of their Pb adsorption characteristics. *Applied and Environmental Microbiology,* 65(1)**,** 175-180.

Nelson, Y. M., Lion, L. W., Shuler, M. L. and Ghiorse, W. C. (2002). Effect of Oxide Formation Mechanisms on Lead Adsorption by Biogenic Manganese (Hydr)oxides, Iron (Hydr)oxides, and Their Mixtures. *Environmental Science & Technology,* 36(3)**,** 421-425.

Newsome, L., Morris, K. and Lloyd, J. R. (2014). The biogeochemistry and bioremediation of uranium and other priority radionuclides. *Chemical Geology,* 363**,** 164-184.

Nichols, A. L., Aldama, D. L. and Verpelli, M. (2008). *Handbook of Nuclear Data for Safeguards: Database Extensions, August 2008*. Vienna.

Nitsche, H. (1987). Effects of temperature on the solubility and speciation of selected actinides in near-neutral solution. *Inorganica Chimica Acta,* 127(1)**,** 121-128.

Nitsche, H. (1991). Solubility Studies of Transuranium Elements for Nuclear Waste Disposal: Principles and Overview. *Radiochimica Acta,* 52-53(1)**,** 3-8.

Nitsche, H. and Edelstein, N. M. (1985). Solubilities and speciation of selected transuranium ions. a comparison of a non-complexing solution with a groundwater from the nevada tuff site. *Radiochimica Acta,* 39(1)**,** 23-34.

Nitsche, H., Roberts, K., Prussin, T., Keeney, D., Carpenter, S. A., Becraft, K. and Gatti, R. C. (1993). Radionuclide solubility and speciation studies for the Yucca Mountain site characterization project. *High Level Radioactive Waste Management.*

Nonat, A. (2004). The structure and stoichiometry of C-S-H. *Cement and Concrete Research,* 34(9)**,** 1521-1528.

Novak, C. F., Nitsche, H., Silber, H. B., Roberts, K., Torretto, P. C., Prussin, T., Becraft, K., Carpenter, S. A., Hobart, D. E. and AlMahamid, I. (1996). Neptunium(V) and Neptunium(VI) Solubilities in Synthetic Brines of Interest to the Waste Isolation Pilot Plant (WIPP). *Radiochimica Acta,* 74**,** 31-36.

Novikov, A. P., Kalmykov, S. N., Utsunomiya, S., Ewing, R. C., Horreard, F., Merkulov, A., Clark, S. B., Tkachev, V. V. and Myasoedov, B. F. (2006). Colloid transport of plutonium in the far-field of the Mayak Production Association, Russia. *Science,* 314(5799)**,** 638-641.

O'Loughlin, E. J., Kelly, S. D. and Kemner, K. M. (2010). XAFS investigation of the interactions of UVI with secondary mineralization products from the bioreduction of FeIII oxides. *Environmental Science & Technology,* 44(5)**,** 1656-1661.

OECD and NEA. (2012). *Thermodynamic Sorption Modelling in Support of Radioactive Waste Disposal Safety Cases*: OECD Publishing.

Ojovan, M. I. and Lee, W. E. (2014). *An Introduction to Nuclear Waste Immobilisation* (2nd ed.). Kidlington, Oxford: Elsevier.

Pan, G., Qin, Y., Li, X., Hu, T., Wu, Z. and Xie, Y. (2004). EXAFS studies on adsorption–desorption reversibility at manganese oxides–water interfaces: I. Irreversible adsorption of zinc onto manganite (γ-MnOOH). *Journal of Colloid and Interface Science,* 271(1)**,** 28-34.

Park, C. K. and Hahn, P. S. (1999). Reversibility and Linearity of Sorption for Some Cations onto a Bulguksa Granite. *Korean Journal of Chemical Engineering,* 16(6)**,** 758-763.

Parry, S. A., O'Brien, L., Fellerman, A. S., Eaves, C. J., Milestone, N. B., Bryan, N. D. and Livens, F. R. (2011). Plutonium behaviour in nuclear fuel storage pond effluents. *Energy & Environmental Science,* 4(4)**,** 1457.

Parsons, J. G., Lopez, M. L., Peralta-Videa, J. R. and Gardea-Torresdey, J. L. (2009). Determination of arsenic(III) and arsenic(V) binding to microwave assisted hydrothermal synthetically prepared Fe3O4, Mn3O4, and MnFe2O4 nanoadsorbents. *Microchemical Journal,* 91(1)**,** 100-106.

PCA. (2016). *Cement and Concrete Basics* [Online]. Available: http://www.cement.org/cement-concrete-basics [Accessed 29/09/2016 2016].

Peacock, C. L. and Moon, E. M. (2012). Oxidative scavenging of thallium by birnessite: Explanation for thallium enrichment and stable isotope fractionation in marine ferromanganese precipitates. *Geochimica et Cosmochimica Acta,* 84**,** 297-313.

Pearce, C., I., Henderson, C. M. B., Pattrick Richard, A. D., Laan Gerrit Van, D. and Vaughan David, J. (2006). Direct determination of cation site occupancies in natural ferrite spinels by L2,3 X-ray absorption spectroscopy and X-ray magnetic circular dichroism. *American Mineralogist,* 91(5-6)**,** 880.

Pointeau, I., Landesman, C., Giffaut, E. and Reiller, P. (2004). Reproducibility of the uptake of U(VI) onto degraded cement pastes and calcium silicate hydrate phases. *Radiochimica Acta,* 92(9-11)**,** 645-650.

Pointeau, I., Piriou, B., Fedoroff, M., Barthes, M. G., Marmier, N. and Fromage, F. (2001). Sorption mechanisms of Eu3+ on CSH phases of hydrated cements. *Journal of Colloid and Interface Science,* 236(2)**,** 252-259.

POST. (2016). *Managing the UK Plutonium Stockpile*. POSTNOTE 531.

Post, J. E. (1999). Manganese oxide minerals: Crystal structures and economic and environmental significance. *Proceedings of the National Academy of Sciences,* 96(7)**,** 3447-3454.

Post, J. E., Heaney, P. J. and Ertl, A. (2008). Rietveld refinement of the ranciéite structure using synchrotron powder diffraction data. *Powder Diffraction,* 23(1)**,** 10-14.

Post, J. E., Heaney, P. J. and Hanson, J. (2002). Rietveld refinement of a triclinic structure for synthetic Na-birnessite using synchrotron powder diffraction data. *Powder Diffraction,* 17(3)**,** 218-221.

Powell, B. A., Duff, M. C., Kaplan, D. I., Fjeld, R. A., Newville, M., Hunter, D. B., Bertsch, P. M., Coates, J. T., Eng, P., Rivers, M. L., Sutton, S. R., Triay, I. R. and Vaniman, D. T. (2006). Plutonium oxidation and subsequent reduction by Mn(IV) minerals in Yucca Mountain tuff. *Environmental Science & Technology,* 40(11)**,** 3508-3514.

Prikryl, J. D., Jain, A., Turner, D. R. and Pabalan, R. T. (2001). UraniumVI sorption behavior on silicate mineral mixtures. *Journal of Contaminant Hydrology,* 47(2-4)**,** 241-253.

Reeder, R. J., Elzinga, E. J., Tait, C. D., Rector, K. D., Donohoe, R. J. and Morris, D. E. (2004). Site-specific incorporation of uranyl carbonate species at the calcite surface. *Geochimica et Cosmochimica Acta,* 68(23)**,** 4799-4808.

Reeder, R. J., Nugent, M., Lamble, G. M., Tait, C. D. and Morris, D. E. (2000). Uranyl Incorporation into Calcite and Aragonite: XAFS and Luminescence Studies. *Environmental Science & Technology,* 34(4)**,** 638-644.

Reeder, R. J., Nugent, M., Tait, C. D., Morris, D. E., Heald, S. M., Beck, K. M., Hess, W. P. and Lanzirotti, A. (2001). Coprecipitation of Uranium(VI) with Calcite: XAFS, micro-XAS, and luminescence characterization. *Geochimica et Cosmochimica Acta,* 65(20)**,** 3491-3503.

Renshaw, J. C., Handley-Sidhu, S. and Brookshaw, D. R. (2011). Pathways of Radioactive Substances in the Environment. *In:* Hester, R. E. & Harrison, R. M. (eds.) *Nuclear Power and the Environment.* Royal Society of Chemistry.

Richardson, I. G. (2004). Tobermorite/jennite- and tobermorite/calcium hydroxide-based models for the structure of C-S-H: applicability to hardened pastes of tricalcium silicate, β-dicalcium silicate, Portland cement, and blends of Portland cement with blast-furnace slag, metakaolin, or silica fume. *Cement and Concrete Research,* 34(9)**,** 1733-1777.

Richter, C., Müller, K., Drobot, B., Steudtner, R., Großmann, K., Stockmann, M. and Brendler, V. (2016). Macroscopic and spectroscopic characterization of uranium(VI) sorption onto orthoclase and muscovite and the influence of competing Ca2+. *Geochimica et Cosmochimica Acta,* 189**,** 143-157.

Rieder, M., Cavazzini, G., D'Yakonov, Y. U., Frank-Kamenetskii, V. A., Gottardi, G., Guggenheim, S., Koval, P. V., Muller, G., Neiva, A. M. R., Radoslovich, E. W., Robert, J.-L., Sassi, F. P., Takeda, H., Weiss, Z. and Wones, D. R. (1999). Nomenclature of the micas. *Mineralogical Magazine,* 63(2)**,** 267-279.

Rigol, A., Vidal, M. and Rauret, G. (2000). Laboratory experiments to study radiocaesium interaction in organic soils. *International Journal of Environmental Analytical Chemistry,* 78(3-4)**,** 441-454.

Rihs, S., Gaillard, C., Reich, T. and Kohler, S. J. (2014). Uranyl sorption onto birnessite: A surface complexation modeling and EXAFS study. *Chemical Geology,* 373**,** 59-70.

Rihs, S., Sturchio, N. C., Orlandini, K., Cheng, L., Teng, H., Fenter, P. and Bedzyk, M. J. (2004). Interaction of uranyl with calcite in the presence of EDTA. *Environmental Science & Technology,* 38(19)**,** 5078-5086.

Roy, S. (1981). *Manganese Deposits*. London: Academic Press.

Runde, W. (2000). The Chemical Interactions of Actinides in the Environment. *Los Alamos Science.*

Runde, W., Neu, M. P. and Clark, D. L. (1996). Neptunium(V) hydrolysis and carbonate complexation: Experimental and predicted neptunyl solubility in concentrated NaCl using the Pitzer approach. *Geochimica et Cosmochimica Acta,* 60(12)**,** 2065-2073.

Sajih, M., Bryan, N. D., Livens, F. R., Vaughan, D. J., Descostes, M., Phrommavanh, V., Nos, J. and Morris, K. (2014). Adsorption of radium and barium on goethite and ferrihydrite: A kinetic and surface complexation modelling study. *Geochimica et Cosmochimica Acta,* 146**,** 150-163.

Samson, S. D., Nagy, K. L. and Cotton Iii, W. B. (2005). Transient and quasi-steady-state dissolution of biotite at 22-25°C in high pH, sodium, nitrate, and aluminate solutions. *Geochimica et Cosmochimica Acta,* 69(2)**,** 399-413.

Savoye, S., Michelot, J. L. and Wittebroodt, C. (2006). Evaluation of the reversibility of iodide uptake by argillaceous rocks by the radial diffusion method. *Radiochimica Acta,* 94(9-11)**,** 699-704.

Schlegel, M. L., Pointeau, I., Coreau, N. and Reiller, P. (2004). Mechanism of europium retention by calcium silicate hydrates: An EXAFS study. *Environmental Science & Technology,* 38(16)**,** 4423-4431.

Schmeide, K. and Bernhard, G. (2010). Sorption of Np(V) and Np(IV) onto kaolinite: Effects of pH, ionic strength, carbonate and humic acid. *Applied Geochemistry,* 25**,** 1238-1247.

Schmeide, K., Pompe, S., Bubner, M., Heise, K. H., Bernhard, G. and Nitsche, H. (2000). Uranium(VI) sorption onto phyllite and selected minerals in the presence of humic acid. *Radiochimica Acta,* 88(9-11)**,** 723-728.

Schulze, D. G. (2002). An Introduction to Soil Mineralogy. *In:* Dick, W. A. (ed.) *Soil Mineralogy with Environmental Applications.* Madison, Wisconsin: Soil Science Society of America.

Seliman, A. F., Lasheen, Y. F., Youssief, M. A. E., Abo-Aly, M. M. and Shehata, F. A. (2014). Removal of some radionuclides from contaminated solution using natural clay: bentonite. *Journal of Radioanalytical and Nuclear Chemistry,* 300(3)**,** 969-979.

Sellafield Ltd. (2016a). *Facts* [Online]. Available: http://www.sellafieldsites.com/press-office/facts/ [Accessed 12/09/2016 2016].

Sellafield Ltd. (2016b). *Thorp Reprocessing* [Online]. Available: http://www.sellafieldsites.com/solution/spent-fuel-management/thorp-reprocessing/ [Accessed 12/09/2016 2016].

Sellafield Ltd. (2014). *Groundwater Monitoring at Sellafield: Annual Data Review 2014* LQTD000080.

Sharrad, C. A., Harwood, L. M. and Livens, F. R. (2011). Nuclear Fuel Cycles: Interfaces with the Environment. *In:* Hester, R. E. & Harrison, R. M. (eds.) *Nuclear Power and the Environment.* Royal Society of Chemistry.

Shaughnessy, D. A., Nitsche, H., Booth, C. H., Shuh, D. K., Waychunas, G. A., Wilson, R. E., Gill, H., Cantrell, K. J. and Serne, R. J. (2003). Molecular interfacial reactions between Pu(VI) and manganese oxide minerals manganite and hausmannite. *Environmental Science & Technology,* 37(15)**,** 3367-3374.

Shelobolina, E. S., Sullivan, S. A., O'Neill, K. R., Nevin, K. P. and Lovley, D. R. (2004). Isolation, characterization, and U(VI)-reducing potential of a facultatively anaerobic, acid-resistant bacterium from low-pH, nitrate- and U(VI)-contaminated subsurface sediment and description of Salmonella subterranea sp. nov. *Applied and Environmental Microbiology* 2959–2965.

Sheng, G. D., Yang, S. T., Li, Y. M., Gao, X., Huang, Y. Y., Hu, J. and Wang, X. K. (2014). Retention mechanisms and microstructure of Eu(III) on manganese dioxide studied by batch and high resolution EXAFS technique. *Radiochimica Acta,* 102(1-2)**,** 155-167.

Sherman, D. M., Peacock, C. L. and Hubbard, C. G. (2008). Surface complexation of U(VI) on goethite (α-FeOOH). *Geochimica et Cosmochimica Acta,* 72(2)**,** 298-310.

Sherriff, N., Issa, R., Morris, K., Livens, F., Heath, S. and Bryan, N. (2015). Reversibility in radionuclide/bentonite bulk and colloidal ternary systems. *Mineralogical Magazine,* 79(6)**,** 1307-1315.

Sidhu, S. P., Gilkes, R. J. and Posner, A. M. (1978). The Synthesis and Some Properties of Co, Ni, Zn, Cu, Mn and Cd Substituted Magnetites. *Journal of Inorganic and Nuclear Chemistry,* 40(3)**,** 429-435.

Silva, G. C., Almeida, F. S., Ferreira, A. M. and Ciminelli, V. S. T. (2012). Preparation and application of a magnetic composite (Mn3O4/Fe3O4) for removal of as(III) from aqueous solutions. *Materials Research,* 15(3)**,** 403-408.

Sims, R., Lawless, T. A., Alexander, J. L., Bennett, D. G. and Read, D. (1996). Uranium migration through intact sandstone: Effect of pollutant concentration and the reversibility of uptake. *Journal of Contaminant Hydrology,* 21(1-4)**,** 215-228.

Small, J. S. and Thompson, O. R. (2009). Modelling the spatial and temporal evolution of pH in the cementitious backfill of a geological disposal facility. *In:* Hyatt, N. C., Pickett, D. A. & Rebak, R. B. (eds.) *Scientific Basis for Nuclear Waste Management Xxxii.*

Smith, K. F., Bryan, N. D., Swinburne, A. N., Bots, P., Shaw, S., Natrajan, L. S., Mosselmans, J. F. W., Livens, F. R. and Morris, K. (2015). U(VI) behaviour in hyperalkaline calcite systems. *Geochimica et Cosmochimica Acta,* 148**,** 343-359.

Spiro, T. G., Bargar, J. R., Sposito, G. and Tebo, B. M. (2010). Bacteriogenic Manganese Oxides. *Accounts of Chemical Research,* 43(1)**,** 2-9.

Sposito, G. (2004). *The Surface Chemistry of Natural Particles*. New York: Oxford University Press.

Stewart, B. D., Mayes, M. A. and Fendorf, S. (2010). Impact of Uranyl−Calcium−Carbonato Complexes on Uranium(VI) Adsorption to Synthetic and Natural Sediments. *Environmental Science & Technology,* 44(3)**,** 928-934.

Strawn, D. G. and Sparks, D. L. (1999). The Use of XAFS to Distinguish between Inner- and Outer-Sphere Lead Adsorption Complexes on Montmorillonite. *Journal of Colloid and Interface Science,* 216(2)**,** 257-269.

Stumm, W. and Morgan, J. J. (1996). *Aquatic Geochmistry: Chemical Equilibria and Rates in Natural Waters*. New York: John Wiley & Sons Inc.

Sturchio, N. C., Antonio, M. R., Soderholm, L., Sutton, S. R. and Brannon, J. C. (1998). Tetravalent Uranium in Calcite. *Science,* 281(5379)**,** 971.

Sugimori, H., Iwatsuki, T. and Murakami, T. (2008). Chlorite and biotite weathering, Fe2+-rich corrensite formation, and Fe behavior under low pO2 conditions and their implication for precambrian weathering. *American Mineralogist,* 93(7)**,** 1080-1089.

Sun, Y. B., Yang, S., Sheng, G. D., Wang, Q., Guo, Z. Q. and Wang, X. K. (2012). Removal of U(VI) from aqueous solutions by the nano-iron oxyhydroxides. *Radiochimica Acta,* 100(10)**,** 779-784.

Suzuki, Y. and Banfield, J. F. (1999). Geomicrobiology of uranium. *Reviews in Mineralogy and Geochemistry,* 38**,** 393-432.

Swanton, S. W., Alexander, W. R. and Berry, J. A. (2009). *Review of the behaviour of colloids in the near field of a cementitious repository* SERCO/TAS/000475/01.

Tanaka, K., Tani, Y. and Toshihiko. (2011). Specific Sorption Behaviour of Actinoids on Bengenic Mn Oxide. *Chemistry Letters,* 40**,** 806-807.

Tani, Y., Ohashi, M., Miyata, N., Seyama, H., Iwahori, K. and Soma, M. (2004). Sorption of Co(II), Ni(II), and Zn(II) on Biogenic Manganese Oxides Produced by a Mn-Oxidizing Fungus, Strain KR21-2. *Journal of Environmental Science and Health, Part A,* 39(10)**,** 2641-2660.

Tebo, B. M. (1991). Manganese(II) oxidation in the suboxic zone of the Black Sea. *Deep Sea Research Part A. Oceanographic Research Papers,* 38**,** S883-S905.

Tebo, B. M., Bargar, J. R., Clement, B. G., Dick, G. J., Murray, K. J., Parker, D., Verity, R. and Webb, S. M. (2004). Biogenic Manganese Oxides: Properties and Mechanisms of Formation. *Annual Review of Earth and Planetary Sciences,* 32(1)**,** 287-328.

Tebo, B. M., Ghiorse, W. C., Van Waasbergen, L. G., Siering, P. L. and Caspi, R. (1997). Bacterially mediated mineral formation: insights into manganese(h) oxidation from molecular genetic and biochemical studies. *Reviews in Mineralogy,* 35**,** 259-266.

Tebo, B. M., Nealson, K. H., Emerson, S. and Jacobs, L. (1984). Microbial mediation of Mn(II) and Co(II) precipitation at the O2/H2S interfaces in two anoxic fjords1. *Limnology and Oceanography,* 29(6)**,** 1247-1258.

Telchadder, R., Smith, K. and Bryan, N. D. (2012). Europium interaction with a vault backfill at high pH. *Mineralogical Magazine,* 76(8)**,** 3083-3093.

Teng, H. H., Fenter, P., Cheng, L. and Strurchio, N. C. (2001). Resolving orthoclase dissolution processes with atomic force microscopy and X-ray reflectivity. *Geochimica et Cosmochimica Acta,* 65(20)**,** 3459-3474.

The Scottish Government. (2011). *Scotland's Higher Activity Radioactive Waste Policy 2011*.

Thorpe, C. L., Morris, K., Lloyd, J. R., Denecke, M. A., Law, K. A., Dardenne, K., Boothman, C., Bots, P. and Law, G. T. W. (2015). Neptunium and manganese biocycling in nuclear legacy sediment systems. *Applied Geochemistry,* 63**,** 303-309.

Tits, J., Fujita, T., Tsukamoto, M. and Wieland, E. (2008). Uranium(VI) Uptake by Synthetic Calcium Silicate Hydrates. *Materials Research Society Symposium Proceedings,* 1107**,** 467-474.

Tits, J., Geipel, G., Macé, N., Eilzer, M. and Wieland, E. (2011). Determination of uranium(VI) sorbed species in calcium silicate hydrate phases: a laser-induced luminescence spectroscopy and batch sorption study. *Journal of Colloid and Interface Science,* 359(1)**,** 248-256.

Turner, D. R., Pabalan, R. T. and Bertetti, F. P. (1998). Neptunium (V) sorption on montmorillonite: an experimental and surface complexation modelling study. *Clays and Clay Minerals,* 46(3)**,** 256-269.

Um, W., Serne, R. J. and Krupka, K. M. (2004). Linearity and reversibility of iodide adsorption on sediments from Hanford, Washington under water saturated conditions. *Water Research,* 38(8)**,** 2009-2016.

UNSCEAR. (2000). *Sources and Effects of Ionizing Radiation*. New York.

USNRC. (2014). *Backgrounder on the Three Mile Island Accident* [Online]. Available: http://www.nrc.gov/reading-rm/doc-collections/fact-sheets/3mile-isle.html [Accessed 12/09/2016 2016].

USNRC. (2016a). *Uranium Enrichment* [Online]. Available: http://www.nrc.gov/materials/fuel-cycle-fac/ur-enrichment.html [Accessed 12/09/2016 2016].

USNRC. (2016b). *Fuel Fabrication* [Online]. Available: http://www.nrc.gov/materials/fuel-cycle-fac/fuel-fab.html [Accessed 12/09/2916 2016].

USNRC. (2016c). *Stages of the Nuclear Fuel Cycle* [Online]. Available: http://www.nrc.gov/materials/fuel-cycle-fac/stages-fuel-cycle.html [Accessed 26/09/2016 2016].

Utsunomiya, S., Kersting, A. B. and Ewing, R. C. (2009). Groundwater Nanoparticles in the Far-Field at the Nevada Test Site: Mechanism for Radionuclide Transport. *Environmental Science & Technology,* 43**,** 1293-1298.

Villalobos, M., Bargar, J. and Sposito, G. (2005). Trace Metal Retention on Biogenic Manganese Oxide Nanoparticles. *Elements,* 1(4)**,** 223-226.

Villalobos, M., Toner, B., Bargar, J. and Sposito, G. (2003). Characterization of the manganese oxide produced by Pseudomonas putida strain MnB1. *Geochimica et Cosmochimica Acta,* 67(14)**,** 2649-2662.

Vines, S. and Beard, R. (2012). An overview of radionuclide behaviour research for the UK geological disposal programme. *Mineralogical Magazine,* 76(8)**,** 3373-3380.

Waite, T. D., Davis, J. A., Payne, T. E., Waychunas, G. A. and Xu, N. (1994). Uranium(VI) adsorption to ferrihydrite: Application of a surface complexation model. *Geochimica et Cosmochimica Acta,* 58(24)**,** 5465-5478.

Walls, J. (2011). Nuclear Power Generation - Past, Present and Future. *In:* Hester, R. E. & Harrison, R. M. (eds.) *Nuclear Power and the Environment.* Royal Society of Chemistry.

Walter, M., Arnold, T., Geipel, G., Scheinost, A. and Bernhard, G. (2005). An EXAFS and TRLFS investigation on uranium(VI) sorption to pristine and leached albite surfaces. *Journal of Colloid and Interface Science,* 282(2)**,** 293-305.

Walther, C. and Denecke, M. A. (2013). Actinide Colloids and Particles of Environmental Concern. *Chemical Reviews,* 113(2)**,** 995-1015.

Wang, Z., Lee, S. W., Catalano, J. G., Lezama-Pacheco, J. S., Bargar, J. R., Tebo, B. M. and Giammar, D. E. (2013). Adsorption of uranium(VI) to manganese oxides: X-ray absorption spectroscopy and surface complexation modeling. *Environmental Science & Technology,* 47(2)**,** 850-858.

Wang, Z., Zachara, J. M., McKinley, J. P. and Smith, S. C. (2005). Cryogenic Laser Induced U(VI) Fluorescence Studies of a U(VI) Substituted Natural Calcite: Implications to U(VI) Speciation in Contaminated Hanford Sediments. *Environmental Science & Technology,* 39(8)**,** 2651-2659.

Weaver, R. M. and Hochella Jr, M. F. (2003). The reactivity of seven Mn-oxides with Cr3+ aq: A comparative analysis of a complex, enviromentally important redox reaction. *American Mineralogist,* 88(11-12 PART 2)**,** 2016-2027.

Webb, S. M., Fuller, C. C., Tebo, B. M. and Bargar, J. R. (2006). Determination of Uranyl Incoporation into Biogenic Manganese Oxides Using X-ray Absorption Spectroscopy and Scattering. *Environmental Science & Technology,* 40**,** 771-777.

Webb, S. M., Tebo, B. M. and Bargar, J. R. (2005). Structural characterization of biogenic Mn oxides produced in seawater by the marine *bacillus sp.* strain SG-1. *American Mineralogist,* 90**,** 1342-1357.

West, J. M., Humphreys, P. N. and Metcalfe, R. (2010). *Microbial Effects on Respository Performance* QRS-1378Q-1.

White, W. M. (2013). Aquatic Chemistry. *Geochemistry.* Chichester, West Sussex: John Wiley & Sons Ltd.

Wieland, E., Macé, N., Dähn, R., Kunz, D. and Tits, J. (2010). Macro- and micro-scale studies on U(VI) immobilization in hardened cement paste. *Journal of Radioanalytical and Nuclear Chemistry,* 286(3)**,** 793-800.

Wilk, P. A., Shaughnessy, D. A., Wilson, R. E. and Nitsche, H. (2005). Interfacial Interactions between Np(V) and Manganese Oxide Minerals Manganite and Hausmannite. *Environmental Science & Technology,* 39**,** 2608-2615.

Wilson, P. D. (1996). *The Nuclear Fuel Cycle: From Ore to Wastes*. Oxford: Oxford University Press.

Wold, S. (2010). *Sorption of prioritized elements on montmorillonite colloids and their potential to transport radionuclides* TR-10-20.

World Nuclear Association. (2016a). *Mining of Uranium* [Online]. Available: http://www.world-nuclear.org/information-library/nuclear-fuel-cycle/mining-of-uranium/uranium-mining-overview.aspx [Accessed 12/09/2016 2016].

World Nuclear Association. (2016b). *Fukushima Accident* [Online]. [Accessed 10/09/2016].

World Nuclear Association. (2016c). *Processing of Used Nuclear Fuel* [Online]. Available: http://www.world-nuclear.org/information-library/nuclear-fuel-cycle/fuel-recycling/processing-of-used-nuclear-fuel.aspx [Accessed 12/09/2016 2016].

Wu, W.-M., Carley, J., Gentry, T., Ginder-Vogel, M. A., Fienen, M., Mehlhorn, T., Yan, H., Caroll, S., Pace, M. N., Nyman, J., Luo, J., Gentile, M. E., Fields, M. W., Hickey, R. F., Gu, B., Watson, D., Cirpka, O. A., Zhou, J., Fendorf, S., Kitanidis, P. K., Jardine, P. M. and Criddle, C. S. (2006). Pilot-Scale in Situ Bioremedation of Uranium in a Highly Contaminated Aquifer. 2. Reduction of U(VI) and Geochemical Control of U(VI) Bioavailability. *Environmental Science & Technology,* 40(12)**,** 3986-3995.

Yamamoto, M., Yamauchi, Y., Komura, K., Ueno, K. and Assinder, D. J. (1991). Chemical leaching behavior of ^{237}Np from intertidal coastal sediment in the Irish Sea. *Journal of Radioanalytical and Nuclear Chemistry,* 154(5)**,** 299-307.

Yamamura, T., Kitamura, A., Fukui, A., Nishikawa, S., Yamamoto, T. and Moriyama, H. (1998). Solubility of U(VI) in highly basic solutions. *Radiochimica Acta,* 83(3)**,** 139-146.

Yoshida, H. (1994). Relation between U-series nuclide migration and microstructural properties of sedimentary rocks. *Applied Geochemistry,* 9(5)**,** 479-490.

Yoshida, Z., Johnson, S. G., Kimura, T. and Krisul, J. R. (2011). Neptunium. *In:* Morss, L. R., Edelstein, N. M. & Fuger, J. (eds.) *The chemistry of the actinide and transactide elements.* 4th ed. Dordrecht: Springer.

Yusan, S. and Akyil, S. (2008). Sorption of uranium(VI) from aqueous solutions by akaganeite. *Journal of Hazardous Materials,* 160(2-3)**,** 388-395.

Zavarin, M., Powell, B. A., Bourbin, M., Zhao, P. and Kersting, A. B. (2012). Np(V) and Pu(V) Ion Exchange and Surface-Mediated Reduction Mechanisms on Montmorillonite. *Environmental Science & Technology,* 46(5)**,** 2692-2698.

Zou, W., Zhao, L. and Han, R. (2010). Adsorption characteristics of uranyl ions by manganese oxide coated sand in batch mode. *Journal of Radioanalytical and Nuclear Chemistry,* 288(1)**,** 239-249.

3. Experimental Methods

This project has utilised a range of geochemical, mineralogical, radiometric, and spectroscopic techniques to understand the interaction of uranium and neptunium with mineral phases. This chapter focuses on the theory of each technique; experimental details relevant to each research chapter are also provided.

3.1. Safety

All chemicals used and reactions undertaken during the preparation of this thesis were first subject to a risk-assessment in accordance with the Control of Substances Hazardous to Heath (COSHH) and subsequently appropriate precautions were then taken. In addition, statutory controls manage the supply and manipulation of radioactive materials, and ionisation radiation can be harmful to human health. Therefore, safety training was required prior to work, and strict protocols and operating procedures were in place throughout this project. All work was conducted in compliance with the institution's guidelines, Ionising Radiation Regulations 1999, Environmental Permitting Regulations 2010, and the Health and Safety at Work Act 1974.

3.2. Thermodynamic Calculations

Thermodynamic calculations were performed using PHREEQC V3.3.7 (Parkhurst and Appelo, 2013) to determine the saturation indices of a range of mineral phases. In work investigating U(VI) colloids and their stability (Chapter 4 and 5) the impact of changing the solution chemistry on the supersaturated phases was investigated. In Chapters 6 and 7, PHREEQC was used to ensure the radionuclide concentrations used were below the solubility limits. Both the SIT (Specific-ion Interaction Theory; ThermoChimie v.8.0 September 2011) and the Lawrence Livermore National Laboratory (LLNL, V8 R6, April 2015) databases were used.

3.3. Atmospheric Controls

A large portion of this work was performed at high pH, and as a result CO_2 exclusion was required. In addition, some experiments (*e.g.* those investigating hausmannite) also required the exclusion of O_2. For atmosphere sensitive work a glove box was used, with O_2 sensitive experiments conducted under argon (British Oxygen Company (BOC)) or Oxygen Free Nitrogen (BOC), and CO_2 sensitive experiments conducted under Oxygen Free Nitrogen (BOC) or lab air which had been passed through three dreschels containing 14 M NaOH (laboratory grade) which were used to remove CO_2.

3.4. Cement Leachate, Uranium Colloid, and Cement / Mineral Preparations

The chemicals used throughout were analytical reagent grade, except where otherwise stated, and all solutions were made using Milli-Q (18.2 ΩM) water.

3.4.1. Cement Leachate and Uranium Colloid Preparation

Colloidal U(VI) nanoparticles were prepared in a pH 13.3 synthetic cement leachate representative of the young cement leachate expected in UK ILW disposal (Berner, 1992; Bots et al., 2014). Here, 5.19 g KOH (0.1 mol), 3.80 g NaOH (0.1 mol), and 10.1 mg $Ca(OH)_2$ (0.14 mmol) were dissolved in 1 L of degassed water (final pH 13.3 ± 0.1) and filtered to < 0.22 μm (PVDF filter). The young cement leachate was then spiked with a U(VI) stock solution (2.52 mM U(VI) in 0.001 M HCl) to a final concentration of 42 μM U(VI) in order to generate stable colloidal U(VI) nanoparticles (Bots et al., 2014; Smith et al., 2015).

3.4.2. Cement

Cement representative of the backfill material used in the UK generic intermediate level safety case was prepared (Telchadder et al., 2012) under CO_2 free conditions from Ordinary Portland Cement (OPC), limestone flour and hydrated lime in the wt:wt ratio

265:291:100. Once mixed the cement was reacted for 20 minutes and then hydrated at a ratio of 1.8:1 (solid:water). The mixture was then stirred for 3 hours prior to curing for 28 days. Once cured, the cement was crushed with a pestle and mortar and sieved to < 63 µm. The surface area of the crushed and sieved fraction was measured using N_2 Brunauer-Emmett-Teller (BET; section 3.11) analysis. Synthesis was confirmed by XRD (section 3.10), environmental scanning electron microscopy (ESEM; section 3.12.1), and energy dispersive X-ray spectroscopy (EDX; section 3.12.2).

3.4.3. δ-Mn(VI)O_2

The δ-MnO_2 synthesis was adapted from Villalobos et al. (2003). $KMnO_4$ solution (0.2 M, 1.28 L) was added slowly over 5 minutes, with vigorous stirring, to a solution of $MnCl_2$ (0.3 M, 1.28 L). A NaOH (0.5 M, 1.44 L) solution was then added to the mixture slowly over 35 minutes, with vigorous stirring, to form a black precipitate. The suspension was then allowed to settle for 4 hours before determining the pH as 7.0 and decanting and discarding the supernatant. The remaining suspension was centrifuged (17000 *g*, 20 minutes, 20°C) and the supernatant discarded. The resulting mineral paste was washed 5 times with NaCl (1 M) and then 10 times with Milli-Q water with centrifuging (17000 *g*, 20 minutes, 20°C) performed between washing steps. The final mineral suspension was confirmed to be pH 8.0 and was then stored below 5°C in the dark. Synthesis was confirmed by XRD (section 3.10), ESEM (section 3.12.1), and EDX (section 3.12.2); BET (section 3.11) was used to determine the surface area.

3.4.4. Triclinic (Na)-Birnessite [$Na_{0.5}Mn(III/IV)_2O_4 \cdot 1.5H_2O$]

The triclinic (Na)-birnessite synthesis was adapted from Villalobos et al. (2003). $MnCl_2$ (0.16 M, 0.32 L) solution was added slowly, over 40 minutes to a NaOH (7.6 M, 0.36 L) solution, to form a pink gel like phase. $KMnO_4$ (0.2 M, 0.32 L) solution was then added to the mixture slowly, over 50 minutes, with vigorous stirring, to form a dark grey precipitate.

The mixture was stirred for a further 2 hours before heating to 55°C for 24 hours. The supernantant was then discarded; the mineral paste was washed 5 times with NaCl (1 M), and then with Milli-Q water until the pH of the suspension reached 9.8, with centrifuging (17000 *g*, 20 minutes, 20°C) performed between washing steps. This was stored below 5°C in the dark. Synthesis was confirmed by XRD (section 3.10), ESEM (section 3.12.1), and EDX (section 3.12.2); BET (section 3.11) was used to determine the surface area.

3.4.5. Hausmannite [$Mn(II/III)_3O_4$]

The hausmannite synthesis was adapted from McArdell et al. (1998). All solutions were sparged with N_2 prior to reaction. The synthesis and subsequent manipulations were carried out under N_2 to prevent the conversion of hausmannite to manganite (Kirillov et al., 2009). A solution of $MnSO_4$ (0.06 M, 1.5 L) was heated to 60°C before the addition of H_2O_2 (8.8 M, 30.75 mL). To this, NH_4OH (0.2 M, 0.45 L) solution was added slowly (1 mL per second). The resulting suspension was heated to 95°C and maintained at this temperature for 6 hours before being allowed to cool overnight. The mineral was then washed 10 times with Milli-Q water (with centrifuging (17000 *g*, 20 minutes, 20°C) performed between washing steps), re-suspended, and stored under N_2. Synthesis was confirmed by XRD (section 3.10), ESEM (section 3.12.1), and EDX (section 3.12.2); BET (section 3.11) was used to determine the surface area.

3.4.6. Rhodochrosite [$MnCO_3$]

Rhodochrosite was purchased from Alfa Aesar and characterised using XRD (section 3.10), ESEM (section 3.12.1), EDX (section 3.12.2), and BET (section 3.11) prior to use.

3.5. ^{232}U Separation

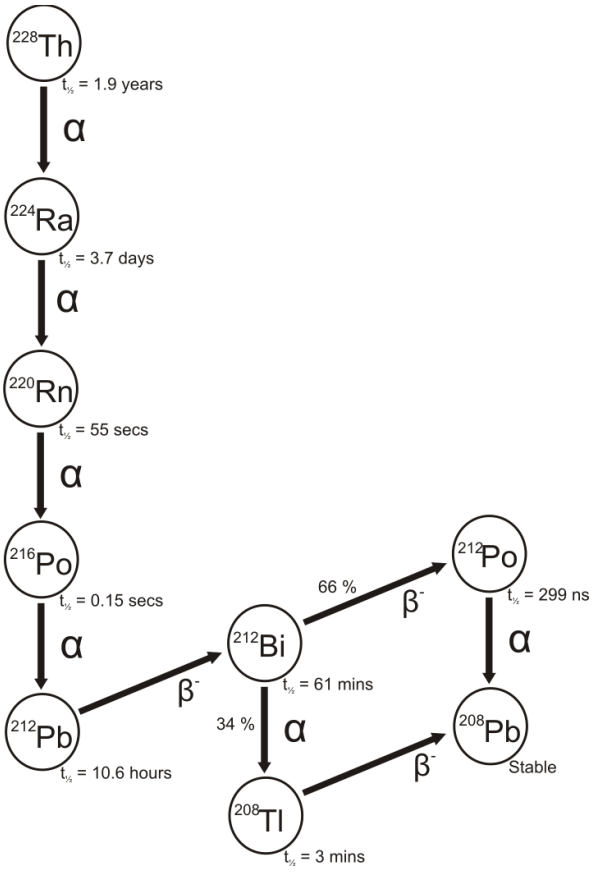

Figure 3.1: The ^{228}Th decay series.

The half-life of ^{232}U is 68.9 years with the radionuclide undergoing α decay to ^{228}Th. This and further daughters are also unstable and undergo further radioactive decay (Figure 3.1) (Smith et al., 1988) and as a result, ^{232}U must be separated from its daughters prior to use as a U tracer. This can be achieved by exploiting the differing chemical behaviour of U(VI) from that of its daughters (Figure 3.1). Under acidic conditions (5 M HCl) U(VI) has a higher affinity for UTEVA resin (Morgenstern et al., 2002). A 5 M HCl solution of ^{232}U(VI) in secular equilibrium (purchased from Areva) was therefore passed through a column containing UTEVA resin, so that only the U(VI) was taken up by the column. Subsequent washes with 5 M HCl ensured any remaining daughters were eluted. The ^{232}U(VI) fraction was then removed from the column by washing with a less acidic HCl solution (0.1 M). Once collected, the ^{232}U(VI) fraction was concentrated *via* evaporation

and then partially re-diluted using water. This was done to both increase the specific activity and to increase the pH (to pH 3) of the spike so that any pH adjustment caused to the mineral-containing solutions was minimised and resulted in a spike of $UO_2Cl_{2(aq)}$ in HCl. All HCl used was analytical regent grade and all solutions were made using Milli-Q (18.2 MΩ) water.

Due to the ingrowth of ^{228}Th and its daughters, experiments utilising ^{232}U to investigate U behaviour are time limited. Following separation, a 3 month window was employed during which the ingrowth of daughters into ^{232}U was considered to be negligible.

3.6. Batch experiments

Batch experiments have been utilised to assess the formation and stability of U(VI) nanoparticles in pH 13.3 young cement leachate in the presence of a range of mineral phases. They have also be used to investigate the interactions of U(VI) and Np(V) with a range of Mn minerals over circumneutral to alkaline pH, in solutions containing a background electrolyte of 0.01 M $NaClO_4$. All chemicals used were analytical regent grade and all solutions were made using Milli-Q (18.2 MΩ) water.

3.6.1. U(VI) Nanoparticle Formation

Young cement leachate was spiked with $U(VI)O_2Cl_{2(aq)}$ in HCl (purchased from British Nuclear Fuels Limited) to give experiments with three U(VI) concentrations, 4.2 µM, 42 µM (run in triplicate), and a single 252 µM U(VI) system. Solution samples were removed periodically and filtered using 0.22 µm PVDF, 0.10 µm PVDF, and 0.02 µm Anotop syringe filters, as well as collecting unfiltered settled solutions to characterise the different colloidal fractions in the reacted solutions (Bots et al., 2014). Samples were acidified with H_2SO_4 (4 M) prior to storage, and after an appropriate dilution the major cations in solution samples were analysed by inductively coupled plasma – atomic emission spectrometry (ICP-AES) and ICP – mass spectrometry (ICP-MS; section 3.7).

Solid samples were collected from the 252 μM system after centrifugation at 1700 *g* for 5 minutes. At selected timepoints, suspended particles were captured on positively charged C-SMART Plus (Dune Sciences) or carbon coated (Agar Scientific) TEM grids. Isopropanol was used the remove the supernatant in order to minimize the effect of drying on the solids.

3.6.2. U(VI) Nanoparticle Stability

Young cement leachate containing U(VI) colloids was equilibrated for 24 hours and the pH was determined as 13.3. The pH then remained stable throughout the experiments (within 0.2 pH units). 10 g L^{-1} of the crushed and sieved (< 63 μm) cement was added to the batch reaction systems. Experiments were run at three U(VI) concentrations, 4.2 μM, 42 μM (run in triplicate), and a single 252 μM U(VI) system. Solution samples were filtered using 0.22 μm PVDF, 0.10 μm PVDF, and 0.02 μm Anotop syringe filters, as well as collecting unfiltered settled solutions to characterise the different colloidal fractions in the reacted solutions (Bots et al., 2014). Samples were acidified with H_2SO_4 (4 M) prior to storage, and after an appropriate dilution the major cations in solution samples were analysed by ICP-AES and ICP-MS (section 3.7). Solid samples were also collected periodically after centrifugation at 1700 *g* for 5 minutes.

3.6.3. Radionuclide sorption to Mn minerals

3.6.3.1. Uranium

Tracer level (5.27 x 10^{-5} μM) sorption experiments were carried out using $^{232}U(VI)$ (prepared as described in section 3.5) to investigate the behaviour of environmentally relevant concentrations of U(VI) with varying Mn minerals. A depleted uranium (DU) stock (2.10 mM $U(VI)O_2Cl_{2(aq)}$ (British Nuclear Fuels Limited) in 0.001 M HCl) was also used to investigate U(VI) uptake at higher concentration (1 μM) and to allow XAS analysis.

Tracer sorption experiments were performed in 100 mL batch experiments in triplicate at pH 10.5, 9.0, and 7.5. Here, the mineral slurry (or solid rhodochrosite) (0.01 g) was added to water, containing $NaClO_4$ (0.01 M) as background electrolyte. These were adjusted to the appropriate pH using HCl and NaOH, prior to spiking with $^{232}U(VI)$ (40 kBq mL^{-1}) to give a ^{232}U concentration of 10 Bq mL^{-1} (5.27 x 10^{-5} µM). Samples were taken periodically, centrifuged (10 mins, 15000 *g*), acidified, mixed with scintillation cocktail, and counted using liquid scintillation counting (LSC; section 3.9) to determine the concentration of ^{232}U remaining in solution. Samples were also taken to monitor the pH.

Experiments using depleted uranium were performed in the same way and were also carried out in triplicate at pH 10.5, 9.0, and 7.5. However, the experiments were spiked to a U(VI) concentration of 1 µM, analysed using ICP-MS, and scaled to 1 L batch experiments to provide sufficient mineral for XAS.

3.6.3.2. Neptunium

The sorption of $^{237}Np(V)$ to Mn minerals at pH 7.5 was investigated using 100 mL batch experiments. Mineral slurry (or solid rhodochrosite) (0.5 g) was added to water, containing $NaClO_4$ (0.01 M) as background electrolyte. The pH was adjusted using HCl and NaOH prior to spiking with $^{237}Np(V)$ (3.67 kBq mL^{-1}; 0.59 mM $Np(V)O_2NO_{3(aq)}$ in 0.1 M HNO_3; purchased from the National Physics Laboratory) to give a ^{237}Np concentration of 32.4 Bq mL^{-1} (5.23 µM). Samples were taken periodically, centrifuged (10 mins, 15000 *g*), acidified, mixed with scintillation cocktail and counted using LSC (section 3.9) to determine the concentration of ^{237}Np remaining in solution. Samples were also taken to monitor the pH.

3.6.4. Reversibility Experiments

The reversibility of U(VI) sorption at both tracer (5.27 x 10^{-5} μM) and depleted (1 μM) U(VI) concentrations was investigated using triplicate experiments at pH 10.5, 9.0, and 7.5.

Batch experiments (comparable to the sorption experiments described in section 3.6.2.1.), containing 0.005 g of Mn mineral were set up in 50 mL centrifuge tubes. These were pH adjusted using HCl and NaOH, spiked with U(VI), and allowed to equilibrate for at least 1 week. Equilibration was confirmed by determining the solution phase U concentration. The experiments were then centrifuged (20 mins, 6000 *g*) and the supernatant replaced with an identical solution without U. The mineral was then re-suspended. Samples were taken periodically and analysed, as described above (section 2.5.2), to determine the pH and U concentration (as well as Mn concentration in experiments containing 1 μM U).

3.7. Inductively-Coupled Plasma Mass Spectrometry (ICP-MS) and Inductively-Coupled Plasma Atomic Emission Spectrometry (ICP-AES)

ICP-MS and ICP-AES were used to measure the solution concentration of U and Mn in experiments investigating sorption of 1 μM U(VI) to Mn minerals, and concentration of U and other cations (K, Na, Ca, Al, Si), in experiments investigating the stability of U(VI) nanoparticles. ICP-MS has a lower tolerance than ICP-AES for dissolved solids (< 0.1 versus 1 – 5 %) but has lower limits of detection (0.01 versus 10 ppb). Both techniques use a nebuliser to form an aerosol, which is then injected into an Ar plasma and ionised in an inductively coupled plasma. Different methods are then used to measure the concentration of the ions (Mendham et al., 2000).

In ICP-MS a quadrupole is used to select for ions with a specific mass/charge ratio which then generate a pulse when they reach the detector, allowing quantification of ions with a particular m/z. ICP-AES promotes the ions into an excited state and then measures the

intensity of the light emitted at wavelengths characteristic of the relaxation of the element of interest to its ground state electronic configuration (Mendham et al., 2000).

Samples were prepared for analysis by centrifugation to remove any suspended solids and diluted with 2 % nitric acid (ARISTAR) to an appropriate concentration (< 100 ppb for ICP-MS, < 10 ppm for ICP-AES). Analysis was performed on an Agilent 7500CX using a MicroMist nebuliser (ICP-MS) or a Perkin-Elmer Optima 5300 DV (ICP-AES). Standards were diluted from a 10 ppm VWR certified standard and run every 10 samples.

Plasma gas flow rate	15 mL/min
Auxiliary gas flow rate	0.2 mL/min
Nebuliser gas flow rate	0.75 mL/min
RF power	1300 w
Sample pump speed	1.5 mL/min

Table 3.1: ICP-AES machine parameters.

3.8. pH

Solution pH was measured using a Mettler Toledo SevenEasy meter with a Mettler Toledo InLab®Micro Pro (51343162) pH electrode. This was calibrated using 3 buffers (pH 4, 7, 10, or 12.46, depending on the expected pH of the sample). The electrode was immersed in the solution to be measured and, once stable, a reading was taken. If stability had not yet been reached after 30 seconds, a reading was taken at this point (due to the tendency of the pH to drift upward as a result of carbonate equilibria). pH measurements were recorded to 2 decimal places and quoted to 1 decimal place with an error of ± 0.1 pH units.

3.9. Liquid Scintillation Counting (LSC)

Liquid scintillation counting was used to measure the concentration of ^{232}U and ^{237}Np in solution – both are α emitting radionuclides. Samples were neutralised using HCl (2 %; analytical reagent grade) and mixed with scintillation cocktail. The vials were then shaken

and left in a dark fridge for 24 hours prior to counting on a 1220 QUANTULUS ultra-low level scintillation spectrometer. Both Scintisafe 3 (Fisher Scientific) and Optiphase Hisafe 3 (Perkin Elmer) were used for the ^{232}U work, analysis with ^{232}U standards showed that results obtained using these scintillation cocktails were comparable. All analysis of ^{237}Np was done using Optiphase Hisafe 3 (Perkin Elmer) as a scintillation cocktail.

Scintillation cocktails contain a solvent which absorbs energy released during α or β decay and becomes excited. This energy is then transferred to a scintillator molecule which then relaxes back to its ground state electronic configuration, emitting a photon. The emitted photons can then be counted allowing the activity of the sample to be calculated since each α or β decay results in the emission of one photon (Neame and Homewood, 1974). Blanks, containing Milli-Q (18.2 MΩ) water, HCl, and scintillation cocktail, as well as standards, were run confirming a low background (< 3 counts per hour) and 100 % efficiency.

3.10. X-Ray Diffraction (XRD)

Powder X-ray diffraction (XRD) was used to confirm the identity of mineral phases. A dried sample was ground using a pestle and mortar and suspended in isopropanol (IPA). The suspension was then transferred to a glass slide and the IPA allowed to evaporate prior to analysis using a Bruker D8 Advance X-ray diffractometer. For air sensitive samples, sample preparation was performed inside a N_2 atmosphere glovebox with the sample then transferred to and analysed inside an air-tight sample holder. The sample was rotated through 360° throughout analysis (except air-sensitive samples where the sample holder prevented this) in an attempt to reduce any preferred orientation *bias* and ensure all *d*-spacings were represented. The X-ray angle of incidence was varied to give diffraction angles (2θ) of 5° to 70°, the intensity of the diffracted X-ray beam was then measured at each angle to generate a diffraction pattern. This diffraction pattern is characteristic of the mineral since the peaks are representative of the *d*-spacings between the layers within the mineral, as described by Bragg's law ($2d \sin\theta = n\lambda$) (Putnis, 1992).

Background subtraction of XRD patterns was performed using EVA (Bruker AXS V3) and peaks were matched to reference patterns from the International Centre for Diffraction Data (ICDD) Powder Diffraction Database. Typically, crystalline phases comprising more than 5 % of a sample can be detected using XRD, although amorphous phases can be more difficult to detect.

3.11. Brunauer-Emmett-Teller (BET)

The Brunauer-Emmett-Teller (BET) method was used to determine the specific surface area of mineral samples (Brunauer et al., 1938). A mineral sample was dried under a flow of N_2, using a Micrometrics FlowPrep 060 sample degas system, for more than 19 hours. The adsorption of N_2 to the sample was then determined over a range of negative pressures at liquid nitrogen temperature using a Micromeritics Gemini V BET surface area analyser. Since the volume of N_2 required to form a monolayer can be measured, this allowed the surface area to be calculated per unit mass of solid.

3.12. Electron Microscopy

Since electrons have a much shorter wavelength than visible light, electron microscopy provides a much higher resolution image than is possible using light microscopy. Electron microscopy was used to identify mineral phases and to look for minor contaminant phases. Energy-Dispersive X-ray spectroscopy (EDX) was used to obtain information about the elemental composition of a sample, while selected area electron diffraction (SAED) provided crystallographic information.

3.12.1. Environmental Scanning Electron Microscopy (ESEM)

An ESEM (Philips XL30 ESEM-FEG) was used to confirm the identity and purity of mineral phases using both imaging and EDX (section 3.12.2) techniques. ESEM is advantageous over SEM since it allows the sample chamber to remain hydrated, meaning samples do not have to be dry in order to be analysed. Here, an electron beam passes

through an atmosphere of water vapour before striking the sample (Griffin, 2007). Secondary electrons are then liberated from the sample and are captured by the detector, generating an image when the beam is scanned across the sample. In addition to facilitating the imaging of moist samples and enabling the use of a lower vacuum, the presence of the water vapour also reduces surface charging. However, this functionality was not utilised in this thesis and analysis was performed in high-vacuum mode. Backscattered electrons, originating in the beam and scattered backwards by the sample, can also be used to generate images. Since the heavier elements backscatter more electrons, these appear brighter in images collected in backscattered mode (Davis, 2005).

3.12.2. Energy Dispersive X-ray Spectroscopy (EDX)

Energy dispersive X-ray spectroscopy was performed on both the ESEM and TEM (sections 3.12.1 and 3.12.3, respectively) using an Oxford Instruments INCA EDX (ESEM) or Oxford X-max SD detector (TEM) system to investigate the chemical composition of the sample. This technique uses the electron beam to promote atoms within the sample into an excited state. These then relax back to their ground state electronic configuration, emitting X-rays of energy characteristic of the transition, which allows the originating element to be identified (McLaren, 1991; Brydson, 2011).

3.12.3. Transmission Electron Microscopy (TEM)

Transmission electron microscopy was used to investigate the location and local coordination of radionuclides associated with mineral phases. In this technique an electron beam, in a vacuum, is focussed using a series of electromagnetic lenses before being passed through the sample, and entering the detector. Analysis was performed on a Philips CM200 field emission gun transmission electron microscope (FEG-TEM) with an Oxford Instruments 80 mm X-Max SD detector.

3.12.4. Selected Area Electron Diffraction (SAED)

Since the electron beam passes through the sample in TEM, crystal planes can diffract the electrons, producing SAED patterns. These SAED patterns can give either spot patterns or rings depending on the crystallinity of the sample. Spots can provide information about the position of specific atoms, while rings give information about lattice spacing between planes (similar to XRD, section 3.10). SAED patterns can be used to identify mineral phases by matching the ring spacing to reference standards from the International Centre for Diffraction Data (ICDD) database.

3.13. X-Ray Absorption Spectroscopy (XAS)

XAS is an element specific synchrotron technique used to determine the oxidation state and local coordination environment of targeted elements. Synchrotrons generate a broad spectrum of electromagnetic radiation by accelerating electrons. The electrons are held at a constant relativistic speed and their path bent into a circle using bending magnets. When the path of the electrons is altered by the bending magnets (or by insertion devices) electromagnetic radiation is emitted. In order to use this radiation for XAS, a monochromator is used to select only X-rays of the desired energy, meaning a very pure beam of X-rays of a variable energy can be produced (Calvin, 2013).

This X-ray beam is used to eject a core electron from atoms of the target element within the sample, leaving a core vacancy. As a result an electron from a higher energy orbital 'falls' down to fill the vacancy, and the atom relaxes back to its ground state electronic configuration. This relaxation is associated with an energy release characteristic of the particular transition which occurred; this energy is released as an X-ray. Since different electrons within the absorbing atom have different binding energies dependent on their orbital, the energy of the incident X-ray beam can be altered to target electrons in a particular orbital. The shell from which an excited electron originates is denoted as K, L, or

M representing the 1st, 2nd, and 3rd principle quantum numbers, respectively. In XAS the energy of the incident X-ray beam is increased gradually until it has enough energy to eject the target electron. At this point the measured absorption increases dramatically creating a feature known as the edge, giving rise to the terms K-edge, L-edge, and M-edge (Calvin, 2013).

An XAS spectrum can be spilt into two regions, the XANES and the EXAFS (sections 3.13.1 and 3.13.2, respectively). The XANES region includes the pre-edge, absorption edge, and first ~ 50 eV of the post-edge (the near-edge) and can be used to identify the average oxidation state of the absorbing element. The EXAFS region extends from ~ 50 eV above the edge up to 1000 eV into the post-edge and can provide information about the coordination environment of the absorbing atom (Calvin, 2013).

3.13.1. X-ray Absorption Near Edge Structure (XANES)

Features in the XANES region as well as the position of the edge, can be used to identify the average oxidation state of the element of interest. Pre-edge features can result from the excitation of a core electron to a higher energy orbital rather than into the continuum, while the binding energies, and therefore the position of the edge, can be slightly altered by the valence state of the absorber. For example, the increased charge density of U(VI) compared to U(IV) means its electrons have slightly high binding energies and U(VI) therefore has an edge energy ~ 4 - 8 eV higher than that of U(IV). The comparison of XANES with reference spectra can also be used to provide limited information about the coordination environment, for example, whether U(VI) is located in a uranyl or uranate environment. A uranyl coordination environment produces a characteristic shoulder at ~ 17190 eV due to the short axial U=O bonds, this feature is absent in the XANES of U(VI) in uranate coordination environments (Farges et al., 1992).

3.13.2. Extended X-ray Absorption Fine Structure (EXAFS)

The EXAFS region can extend up to 1000 eV into the post-edge, although this is dependent on the sample and data quality is typically poor further from the absorption edge. The oscillations observed in this region are due to the X-rays emitted during the relaxation of the absorbing atom propagating out through the material. These X-rays can be elastically scattered by neighbouring atoms, some will also be backscattered and will return to the absorber undergoing constructive or destructive interference as they do so. This means that the atoms surrounding the absorber determine the EXAFS spectrum which can therefore be used to deduce structural information. The frequency of an oscillation is inversely proportional to the distance of the scatterer from the absorber, the amplitude is a result of the degeneracy of the scatterer, and the shape is related to the chemical identity of the scatterer. However, since EXAFS is the sum of all of the fluoresced and back-scattered X-rays within a sample area, it provides information on the average coordination environment (Calvin, 2013).

3.13.3. XAS Sample preparation, data collection, and analysis

The XAS contained in this thesis was performed at Diamond Light Source (UK) on beamlines B18 and I20, at The SOLEIL synchrotron (France) on the MARS beamline, and at ANKA Light Source (Germany) on the INE-beamline. Spectra were collected using either a 9 or a 36 element Ge detector on B18, a 36 element Ge detector on I20, a 12 element Ge detector on MARS, and a 5 element detector on INE. Both U and Np spectra were collected on their respective L_{III} edges and, where possible, Y or Zr in-line standards (K-edge) were used as a reference.

Mineral phases containing ~ 1000 – 2500 ppm U, or 1000 – 300 ppm ^{237}Np, were analysed using XAS. For U analysis performed on B18 at Diamond Light Source the solid U containing samples were sandwiched between wax pellets and loaded into cryo-vials, while

samples analysed on the MARS beamline at The SOLIEIL synchrotron were loaded into specially designed aluminium and tooled steel sample holders with Kapton windows. Solution samples were also loaded into cryo-vials. Neptunium containing samples were measured on I20 at Diamond Light Source and on the INE-beamline at ANKA Light Source and were loaded into specially prepared Perspex holders, sealed with 2 layers of Kapton tape, and heat sealed into a plastic bag. All data were collected in fluorescence mode and, where possible, at liquid nitrogen temperatures.

The Demeter software package was used to background subtract and normalise the data, and to fit the EXAFS (Ravel and Newville, 2005). The significance of adding additional shells to EXAFS models was assessed using the F-test (Downward et al., 2007).

3.14. Small Angle X-ray Scattering (SAXS)

Small angle X-ray scattering (SAXS; Porod, 1951; Guinier, 1963; Hiemenz and Rajagopalan, 1997) can provide information about the size, morphology, and concentration of particles. Like XAS (section 3.13), SAXS experiments are often performed at synchrotron facilities to utilise high intensity X-rays and improve sensitivity. An X-ray beam is passed through a sample and the extent of elastic scattering determined by detectors placed a given distance and angle from the sample. The scattering pattern can then be used to determine the size, size distribution, and surface properties of the particles within the sample, as well as the density of said particles.

3.15. References

Berner, U. R. (1992). Cementitious Materials in Radioactive Waste Management Evolution of pore water chemistry during degradation of cement in a radioactive waste repository environment. *Waste Management,* 12(2)**,** 201-219.

Bots, P., Morris, K., Hibberd, R., Law, G. T. W., Mosselmans, J. F. W., Brown, A. P., Doutch, J., Smith, A. J. and Shaw, S. (2014). Formation of Stable Uranium(VI) Colloidal Nanoparticles in Conditions Relevant to Radioactive Waste Disposal. *Langmuir,* 30(48)**,** 14396-14405.

Brunauer, S., Emmett, P. H. and Teller, E. (1938). Adsorption of Gases in Multimolecular Layers. *Journal of the American Chemical Society,* 60(2)**,** 309-319.

Brydson, R. (2011). *Abberation-Corrected Analytical transmission Electron Miscroscopy*. Chichester, UK: Wiley.

Calvin, S. (2013). *XAFS for Everyone*. Boca Raton: CRC Press, Taylor & Francis Group.

Davis, S. (2005). Electron Microscopy. *In:* Cosgrove, T. (ed.) *Colloid Science: Principles, Methods and Applications.* Oxford: Blackwell Publishing.

Downward, L., Booth, C. H., Lukens, W. W. and Bridges, F. (2007). A variation of the F-Test for determining statistical relevance of particular parameters in EXAFS fits. *In:* Hedman, B. & Painetta, P. (eds.) *X-Ray Absorption Fine Structure-XAFS13.* Melville: American Institute of Physics.

Farges, F., Ponader, C. W., Calas, G. and Brown, G. E. (1992). Structural Environment of Incompatible Elements in Silicate Glass Melt Systems 2. UIV, UV, and UVI. *Geochimica et Cosmochimica Acta,* 56(12)**,** 4205-4220.

Griffin, B. J. (2007). *Variable Pressure and Environmental Scanning Electron Microscopy* (Second Edition ed.). Totowa, New Jersey: Humana Press.

Guinier, A. (1963). *X-ray Diffraction in Crystals, Imperfect Crystals, and Amorphous Bodies*. San Francisco: W. H. Freeman and Company.

Hiemenz, P. C. and Rajagopalan, R. (1997). *Principle of colloid and surface chemistry* (Third ed.): CRC Press.

Kirillov, S. A., Aleksandrova, V. S., Lisnycha, T. V., Dzanashvili, D. I., Khainakov, S. A., García, J. R., Visloguzova, N. M. and Pendelyuk, O. I. (2009). Oxidation of synthetic hausmannite (Mn3O4) to manganite (MnOOH). *Journal of Molecular Structure,* 928(1-3)**,** 89-94.

McArdell, C. S., Stone, A. T. and Tian, J. (1998). Reaction of EDTA and related aminocarboxylate chelating agents with Co(III)OOH (heterogenite) and Mn(III)OOH (manganite). *Environmental Science & Technology,* 32(19)**,** 2923-2930.

McLaren, A. C. (1991). *Transmission electron microscopy of minerals and rocks*. Cambridge: Cambridge University Press.

Mendham, J., Denney, R. C., Barnes, J. D. and Thomas, M. (2000). *Vogel's Textbook of Quantitative Chemical Analysis* (Sixth Edition ed.). Harlow, UK: Prentice Hall.

Morgenstern, A., Apostolidis, C., Carlos-Marquez, R., Mayer, K. and Molinet, R. (2002). Single-column extraction chromatographic separation of U, Pu, Np and Am. *Radiochimica Acta,* 90(2)**,** 81-35.

Neame, K. D. and Homewood, C. A. (1974). *Introduction to liquid scintillation counting*. London: Butterworth & Co.

Parkhurst, D. L. and Appelo, C. A. J. (2013). *Description of input and examples for PHREEQC version 3—A computer program for speciation, batch-reaction, one-dimensional transport, and inverse geochemical calculations* [Online]. available only at http://pubs.usgs.gov/tm/06/a43/. [Accessed 06/11/2015].

Porod, G. (1951). Die Röntgenkleinwinkelstreuung von dichtgepackten kolloiden Systemen. *Kolloid-Zeitschrift,* 124(2)**,** 83-114.

Putnis, A. (1992). *Introduction to Mineral Sciences*. Cambidge: Cambridge University Press.

Ravel, B. and Newville, M. (2005). ATHENA, ARTEMIS, HEPHAESTUS: data analysis for X-ray absorption spectroscopy using IFEFFIT. *Journal of Synchrotron Radiation,* 12(Pt 4)**,** 537-541.

Smith, K. F., Bryan, N. D., Swinburne, A. N., Bots, P., Shaw, S., Natrajan, L. S., Mosselmans, J. F. W., Livens, F. R. and Morris, K. (2015). U(VI) behaviour in hyperalkaline calcite systems. *Geochimica et Cosmochimica Acta,* 148**,** 343-359.

Smith, M. R., Lautensleger, A. W. and Laul, J. C. (1988). A new method for the determination of radium-228, thorium-228, and radium-224 in groundwaters via thoron (radon-220). *Journal of Radioanalytical and Nuclear Chemistry,* 123(1)**,** 107-119.

Telchadder, R., Smith, K. and Bryan, N. D. (2012). Europium interaction with a vault backfill at high pH. *Mineralogical Magazine,* 76(8)**,** 3083-3093.

Villalobos, M., Toner, B., Bargar, J. and Sposito, G. (2003). Characterization of the manganese oxide produced by Pseudomonas putida strain MnB1. *Geochimica et Cosmochimica Acta,* 67(14)**,** 2649-2662.

Chapter 4. Formation of Stable Uranium(VI) Colloidal Nanoparticles in Conditions Relevant to Radioactive Waste Disposal

This chapter is a manuscript published in the journal Langmuir in October 2014. Supporting Information published with this manuscript is included following the manuscript.

The full citation of the published manuscript is as follows:

Bots, P., Morris, K., Hibberd, R., Law, G.T.W., Mosselmans, J.F.W., Brown, A.P., Doutch, J., Smith, A.J., Shaw, S., (2014). Formation of Stable Uranium(VI) Colloidal Nanoparticles in Conditions Relevant to Radioactive Waste Disposal. *Langmuir* 30, 14396 – 14405. doi:10.1021/la502832j

Langmuir

Article

pubs.acs.org/Langmuir

Formation of Stable Uranium(VI) Colloidal Nanoparticles in Conditions Relevant to Radioactive Waste Disposal

Pieter Bots,[†] Katherine Morris,[†] Rosemary Hibberd,[†,‡] Gareth T. W. Law,[‡] J. Frederick W. Mosselmans,[§] Andy P. Brown,[∥] James Doutch,[§] Andrew J. Smith,[§] and Samuel Shaw*[,†]

[†]Research Centre for Radwaste & Disposal, and Williamson Research Centre, School of Earth, Atmospheric and Environmental Sciences, Faculty of Engineering and Physical Sciences, The University of Manchester, Manchester M13 9PL, U.K.

[‡]Centre for Radiochemistry Research, School of Chemistry, Faculty of Engineering and Physical Sciences, The University of Manchester, Manchester M13 9PL, U.K.

[§]Diamond Light Source Ltd., Diamond House, Harwell Science and Innovation Campus, Didcot, Oxfordshire OX11 0DE, U.K.

[∥]School of Process, Environmental and Materials Engineering, Faculty of Engineering, University of Leeds, Leeds LS2 9JT, U.K.

Supporting Information

ABSTRACT: The favored pathway for disposal of higher activity radioactive wastes is via deep geological disposal. Many geological disposal facility designs include cement in their engineering design. Over the long term, interaction of groundwater with the cement and waste will form a plume of a hyperalkaline leachate (pH 10−13), and the behavior of radionuclides needs to be constrained under these extreme conditions to minimize the environmental hazard from the wastes. For uranium, a key component of many radioactive wastes, thermodynamic modeling predicts that, at high pH, U(VI) solubility will be very low (nM or lower) and controlled by equilibrium with solid phase alkali and alkaline-earth uranates. However, the formation of U(VI) colloids could potentially enhance the mobility of U(VI) under these conditions, and characterizing the potential for formation and medium-term stability of U(VI) colloids is important in underpinning our understanding of U behavior in waste disposal. Reflecting this, we applied conventional geochemical and microscopy techniques combined with synchrotron based *in situ* and *ex situ* X-ray techniques (small-angle X-ray scattering and X-ray adsorption spectroscopy (XAS)) to characterize colloidal U(VI) nanoparticles in a synthetic cement leachate (pH > 13) containing 4.2−252 μM U(VI). The results show that in cement leachates with 42 μM U(VI), colloids formed within hours and remained stable for several years. The colloids consisted of 1.5−1.8 nm nanoparticles with a proportion forming 20−60 nm aggregates. Using XAS and electron microscopy, we were able to determine that the colloidal nanoparticles had a clarkeite (sodium−uranate)-type crystallographic structure. The presented results have clear and hitherto unrecognized implications for the mobility of U(VI) in cementitious environments, in particular those associated with the geological disposal of nuclear waste.

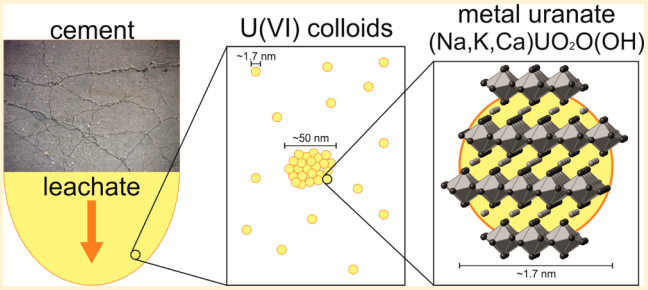

INTRODUCTION

Many countries including the U.K., USA, and former Soviet Union have significant legacies of radioactive waste materials due to their long history of nuclear power generation and military activities. Typically, the long-term strategy for nuclear waste management of higher activity materials is containment in a geological disposal facility (GDF) within the deep subsurface.[1] Currently, in many nations, GDF designs are at a generic stage and will be developed as site selection proceeds. Essentially, the design of a GDF is focused on limiting the mobility and migration of radionuclides.[2] Typically, the mobility of radionuclides, and particularly uranium, in the subsurface is governed by solubility and adsorption to geological materials.[3] In addition, colloidal transport has the potential to significantly enhance radionuclide migration in geodisposal relevant conditions.[3,4] However, it is not known whether stable U(VI) colloids form under geochemical conditions relevant to radioactive waste disposal in GDFs.

Most scenarios for intermediate level waste (ILW) disposal in a GDF utilize cementitious materials. For example, ILW is typically grouted with Portland cement and emplaced in steel drums, and engineering of any subsurface disposal facility will require use of structural cement.[5,6] In addition, some GDF designs are likely to utilize cementitious backfill.[2,5,7,8] Post closure, groundwater will resaturate the GDF and interact with the cementitious material forming hyperalkaline leachate (pH 10−13) with elevated concentrations of K, Na, and Ca.[9] Specifically, during the initial stages of the evolution of a GDF,

Received: July 18, 2014
Revised: October 4, 2014
Published: October 23, 2014

the pH of the hyperalkaline leachate may reach values in excess of 13 due to dissolution of sodium and potassium hydroxide phases present in the cementitious materials used.[9] During operation, the GDF will be open to the atmosphere and hence will be aerobic. Chemically reducing conditions are expected to dominate post closure as iron corrosion will consume any oxidants. Typically, within ILW, uranium will be the most significant radionuclide by mass.[5] Furthermore, the ILW will contain uranium in both oxidation states, i.e., U(VI) and U(IV). However, it is noteworthy that under alkaline and slightly reducing conditions U(VI) is expected to be relatively stable and may exist within a GDF for a significant period post closure.[10]

The benefit of using cementitious materials in the design of a GDF is that U(VI) is expected to exhibit low solubility in the resulting hyperalkaline environment.[11] At the pH values of cement leachates (pH 10−13), aqueous U(VI) concentration in equilibrium with, i.e., alkali/alkaline-earth uranates (e.g., $Na(UO_2)O(OH)\cdot(H_2O)_{0-1}$ and $CaUO_4$) will be very low ($\sim 10^{-9}$ M).[11,12] Furthermore, U(VI) adsorbs strongly to the surfaces of many solid phases (e.g., iron oxides,[13−15] silicates,[14,16] and cement related phases[17,18]) which will be ubiquitous in the GDF. These factors are predicted to significantly reduce the concentration of aqueous U(VI) in a cementitious GDF. Furthermore, even though the aqueous concentration of carbonate is expected to be low in the deep subsurface, it is noteworthy that the presence of carbonate could significantly enhance U(VI) mobility through the formation of soluble uranium(VI)−carbonate and calcium−uranium(VI)−carbonate complexes.[12−14,19]

Significantly, U(VI) mobility could also be enhanced by colloids formed within or transported through the GDF.[3,20] Depending on the physical and chemical state of these colloidal nanoparticles (e.g., surface charge) and the prevailing geochemical conditions, colloids could facilitate the transport of U(VI) into the geosphere.[3,4] Previous studies have identified cement and sediment derived colloidal particles[3,20] with complexed radionuclides[3] and intrinsic radionuclide colloids (e.g., ThO_2[4] and $Pu(OH)_4$[21]) as potentially important transport vectors.[3,4] Recently, complexation of uranium and plutonium to iron oxides has been implicated in their migration in groundwater.[22] Furthermore, uranates, among other U(VI) colloids, have been identified as a potential transport vector,[23] and plutonium(IV) colloidal transport has been inferred at the Nevada Test Site, Nye County, NV, USA.[24,25]

Despite the widely recognized relevance of colloidal transport in radioactive waste disposal and the potential significance of U(VI) in waste disposal, few studies have focused on the formation of colloidal U(VI) nanoparticles. As a result, the aim of this study was to explore the potential for colloidal U(VI) nanoparticle formation in a hyperalkaline synthetic cement leachate (pH > 13) representative of the early stages of the evolution of a GDF. Additionally, where colloidal nanoparticles were found to be present, their characteristics and stability were then determined by conventional chemical and microscopy techniques combined with synchrotron based *in situ* small-angle X-ray scattering (SAXS) and X-ray adsorption spectroscopy (XAS).

METHODS

To investigate the speciation of U(VI) in conditions relevant to cementitious GDFs, a synthetic cement leachate (pH ∼ 13.1) was prepared by dissolving KOH (0.19 mol), NaOH (0.19 mol), and $Ca(OH)_2$ (0.27 mmol) (all AnalaR grade) in 2 L of degassed, deionized water.[9,17,18] Prior to use, this was filtered through a 0.22 μm polyvinylidene fluoride (PVDF) syringe filter in a CO_2 controlled (<1 ppm of CO_2) anaerobic chamber where all subsequent manipulations were performed. A 2.52 mM $U(VI)O_2(NO_3)_2$ stock solution (pH ∼ 2.3) was used to spike the cement leachate to 4.2, 42, and 252 μM U(VI), after which the pH of 13.1 was confirmed. A time point series of samples were then taken up to 32 months. At each time point, separate samples were filtered using 0.22 μm (PVDF), 0.10 μm (PVDF), and 0.02 μm (Anotop) syringe filters, and one sample was unfiltered and undisturbed. The resulting samples were acidified to 2% HNO_3 and analyzed for total U using ICP-MS (Agilent 7500cx).

PHREEQC[26] calculations were performed to determine the equilibrium concentrations of U(VI) in the synthetic cement leachate when a single U(VI) phase precipitated. These phases included the minerals clarkeite ($Na(UO_2)O(OH)\cdot(H_2O)_{0-1}$), becquerelite ($Ca(UO_2)_6O_4(OH)_6\cdot(H_2O)_8$), compreignacite ($K_2(UO_2)_6O_4(OH)_6\cdot(H_2O)_7$), and several Ca/Na uranate phases. The PHREEQC calculations were performed using the SIT (specific ionic theory) database, which includes thermodynamic information on clarkeite, becquerelite, and compreignacite from Gorman-Lewis et al.[12] and sodium and calcium uranates from O'Hare et al.[27] The thermodynamic equilibrium constants of uranyl hydroxide complexes as determined by Zanonato et al.[28] were also included.

Small Angle X-ray Scattering. SAXS was used to characterize suspended/colloidal particles in the 42 μM U(VI) experiments, as described earlier, using beamline I22 at Diamond Light Source. All analyses were performed using a monochromatic X-ray beam at 12 keV and a 4 or 10 m camera length. Scattering patterns were collected using a 2D PILATUS 2 M detector.[29] Two sets of experiments were performed. First, samples aged for 1 week, 20 months, and 32 months were characterized. Here, the samples were injected into a quartz capillary in line with the X-ray beam and SAXS patterns were collected. Second, *in situ* time-resolved SAXS analyses were performed to study the formation of colloidal U(VI) nanoparticles. These experiments were performed at the I22 experimental hutch by spiking the synthetic cement leachate to a final concentration of 42 μM U(VI). The solution was then stirred for ∼15 s, injected into a quartz capillary in-line with the X-ray beam, and sealed. SAXS measurements were started concurrently to the U(VI) spike. Typically, the first full scattering frame was acquired at ∼2 min after the injection of the U(VI) spike. Scattering patterns were collected for up to 7 h at a 1−10 s/frame collection rate.

SAXS Data Analyses. The scattering patterns from the aged samples, collected using the 4 and 10 m camera lengths, were combined to form a single scattering pattern with a large scattering vector ($\mathbf{q}$) range. All SAXS patterns were modeled using the Irena macro for Igor Pro.[30] Additionally, the SAXS patterns from the *in situ* time-resolved experiments were analyzed to determine the invariant (Q) and $I(0)$,[31] described in detail in the Supporting Information (SI). In short, Q and $I(0)$ are a function of the scattering volume and the density of the scatterers and $I(0)/Q$ is a function of the particle volume (eq 1, V_p is the particle volume in Å^3).[31−33] Additionally, separate Q and $I(0)$, and thus $I(0)/Q$, can be estimated for particle populations with different particle volumes in a dilute suspension[34] to track the evolution of different particle populations.

$$\frac{I(0)}{Q} \approx V_p \tag{1}$$

Solid Characterization. At selected time points, suspended particles were captured on either carbon coated (Agar Scientific) or positively charged C-SMART PLUS (Dune Sciences) transmission electron microscope (TEM) grids and the supernatant was removed using isopropanol to minimize the effect of drying on the solids formed during the experiments. TEM images were taken using a Philips CM200 field emission electron gun transmission electron microscope (FEG-TEM). Chemical composition of the solids was analyzed using energy dispersive X-ray spectroscopy (EDX) with an Oxford Instruments 80 mm X-Max SD detector running the AZTEC

dx.doi.org/10.1021/la502832j | Langmuir 2014, 30, 14396−14405

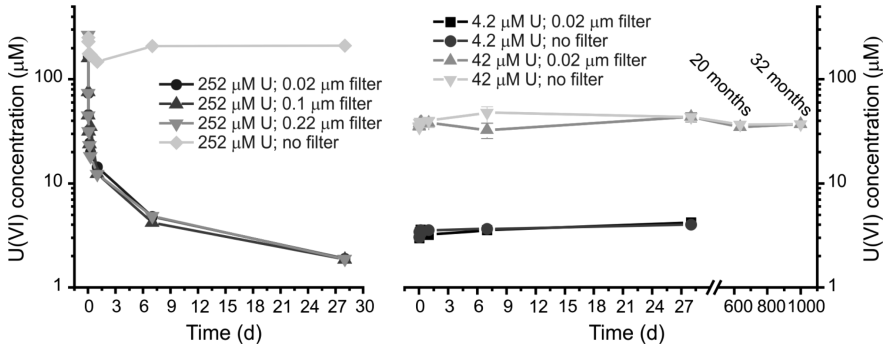

Figure 1. Solution data from the 252 μM U(VI) experiment (a) and the 42 and 4.2 μM U(VI) experiments (b). The error bars on the data from the 42 μM U(VI) experiment are the standard deviation of triplicate experiments; the results from filtering the solutions through 0.1 and 0.22 μm filters from the 42 and 4.2 μM U(VI) experiments showed no differences compared to the plotted results and are given in Figure 2 in the SI.

Table 1. PHREEQC[26] Calculations on the Concentration of U(VI) in Equilibrium with Selected Phases in the Cement Leachate[a]

		U(VI) concn (μM) in equilibrium with solid phase				
exp (μM U(VI))	measd U(VI) concn (μM)	Comp[b]	$CaUO_4$	CaU_2O_7[c]	Becq[d]	clarkeite[e]
252	1.88 ± 0.02[f]	180	131	35.8	50.4	0.00935
42	44.7 ± 2.9	42.0	9.15×10^{-6}	13.4	42.0	0.00926
4.2	4.27 ± 0.05	4.20	6.21×10^{-6}	4.20	4.20	0.00925

[a]Note that when the concentrations calculated are identical to the input concentrations, these phases are below saturation in the corresponding experiment. [b]Compreignacite: $K_2(UO_2)_6O_4(OH)_6\cdot(H_2O)_7$ [c]Calcium uranate trihydrate: $CaU_2O_7\cdot(H_2O)_3$ [d]Becquerelite: $Ca(UO_2)_6O_4(OH)_6\cdot(H_2O)_8$ [e]Clarkeite: $Na(UO_2)O(OH)\cdot(H_2O)_{0\text{-}1}$ [f]The printed values are the averages of all filtered samples and their standard deviation

software. TEM images were analyzed using image processing software ImageJ.[35]

X-ray absorption spectroscopy (XAS) analyses were performed at beamline B18 at Diamond Light Source, at the U L_{III}-edge using a Si(111) monochromator at liquid nitrogen temperature. Two samples were analyzed; first, a solid sample from the 252 μM U(VI) experiment was prepared by centrifuging at 2600*g*. The residue was then analyzed in transmission mode. Second, a 1 mL solution aliquot of the 42 μM U(VI) experiment aged for 1 month was analyzed in fluorescence mode. XAS data analyses were performed using Athena and Artemis from the Demeter software package using FEFF6.[36]

RESULTS AND DISCUSSION

During the 252 μM U(VI) experiments a yellow precipitate formed and solution analyses showed that the U(VI) concentration in all of the filtered samples decreased to 1.4 μM (Figure 1a) over 28 days. Conversely, the unfiltered (and undisturbed) solution samples only showed a minor decrease in the U(VI) concentration to ~200 μM U(VI) (Figure 1a) suggesting the presence of a colloidal U(VI) component with particle size > 0.22 μm in the 252 μM U(VI) experiment. Interestingly, the 42 and 4.2 μM U(VI) experiments did not show any visible precipitation or removal of U(VI) from solution during filtration up to 32 months (Figure 1b). This is in contrast to the thermodynamic modeling using PHREEQC,[26] which showed the solutions were (highly) supersaturated with respect to several calcium and sodium uranate phases (Table 1). It is worth noting that the introduction of carbonate (including $Ca-UO_2-CO_3$ complexes[19]) due to the dissolution of calcite had no significant effect on the equilibrium concentrations in Table 1. These results indicated that, in the 42 and 4.2 μM systems, U(VI) was either dissolved in a supersaturated metastable state or that stable colloidal U(VI) nanoparticles (≤0.02 μm) were present.

Small Angle X-ray Scattering. SAXS patterns of the aged solutions from the 42 μM U(VI) experiments are presented in Figure 2a. The observed scattering intensity suggests that colloidal U(VI) was present in the 42 μM U(VI) experiments. The best fit to the SAXS patterns using the Irena fitting package consisted of a two particle population model: Smaller/primary particles (high q values) were modeled using a form factor for spherical particles, and larger particles (low q values), presumptively aggregates of the primary particles, were modeled using the form factor for algebraic globules.[37,38] In all cases the scattering patterns were modeled as dilute systems reflecting the (relatively) low concentration of U(VI). Fits to the respective scattering patterns are shown in Figure 2a, and the fit parameters are given in Table 2. Briefly, by 2.3 h, the primary particles reached a mean diameter of 1.54 ± 0.05 nm and 57 ± 12% of the scattering solids formed aggregates with a mean diameter of 22.4 ± 2.8 nm (Table 2). Beyond 2.3 h, there was little significant change in the particle populations over 32 months, with a primary particle diameter of 1.60−1.82 nm and between 33−57% of the scattering solids within aggregates of 42.2−60.0 nm. The only significant change in the particles over the observation period was an increase in the mean aggregate diameter from 22.4 to 56.0 nm between 2.3 h and 1 week. The results from the SAXS patterns were supported by TEM images of 1 h and 1 month samples from parallel experiments, with evidence for 1−2 nm primary particles which formed aggregates to 20−60 nm in size (Figure 2b). The aggregate morphology observed by TEM was consistent with the algebraic globules form factor used in the SAXS modeling approach. It should however be noted that air drying nanoparticle suspensions for TEM analysis could alter aggregate morphology;[39] however, due to the consistency between the SAXS and TEM analyses we are confident that the TEM images are a representation of the *in situ* colloidal nanoparticles. Overall, the SAXS analyses indicate that the U(VI) in this system was present as colloidal U(VI) nanoparticles and underwent very little change from 2.3 h up

dx.doi.org/10.1021/la502832j | *Langmuir* 2014, 30, 14396−14405

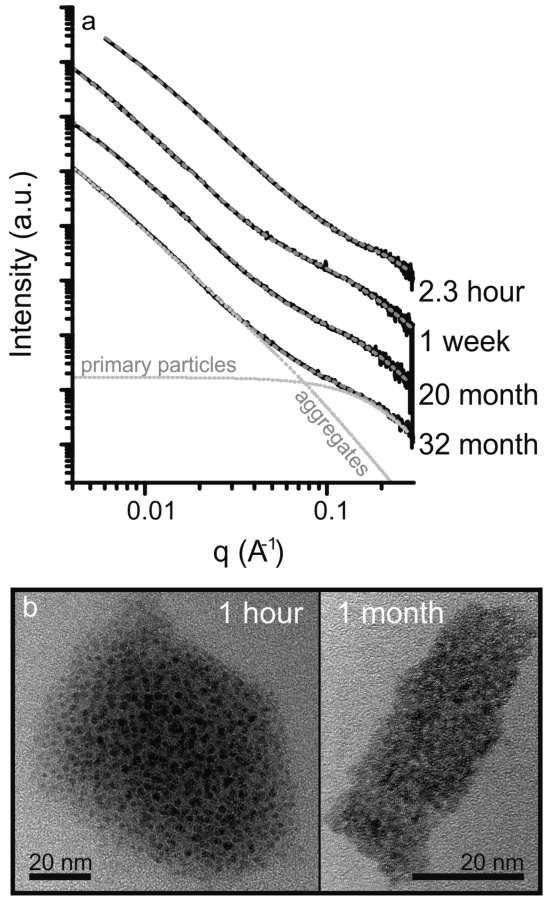

Figure 2. (a) Small angle X-ray scattering patterns from the 42 μM U(VI) experiments (continuous black lines) including the fits (dashed gray lines). The fit to the pattern collected from the 32 month sample has also been divided between the scattering from the primary particles and the aggregates (dotted gray lines). (b) TEM images of the colloidal U(VI) nanoparticle 1 h and 1 month after spiking the cement leachate with U(VI).

to 32 months. Interestingly, the 0.02 μm filtration samples from the 42 μM U(VI) experiment showed no removal from solution (Figure 1) even though TEM and SAXS analysis suggest the presence of aggregates > 20 nm (Figure 2 and Table 2). This suggests artifacts from filtration and/or facile disaggregation of colloidal nanoparticles upon forced filtration through 20 nm pores.

Time-resolved $I(0)$ data from the *in situ* 42 μM U(VI) experiments (4 and 10 m camera length) are shown in Figure 3a. The above background $I(0)$ in the first scattering pattern collected (at ~2 min; Figure 3a) suggested particle formation prior to ~2 min. Between 2 min and 2.3 h, $I(0)$ increased 10-fold (Figure 3a, dashed vertical line). After this initial increase, $I(0)$ decreased slightly (Figure 3a) possibly due to aggregate growth (Table 2).

Fitting (Irena) the SAXS patterns from the 42 μM U(VI) experiments yielded time-resolved size information for the aggregates, but due to the low intensity of the scattering patterns at high q values, fitting of the primary particle model was not achieved. However, it was possible to determine $I(0)$ and Q for each particle population. Figure 3b shows the $I(0)/Q$ (which relates to particle volume; eq 1[31−33]) for the aggregates and primary particles, and aggregate volume, calculated from the size determined using Irena. The aggregate volume (Irena) and $I(0)/Q$ values as a function of time are consistent (Figure 3b), giving confidence that $I(0)/Q$ reflects particle volume trends in the 42 μM U(VI) experiment. The aggregate diameter increased up to ~22.4 nm (Figure 3b and Table 2) during the first 1.5 h of the experiment (Figure 3b, vertical line) and then remained constant. This initial growth of the aggregates was presumably due to primary particle aggregation and/or nucleation of particles on the aggregate surface. Between ~1.5 and ~2.3 h the aggregate size did not increase, while $I(0)$ increased about 3-fold (Figure 3). This indicates that continuous formation of colloidal nanoparticles/aggregates occurred after the aggregate size reached a maximum. The $I(0)/Q$ for the primary particles remained constant (Figure 3b), indicating that the primary particles formed at ~1.5 nm (Table 2) in diameter and did not change in size. Thus, the formation mechanism of the primary particles was likely nucleation dominated, with no significant particle growth occurring (e.g., ripening).[40,41]

The persistence of a significant fraction of unaggregated primary particles (Table 2) could have been caused by the high pH. The pH at the point of zero charge for several uranyl oxyhydroxides is 4−4.5.[42] It is thus clear that U(VI) (oxyhydr)oxide nanoparticles would have a highly negative surface charge at pH 13.1. Thus, electrostatic repulsion would minimize (further) particle aggregation consistent with our observations and potentially reduce the interaction of U(VI) with materials present in a cementitious GDF system.

Solid Characterization. HR-TEM images of the colloidal nanoparticles (1 day and 1 month) from the 42 μM U(VI) experiment are shown in Figure 4b,d. The 1−2 nm particles collected after 1 h (Figure 2b) lacked any resolvable lattice fringes, suggesting an amorphous character. By contrast, the nanoparticles from 1 day to 1 month had visible lattice fringes (emphasized by circles, Figure 4b,d) which were spaced at 3.0−3.3 Å. Reflecting on this, the primary particles in the 42 μM U(VI) experiments initially formed as amorphous nanoparticles, potentially due to the aggregation of stable prenucleation clusters akin to the observed dynamically ordered liquid-like oxy-anion polymers (DOLLOP) observed during the

Table 2. Results of the Fits from the SAXS Patterns from the 42 μM U(VI) Experiments

	primary particles		aggregates		fraction of aggregated particles
sample name	mean diam (nm)[a]	polydispersity[a,b]	mean diam (nm)[a]	polydispersity[a,b]	$[V_{aggr}/(V_{aggr} + V_{prim})] \times 100$ (%)[a,c]
2.3 h	1.54 ± 0.05	0.20 ± 0.20	22.4 ± 2.8	1.62 ± 0.25	57 ± 12
1 week	1.60 ± 0.26	0.63 ± 0.11	56.0 ± 18.2	1.06 ± 0.23	33 ± 15
20 month	1.82 ± 0.22	0.48 ± 0.15	42.2 ± 11.6	1.48 ± 0.86	44 ± 16
32 month	1.75 ± 0.16	0.47 ± 0.11	60.0 ± 30.0	2.44 ± 0.17	57 ± 14

[a]The errors were evaluated by calculating the range less 1.05 times the minimum χ^2. [b]The polydispersity is defined as the standard deviation of the log-normal distribution of the particles. [c]V_{prim} and V_{aggr} represent the calculated volumes for the primary particles and aggregates respectively.

dx.doi.org/10.1021/la502832j | *Langmuir* 2014, 30, 14396−14405

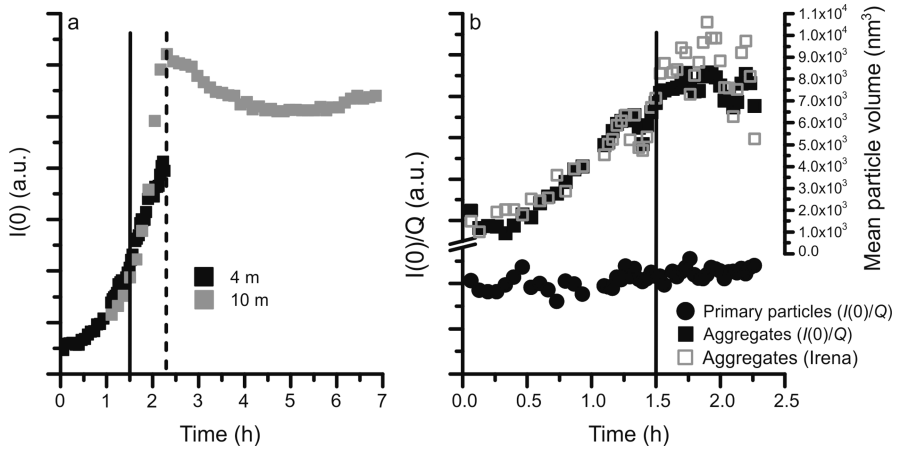

Figure 3. a) $I(0)$ for the 42 μM U(VI) experiments collected using a 4 and 10 m camera length; the data from both experiments were aligned for clarity; b) $I(0)/Q$ (particle volume; eq 1 and SI) for the aggregates and the primary particles calculated from the experiment performed using the 4m camera length including the aggregate volume calculated from the fitting results using the Irena macro.

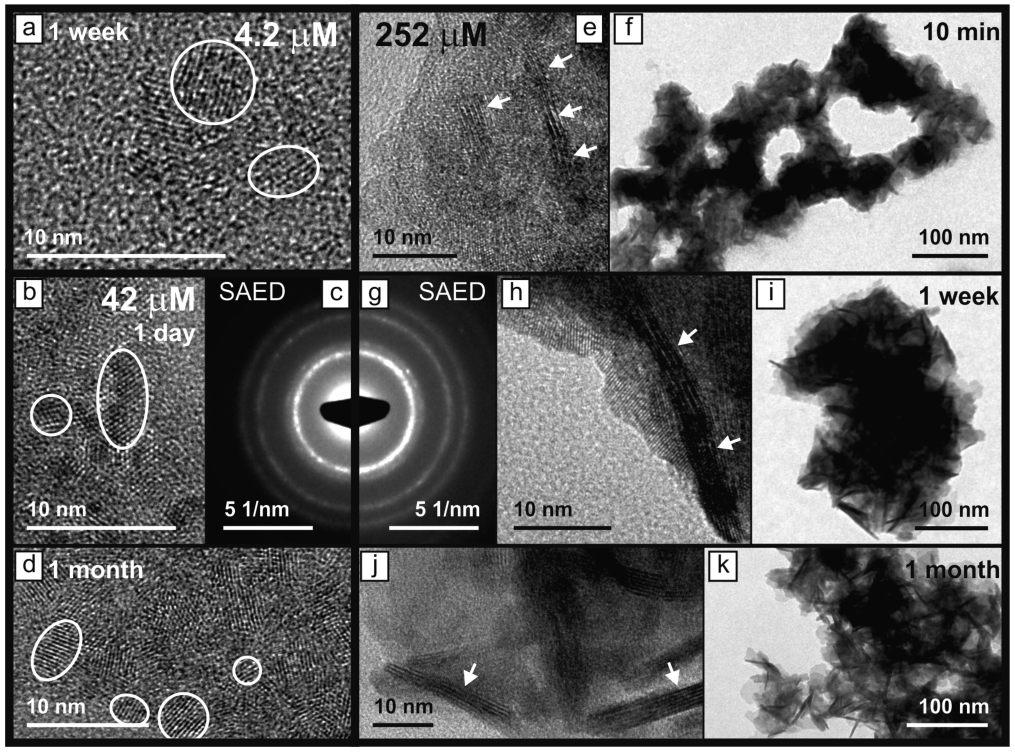

Figure 4. High-resolution TEM images from the 4.2 μM U(VI) experiment after 1 week (a) and the 42 μM U(VI) experiments after 1 day (b) and 1 month (d), including a SAED image from the particles after 1 day (c); selected primary particles with lattice spacings of 3.0−3.3 Å in the images are highlighted by white circles (a, b, and d); also shown are TEM images of the uranium particles formed during the 252 μM U(VI) experiments after 10 min (e and f), 1 week (h and i), and 1 month (j and k), including a SAED image from the particles after 1 week (g); the arrows in the images (e, h, and j) point toward the platelets where lattice spacings of 5.9−6.2 Å are visible.

formation of amorphous calcium carbonate.[43,44] Furthermore, the amorphous uranium nanoparticles became nanocrystalline during the course of a day. The crystallinity of the nanoparticles is also emphasized by visible polycrystalline rings in the selected area electron diffraction patterns (SAED, Figure 4c) collected from the 1 day sample. Additionally, the EDX analyses of the nanoparticles formed during the 42 μM U(VI) experiments show that the particles consisted of U, Na, K, and Ca (Figure 5).

HR-TEM image from a 1 week sample collected from the 4.2 μM U(VI) experiment shows crystalline nanoparticles of 2−5 nm within a ~10 nm aggregate (Figure 4a). This confirms that U(VI) colloids also formed in the 4.2 μM U(VI) experiment and were of a similar size and aggregation state to those formed in the 42 μM U(VI) experiment. Furthermore, TEM characterization shows that the crystallinity (lattice fringes spaced at 3.0−3.3 Å, emphasized by circles in Figure 4a) and composition (U, Na, K, and Ca, Figure 5) of the nanoparticles were also similar to those from the 42 μM U(VI) experiment.

High-resolution TEM (HR-TEM) images of the particles throughout the 252 μM experiments show small crystalline platelets with lattice fringes spaced at 5.9−6.2 Å (arrows, Figure

dx.doi.org/10.1021/la502832j | Langmuir 2014, 30, 14396−14405

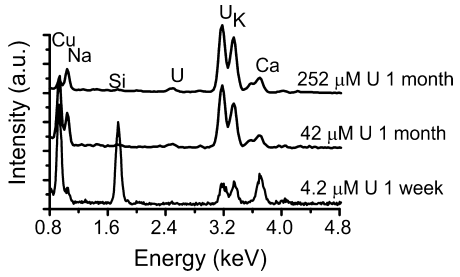

Figure 5. EDX spectra from the uranium particles, imaged using TEM (Figure 4a,d,j). The EDX peaks are indexed with the corresponding chemical symbol (for uranium the *L* and *M* lines were observed; only the latter are shown), the copper in the EDX spectra is caused by the TEM grids, and the silicon is likely caused by contamination from the TEM grid box.

4e,h,j) and 3.0−3.3 Å. These particles formed part of larger aggregated structures (Figure 4f,I,k). At 10 min, these platelets were 2−10 nm in size and the 5.9−6.2 Å lattice fringes were aligned in some adjacent particles, indicating that the particle size may be increasing via oriented attachment.[45] After 1 month, the crystalline domains with 5.9−6.2 Å lattice fringes grew to about 25 nm in diameter with a width of ∼4 nm (arrows, Figure 4j). These observations confirm that initially nanocrystalline particles formed from solution and grew through oriented attachment.[45]

The SAED patterns from the 42 and 252 μM U(VI) experiments (Figure 4c,g) and EDX spectra (Figure 5) from the aggregates from the 4.2, 42, and 252 μM U(VI) experiments were all similar (Figure 4a,b,d,e,h,j). This implies the same phase formed in all three systems even though their morphologies (Figure 4) and filtration behavior (Figure 1) differed. The positions of the dominant diffraction rings in the SAED images (Figure 4c,g) correspond to *d*-spacings of ∼3.2, ∼2.7, 1.9, and 1.6 Å, which indicates that the particles were the alkali/alkaline-earth metal uranate phase clarkeite (Figure 3 in the SI).[46,47] This explains the 5.9−6.2 Å lattice fringes which correspond to the *d*-spacing of the (003) diffraction peak, which can be related to the distance between adjacent U layers in the uranate structure. The lack of the 5.9−6.2 Å lattice fringes in the particles from the 4.2 and 42 μM U(VI) experiments is likely caused by the limited size of the nanoparticles or limited order between adjacent U layers. Finally, TEM analyses suggest that in all experiments, initially nanoparticles formed (1−5 nm) from solution which then aggregated. In the 252 μM experiment the freshly formed nanoparticles crystallized presumably via oriented attachment to form larger platelets.

The U L_{III}-edge XANES spectra from the 252 μM U(VI) experiment precipitate and a solution aliquot from the 42 μM U(VI) experiments are plotted in Figure 6a. Also plotted are the XANES from uranate[17,48] and uranyl standard (Figure 6a) compounds. Both spectra from the experimental samples show relatively broad white lines at ∼17.178 keV (dashed line B, Figure 6a) similar to the uranate standard, while the uranyl standard has a sharper white line at ∼17.176 keV (dashed line A, Figure 6a). In addition, the positions of the resonance features in both experimental XANES spectra match those of

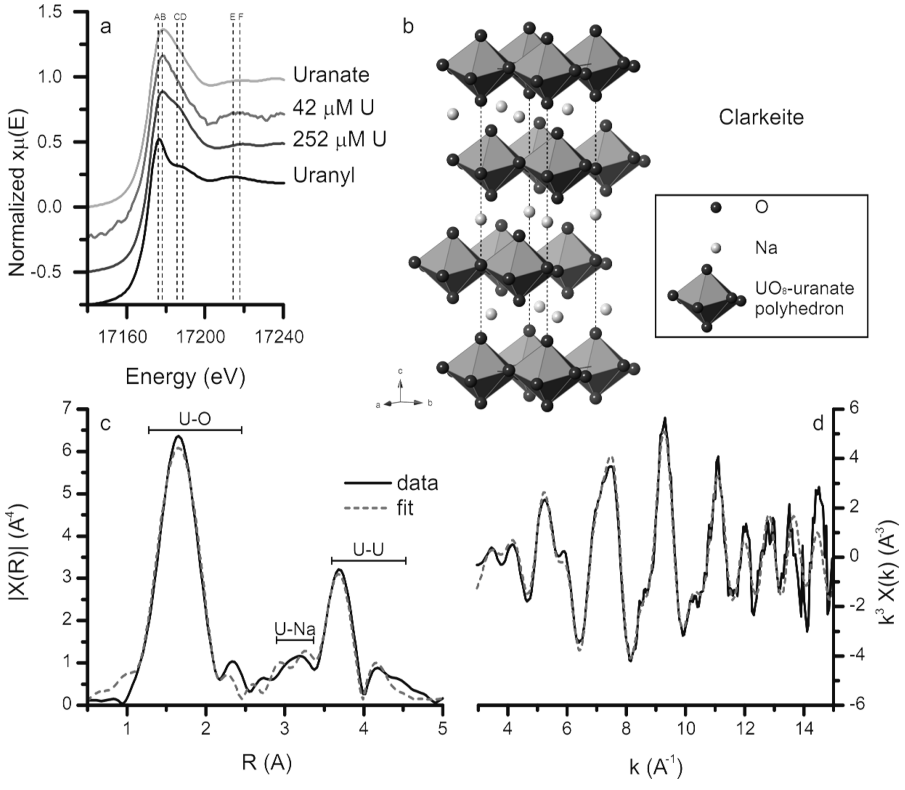

Figure 6. (a) Normalized XANES spectra from the precipitate from the 252 μM U(VI) experiment and the 42 μM U(VI) solution samples and a uranate ($CaUO_4$)[17,48] and an in-house uranyl (UO_3) standard. The vertical dashed line represents the position of the multiple scattering of the axial U═O bonds from uranyl. (b) Stick and ball representation of the clarkeite structure used to model the EXAFS spectrum, the dashed outline shape denotes the unit cell of clarkeite. (c) Fourier transform of the EXAFS collected from the precipitate of the 252 μM U(VI) experiment. (d) EXAFS from the precipitate of the 252 μM U(VI) experiment.

dx.doi.org/10.1021/la502832j | *Langmuir* 2014, 30, 14396−14405

Table 3. Summary of the EXAFS Parameters Fitted for a Uranium Phase without Na, for Clarkeite ($NaUO_2O(OH)\cdot(H_2O)_{0-1}$) and for Clarkeite Where Sodium Was Substituted for Potassium and Calcium (K-Clarkeite and Ca-Clarkeite, Respectively)

		no Na		clarkeite		K-clarkeite		Ca-clarkeite	
	reduced χ^2	80.93		49.56		67.30		64.67	
	R-factor	0.0140		0.00835		0.0118		0.0113	
	confidence[a] (%)			95		62		70	
	E_0	1.37(82)		2.04(66)		1.28(85)		1.44(81)	
	N^b	R^b	σ^{2b}	R^b	σ^{2b}	R^b	σ^{2b}	R^b	σ^{2b}
U−O_{ax}	2	1.87(1)	0.0047(9)	1.87(1)	0.0040(4)	1.87(1)	0.0041(5)	1.87(1)	0.0041(4)
U−O_{eq}	4.5	2.22(1)	0.006(1)	2.22(1)	0.0055(3)	2.22(1)	0.0054(4)	2.22(1)	0.0054(4)
U−O_{eq}	1	2.53(3)	0.008(4)	2.54(2)	0.009(3)	2.54(3)	0.008(3)	2.54(3)	0.008(3)
U−Na	1			3.54(2)	0.004(2)				
U−K	1					3.76(5)	0.011(6)		
U−Ca	1							3.72(4)	0.011(5)
U−U	3	3.83(1)	0.0060(9)	3.83(1)	0.0055(5)	3.82(1)	0.0054(5)	3.82(1)	0.0054(5)
U−U	1	4.30(3)	0.0060[c]	4.30(2)	0.0055[c]	4.29(2)	0.0054[c]	4.29(2)	0.0054[c]

[a]Confidence level whether the fit was significantly improved by adding the Na, K, or Ca shell compared to the uranium phase without Na; calculated using the *F*-test for EXAFS.[50] [b]*N* is the coordination number, *R* is the distance between uranium and the scatterer, and σ^2 is the Debye−Waller factor. [c]Constrained parameter.

the uranate standard (dashed lines C−F, Figure 6a).[49] This indicates that, in the 42 μM U(VI) experiment, uranium is predominantly present as colloidal uranate nanoparticles, rather than as dissolved uranyl or a solid uranyl compound.

The extended X-ray adsorption fine structure (EXAFS) spectrum and corresponding Fourier transform for the 252 μM U(VI) precipitate are shown in Figure 6c,d. Four consecutive fits were performed on the EXAFS spectrum. The first fit was calculated using only U−O and U−U bonds from clarkeite.[47,51] As observed in the TEM-EDX analyses, the composition of the precipitated phase included Na, Ca, and K (Figure 5). Thus, three subsequent fits were refined by including Na, K, or Ca.[47] The U−O_{axial} bond length of 1.87 Å corresponds to the U−O_{axial} bond lengths in uranate phases (1.86−1.97 Å)[17,51,52] and is longer than the U−O_{axial} bond lengths in uranyl phases (1.70−1.82 Å).[52,53] Furthermore, the U−O_{eq1} of 2.22 Å is comparable to U−O_{eq1} distances calculated for several layered metal uranate phases at 2.15−2.30 Å[17,51,52] while U O_{eq1} distances in uranyl phases are 2.27−2.49 Å.[51,53] Combined with the SAED (Figure 4g) and the XANES (Figure 6a), this confirms the formation of an alkali/alkaline-earth uranate phase in the 252 μM U(VI) experiments (and, by extension, in the 4.2 and the 42 μM U(VI) experiments). Furthermore, adding Na, K, or Ca to the EXAFS model significantly improved the overall fit (Table 3) with the result resembling the structure of clarkeite ($(Na,K,Ca)UO_2O(OH)\cdot(H_2O)_{0-1}$, Table 4 and Figure 6b−d).[47,51] However, in relation to the structure previously determined,[47] the oxygen coordination around uranium appears distorted; the U − O_{eq} distances were split between bond lengths of 2.22 and 2.54 Å (Table 3) instead of only at 2.30 Å (Table 4). This is similar to the observation of Catalano and Brown[51] (Table 4) who explained this by suggesting clarkeite is not truly hexagonal, and variable hydration of clarkeite could cause multiple uranium crystallographic positions and changes in the cation occupation. Furthermore, the U−Na distance is ∼5% shorter than previously determined,[47,51] which could be caused by distortions induced by variable hydration or the incorporation of foreign elements such as Ca and K in the interlayer (Figure 5).[51] Interestingly, the EXAFS fits were also improved by the addition of K and Ca (Table 3), indicating that these may be replacing some of the Na in the interlayer of clarkeite, which has been observed previously in natural samples.[47] Thus, the identification of a clarkeite-type phase containing a mixture of Na, K, and Ca is confirmed, which is consistent with the formation of similar phases in other high-pH systems.[54,55]

Table 4. Clarkeite Uranium Coordination Environment Obtained from Literature, Modeled from an XRD Pattern and an EXAFS Spectrum

clarkeite		*N*	*R*
XRD[47]	U−O_{ax}	2	1.888
	U−O_{eq}	6	2.299
	U−Na	6	3.725
	U−U	6	3.954
EXAFS[51]	U-O_{ax}	2	1.868
	U-O_{eq}	3.3	2.28
	U-O_{eq}	1.7	2.51
	U−Na	2	3.71
	U−U	2	3.73
	U−U	2	3.88
	U−U	2	4.60

Nanoparticle Solubility. As discussed previously uranium in the 4.2 and 42 μM U(VI) experiments (Figure 6a) was present as colloidal clarkeite nanoparticles. Additionally, the PHREEQC calculations show that if the solutions were in equilibrium with clarkeite, 100.0 and 99.8% of the U(VI) would be in the solid phase in the 42 and 4.2 μM U(VI) experiments, respectively. However, because reducing the size of nanoparticle tends to increase their solubility,[56] a smaller proportion of U(VI) could be in the solid phase. The solubility of a phase tends to increase with decreasing nanoparticle size as described (increasing specific surface area, *A* (m^2/mol)) via eq 2,[57−59]

$$\log[K_{sp,nano}] = \log[K_{sp}] + A\frac{2\sigma}{3RT} \quad (2)$$

where K_{sp} and $K_{sp,nano}$ are the ion activity products at equilibrium with a bulk and nanoparticulate phase, respectively ($K_{sp} = 10^{9.4}$),[12] *T* is the absolute temperature (239 K), *R* is the universal gas constant (8.3145 J/K), and σ is the surface free energy (J/m^2). However, the surface free energy of clarkeite is

dx.doi.org/10.1021/la502832j | Langmuir 2014, 30, 14396−14405

unknown; therefore, we have estimated $\sigma_{clarkeite}$ using the Gibbs−Thomson equation (eq 3).[60]

$$r^* = \frac{2\Omega\sigma}{\left[k_B T \ln\left(\frac{IAP}{K_{sp}}\right)\right]} \quad (3)$$

where r^* is the critical nucleus radius (m), k_B is the Boltzmann constant (1.38×10^{-23} J/K), IAP is the ion activity product of the solution with respect to clarkeite prior to nucleation (calculated for the 42 μM U(VI) experiment as $10^{13.35}$), and Ω is the crystal volume per unit formula as described by the IAP (a third of the unit cell of clarkeite, 0.0797 nm^3).[12,47] It is noteworthy that the nanoparticles nucleate as an amorphous phase. However, no thermodynamic information is available on amorphous uranate phases. Thus, we assumed that the thermodynamic properties of the amorphous phase are close to clarkeite. As discussed earlier, the SAXS and TEM analyses indicate that the U(VI) nucleated as ∼1.5 nm particles ($r^* \approx$ 0.75 nm); therefore this value was used as an upper limit for the critical nucleus size. The clarkeite unit cell size was used as the lower limit of the critical nucleus size ($r^* \approx$ 0.4 nm). Using these values resulted in a σ for clarkeite of 0.085−0.16 J/m^2, which is low compared to the σ of metaschoepite (0.94 J/m^2) and uraninite (0.47 J/m^2).[57,61] The rate of crystal growth and ripening (e.g., Ostwald ripening) are proportional to σ;[58,59] therefore, such a low σ could explain the lack of significant ripening of the primary particles following nucleation. Combined with the inhibition of aggregation caused by a highly negative surface charge, this explains the long-term stability (>32 months) of the colloidal U(VI) nanoparticles.

The σ of 0.085−0.16 J/m^2 can now be used in eq 2 to estimate the solubility of clarkeite nanoparticles with a diameter of 1.5 nm ($A \approx 1.9 \times 10^4$ m^2/mol). The resulting $K_{sp,nano}$ ($10^{9.8}$−$10^{10.2}$) was included in the PHREEQC calculations on U(VI) equilibrium concentrations in the experimental solutions (95 mM Na, 95 mM K, and 0.14 mM Ca) with 42 and 4.2 μM U(VI) experiments. This predicted equilibrium concentrations of ≤0.07 μM U(VI), and as described previously, the equilibrium concentration changed minimally (∼0.074 μM U(VI)) when equilibrium with calcite was added to the PHREEQC calculations. These values would mean that 99.8 and 98.3% of the U(VI) would be in the solid phase in the 42 and 4.2 μM U(VI) experiments, respectively. This supports our interpretation that U(VI) is predominantly colloidal in all experiments rather than dissolved uranyl.

CONCLUDING REMARKS

This study has identified the formation of nanoparticulate, stable U(VI) clarkeite-type colloids at high-pH conditions relevant to geological disposal and contaminated land.[8,9,23,55] Time-resolved scattering data and TEM images showed that these particles nucleate as amorphous nanoparticles (o.d. = 1.5−1.8 nm) within a few minutes and that ∼50% of the colloids are present as aggregates 20−60 nm in size, which is stable for over 2.5 years. Within 1 day the nanoparticles crystallize and exhibit a clarkeite-type crystal structure.

The long-term stability of U(VI) as a nanoparticulate phase at high-pH conditions is a significant new observation. Thermodynamic calculations show that clarkeite-type U(VI) nanoparticles are oversaturated at very low concentrations (> 0.07 μM) even when including equilibrium with calcium carbonate into the system. This suggests that these clarkeite nanoparticles may be significant across a range of systems and may help explain the high "solubility" of U(VI) observed under high-pH conditions by past workers[18] which was previously ascribed to formation of aqueous $UO_2(OH)_4^{2-}$ species. The results presented suggest that under high-pH conditions there is a potential new mechanism for U(VI) to be transported as a colloidal phase in cementitious environments.

ASSOCIATED CONTENT

Supporting Information

Text describing addiitional SAXS data analyses and accompanying references, figures showing SAXS pattern simulation and the corresponding Kratky plot, uranium solution analyses from 42 and 4.2 μM U(VI) experiments, and a selected area electron diffraction image from the clarkeite nanoparticle, and a table listing simulated SAXS pattern calculations. This material is available free of charge via the Internet at http://pubs.acs.org.

AUTHOR INFORMATION

Corresponding Author

*E-mail: sam.shaw@manchester.ac.uk. Tel.: +44 (0) 161275 3826.

Notes

The authors declare no competing financial interest.

ACKNOWLEDGMENTS

This project has been funded as part of the U.K. Natural Environment Research Council (NERC) BIGRAD consortium through Grant No. NE/H007768/1. Diamond Light Source is thanked for providing beamtime Grants SP5975 (SAXS) and SP8544 (XAS) and Dr. Steve Parry and Richard Doull for assistance at Diamond. We also thank Paul Lythgoe for his assistance with the ICP-MS analyses.

REFERENCES

(1) Defra; BERR; Devolved Administrations for Wales and Northern Ireland*Managing Radioactive Waste Safely: A Framework for Implementing Geodisposal*, A White Paper; The Stationary Office (TSO): Norwich, U.K., 2008.

(2) Morris, K.; Law, G. T. W.; Bryan, N. D., Geodisposal of Higher Activity Wastes. *Nuclear Power and the Environment*; The Royal Society of Chemistry: Cambridge, U.K., 2011; pp 129−151.

(3) Silva, R. J.; Nitsche, H. Actinide environmental chemistry. *Radiochim. Acta* **1995**, *70-1*, 377−396.

(4) Walther, C.; Denecke, M. A. Actinide Colloids and Particles of Environmental Concern. *Chem. Rev.* **2013**, *113* (2), 995−1015.

(5) *Geological Disposal—An overview of the generic Disposal System Safety Case December 2010*, NDA Report No. NDA/RWMD/010; Nuclear Decommissioning Authority: Oxon, U.K., 2010.

(6) Wieland, E.; Spieler, P. Colloids in the mortar backfill of a cementitious repository for radioactive waste. *Waste Manage.* **2001**, *21* (6), 511−523.

(7) *Geological Disposal; Generic Post-closure Safety Assessment*, NDA Report No. NDA/RWMD/030; Nuclear Decommissioning Authority: Oxon, U.K., 2010; http://www.nda.gov.uk/publication/geological-disposal-generic-post-closure-safety-assessment-december-2010/.

(8) Wieland, E.; Bonhoure, I.; Fujita, T.; Tits, J.; Scheidegger, A. M. Combined wet chemistry and EXAFS studies on the radionuclide immobilisation by cement and calcium silicate hydrates. *Geochim. Cosmochim. Acta* **2003**, *67* (18), A532−A532.

(9) Small, J. S.; Thompson, O. R. Modelling the spatial and temporal evolution of pH in the cementitious backfill of a geological disposal facility. In *Scientific Basis for Nuclear Waste Management XXXII*; Hyatt, N. C., Pickett, D. A., Rebak, R. B., Eds.; Cambridge University Press: Cambridge, U.K., 2009; Vol. *1124*, pp 327−332.

(10) Gaona, X.; Kulik, D. A.; Mace, N.; Wieland, E. Aqueous-solid solution thermodynamic model of U(VI) uptake in C-S-H phases. *Appl. Geochem.* **2012**, *27* (1), 81−95.
(11) Yamamura, T.; Kitamura, A.; Fukui, A.; Nishikawa, S.; Yamamoto, T.; Moriyama, H. Solubility of U(VI) in highly basic solutions. *Radiochim. Acta* **1998**, *83* (3), 139−146.
(12) Gorman-Lewis, D.; Fein, J. B.; Burns, P. C.; Szymanowski, J. E. S.; Converse, J. Solubility measurements of the uranyl oxide hydrate phases metaschoepite, compreignacite, Na−compreignacite, becquerelite, and clarkeite. *J. Chem. Thermodyn.* **2008**, *40* (6), 980−990.
(13) Waite, T. D.; Davis, J. A.; Payne, T. E.; Waychunas, G. A.; Xu, N. Uranium(VI) adsorption to ferrihydrite: Application of a surface complexation model. *Geochim. Cosmochim. Acta* **1994**, *58* (24), 5465−5478.
(14) Davis, J. A.; Meece, D. E.; Kohler, M.; Curtis, G. P. Approaches to surface complexation modeling of uranium(VI) adsorption on aquifer sediments. *Geochim. Cosmochim. Acta* **2004**, *68* (18), 3621−3641.
(15) Duff, M. C.; Coughlin, J. U.; Hunter, D. B. Uranium co-precipitation with iron oxide minerals. *Geochim. Cosmochim. Acta* **2002**, *66* (20), 3533−3547.
(16) Sylwester, E. R.; Hudson, E. A.; Allen, P. G. The structure of uranium (VI) sorption complexes on silica, alumina, and montmorillonite. *Geochim. Cosmochim. Acta* **2000**, *64* (14), 2431−2438.
(17) Macé, N.; Wieland, E.; Dähn, R.; Tits, J.; Scheinost4, A. C. EXAFS investigation on U(VI) immobilization in hardened cement paste: Influence of experimental conditions on speciation. *Radiochim. Acta* **2013**, *101* (6), 379−389.
(18) Tits, J.; Geipel, G.; Mace, N.; Eilzer, M.; Wieland, E. Determination of uranium(VI) sorbed species in calcium silicate hydrate phases: A laser-induced luminescence spectroscopy and batch sorption study. *J. Colloid Interface Sci.* **2011**, *359* (1), 248−256.
(19) Dong, W.; Brooks, S. C. Determination of the Formation Constants of Ternary Complexes of Uranyl and Carbonate with Alkaline Earth Metals (Mg^{2+}, Ca^{2+}, Sr^{2+}, and Ba^{2+}) Using Anion Exchange Method. *Environ. Sci. Technol.* **2006**, *40* (15), 4689−4695.
(20) Li, D.; Kaplan, D. I.; Roberts, K. A.; Seaman, J. C. Mobile Colloid Generation Induced by a Cementitious Plume: Mineral Surface-Charge Controls on Mobilization. *Environ. Sci. Technol.* **2012**, *46* (5), 2755−2763.
(21) Parry, S. A.; O'Brien, L.; Fellerman, A. S.; Eaves, C. J.; Milestone, N. B.; Bryan, N. D.; Livens, F. R. Plutonium behaviour in nuclear fuel storage pond effluents. *Energy Environ. Sci.* **2011**, *4* (4), 1457−1464.
(22) Novikov, A. P.; Kalmykov, S. N.; Utsunomiya, S.; Ewing, R. C.; Horreard, F.; Merkulov, A.; Clark, S. B.; Tkachev, V. V.; Myasoedov, B. F. Colloid Transport of Plutonium in the Far-Field of the Mayak Production Association, Russia. *Science* **2006**, *314* (5799), 638−641.
(23) Utsunomiya, S.; Kersting, A. B.; Ewing, R. C. Groundwater nanoparticles in the far-field at the nevada test site: Mechanism for radionuclide transport. *Environ. Sci. Technol.* **2009**, *43* (5), 1293−1298.
(24) Kersting, A. B.; Efurd, D. W.; Finnegan, D. L.; Rokop, D. J.; Smith, D. K.; Thompson, J. L. Migration of plutonium in ground water at the Nevada Test Site. *Nature* **1999**, *397* (6714), 56−59.
(25) Powell, B. A.; Dai, Z.; Zavarin, M.; Zhao, P.; Kersting, A. B. Stabilization of Plutonium Nano-Colloids by Epitaxial Distortion on Mineral Surfaces. *Environ. Sci. Technol.* **2011**, *45* (7), 2698−2703.
(26) Parkhurst, D. L.; Appelo, C. A. J. *User's guide to PHREEQC (version 2)—A computer program for speciation, batch-reaction, one-dimensional transport, and inverse geochemical calculations*; U.S. Geological Survey: Denver, CO, USA, 1999; p 312.
(27) O'Hare, P. A. G.; Boerio, J.; Hoekstra, H. R. Thermochemistry of uranium compounds VIII. Standard enthalpies of formation at 298.15 K of the uranates of calcium ($CaUO_4$) and barium ($BaUO_4$). Thermodynamics of the behavior of barium in nuclear fuels. *J. Chem. Thermodyn.* **1976**, *8* (9), 845−855.
(28) Zanonato, P. L.; Di Bernardo, P.; Grenthe, I. A calorimetric study of the hydrolysis and peroxide complex formation of the uranyl(VI) ion. *Dalton Trans.* **2014**, 43.
(29) Kraft, P. *PILATUS 2M; A detector for small angle X-ray scattering*; ETH Zürich, Zurich, Switzerland, 2010.
(30) Ilavsky, J.; Jemian, P. R. Irena: Tool suite for modeling and analysis of small-angle scattering. *J. Appl. Crystallogr.* **2009**, *42* (2), 347−353.
(31) Liu, J.; Pancera, S.; Boyko, V.; Shukla, A.; Narayanan, T.; Huber, K. Evaluation of the Particle Growth of Amorphous Calcium Carbonate in Water by Means of the Porod Invariant from SAXS. *Langmuir* **2010**, *26* (22), 17405−17412.
(32) Glatter, O.; Kratky, O. *Small Angle X-ray Scattering*; Academic Press: London, 1982.
(33) Porod, G. Die Rontgenkleinwinkelstreuung Von Dichtgepackten Kolloiden Systemen.1. *Kolloid Z. Z. Polym.* **1951**, *124* (2), 83−114.
(34) Rose, A. L.; Bligh, M. W.; Collins, R. N.; Waite, T. D. Resolving early stages of homogeneous iron(III) oxyhydroxide formation from iron(III) nitrate solutions at pH 3 using time-resolved SAXS. *Langmuir* **2014**, *30* (12), 3548−3556.
(35) Abràmoff, M. D.; Magalhães, P. J.; Ram, S. J. Image Processing with ImageJ. *Biophotonics Int.* **2004**, *11* (7), 36−42.
(36) Ravel, B.; Newville, M. ATHENA, ARTEMIS, HEPHAESTUS: Data analysis for X-ray absorption spectroscopy using IFEFFIT. *J. Synchrotron Radiat.* **2005**, *12*, 537−541.
(37) Allen, A. J.; Livingston, R. A. Relationship between differences in silica fume additives and fine-scale microstructural evolution in cement based materials. *Adv. Cem. Based Mater.* **1998**, *8* (3−4), 118−131.
(38) Reidy, R. F.; Allen, A. J.; Krueger, S. Small angle neutron scattering characterization of colloidal and fractal aerogels. *J. Non-Cryst. Solids* **2001**, *285* (1−3), 181−186.
(39) Hondow, N.; Brydson, R.; Wang, P.; Holton, M. D.; Brown, M. R.; Rees, P.; Summers, H. D.; Brown, A. Quantitative characterization of nanoparticle agglomeration within biological media. *J. Nanopart. Res.* **2012**, *14* (7), No. 977.
(40) Bots, P.; Benning, L. G.; Rodriguez-Blanco, J.-D.; Roncal-Herrero, T.; Shaw, S. Mechanistic Insights into the Crystallization of Amorphous Calcium Carbonate (ACC). *Cryst. Growth Des.* **2012**, *12* (7), 3806−3814.
(41) Tobler, D. J.; Shaw, S.; Benning, L. G. Quantification of initial steps of nucleation and growth of silica nanoparticles: An in-situ SAXS and DLS study. *Geochim. Cosmochim. Acta* **2009**, *73* (18), 5377−5393.
(42) Vochten, R.; Van Haverbeke, L.; Sobry, R. Transformation of schoepite into uranyl oxide hydrates of the bivalent cations Mg^{2+}, Mn^{2+} and Ni^{2+}. *J. Mater. Chem.* **1991**, *1* (4), 637−642.
(43) Demichelis, R.; Raiteri, P.; Gale, J. D.; Quigley, D.; Gebauer, D. Stable prenucleation mineral clusters are liquid-like ionic polymers. *Nat. Commun.* **2011**, *2*, No. 590.
(44) Gebauer, D.; Völkel, A.; Cölfen, H. Stable Prenucleation Calcium Carbonate Clusters. *Science* **2008**, *322* (5909), 1819−1822.
(45) Van Driessche, A. E. S.; Benning, L. G.; Rodriguez-Blanco, J. D.; Ossorio, M.; Bots, P.; Garcia-Ruiz, J. M. The Role and Implications of Bassanite as a Stable Precursor Phase to Gypsum Precipitation. *Science* **2012**, *336* (6077), 69−72.
(46) Loopstra, B.; Rietveld, H. The structure of some alkaline-earth metal uranates. *Acta Crystallogr., Sect. B: Struct. Crystallogr. Cryst. Chem.* **1969**, *25* (4), 787−791.
(47) Finch, R. J.; Ewing, R. C. Clarkeite: New chemical and structural data. *Am. Mineral.* **1997**, *82* (5), 607−619.
(48) Scheinost, A. C.; Schmeisser, N.; Banerjee, D.; Rossberg, A.; Denecke, M.; Dardenne, K.; Rothe, J.; Daehn, R. AcXAS An Actinide Reference X-ray Absorption Spectroscopy Database. https://www.hzdr.de/acxas 2013.
(49) Connelly, A. J.; Hyatt, N. C.; Travis, K. P.; Hand, R. J.; Stennett, M. C.; Gandy, A. S.; Brown, A. P.; Apperley, D. C. The effect of uranium oxide additions on the structure of alkali borosilicate glasses. *J. Non-Cryst. Solids* **2013**, *378* (0), 282−289.
(50) Downward, L.; Booth, C.; Lukens, W.; Bridges, F. A variation of the F-test for determining statistical relevance of particular parameters in EXAFS fits. *AIP Conf. Proc.* **2007**, *882* (1), 129−131.

(51) Catalano, J. G.; Brown, G. E. Analysis of uranyl-bearing phases by EXAFS spectroscopy: Interferences, multiple scattering, accuracy of structural parameters, and spectral differences. *Am. Mineral.* **2004**, *89* (7), 1004−1021.
(52) King, R. B. Some Aspects of Structure and Bonding in Binary and Ternary Uranium(VI) Oxides. *Chem. Mater.* **2002**, *14* (9), 3628−3635.
(53) Thompson, H. A.; Brown, G. E.; Parks, G. A. XAFS spectroscopic study of uranyl coordination in solids and aqueous solution. *Am. Mineral.* **1997**, *82* (5), 483−496.
(54) Kim, K. W.; Kim, Y. H.; Lee, S. Y.; Lee, J. W.; Joe, K. S.; Lee, E. H.; Kim, J. S.; Song, K.; Song, K. C. Precipitation Characteristics of Uranyl Ions at Different pHs Depending on the Presence of Carbonate Ions and Hydrogen Peroxide. *Environ. Sci. Technol.* **2009**, *43* (7), 2355−2361.
(55) Cantrell, K. J.; Um, W.; Williams, B. D.; Bowden, M. E.; Gartman, B.; Lukens, W. W.; Buck, E. C.; Mausolf, E. J. Chemical stabilization of Hanford tank residual waste. *J. Nucl. Mater.* **2014**, *446* (1-3), 246−256.
(56) Navrotsky, A. Energetic clues to pathways to biomineralization: Precursors, clusters, and nanoparticles. *Proc. Natl. Acad. Sci. U. S. A.* **2004**, *101* (33), 12096−12101.
(57) Giammar, D. E.; Hering, J. G. Influence of Dissolved Sodium and Cesium on Uranyl Oxide Hydrate Solubility. *Environ. Sci. Technol.* **2004**, *38* (1), 171−179.
(58) Lifshitz, I. M.; Slyozov, V. V. The kinetics of precipitation from supersaturated solid solutions. *J. Phys. Chem. Solids* **1961**, *19* (1-2), 35−50.
(59) Wagner, C. Theorie der Alterung von Niederschlägen durch Umlösen (Ostwald-Reifung). *Z. Elektrochem.* **1961**, *65* (7−8), 581−591.
(60) De Yoreo, J. J.; Vekilov, P. G. Principles of crystal nucleation and growth. *Rev. Mineral. Geochem.* **2003**, *54* (1), 57−93.
(61) Abramowski, M.; Redfern, S. E.; Grimes, R. W.; Owens, S. Modification of UO_2 crystal morphologies through hydroxylation. *Surf. Sci.* **2001**, *490* (3), 415−420.

Electronic Supplementary Information to: Formation of Stable Uranium(VI) Colloidal Nanoparticles in Conditions Relevant to Radioactive Waste Disposal

Pieter Bots, Katherine Morris, Rosemary Hibberd, Gareth T.W. Law, J. Frederick W. Mosselmans, Andrew P. Brown, James Doutch, Andrew J. Smith and Samuel Shaw

SAXS data analyses

The Irena macro uses an extension of equation 1 (a summation to account for multiple particle shapes, sizes and polydispersity) to fit the scattering intensity within a Small Angle X-ray Scattering (SAXS) pattern [1, 2]:

$$I(q) = K_{SAXS} c M_W P(q,d) S(q) \quad (1)$$

where $I(q)$ is the scattering intensity at each value of the scattering vector q (Å^{-1}). The absolute scattering intensity caused by particles in a medium is dependent on the particle concentration in g / ml (c) and the electron density of all the particles in mole equivalents / g (M_W). I(q) is described by the form factor ($P(q,d)$) which accounts for the intra-particle interference of particles with a diameter of d, and the structure factor ($S(q)$) which accounts for all inter-particle interferences of X-rays. Scattering analyses were performed on very dilute solutions (e.g. 42 µM U(VI)), thus inter-particle interferences of X-rays can be neglected and the structure factor approximates unity. K_{SAXS} is a constant that represents the scattering contrast in SAXS.

Additionally, the SAXS patterns from the *in-situ* time resolved experiments were also analysed using the method described by Liu et al.[3]. The Guinier region of a SAXS scattering pattern ($qR_g < 1.3$) can be approximated with equation 2[2, 4-6] where R_g is the radius of gyration (equation 3).[2] The $I(0)$ is the extrapolated intensity at $q=0$ in a $ln(I(q))$ *vs.* q^2 plot (a Guinier plot), and is a function of the particle volume (V_p), particle number (n) and electron density difference between the particles and the medium ($\Delta\rho$; equation 4). [2, 3, 7]

$$I(q) = I(0)\exp\left[-\frac{q^2 R_g^2}{3}\right] \quad (2)$$

$$R_g^2 = \frac{3}{5}R^2 \quad (3)$$

$$I(0) = V_p^2 n(\Delta\rho)^2 \quad (4)$$

SAXS patterns can be visualized using a Kratky plot ($I(q)q^2$ *vs.* q (Fig. 1). From a Kratky plot, the invariant (Q) can be calculated by integration of the scattering pattern from $q = 0$ to $q = \infty$ (equation 5)[2, 5, 7]. Q is a function of the fraction of the scattering particles (φ) and $\Delta\rho$ (equation 6).[2, 3, 7] In equation 6, $(1 - \varphi)$ can be assumed to be approximately unity in a dilute system. Hence, equation 7 can be rewritten as a function of the particle volume and particle number (equation 7).

$$Q = \frac{1}{2\pi^2}\int_0^\infty I(q)q^2 dq \quad (5)$$

$$Q = \varphi(1-\varphi)(\Delta\rho)^2 \quad (6)$$

$$Q \approx V_p n(\Delta\rho)^2 \quad (7)$$

When $I(0)$ and Q have been determined, these can be used to calculate the particle volume and particle number using equations 8 and 9, respectively.[2-4]

$$\frac{I(0)}{Q} \approx V_p \quad (8)$$

$$\frac{Q^2}{I(0)} \approx n(\Delta\rho)^2 \quad (9)$$

If a dilute suspension (no inter-particle interferences of X-rays) has two particle populations with a sufficient difference in particle size, the scattering from the individual particle populations show features at different q values in the scattering patterns and Kratky plots (Fig. 1). From this, a Q and $I(0)$ can be estimated for both particle populations, separately. Thus equation 8 and 9 can also be used to estimate the V_p (and thus the particle diameter) and particle number (and thus the volume fraction for each particle population) for both particle populations. An example of this type of analysis from a simulated scattering pattern with two particle population is given in Fig. 1 and Table 1.[8]

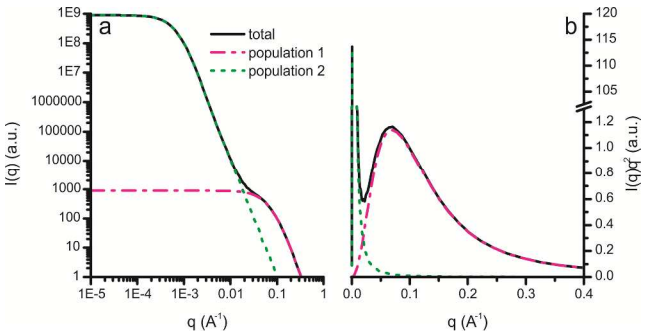

Fig. 1 Simulation of a SAXS pattern on a log-log scale (a) and the corresponding Kratky plot (b) from a system with 2 particle populations as described in Table 1.

Table 1 Calculations performed on the simulated SAXS pattern shown in Fig. 1.

	Simulated		Estimated using equation 5, 7 and 8			
Population	Particle diameter	Volume fraction	I(0)	Q	Particle diameter	Volume fraction
1	20 nm	50 %	1143	0.0306	20.7 nm	49 %
2	2000 nm	50 %	8.96E8	0.0316	1892 nm	51 %

It has to be noted that the results from equations 8 and 9 are only quantitative when full scattering patterns ($q_{min} \to 0$ and $q_{max} \to \infty$) are collected and the absolute intensity is known.[9] If data are missing at large q values then V_p will be overestimated,

while if data are missing at low q values of V_p will be underestimated. Furthermore, additional information on the structure of the particles would need to be collected (Δρ) to allow the calculation of the absolute particle numbers.

Solution chemistry

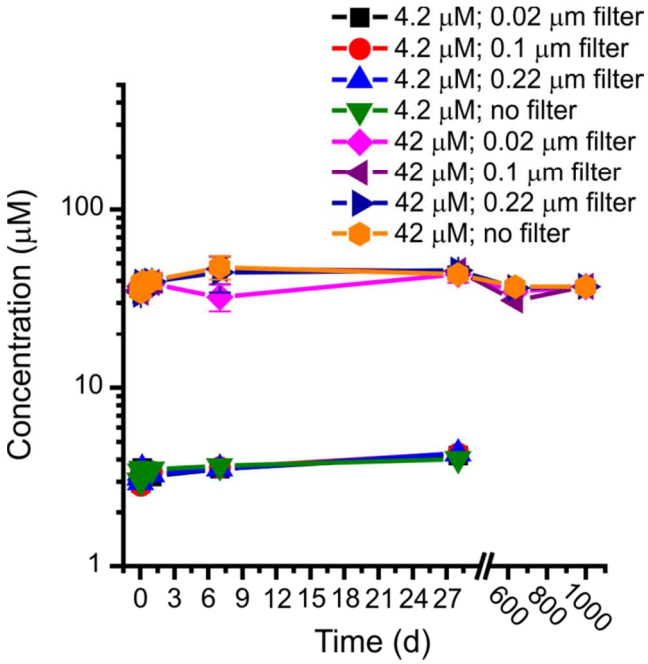

Fig.2 Solution data from the 42 μM U(VI) and 4.2 μM U(VI) experiments; the error bars on the data from the 42 μM U(VI) experiment are the standard deviation of triplicate experiments

Selected Area Electron Diffraction

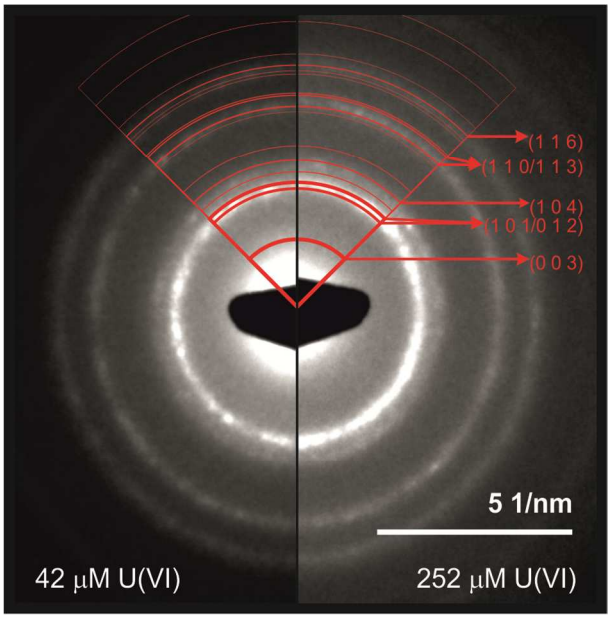

Fig. 3 Selected Area Electron Diffraction images from the 1 day 42 μM U(VI) and the 1 week 252 μM U(VI) experiments, the quarter circles represent the Bragg reflections for clarkeite that are more than 10% the intensity of the maximum intensity peak (the thickness of the quarter circles is proportional to the intensity of the reflections). Miller indices for Bragg reflections more than 25% the intensity of the maximum intensity peak are labelled

References

1. J. Ilavsky and P. R. Jemian, *Journal of Applied Crystallography*, 2009, **42**, 347; A. Guinier and G. Fournet, *Small-angle scattering of X-rays*, John Wiley and Sons, London, 1955.
2. O. Glatter and O. Kratky, *Small Angle X-Ray Scattering*, Academic Press, London, 1982.
3. J. Liu, S. Pancera, V. Boyko, A. Shukla, T. Narayanan and K. Huber, *Langmuir*, 2010, **26**, 17405.
4. A. Guinier, *X-ray Diffraction in Crystals, Imperfect Crystals, and Amorphous Bodies*, W. H. Freeman, San Francisco, 1963.
5. G. Porod, *Kolloid-Zeitschrift and Zeitschrift Fur Polymere*, 1951, **124**, 83.
6. C. D. Putnam, M. Hammel, G. L. Hura and J. A. Tainer, *Quarterly Reviews of Biophysics*, 2007, **40**, 191.
7. W. Bras, G. N. Greaves, M. Oversluizen, S. M. Clark and G. Eeckhaut, *Journal of Non-Crystalline Solids*, 2005, **351**, 2178.
8. A. L. Rose, M. W. Bligh, R. N. Collins and T. D. Waite, *Langmuir*, 2014.
9. I. Pilz, *Journal of Colloid and Interface Science*, 1969, **30**, 140; I. Pilz and O. Kratky, *Journal of Colloid and Interface Science*, 1967, **24**, 211; O. Kratky, I. Pilz and P. J. Schmitz, *Journal of Colloid and Interface Science*, 1966, **21**, 24.

Chapter 5. U(VI) Nanoparticle Stability Under Alkaline Conditions in the Presence of Rock Forming Minerals and Cement

This chapter is a manuscript prepared for submission to the journal *Applied Geochemistry*. Supporting Information supplied with this manuscript is included following the manuscript.

U(VI) Nanoparticle Stability Under Alkaline Conditions in the Presence of Rock Forming Minerals and Cement

Rosemary Hibberd[a, b], Gareth T. W. Law[a, b], Nicholas D. Bryan[a, c], Samuel Shaw[a], Pieter Bots[a, 1], Kurt F. Smith[a, b], Timothy A. Marshall[a, 2], Ryan Telchadder[b], Adam Swinbourne[b], Louise Natrajan[b], Rebecca Beard[d], Steve Williams[d], Katherine Morris[a*]

[a]Research Centre for Radwaste Disposal and Williamson Research Centre for Molecular Environmental Science, School of Earth and Environmental Sciences, The University of Manchester, Oxford Road, Manchester, M13 9PL, UK.

[b]Centre for Radiochemistry Research, School of Chemistry, The University of Manchester, Oxford Road, Manchester, M13 9PL, UK.

[c]National Nuclear Laboratory, 5th Floor, Chadwick House, Birchwood Park, Warrington Road, Warrington, WA3 6AE, UK.

[d]Radioactive Waste Management Limited, Harwell, Oxfordshire, OX11 0RH, UK.

[1]Present address: Department of Civil and Environmental Engineering, University of Strathclyde, Glasgow, G1 1XQ, UK.

[2]Present address: Office of Nuclear Regulation, Building 4, Redgrave Court, Bootle, Merseyside, L20 7HS, UK.

[*]Corresponding author, Tel: +44 (0) 161 275 7541; Email: katherine.morris@manchestester.ac.uk

Keywords: uranium, cement, biotite, orthoclase, quartz, radioactive waste

Abstract

Colloidal U(VI) nanoparticles have been observed and fully characterised in high pH (pH > 13.1) synthetic cement leachate as uranate-like phases. Here, we investigate the stability of these colloids (42 μM U) in reaction systems containing rock-forming minerals and cement phases at pH 13.3. These conditions are relevant to the early stages of intermediate level radioactive waste disposal where cementitious materials will be utilised and where extremely high pH cement leachate is expected post-disposal. The U(VI) colloids were stable and remained largely in solution in the presence of biotite, orthoclase, and quartz for at least 18 months. By contrast, when contacted with cement, > 97 % of the U(VI) colloids were retained on solids over 21 months. Experiments conducted at trace concentrations of U(VI) (2.0×10^{-10} M) showed similar levels of sorption to cement with less than 4 % U remaining in solution after 48 hours. Even at this trace concentration, under the high pH conditions of the experiment, ultrafiltration showed that nearly all of the U (~ 79 %) was present in the 3 – 10 kDa size range as colloids. Together, these data confirm that U(VI) colloids are poorly reactive with biotite, orthoclase, and quartz but that significant reactivity occurs in systems containing cement phases. EDTA was then used as a competing ligand to test the strength and reversibility of the U(VI) interaction with cement at low U concentrations (2.0×10^{-10} M). Here, high concentrations of EDTA (> 0.01 M) reduced the extent of U(VI) sorption at apparent equilibrium when the ligand was added to the radionuclide prior to contact with cement. In contrast, the addition of EDTA to a pre-equilibrated system of U(VI) and cement resulted in significantly less desorption suggesting some fraction of the U(VI) was irreversibly bound. Luminescence spectroscopy was used to analyse U sorption in these experiments and here, the dominant spectral contribution was from a U(VI) species consistent with surface complexation or incorporation, but a feature consistent with the presence of uranate was also apparent. X-ray Absorption Spectroscopy from the higher U concentration cement experiment also

found that U(VI) was either sorbed or incorporated and/or precipitated in a uranophane-like coordination environment. This suggests that changes in solution chemistry, surface-mediated precipitation, or sorption of the U(VI) nanoparticles to the cement surface also contributed to the removal of U(VI) from solution. These results have important implications for U(VI) mobility under geological disposal facility conditions.

1. Introduction

The development of a safe method for the disposal of higher activity radioactive wastes (HAW) is a priority issue globally (DECC, 2010; Morris et al., 2011; NDA, 2013; Ministry of the Environment Sweden, 2014). Currently, the United Kingdom (UK) intends to implement geological disposal of its HAWs, underground (200 – 1000 m) in a purpose built Geological Disposal Facility (DECC, 2015). At present the UK has a generic design for Intermediate Level Waste (ILW) disposal, utilising a multi-barrier concept. This consists of the waste-form (grouted ILW), the waste container (typically steel/iron), and backfill, with the geosphere providing the final and ultimate barrier to radionuclide migration (Morris et al., 2011; NDA, 2014). One backfill currently being considered is a cementitious material, Nirex Reference Vault Backfill (NRVB), a mixture of Ordinary Portland Cement (OPC), limestone flour, and hydrated lime (NDA, 2014). In addition, cementitious grout, which also contains OPC, will be used to encapsulate ILW (Cronin and Collier, 2012), and a significant amount of cement will likely be employed in the construction of the geological disposal facility (GDF) structure. After the closure of any GDF located in a higher strength host rock, the facility will become saturated with regional groundwater (NDA, 2014). This groundwater will initially cause dissolution of the NaOH and KOH constituents of the cementitious phases, followed by the portlandite (CaO) fraction and Calcium-Silicate-Hydrate (C-S-H) phases, generating hyperalkaline (pH 10 – >13) leachate with elevated levels of K^+, Na^+, and Ca^{2+} ions (Small and Thompson, 2009; Butcher et al., 2012). These leachates will form a high pH Chemically Disturbed Zone (CDZ) in the surrounding host rock (Berner, 1992; Bots et al., 2014; Moyce et al., 2014). After closure, the engineered barrier system will degrade and long-lived radionuclides in the packaged waste are expected to be released.

By mass, uranium is the most significant radionuclide present in ILW (Marshall et al., 2014; RWM, 2015). The UK also has a significant stockpile (approximately

185,000 tonnes) of depleted, natural and low enriched uranium from reprocessing operations which may also be designated for disposal in the deep subsurface, and U(VI) may comprise a significant component of this waste (RWM, 2015).

Initially, conditions within the GDF will be oxic, and will develop to become reducing over 100's of years (Grive et al., 2009; NDA, 2010; Grive et al., 2011). Despite the chemically reducing environment, under alkaline conditions U(VI) may be stabilised and could therefore persist for a significant period post closure (Gaona et al., 2012; Bots et al., 2014; Smith et al., 2015). One of reasons for using a cementitious backfill is the low predicted solubility of uranium in the hyperalkaline cement leachates (Yamamura et al., 1998). The alkali and alkali-earth uranates (e.g., $Na(UO_2)O(OH)\cdot(H_2O)_{0-1}$ and $CaUO_4$) are highly insoluble at elevated pH, so that aqueous U(VI) concentrations at pH 10 are predicted to be in the order of 10^{-9} M at equilibrium (Yamamura et al., 1998; Gorman-Lewis et al., 2008). The concentration of U(VI) in the CDZ is also expected to be low as a result of its adsorption to, and incorporation within, mineral phases, including the abundant cementitious materials present within the facility and silicate minerals in the host rock (Moyce et al., 2014). Several studies have observed that the introduction of hardened cement paste into a system containing aqueous U(VI) results in the removal of U from solution (Harfouche et al., 2006; Tits et al., 2008; Wieland et al., 2010; Tits et al., 2011; Macé et al., 2013). Macé et al. (2013) found that U(VI) uptake was controlled by sorption to C-S-H phases at pH 13.3. Both extended X-ray absorption fine structure spectroscopy (EXAFS ;Harfouche et al., 2006; Macé et al., 2013) and luminescence spectroscopy (Tits et al., 2011) have been used to probe the coordination environment of U associated with cement phases on reaction with aqueous U(VI) between pH 10 and 13.3. These studies concluded that the uranyl hydroxide species, $U(VI)O_2(OH)_4^{2-}$, was sorbed to the surface or incorporated into the interlayer of the C-S-H phases in a uranyl silicate, uranophane-like environment, when the initial aqueous U(VI) concentration was below ~ 0.5 mM. In

addition, at concentrations > ~ 0.5 mM U(VI), a Ca-uranate-like precipitate was also observed suggesting that precipitation of uranate phases controls U(VI) solubility at elevated concentrations (Macé et al., 2013). The Ca-uranate like environment has also been observed by Moroni and Glasser (1995), and Tits et al. (2008; 2011) over a variety of U(VI) concentrations.

U(VI) has also been shown to sorb strongly to a range of naturally occurring minerals likely present within the CDZ of a GDF. These include iron oxides (Moyes et al., 2000; Dodge et al., 2002), which have a high sorption capacity and are ubiquitous in the subsurface, as well as common rock forming silicates (Sylwester et al., 2000; Davis et al., 2004), and carbonates (Smith et al., 2015). The sorption of aqueous U(VI) on to biotite (Ames et al., 1983; Ilton et al., 2004; Brookshaw et al., 2015), chlorite (Singer et al., 2009; Brookshaw et al., 2015), orthoclase (Kerisit and Liu, 2014), and quartz (Froideval et al., 2003; Uyuşur et al., 2014) has been observed under ambient pH and low carbonate conditions, relevant to geological disposal. The presence of carbonate in the system can have a marked impact on the mobility of U(VI) as soluble uranyl-carbonate complexes can form, preventing sorption to, or incorporation within, mineral surfaces thereby maintaining U(VI) mobility (Grenthe et al., 1992; Pabalan and Turner, 1997; Murphy and Shock, 1999; Reeder et al., 2000). In fact, the concentration of aqueous carbonate will be low within the facility post closure since, under alkaline cementitious conditions, dissolved carbonate is expected to react with Ca leached from the cement and precipitate as calcite to a solubility limit of ~ 0.006 mM at pH 13.3 (Dow and Glasser, 2003; Smith et al., 2015). Aqueous U(VI) is therefore expected to be largely immobile both within and in the CDZ of a GDF as a result of adsorption and solubility constraints.

Interestingly, colloids are widely known to facilitate the transport of heavy metals (e.g. Hg, Ni, Co, Pb) in the subsurface in some systems (Lowry et al., 2004; Sen and Khilar, 2006; Bin et al., 2011) and have been implicated in the migration of uranium (Wang et al., 2013;

Bots et al., 2014; Smith et al., 2015) and plutonium (Kersting et al., 1999; Utsunomiya et al., 2009) in a range of engineered and natural environments. Intrinsic colloids comprised of radionuclides (Walther and Denecke, 2013), as well as mineral colloids with radionuclides bound to them, including cement derived colloids, have been reported (Gardiner et al., 1998; Wieland and Spieler, 2001; Missana et al., 2008). However, in order to facilitate radionuclide migration colloids must remain stable in solution, not aggregate, and/or become attached to surfaces. Recently, the formation of colloidal uranate-like nanoparticles (1 – 2 nm in diameter) has been identified in a pH 13.1 synthetic cement leachate equilibrated with 4.2 μM or 42 μM U(VI), when the solution was supersaturated with respect to sodium and calcium uranate phases (Bots et al., 2014). These colloids were shown to be stable in solution (in the absence of any other solid phase) for periods of > 2.5 years; stability was also observed in the presence of calcite for > 18 months (Smith et al., 2015). These observations have obvious ramifications for enhanced U transport in the deep subsurface. Reflecting this, here we investigate the stability of these colloidal U(VI) nanoparticles in a representative hyperalkaline young cement leachate (pH 13.3) in the presence of biotite, orthoclase, quartz, and cement. Biotite, orthoclase, and quartz were chosen as they are representative of common rock forming minerals expected in higher strength rock (a potential host geology for a GDF), while the cement phase was chosen since both structural cement and cementitious backfill will be abundant within an ILW disposal facility (Morris et al., 2011; NDA, 2014).

2. Materials and Methods

2.1. Solid Phases

Biotite was sourced from Silver Crater Mine, Canada. Orthoclase and quartz were sourced from the British Geological Survey. The single minerals were ground on a mechanical agate ball mill and sieved to obtain a 125-250 μm fraction which was isopropanol washed

prior to use in experiments. Mineral identification was confirmed using X-ray diffraction (XRD; Bruker D8Advance; Supporting Information Figure 1). Morphological characterisation of the mineral fractions was also conducted via scanning electron microscopy (SEM; FEI XL30 ESEM-FEG; Supporting Information Figure 2). Samples were prepared on standard 1 cm aluminium stubs with an adhesive carbon pad and carbon coated prior to imaging. The cement was made under CO_2 free conditions from Ordinary Portland Cement, limestone flour and hydrated lime in the wt:wt ratio 265:291:100 and reacted for 20 minutes. This material is representative of the backfill material used in the UK generic intermediate level safety case (Telchadder et al., 2012). The cement was then hydrated at a ratio of 1.8:1 (solid:water) and the mixture stirred for 3 hours prior to curing for 28 days. Once cured, the cement was crushed with a pestle and mortar under CO_2 free N_2 and sieved to < 63 μM prior to sorption experiments. The surface area of the prepared biotite, orthoclase, quartz, and cement was measured using N_2 Brunauer-Emmett-Teller (BET) analysis (Micromeritics Gemini V, with a Flowprep 060 sample degas system, Supporting Information Table 1). The experimental work described below was carried out under either a CO_2 free, or O_2 and CO_2 free (N_2), atmosphere as appropriate.

2.2. Young Cement Leachate and Uranium Colloid Preparation

Colloidal U(VI) nanoparticles were prepared in a pH 13.3 synthetic cement leachate representative of the young cement leachate expected in ILW disposal (Bots et al., 2014). Briefly, 5.19 g KOH (0.1 mol), 3.80 g NaOH (0.1 mol), and 10.1 mg $Ca(OH)_2$ (0.14 mmol) (all AnalaR grade) were dissolved in 1 L of degassed, deionised water (final pH 13.3 ± 0.1) and filtered to < 0.22 μm (PVDF filter). The young cement leachate was then spiked with a U(VI) stock solution (2.52 mM U(VI) in 0.001 M HCl) to a final concentration of 42 μM U(VI) (~ 10 mg L^{-1}) or 4.2 μM U(VI) (~ 1 mg L^{-1}) to generate stable colloidal U(VI) nanoparticles (Bots et al., 2014; Smith et al., 2015). Select experiments were run at

252 μM U(VI) where U(VI) phases have been shown to be oversaturated (Bots et al., 2014).

2.3. Uranium Colloid Reactions with Minerals and Cement

In all systems, the pH 13.3 young cement leachate containing U(VI) colloids was equilibrated for 24 hours prior to reaction with solids. Here, 10 g L^{-1} of the crushed, sieved, and washed single minerals biotite, orthoclase, and quartz were added to the colloid bearing solution and the pH of these experiments then remained stable throughout (within 0.1 pH units). Periodically, samples were removed from each experiment and centrifuged at 16000 *g* for 5 minutes. Solution samples were taken from the resulting supernatant and filtered (less than 0.45 μm; PES or nylon filters used). Solid samples for XRD and SEM were washed in isopropanol to remove any residual salt and dried in a desiccator under an O_2 and CO_2 free N_2 atmosphere prior to analysis.

For the cement system, the same pre-equilibrated, 10 g L^{-1} set up was used. Cement reaction experiments were run at three U(VI) concentrations, 4.2 μM and 42 μM (run in triplicate) where the U(VI) colloid was stable, and 252 μM U(VI) where U(VI) is oversaturated (Bots et al., 2014). To characterise the different colloidal fractions in the reacted solutions, solution samples were filtered using 0.22 μm, 0.10 μm, and 0.02 μm syringe filters (PVDF or Anotop), as well as collecting unfiltered settled solutions (Bots et al., 2014). Selected solid samples were also collected periodically after centrifugation at 16000 *g* for 5 minutes and prepared for SEM and XRD (as described in section 2.1). Samples for transmission electron microscopy (TEM) were also prepared by submerging C-SMART Plus TEM grids (Dune Sciences) in the suspension to be analysed followed by washing with isopropanol, and drying in a desiccator under an O_2 and CO_2 free N_2 atmosphere prior to characterisation.

The major cations in solution samples were analysed by inductively coupled plasma – atomic emission spectrometry (ICP-AES; Perkin Elmer 2400 DV) and total U by ICP – mass spectrometry (ICP-MS; Agilent 7500cx). PHREEQC (Parkhurst and Appelo, 2013) was used to model the expected thermodynamic speciation of U(VI) in the experimental systems. The ANDRA SIT (ThermoChimie v.8.0 September 2011) database which included the relevant sodium and calcium uranate phases (O'Hare et al., 1976), as well as clarkeite and becquerelite (Gorman-Lewis et al., 2008), was used for all thermodynamic calculations across all U concentration discussed.

2.4 Trace Uranium Reaction with Cement

Batch experiments were also performed at trace uranium concentrations ([U(VI)] = 2.0×10^{-10} M) using the radiotracer ^{232}U. Reactions were completed at two solid : solution ratios, 5 and 20 g L^{-1}. The surface area was measured using N_2 BET analysis (Micromeritics Gemini V, with a Flowprep 060 sample degas system, Supporting Information Table 1). All of the trace U experiments were performed using water which had been pre-equilibrated with cement for 24 hours. The solutions were sampled following centrifugation (15000 *g*; 5 minutes; approximately equivalent to filtration with a 0.5 µm pore size filter). The U concentrations were then measured using a Quantulus 1220 liquid scintillation counter. Etylenediaminetetraacetic (EDTA) concentrations were measured using UV-visible spectroscopy (Cary Varian 500 scan UV-Vis-nIR Spectrophotmeter; range 200-800 nm; typical scan rate 600 nm min^{-1}) (Telchadder et al., 2012). Post reaction, the solution phase was analysed for size fractionation using a Millipore device attached to a nitrogen cylinder, according to the technique of Pitois et al. (2008) with membranes of pore size 100, 10 and 3 kDa (approximately equivalent to 3.1, 1.4 and 0.9 nm, respectively). Before use, the reaction cell and the membranes were washed repeatedly with deionized water and pre-treated with 10^{-4} M $Eu(NO_3)_3$ solution to saturate the

membrane sorption sites to prevent artefacts associated with sorption of radionuclides (Pitois et al., 2008). Experiments were also performed with EDTA to give final concentrations of 0.001 or 0.1 M of the complexant. In some experiments, the ligand was allowed to equilibrate with the U(VI) before the introduction of cement, whilst in others, the U(VI) was added to the cement prior to the addition of the ligand.

2.6. Characterisation of Uranium Interactions with Solids

2.6.1 Luminescence Spectroscopy

Cement (10 g L^{-1}) and portlandite (as a standard) were added to pre-equilibrated young cement leachate containing U(VI) (42 μM), this was allowed to react for 24 hours before separation of the solid phases prior to luminescence spectroscopy analysis to probe the U(VI) speciation. Steady-state emission spectra were recorded in Young's tap appended quartz cuvettes on an Edinburgh Instrument FP920 Phosphorescence Lifetime Spectrometer. The system was equipped with a 5 watt microsecond pulsed xenon flashlamp (with single 300 mm focal length excitation and emission monochromators in Czerny Turner configuration) and a red sensitive photomultiplier in a Peltier (air cooled) housing (Hamamatsu R928P) at 77 K, using a liquid nitrogen cooled Edinburgh Instruments cryo-dewar. A delay and gate were applied during emission measurements where indicated. Lifetime data were recorded following 375 nm and 405 nm excitation with an EPL 375 and EPL 405 picosecond pulsed diode laser (Edinburgh Instruments), using time correlated single photon counting (PCS900 plug-in PC card for fast photon counting). Lifetimes were obtained by a tail fit on the data or by a reconvolution fit using a solution of Ludox in water as the scatterer, and the quality of fit judged by minimization of reduced chi-squared and residuals squared.

2.6.2. X-ray Absorption Spectroscopy

In samples run at 42 μM U(VI) from 1 and 21 months exposure to cement where uranium removal had occurred, solids were collected for X-ray Absorption Spectroscopy (XAS) analysis. Samples were prepared by centrifuging (6000 *g* for 5 minutes) to obtain a mineral paste with a U-loading of approximately 1000 mg kg^{-1}. The paste was then mounted under CO_2 free Ar atmosphere in a double contained, air-tight XAS sample cell and stored at - 80^{o}C prior to analysis. Analysis was performed at beamline B18 at Diamond Light Source on the U-L_{III} absorption edge using a Si(111) monochromator with samples maintained at liquid nitrogen temperature. Samples were analysed in fluorescence mode using a 9 or 36 element Ge detector with an in-line Y-reference used for energy calibration. Background subtraction, data normalisation, and fitting of the EXAFS were performed using the Demeter software package (Ravel and Newville, 2005). During fitting, FEFF 6 was used to calculate structural models of Ca-uranate (Loopstra and Rietveld, 1969), clarkeite (Finch and Ewing, 1997) and α-uranophane (Viswanathan and Harneit, 1986) from their crystal structures. Typically, data were fitted over a k-range of 3 – 13.3 $Å^{-1}$. The Hanning window function was used and all data were fitted in R-space (typical range, 1.25 – 4 Å).

2.6.3. Electron Microscopy

Cement which had been exposed to synthetic young cement leachate containing 42 μM U(VI) colloids for 21 months was examined using SEM. The SEM images were collected on an FEI XL30 ESEM-FEG using backscatter electron imaging, equipped with an Oxford Instruments Inca EDX. SEM samples were mounted on a carbon pad, carbon coated and imaged.

A sample of biotite exposed to young cement leachate containing 42 µM U(VI) was suspended in isopropanol, loaded on to a copper-coated TEM grid with holey-carbon, and the isopropanol was then allowed to evaporate prior to analysis using TEM. TEM images were collected using a Philips CM200 field emission gun TEM/STEM (FEGTEM) with Supertwin Objective lens, cryoshield, Oxford Instruments Inca EDX system and Gatan Imagaing Filter. Images were analysed using the processing software ImageJ (Abramoff et al., 2004).

3. Results and Discussion

3.1. U(VI) Colloid Stability in the Presence of Biotite, Orthoclase, and Quartz

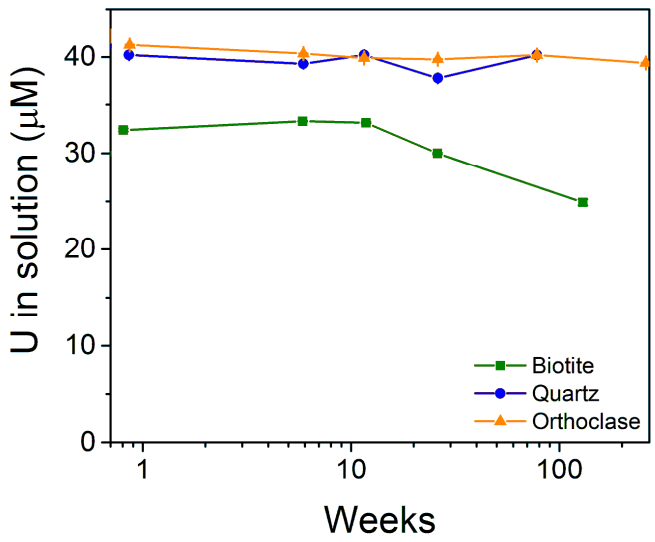

Figure 1. Concentration of uranium remaining in solution (< 0.45 µm) after biotite (■), orthoclase (▲), and quartz (●) were added to young cement leachate containing 42 µM U(VI). Error bars are 1σ from three replicates. Where not visible, error bars are within the symbol size.

To assess the stability of U(VI) colloids in contact with common rock forming minerals, U(VI) colloid bearing young cement leachate (Bots et al., 2014) was reacted with biotite, orthoclase, and quartz (1 : 100 solid : solution ratio) for up to 250 weeks under controlled conditions (Figure 1). Throughout, the majority of the U(VI) remained filterable (< 0.45 µm) when in contact with the minerals over extended periods (Figure 1). This indicates that reaction of the colloidal uranium nanoparticles with the solid phases was limited and indicates the U(VI) remained stable in solution as a colloidal phase. Interestingly, in the case of biotite, approximately 20 % (7 µM) of the U(VI) was removed from the filterable fraction after 2.5 years contact (Figure 1).

	Initial (mM)	Final time point after equilibration with biotite (mM)	Final time point after equilibration with orthoclase (mM)	Final time point after equilibration with quartz (mM)	After 10 minutes equilibration with cement (mM)	After 1 month equilibration with cement (mM)	After 21 months equilibration with cement (mM)
Na	91.1	109	83.7	83.3	78.0 ±0.8	75.7 ± 0.6	75.1
K	75.8	93.1	117	117	65.7 ± 0.6	65.4 ± 0.4	63.3
Ca	0.13	0.066	0.032	0.001	1.4 ± 0.02	1.5 ± 0.06	1.10
Al	-	0.078	0.45	0.044	-	-	0.078
Si	0.08	4.51	1.63	14.8	13.9 ± 2.5	11.4 ± 2.0	0.161

Table 1. Comparison of the initial young cement leachate composition with that measured by ICP-AES after equilibration with 10 g L^{-1} biotite, orthoclase, quartz, and cement after filtration (< 0.45 µm). Errors are 1σ from three replicates.

In filtered samples taken from pure mineral systems, the young cement leachate Na and K concentrations remained relatively stable (100 ± 18 mM; Table 1) throughout the experiment. However, in all reacted systems, increased concentrations of Si and Al were observed compared to the young cement leachate (Table 1) suggesting that partial dissolution of all three minerals occurred. Despite these bulk changes, in the orthoclase and quartz experiments no removal of U(VI) was observed from the filterable (< 0.45 µm) fraction. This suggests that in these systems, U(VI) colloid stability was not significantly

affected by Si and Al dissolution. The Ca concentrations decreased significantly from 0.14 mM in the young cement leachate to 0.07, 0.03, and 0.001 mM in the biotite, orthoclase, and quartz systems, respectively. This is consistent with either the sorption of Ca to the mineral phase (Schaefer, 1991) or the precipitation of Ca containing phase(s) from solution (Heberling et al., 2008). Again, the removal of Ca did not significantly influence U(VI) colloid behaviour in the orthoclase and quartz fractions.

During reaction, the U(VI) was present as uranate-like colloids which are expected to be much more negatively charged than the aqueous $UO_2(OH)_4^{2-}$ species (Bots et al., 2014). This significant change in U(VI) speciation presumably explains the contrast between the poor reactivity of the U(VI) colloidal phase with the single mineral phases observed in our systems compared to parallel studies at ambient pH where aqueous uranyl species will dominate. The sorption of U(VI) to biotite (Ilton et al., 2004; Brookshaw et al., 2015), orthoclase (Arnold et al., 1998; Walter et al., 2005; Nebelung and Brendler, 2010), and quartz (Arnold et al., 1998; Arnold et al., 2001) has previously been observed at circumneutral pH. Up to pH 9.5 under low carbonate (< 3 ppm) conditions, the sorption of aqueous U(VI) to quartz has been observed from solutions with initial U(VI) concentrations of 0.2 μM (Prikryl et al., 2001), despite the formation of negatively charged U(VI) solution species $(UO_2(OH)_3)^-$ and $(UO_2(CO_3)_3)^{4-}$ which will be subject to electrostatic repulsion from the surface. Aqueous U(VI) sorption to biotite (Yoshida, 1994) and orthoclase (Kerisit and Liu, 2014) is also anticipated at modestly high pH (~ 9) under both low and atmospheric carbonate conditions, respectively. This is despite the dominance of negatively charged uranyl hydroxide $(UO_2(OH)_3)^-$ and $((UO_2)_3(OH)_7)^-$ and carbonate $(UO_2(CO_3)_3)^{4-}$ and $(UO_2(CO_3)_2)^{2-}$ species in these systems, which are expected to undergo electrostatic repulsion from the biotite, orthoclase, and quartz surfaces which are also predicted to be negatively charged (point of zero charge: ~ 2, < 1, and ~ 7, respectively; Butler and Ginley, 1978; Vochten et al., 1991; Olin et al., 2006; Kosmulski,

2009; Kosmulski, 2012; Bots et al., 2014). In aqueous systems reaction with the negatively charged mineral surface is expected to occur via the positively charged $UO_2^{2+}{}_{(aq)}$ species, with which the dominant negatively charged species will be in equilibrium (Prikryl et al., 2001). However, our experiments have been designed to investigate the reaction of colloids with mineral surfaces and therefore U(VI) colloids are expected to be the reactive species. Colloidal U(VI) is expected to be more negatively charged than the aqueous U(VI) species (Bots et al., 2014). This is consistent with the experimental data and suggests there is sufficient electrostatic repulsion to prevent sorption to the mineral surfaces as observed in past work in these colloid dominated systems (Smith et al., 2015). Overall, the detection of uranium in the filtered fraction after contact with biotite (2.5 years), orthoclase (5 years), and quartz (1.5 years) demonstrates long term stability of the U(VI) colloidal phase despite some dissolution / reprecipitation of the minerals as evidenced by the removal of Ca from solution and the release of Si and Al observed over the course of the reaction (Table 1). The detection of uranium in the filtered fraction after 5 years contact with orthoclase also extends the period of U(VI) colloid stability probed by Bots et al. (2014).

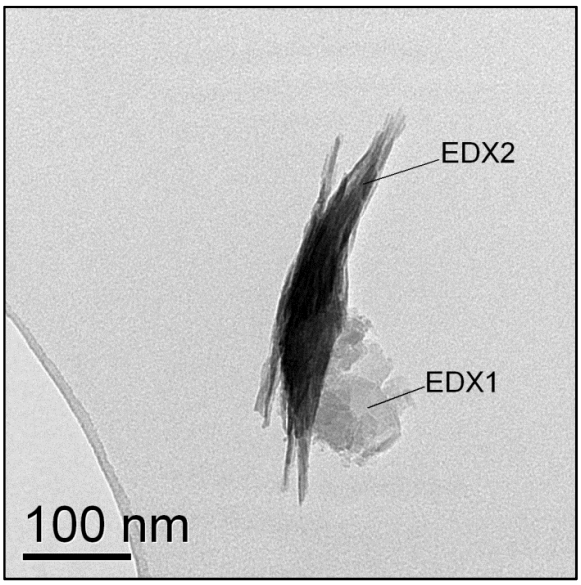

Figure 2. TEM image of a U rich area of the biotite fines after contact with young cement leachate containing 42 µM U(VI) (see Supporting Information Figure 3 for EDX).

Interestingly, while the majority (~ 80 %, 25 μM) of the U(VI) remained filterable (< 0.45 μm) when the colloid was contacted with biotite, ~ 20 % was slowly removed from solution over the course of the experiment (2.5 years; Figure 1). In a sample taken at 18 months, ~ 20 % of the U(VI) colloid had been removed from solution and the reacted biotite was characterised using TEM (Figure 2). Here, energy dispersive X-ray spectroscopy (EDX) showed discrete uranium rich areas within the biotite fines with co-location of U, Fe and Ca (EDX2; Supporting Information Figure 3). The precipitation of U(VI) as Ca-uranate like phase from the biotite containing experiment was stoichiometrically possible (33 – 25 μM U and 130 – 66 μM Ca). Indeed, precipitation of Ca uranate has previously been observed from solutions at pH > 13 (Macé et al., 2013; Smith et al., 2015) with precipitation occurring only in the presence of mineral surfaces (Macé et al., 2013; Smith et al., 2015). However, the precipitation of Ca-uranate seems unlikely to control U(VI) sorption to biotite for two reasons: firstly, in the systems containing orthoclase and quartz, Ca removal occurred but U(VI) was not removed; secondly, the removal of Ca and U(VI) in the biotite system was not clearly correlated (Figure 1 Supporting Information Figure 4). Alternatively, the modest U(VI) removal in biotite may be explained by reductive precipitation of U(VI) to poorly soluble U(IV) via reaction with Fe(II). Here, the slow reduction of U(VI), and the subsequent precipitation or sorption of poorly soluble U(IV) phases has previously been observed in systems containing biotite (Ilton et al., 2004; Ilton et al., 2006; Brookshaw et al., 2015). Overall, removal of a small fraction of U(VI) occurred in the biotite systems forming discreet U, Ca and Fe rich areas in the biotite with both Ca-uranate precipitation and U(VI) reduction possible pathways for this process.

3.2 U(VI) Colloid Stability in the Presence of Cement

3.2.1. Changes in Solution Chemistry in the Cement Systems

The stability of the U(VI) colloids was also assessed in the presence of cement by introducing a solid cement phase to the U(VI) colloid bearing young cement leachate. Past work has shown under these conditions and in young cement leachate the U(VI) colloids consisted of primary particles 1 – 2 nm in diameter which were persistent over 2.5 years (Bots et al., 2014). In systems assessing the reaction of U(VI) colloids with solid cement, filtration was performed using 0.02 µm, 0.10 µm, and 0.22 µm filters to explore the nature of the solution phase more fully. The concentration of U(VI) in all filtrates was essentially the same within error, thus only the < 0.02 µm fraction is fully discussed here (major cation data are supplied in Supporting Information Figure 5 and full U data in Supporting Information Figure 6).

The addition of the solid cement to the U(VI) colloid bearing young cement leachate altered the porewater chemistry within the first 10 minutes of reaction. Compared to the initial leachate, the Ca concentration increased 10 fold, from 0.13 mM to 1.40 ± 0.02 mM, and the concentration of Si increased from 0.02 mM to 13.9 ± 2.5 mM (Table 1; Supporting Information Figure 5). Over the same period the Na and K concentrations both decreased by ~ 15 % (from 91.1 to 87.0 ± 0.8 mM, and from 75.8 to 65.7 ± 0.4 mM, respectively). The increase in Ca concentration was presumably as result of the rapid dissolution of portlandite ($Ca(OH)_2$) within the cement matrix (Berner, 1992), while the elevated Si concentration is typical of a solution in equilibrium with a cement phase in which rapid and partial dissolution of C-S-H phases has occurred (Berner, 1992). Following this initial reactivity, the Ca and Si porewater chemistry then remained stable from 10 minutes to 1 month with respect to K, Na, Ca, Al, and Si concentrations. In order to investigate long term behaviour in this system, a further time point was also taken after 21 months. Between 1 and 21 months, Na, K, and Al concentrations remained constant, the

Ca decreased slightly (from 1.5 to 1.1 mM), and there was a significant reduction in the Si concentration (from 11.4 to 0.16 mM; Table 1 and Supporting Information Figure 5). The decrease in the concentration of Ca and Si between 1 and 21 months suggests the precipitation of Ca / Si containing phases, which has been widely observed under hyperalkaline conditions (Tang et al., 1995; Moyce et al., 2014; Nakashima et al., 2014; Fernández et al., 2016).

3.2.1.1. Thermodynamic Calculations

To further understand the U(VI) behaviour in the cement system, a series of thermodynamic modelling calculations using PHREEQC (V3.3.7) (Parkhurst and Appelo, 2013) were run using the ANDRA SIT (ThermoChimie v.8.0 September 2011) database. In the high pH (13.3) young cement leachate, U(VI) (4.2 – 252 μM) is predicted to be supersaturated with respect to several calcium and sodium uranate phases including Ca-uranate ($CaUO_{4(cr)}$); clarkeite ($NaUO_2O(OH)\cdot(H_2O)_{0\text{-}1}$); and $Na_2U_2O_7$ (Supporting Information Table 2). The solution composition was then re-modelled with the evolved young cement leachate composition after 10 minutes, 1 month, and 21 months reaction with cement. Under these conditions $CaUO_{4(cr)}$, clarkeite, and $Na_2U_2O_7$ remained supersaturated at all time-points and, interestingly, uranophane, a U(VI) silicate phase relevant in cementitious systems (Macé et al., 2013), was also supersaturated after 10 minutes and 1 month of reaction. However, after 21 months of reaction the observed decrease in the aqueous Si concentration in the reacted systems (Table 1) meant that uranophane was no longer predicted to be supersaturated. Since uranophane, which contains uranium in a uranyl coordination environment, is supersaturated at shorter time-points, these modelling data indicate that uranium phases containing uranium in both uranate and uranyl coordination environments (*e.g.* Ca-uranate, clarkeite, $Na_2U_2O_7$, and uranophane) are possible in these systems. For the single mineral phase solutions for

biotite, orthoclase, and quartz at the end of reaction where only limited U(VI) removal (< 20 %) was observed, PHREEQC calculations found that uranophane was undersaturated whilst clarkeite and Ca-uranate were predicted to be supersaturated (Supporting Information Table 3). Overall the thermodynamic modelling data suggest that uranophane is supersaturated in the cement system at shorter timepoints but becomes undersaturated between 1 and 21 months of reaction. This indicates that U(VI) could be present in a uranyl like coordination environment as a uranophane precipitate, or sorbed or incorporated within C-S-H phases, as previously observed in the literature (Zhao et al., 2000; Harfouche et al., 2006; Tits et al., 2011; Macé et al., 2013; Tits et al., 2014).

3.2.2. U(VI) Filtration Results

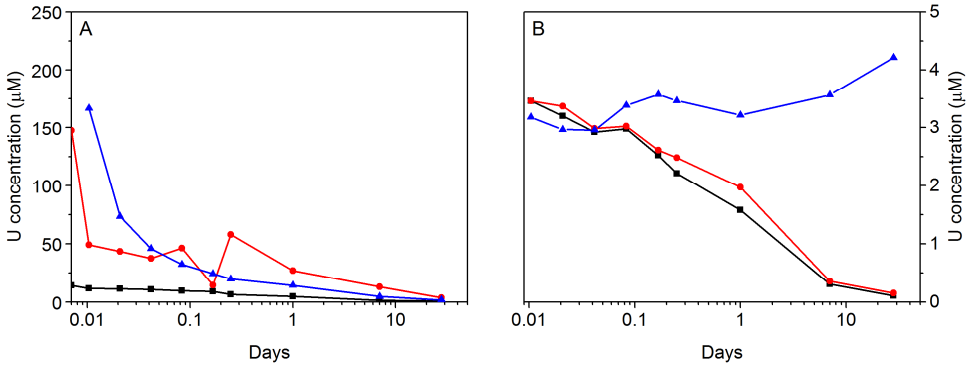

Figure 3. Concentration of uranium remaining in young cement leachate equilibrated with A = 252 µM U(VI) and B = 4.2 µM U(VI) and then exposed to 10 g L^{-1} cement; ■ = 0.02 µm filtered; ● = unfiltered; ▲ = 0.02 µm filtered control containing no cement.

When a solution containing 252 µM U(VI) was contacted with cement, significant (94.3 %) removal of U(VI) occurred during the 24 hour equilibration without mineral present with only 1.0 µM U(VI) remaining filterable (< 0.02, < 0.10, and < 0.22 µm) after 28 days (Figure 3A). This is similar to the behaviour of the control experiment with no

cement, where 1.9 µM U(VI) was filterable (< 0.02 µm) after 28 days (Figure 3A), and showed comparable kinetics. Past work in parallel systems at 252 µM U(VI) documented a similar drop in filterable (< 0.02 µm) U(VI) which was due to the formation and aggregation of a clarkeite-like precipitate (Bots et al., 2014). Thus, in the cement system at 252 µM U(VI), solution data from the current experiments suggest precipitation of an oversaturated uranate-like phase similar to that observed in Bots et al. (2014), rather than any significantly enhanced reactivity with the cement surfaces (Figure 3). Interestingly, thermodynamic calculations using the evolved young cement leachate composition at 1 month showed that the filterable (< 0.02 µm) solutions, which contained 1.0 µM U(VI) at the experimental end point, remained supersaturated with respect to the uranate phases, clarkeite and Ca-uranate (Supporting Information Table 2). This implies even after significant U(VI) removal to solids, the evolved solution was supersaturated with respect to clarkeite and Ca-uranate and therefore likely contains U(VI) colloids.

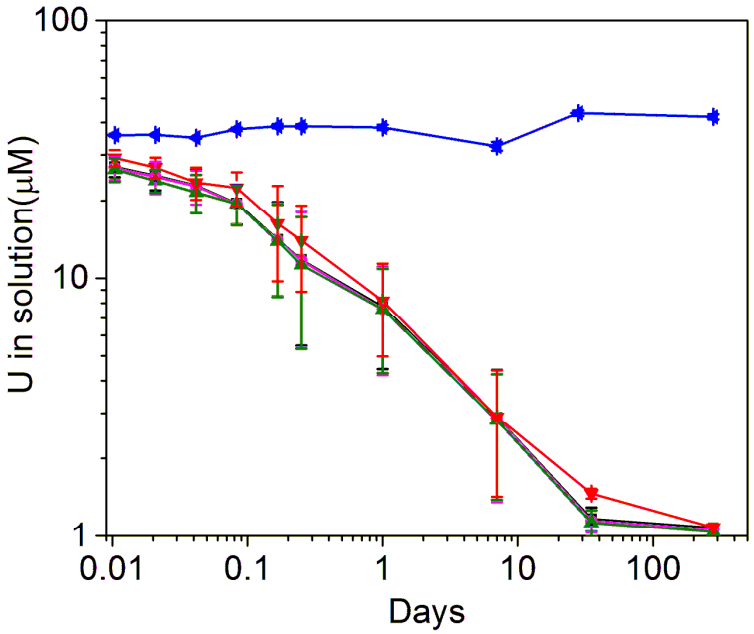

Figure 4. Concentration of uranium remaining in young cement leachate containing 42 µM U(VI) in contact with cement; ■ = 0.02 µm filtered, ● = 0.1 µm filtered, ▲ = 0.22 µm filtered, ▼ = unfiltered, ◀ = 0.02 µm filtered control containing no cement. Error bars are 1σ from three replicates.

In the experiments containing 4.2 μM U(VI), reaction with the cement again lead to significant reduction in the filterable (< 0.02, < 0.10, and < 0.22 μm) U(VI) concentration, with only 0.1 μM U(VI) remaining after 28 days in all three filtrates (Figure 4B). A similar reduction in the filterable (< 0.02 μm) U(VI) concentration was observed in systems containing 42 μM U(VI), where 1.2 ± 0.1 μM U(VI) remained filterable in all three filtrates after 28 days of reaction. Over 21 months this U concentration then remained constant (Figure 4B). Reaction of the U(VI)-colloids with cement led to significant removal of U from the filtrates in the 4.2 and 42 μM U(VI) systems. However, the U(VI) concentrations remaining filterable, after extended reaction in these systems (0.1 and 1.2 ± 0.1 μM, respectively), were still elevated (100 – 1000 fold) compared to the thermodynamically predicted solubility of alkaline earth uranates of ~ 1 nM anticipated in a high pH (10 – 13) cement leachate (Supporting Information Table 2) (Yamamura et al., 1998; Gorman-Lewis et al., 2008; Bots et al., 2014). This predicted oversaturation again suggests that the filterable U(VI) was likely present as U(VI)-colloids. Overall, despite the significantly enhanced reactivity of the U(VI) colloid to cement compared to biotite, orthoclase, and quartz, the filtration results suggest that U(VI) colloids are persistent in the < 0.02 μm filterable fraction over extended times. This has important implications for U-solubility in conditions relevant to geological disposal.

The removal of U(VI) from the < 0.02 μm filterable fraction in the 4.2 μM and 42 μM U(VI) systems is attributed to enhanced reactivity in the cement systems either through the cement dissolution altering porewater chemistry and/or the minerals providing surfaces for reaction. This is because, in the absence of any mineral surface, 42 μM U(VI) remained filterable (< 0.02 μm) over 2.5 years (Bots et al., 2014) and in systems containing calcite (Smith et al., 2015), orthoclase, and quartz (this study) no significant removal occurred. The enhanced reactivity of the U(VI)-colloids with the cement phase could be due to the higher point of zero charge of C-S-H phases (~ pH 10), compared to that of orthoclase and

quartz (< 1 and ~ 7, respectively) (Diamond et al., 1963; Butler and Ginley, 1978; Vochten et al., 1991; Kosmulski, 2009; Kosmulski, 2012). At pH 13.3, cement would be expected to have a lower net negative charge than the single mineral phases investigated. Since the U(VI)-colloids are also expected to be negatively charged at pH 13.3 (Bots et al., 2014), a lower net negative charge on the mineral surface would be expected to reduce the electrostatic repulsion between the U(VI)-colloids and the mineral surface, potentially enhancing reactivity.

In terms of the bulk chemistry of the 42 µM U(VI) cement system between 1 and 21 months of reaction, the filterable (< 0.02 µm) Ca and Si concentrations decreased (Table 1; section 3.2.1). This suggests the precipitation of Ca / Si containing phases was occurring, which is consistent with past work in hyperalkaline systems (Tang et al., 1995; Nakashima et al., 2014; Fernández et al., 2016). However, the majority of the U(VI) (97 %, 40.8 µM) was removed within the first month (Figure 4), during which time the porewater concentration of Ca and Si remained relatively elevated. In fact, as the Ca and Si concentrations are in significant excess compared to the U(VI) concentrations (Table 1), it is difficult to determine whether the removal of either of these elements from the filterable (0.02 µm) fraction coincides with that of uranium. Certainly at bulk scale the U(VI) and Ca removal do not seem to correlate. The removal of colloidal U(VI) as Ca-uranate, from a pH 10.5 cement leachate, has previously been observed in the presence of both a calcite surface and increased (200 µM) Ca porewater concentrations (Smith et al., 2015). In the absence of the calcite surface the U(VI) remained stable in solution at pH 10.5. In cement leachate with a comparable composition to the initial young cement leachate investigated in this study (pH 13.3., 135 µM Ca), no U(VI) was removed from solution in the presence of calcite (Smith et al., 2015). This suggests that both the increased Ca concentration due to portlandite dissolution and the calcite surface are required for Ca-uranate formation (Smith et al., 2015). In our system, the removal of U(VI) from the filterable (< 0.02 µm)

fraction was similarly slow, presumably due to only the small fraction of truly dissolved U(VI) being able to react (Smith et al., 2015). Interestingly, U(VI) remained filterable in contact with orthoclase and quartz for at least 18 months (Figure 1), suggesting the that type of surface present is also important.

3.2.3 Trace ^{232}Uranium Reaction with Cement

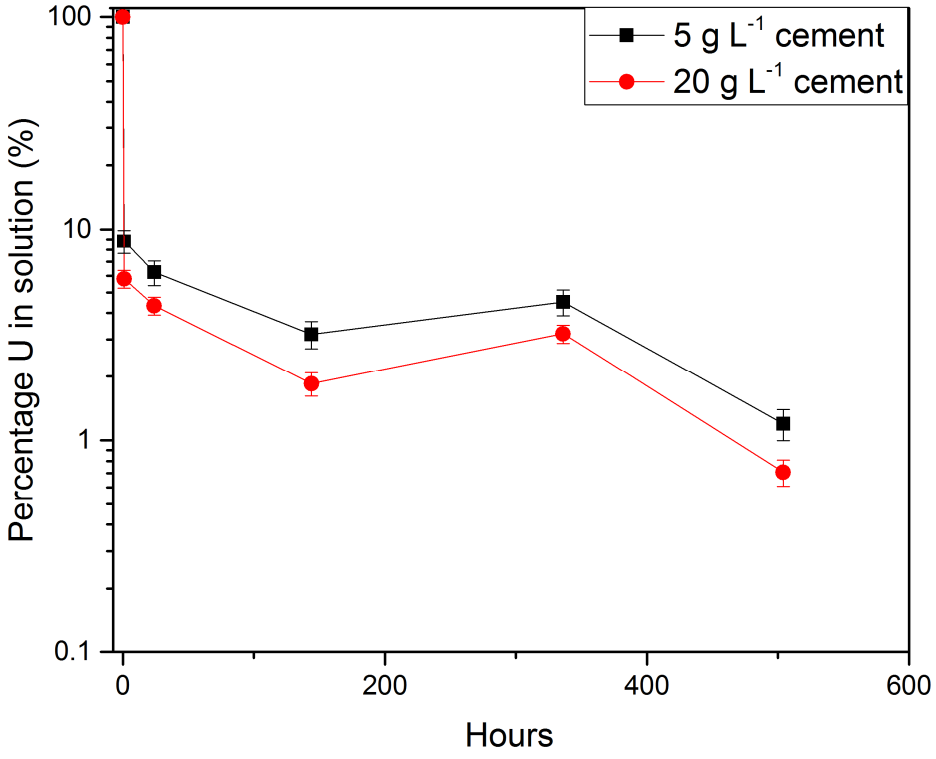

Figure 5. Percentage of $U^{232}_{(aq)}$ remaining in solution after contact with cement ($[U_T] = 2.0 \times 10^{-10}$ M). Error bars are 1σ from three replicates.

^{232}U(VI) was used to further explore the behaviour of U(VI) with cement at ultra-trace concentrations (2.0×10^{-10} M). Figure 5 shows the percentage of ^{232}U(VI) remaining in solution after centrifugation (nominally < 0.5 µm filtration) plotted vs. equilibration time. U(VI) was removed from solution rapidly, and only small quantities (< 4 %) could be detected in solution after 48 hours. Within the narrow range studied here (5 – 20 g L^{-1}), the

solid:solution ratio did not appear to make a large difference to the concentration of U(VI) remaining in solution. However, when the cement was removed from the experiment before the addition of ^{232}U(VI), the majority of the uranium (98 %) remained in solution, showing that the presence of the surface was required to promote U(VI) association with the solid phase, presumably by either surface complexation and/or surface precipitation. After reaction with cement, the supernatant was ultra-filtered to separate different fractions (100, 10, and 3 kDa PES membranes). The results showed that 79 % of the U(VI) in the solution phase was present as clusters or colloidal material (i.e. > 3 kDa fractions, nominally greater than ~1 nm) with only 21 % present as free ions in solution (< 3 kDa, nominally less than ~ 1 nm). Indeed, the majority of the U(VI) (78 %) was present in the 3 – 10 kDa (nominally 0.9 – 1.4 nm) colloidal fraction. Hence, even at the much lower U(VI) concentrations explored with the ^{232}U spike these data suggest the solution phase was still dominated by colloids.

PHREEQC (V3.3.7) (Parkhurst and Appelo, 2013) modelling and the ANDRA SIT (ThermoChimie v.8.0 September 2011) database were used to interpret the solubility of the U(VI) in the tracer experiments. Here, results showed that even at ultra-trace concentrations, the system was supersaturated with respect to Ca-uranate ($CaUO_{4(cr)}$, saturation index +3.96). Interestingly, unlike the cement leachate containing > 4.2 µM U(VI), uranophane was undersaturated at trace (10^{-10} M) concentrations, suggesting that any uranophane-like coordination environments observed in these ultra-trace systems were due to sorption rather than precipitation. The ultrafiltration data show that the majority of the U(VI) remaining in solution after reaction with cement was found in the smallest colloidal fraction (3 – 10 kDa, 78%). The combined modelling and ultrafiltration results, coupled to the recent work of (Bots et al., 2014), suggest that a uranate-like phase is expected to form presumably as a colloidal phase. When a cementitious surface is present, it seems that these colloids are destabilised and similar to the work at higher U

concentrations, U(VI) becomes reactive to the cement phases. For the U(VI) that did remain in true solution, the speciation was predicted to be dominated by just two species ($UO_2(OH)_4^{2-}$, 84 %; $UO_2(OH)_3^-$, 16 %), with negligible contributions from carbonate complexes. However, the ultrafiltration and speciation modelling suggest that the most important competitor for sorption on the cement is likely to be colloids even at these ultra-trace U(VI) concentrations.

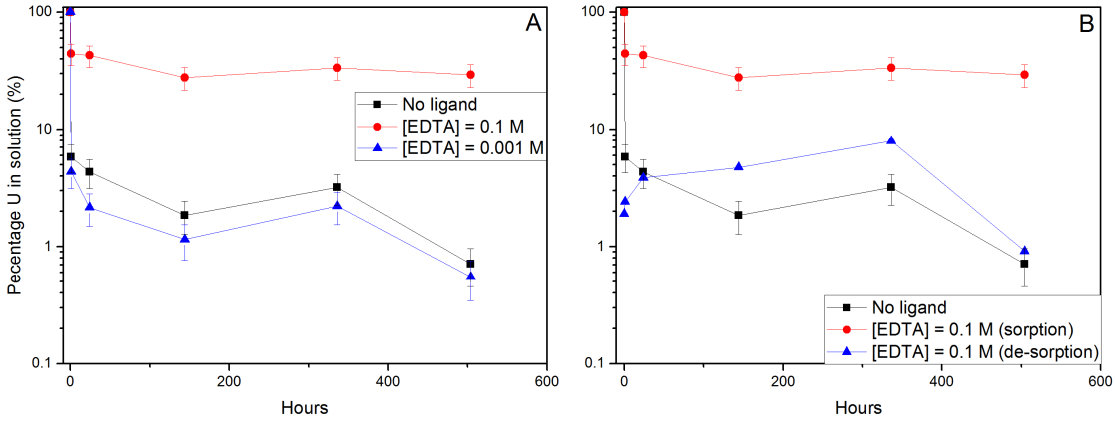

Figure 6. Effect of EDTA on the sorption of ^{232}U to cement (20 g L^{-1}, $[U_T] = 2.0 \times 10^{-10}$ M); (A) effect of EDTA on sorption; (B) comparison of sorption and desorption. Error bars are 1σ from three replicates.

To determine the extent of reversibility of ^{232}U sorption to cement, a series of experiments using EDTA as a competing ligand were performed. No significant sorption of EDTA to cement was detected in the experiments. Figure 6A shows the change in solution phase U(VI) concentration with time as a function of EDTA concentration at a solid:solution ratio of 20 g L^{-1}. In this experiment, the U(VI) and EDTA were allowed to equilibrate prior to the introduction of the cement. The amount of U(VI) remaining in solution increases with increasing EDTA concentration with essentially no enhanced solubility observed for the 0.001 M and 0.01 M EDTA experiments, and with up to 29 % solubility for 0.1 M EDTA.

To determine the reversibility of U(VI) association with the cement phases in the experimental systems, uranyl was pre-equilibrated with cement (20 g L^{-1}) for 48 hours before the addition of EDTA (0.1 M) (Figure 6B). There was a slight temporary enhancement in the solution U(VI) concentration accompanying the addition of EDTA, but this subsequently decreased, and by the end of the experiment, the solution U(VI) concentration was within error of that for the system with no EDTA. The reason for the short-term increase in U(VI) concentration is uncertain, but is probably due to the transient suspension of cement particles following the sudden change in solution chemistry or to the physical disturbance of the system associated with the replacement of the solution. The most significant result is that in the U(VI) uptake experiment, 0.1 M EDTA suppressed U(VI) reaction with the cement. However, when the same concentration of 0.1 M EDTA was added once the U(VI) had become associated with the cement phase, it did not reverse this uptake process. This suggests that the vast majority of U(VI) was irreversibly bound to the cement in the experiments. The origin of the irreversibility cannot be deduced from the batch experimental data. However, it is unlikely to be due to the formation of simple surface complexes, since these should be available for exchange with the solution. It is more likely that the irreversibility is due to the precipitation of a uranium containing phase, in agreement with PHREEQC calculations which also suggested the supersaturation and precipitation of U(VI) phases is possible.

PHREEQC calculations were performed to predict the effect of EDTA on the uranium speciation. The EDTA was predicted not to compete with hydroxide as a uranyl ligand, even at the highest EDTA concentration (0.1 M), where the uranyl EDTA complex accounts for only 3.3×10^{-7} % of the aqueous U(VI), because of competition for EDTA binding from Ca^{2+}. However, PHREEQC does predict an effect on U(VI) solubility, since EDTA is predicted to complex very effectively with Ca^{2+}, reducing the free calcium concentration. The result is that $CaUO_{4(cr)}$ is no longer predicted to be supersaturated.

However, for the lower EDTA concentrations (0.01 and 0.001 M), $CaUO_{4(cr)}$ was still supersaturated, as the EDTA concentration was still too low to suppress the calcium concentration sufficiently. Hence, the speciation predictions are qualitatively consistent with the experimental observations (Figure 6), since 0.1 M EDTA was able to prevent the removal of uranium from solution, whilst the lower concentrations were not: the speciation calculations suggest that the higher concentration could prevent $CaUO_4$ precipitation because of Ca-EDTA complexation, whilst the lower concentrations will not. Hence, the behaviour in the EDTA experiments may be interpreted in terms of a competition between colloid formation in solution and (irreversible) association with the solid.

3.2.4. Luminescence Spectroscopy of Cement Systems

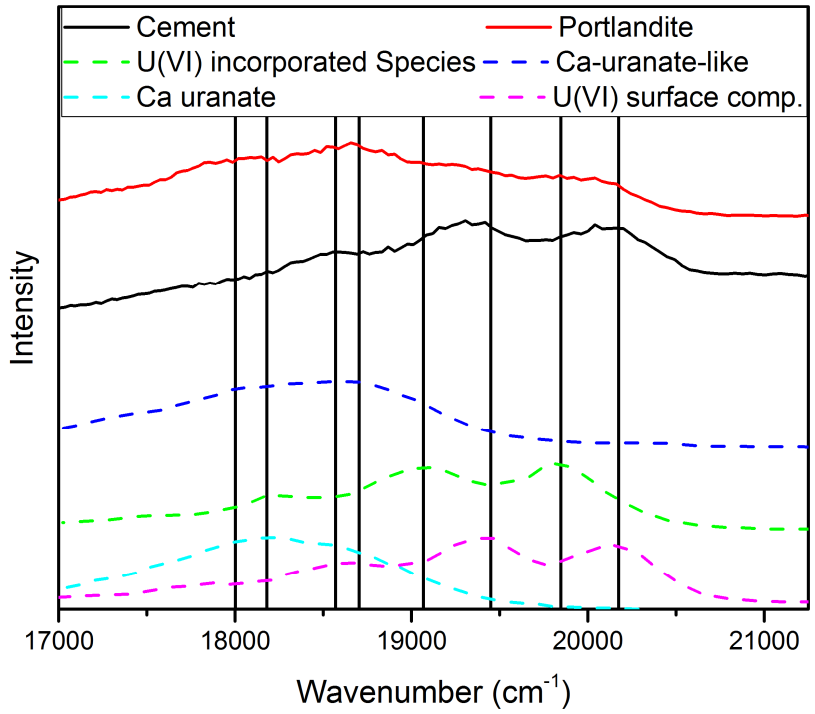

Figure 7. Luminescence data (solid lines) and literature standards from Tits et al. (2011) (dashed lines) of solid phases (10 g L^{-1}) equilibrated with a U(VI) solution (4.2 µM) for 24 hours.

Figure 7 shows the spectra for trace concentrations of U(VI) (4.20 μM) associated with cement and portlandite after 24 hours of reaction. Relevant U(VI) standards (Tits et al., 2011) are also plotted for comparison. The portlandite sample shows the presence of a Ca-uranate-like species. However, there is also an additional feature which does not appear in the Ca-uranate standard, and is located in the region where a surface complexed or incorporated uranyl species would be expected (Tits et al., 2011). The uptake of U(VI) by C-S-H component of cement has previously been observed by Tits et al. (2011) and Aggarwal et al. (1990). Indeed, Tits et al. (2011) identified four different luminescent U(VI) species in C-S-H suspensions which included a spectrum which indicated some incorporation into the framework of C-S-H. In Figure 7 the small peaks in the portlandite sample at around 505 nm (19800 cm^{-1}) suggest that a modest amount of incorporation or surface complexation may have occurred. In contrast to the portlandite sample, the cement spectrum is broad suggesting a heterogeneous nature. The main features are once again in the region expected of surface complexed or incorporated uranyl species. However, given that the majority of the U(VI) was found to be irreversibility bound to the cement after 48 hours equilibration time in experiments utilising EDTA as a competing ligand, it is expected these features in the luminescence spectrum of cement resulted from incorporated uranyl species, as opposed to surface complexes. In addition to these uranyl features, there is also a tail to low energy in the cement spectrum, which appears in the same place as the Ca-uranate feature in the portlandite spectrum, suggesting the presence of mixed uranyl/uranate-like species.

3.3.5. Electron Microscopy of Cement Systems

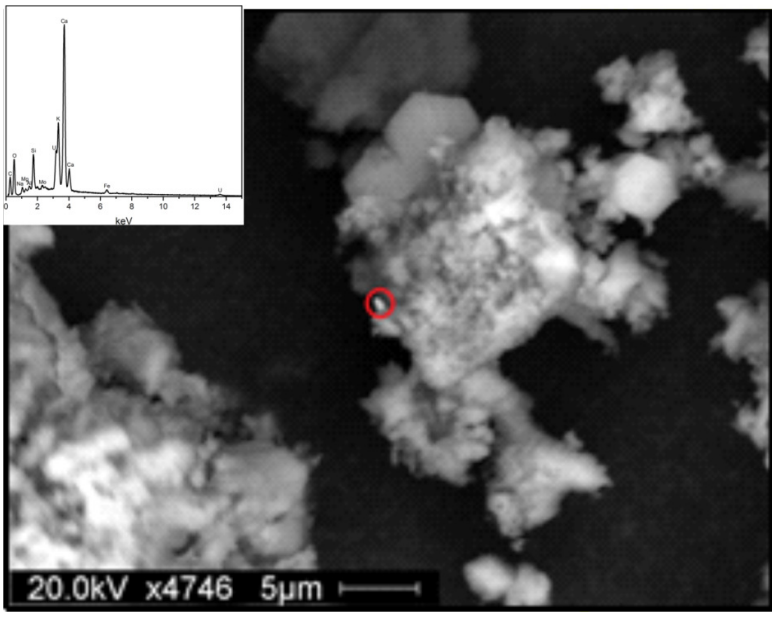

Figure 8. Backscattering electron image of cement reacted young cement leachate containing 42 µM U(VI) for 21 months. The circled area shows a U rich area as determined by EDX (Inset).

To further investigate the nature of U(VI) removal from the filterable (< 0.02 µm) fraction, a sample of the cement which had been exposed to young cement leachate containing 42 µM U(VI) for 21 months was analysed using electron microscopy. SEM images showed the solid reaction products had an amorphous structure similar to that of the fresh cement. In back-scattering mode, it was possible to identify regions of high electron density typically 1 – 2 µm in diameter (Figure 8) and EDX confirmed the presence of uranium in these areas. This suggests that a portion of the uranium has aggregated and been deposited on the cement surface and similar to past work with $U(VI)_{(aq)}$ systems with cement (Tits et al., 2011; Macé et al., 2013).

3.2.6. X-Ray Absorption Spectroscopy of Cement Systems

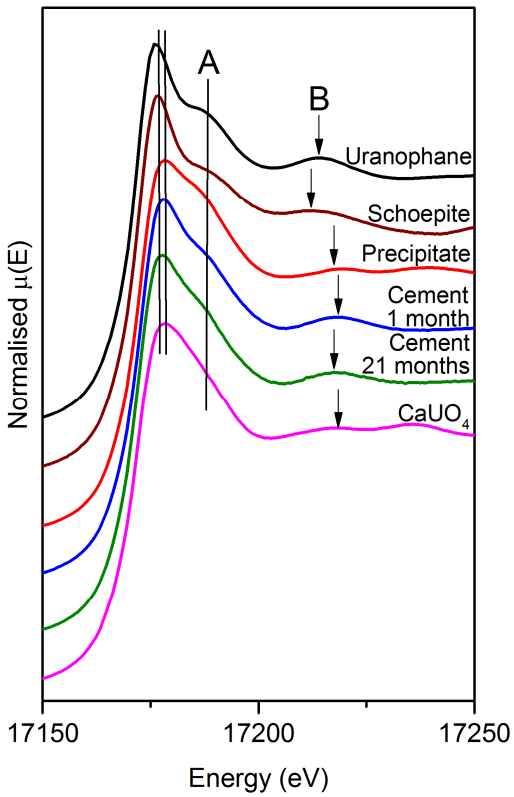

Figure 9. Uranium L_{III}-edge XANES spectra of cement equilibrated with 42 μM U(VI) for 1 and 21 months compared with reference spectra. Black = uranophane (Macé et al., 2013; Scheinost et al., 2013), brown = Schoepite, red = uranate-like precipitate from Bots et al. (2014), blue = 1 month cement equilibrated, green = 21 month cement equilibrated, pink = $CaUO_4$ (Macé et al., 2013; Scheinost et al., 2013). The two vertical lines close to the white line show the position of the top of the white line in the uranyl (scheopite) and uranate ($CaUO_4$) standards. Line (A) and arrows (B) highlight features related to axial and equatorial U – O bonds, respectively.

X-ray absorption spectroscopy was used to further probe the local coordination environment of uranium associated with the solid phase in the cement system after 1 and 21 months of reaction in the pH 13.3 young cement leachate. The edge energy and the post-edge structure of the XANES spectra (Figure 9) were compared with standard

U L_{III}-edge spectra from uranophane [$Ca(UO_2)_2(SiO_3OH)\cdot 5H_2O$] (Macé et al., 2013), schoepite ($UO_3\cdot 2H_2O$), Ca-uranate (Macé et al., 2013; Scheinost et al., 2013), and a clarkeite (sodium uranate)-like phase freshly precipitated from 252 mM U(VI) doped young cement leachate (Bots et al., 2014). The white line of the XANES spectra of the solid cement phase after 1 month reaction with a 42 µM U(VI) colloidal suspension was broad and the edge position (~ 17173 eV) was consistent with both the Ca-uranate standard and the sodium uranate precipitate identified by Bots et al. (2014), suggesting the presence of a significant fraction of uranate in the sample. However, the presence of the resonance feature at ~ 17190 eV (Line (A), Figure 9) in the XANES is characteristic of the uranyl moiety (Farges et al., 1992), as observed in the uranophane standard. Together these observations suggest there is a contribution to the average sample spectrum from U(VI) in both a uranate and a uranyl environment. This is significant since Macé et al. (2013) observed U(VI) sorbed to, or incorporated into, C-S-H phases in a uranyl coordination environment, while U(VI) precipitated from solutions containing U(VI) colloids has been documented in a uranate coordination environment (Bots et al., 2014; Smith et al., 2015). Although it is noteworthy that the uranyl containing phase uranophane was also predicted to be supersaturated after 1 month (Supporting Information Table 2), and may contribute to the uranyl contribution to the XANES. Therefore, the XANES suggests that after 1 month reaction the cement associated uranium is present as both surface uranate precipitates and either sorbed / incorporated uranyl species, or uranophane. After 21 months reaction between the cement and the colloidal suspension, the XANES spectra retained its uranate-like edge positon and structure. However, the characteristic uranyl resonance feature (Line A), Figure 9) became less pronounced in the XANES, suggesting that the U(VI) coordination environment in the aged sample was increasingly dominated by a uranate-like environment with reaction time. Overall, the XANES spectra after 21 months reaction were similar to that of the uranate precipitate identified by Bots et al. (2014) in young

cement leachate doped with 252 μM U(VI), suggesting uranate was increasingly dominant in this sample.

The EXAFS data collected from the U-L_{III} edge of cement reacted with young cement leachate containing 42 μM U(VI) colloids for 1 and 21 months were fitted with clarkeite (sodium uranate, $NaUO_2O(OH)\cdot(H_2O)_{0-1}$), uranophane ($Ca(UO_2)_2(SiO_3OH)_2\cdot 5H_2O$), and Ca-uranate ($CaUO_4$) models to assess the goodness of fit between these different species. The uranophane-like model was chosen since a contribution from a uranyl species was identified in the XANES spectra collected after 1 month reaction (Figure 9). In addition, U(VI) has been found in a uranyl silicate-like environment when removed from solutions containing low mM concentrations (< ~ 0.5 mM) of U(VI) by C-S-H phases (Macé et al., 2013), and U(VI), uranyl bearing silicates were found to control uptake by hardened cement pastes (Wieland et al., 2010). At higher U(VI) concentrations (~ 4 mM), U(VI) is also observed in a Ca-uranate-like coordination environment (Macé et al., 2013). Given the relatively high Ca concentration observed in our experimental system (1.1 – 1.5 mM, Table 1 and Supporting Information Figure 5) and the uranate type features in the XANES (Figure 9), the EXAFS were also fitted using a Ca-uranate model. In recent work in comparable systems but without any reactive solids, a clarkeite (sodium uranate)-like precipitate was identified at high U(VI) (252 μM) concentrations and stable clarkeite-like nanoparticles were found at lower U(VI) (42 μM) concentration (Bots et al., 2014), therefore fitting to a clarkeite (sodium uranate, $NaUO_2O(OH)\cdot(H_2O)_{0-1}$) model was also assessed.

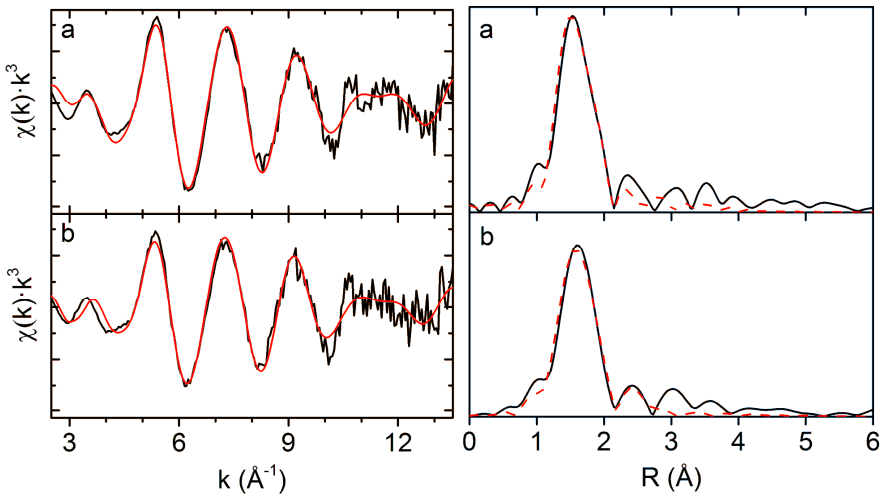

Figure 10. EXAFS of cement equilibrated with young cement leachate containing 42 µM colloidal U(VI) for (A) 1 month and (B) 21 months. The data for fits are for the uranophane model across k-range of 3 -13.3 $Å^{-1}$ and 4 -12.5 $Å^{-1}$.

Reaction Time	Structure and backscatter path	N	R (Å)	σ^2 ($Å^2$)	ΔE^0 (eV)	S_0^2	R-factor
1 month	**Uranophane**						
	O_{ax}	2	1.85(1)	0.0033(7)			
	O_{eq1}	4.5	2.26(2)	0.0059(11)			
	O_{eq2}	1.5	2.44(6)	0.0095(66)			
	Si	2	3.14(4)	0.0150(50)	5.0	1*	0.0178
21 months	**Uranophane**						
	O_{ax}	2	1.87(1)	0.0043(9)			
	O_{eq1}	4.5	2.28(1)	0.0061(12)			
	O_{eq2}	1.5	2.49(4)	0.0086(61)			
	Si	1.5	3.18(4)	0.0114(60)	9.5*	1*	0.0270

Table 2. EXAFS best fit parameters for 42 µM U(VI) equilibrated in young cement leachate and exposed to cement for 1 and 21 months. R = atomic distance; N = coordination number; σ^2 ($Å^2$) = Debye-Waller factor; ΔE^0 (eV) = energy shift from Fermi level; S_0^2 = amplitude factor; R-factor = normalised least squares residual.Coordination numbers were fixed and multiple scattering paths were included for the axial oxygens in all systems. * Denotes fixed parameter. Errors are presented in parentheses and are 1σ of last decimal.

After 1 month reaction, fitting to the uranophane model best reproduced the data (Figure 10, Table 2). When the data were fitted to the clarkeite and Ca-uranate models the Na and Ca distances were unphysically short (3.30 and 3.52 Å, Supporting Information Table 4) (Takahashi et al., 1993; Skakle et al., 1997), as a result these models were considered to be less credible. For the uranophane fit, the model U-O_{ax} bond distance (1.85 Å) was between that expected in uranate (1.86 – 1.97 Å) (King, 2002; Catalano and Brown, 2004; Macé et al., 2013) and uranyl (1.70 – 1.82 Å) (Thompson et al., 1997; King, 2002) coordination environment. However, the split equatorial oxygen shell fitted with U-O_{eq} distances at 2.26 Å and 2.44 Å, these distances are within error of those observed in uranophane (Ginderow, 1988; Macé et al., 2013). The addition of a Si shell at 3.14 Å also significantly improved the fit, as determined by the F-test (see Supporting Information Table 5) (Downward et al., 2007), and again was within error of the Si backscatterer in uranophane (Ginderow, 1988). These data suggest that after 1 month reaction the U(VI) can be best fitted in a uranophane-like coordination environment but clearly there is complexity within the spectrum. The EXAFS spectrum is representative of a range of U(VI) reactivity with both the adsorption of U(VI) or incorporation of U(VI) into C-S-H phases (Macé et al., 2013), and the precipitation of uranophane all relevant to the data.

After 21 months reaction with the colloidal U(VI) suspension modest changes in the EXAFS were observed (Figure 10). Fitting to a clarkeite or Ca-uranate structure, again, gave Na and Ca bond distances which were significantly shorter (3.41 Å and 3.53 Å, respectively) than those expected in these compounds (3.6 – 3.7 Å) (Takahashi et al., 1993; Skakle et al., 1997). When the data were fitted to the uranophane structure, the best fit to the spectrum was produced by a U-O_{ax} distance of 1.87 Å, a split equatorial oxygen shell with U-O_{eq} distances of 2.28 Å and 2.49 Å, and a U-Si distance of 3.18 Å (Table 2). The equatorial oxygen fit and the Si backscatterer are in good agreement with those previously reported for uranophane (Ginderow, 1988; Macé et al., 2013), suggesting a significant

portion of the U(VI) remains present in a uranophane-like coordination environment either as a sorption complex or as a precipitate. However, the clear increase in the U-O_{ax} bond distance from 1.85 Å to 1.87 Å with time suggests that the average U(VI) coordination environment has become increasingly uranate-like. This is supported by the goodness of fit for the 1 month and 21 month samples for a uranophane-like fit which show a worsening of fit with ageing (from 0.0178 to 0.0270). This interpretation is supported by XANES which shows a clear reduction in the "yl" shoulder at ~ 17190 eV after 21 months (A, Figure 9) suggesting a decrease in the proportion of U(VI) present in a uranyl coordination environment. Finally, the PHREEQC calculations suggest that uranophane is no longer oversaturated at 21 months (Supporting Information Table 2).

Overall, the XAS suggest that the proportion of the U(VI) present in a sorbed, incorporated, or precipitated uranyl-silicate environment decreased over time, from 1 to 21 months reaction, and that the proportion present as a uranate precipitate increased over this period. This suggests that over the long term, U(VI) favoured the formation of uranate precipitates over sorption to, or incorporated into, C-S-H phases or the formation of uranophane-like precipitates.

4. Conclusions and Relevance to Geological Disposal

U(VI) colloidal nanoparticles (42 µM) of the type identified by Bots et al. (2014) were found to be stable in contact with orthoclase and quartz in high pH (13.3) young cement leachate over periods of up to 5 years. Interestingly, in contact with biotite, removal of ~ 20 % of the U(VI) was observed from the < 0.02 µm filterable fraction. TEM analysis of the solid biotite from this system found discrete uranium rich areas, co-located with Ca and Fe. This suggested either formation of a Ca and U(VI) containing phase or the reductive precipitation of U(IV). By contrast, when the colloids were in contact with cement, more

than 97 % of the U(VI) was removed from the < 0.02 µm filterable fraction within 1 month. Despite this significant removal, the remaining solution was still supersaturated with respect to a number of uranate phases, suggesting the residual U(VI) in solution likely remained in a colloidal phase. The uptake of the U(VI) colloid by cement was consistent over a wide concentration range (2.0×10^{-10} – 4.2×10^{-5} M). This was likely due to the increase in Ca concentrations observed in the solution reacted with cement compared to the single mineral experiments. X-ray absorption spectroscopy of the U(VI)-amended cement after 1 and 21 months reaction in the young cement leachate was undertaken. After 1 month reaction U(VI) was predominantly present in a uranophane like environment. This was likely due to U(VI) both sorbing to, or incorporating into, the cement in a uranyl-silicate-like environment (or the precipitation of the uranyl phase uranophane) with the XANES suggesting uranate-like uranium was also present in the sample at tens of percent levels (above detection thresholds). Luminescence spectroscopy on 4.2 µM experiments also showed evidence for both U(VI) incorporated into the C-S-H interlayer and precipitated as a uranate-like phase. After 21 months reaction, EXAFS fitting suggested the proportion of the U(VI) present as a uranate-like phase increased. The precipitation of a uranate phase suggests the reduction of the U(VI) concentration in the < 0.02 µm filterable solution is caused by the change in solution chemistry resulting from the partial dissolution of cement over the reaction time. This is in contrast to sorption to, or incorporation into, C-S-H phases, where U(VI) would be expected to be in a uranyl-like uranophane-type environment. There is also evidence of significant irreversibility in these systems, which would be consistent with incorporation within the structure of a mineral phase and/or the precipitation of a very stable surface precipitate, such as calcium uranate. SEM images of cement after 21 months contact with the colloidal suspension show discrete uranium rich areas, consistent with the precipitation of uranate or uranophane like phases.

Overall, U(VI) colloids are poorly reactive with common rock forming minerals, with up to 94 % remaining in the < 0.02 µm filterable fraction after up to 5 years contact. Greater reactivity was observed upon reaction with cement, where 97 % of the U(VI) was removed within the first month. However, 2.4 % (1.0 µM) of the U(VI) remained stable in the < 0.02 µm filterable fraction after 21 months reaction. This stable, colloidal fraction represents 1000 times the solution U(VI) concentration predicted by thermodynamic modelling and could have a significant impact on uranium mobility in hyperalkaline conditions.

Acknowledgements

Rosemary Hibberd was funded via the EPSRC Nuclear FiRST DTC (EP/G037140/1). This work was carried out as part of the Biogeochemical Gradients and Radionuclide Transport (BIGRAD) consortium, funded by NERC (NE/H007768/1). We thank Diamond Light Source for access to beamlines B18 (SP8941-2 & SP10163-2) that contributed to the results presented here. Part of this work was funded by Radioactive Waste Management Limited. The authors would like to thank Paul Lythgoe and John Waters for geochemical analysis and XRD, respectively. NB would like to thank NNL for support.

References

Abramoff, M. D., Magalhaes, P. J. and Ram, S. J. (2004). Image processing with ImageJ. *Biophotonics International,* 11(7)**,** 36-42.

Aggarwal, S., Angus, M. I. and Tyson, A. (1990). Phase characterization of cementitious components of a waste repository and the potential of individual phases for sorption of radioisotopes. *Waste Management,* 90**,** 399-406.

Ames, L. L., McGarrah, J. E. and Walker, B. A. (1983). Sorption of uranium and radium by biotite, muscovite, and phlogopite. *Clays and Clay Minerals,* 31(5)**,** 343-351.

Arnold, T., Zorn, T., Bernhard, G. and Nitsche, H. (1998). Sorption of uranium(VI) onto phyllite. *Chemical Geology,* 151(1-4)**,** 129-141.

Arnold, T., Zorn, T., Zänker, H., Bernhard, G. and Nitsche, H. (2001). Sorption behavior of U(VI) on phyllite: Experiments and modeling. *Journal of Contaminant Hydrology,* 47(2-4)**,** 219-231.

Berner, U. R. (1992). Evolution of pore water chemistry during degradation of cement in a radioactive waste repository environment. *Waste Management,* 12(2)**,** 201-219.

Bin, G., Cao, X., Dong, Y., Luo, Y. and Ma, L. Q. (2011). Colloid Deposition and Release in Soils and Their Association With Heavy Metals. *Critical Reviews in Environmental Science and Technology,* 41(4)**,** 336-372.

Bots, P., Morris, K., Hibberd, R., Law, G. T. W., Mosselmans, J. F. W., Brown, A. P., Doutch, J., Smith, A. J. and Shaw, S. (2014). Formation of Stable Uranium(VI) Colloidal Nanoparticles in Conditions Relevant to Radioactive Waste Disposal. *Langmuir,* 30(48)**,** 14396-14405.

Brookshaw, D. R., Pattrick, R. A. D., Bots, P., Law, G. T. W., Lloyd, J. R., Mosselmans, J. F. W., Vaughan, D. J., Dardenne, K. and Morris, K. (2015). Redox Interactions of Tc(VII), U(VI), and Np(V) with Microbially Reduced Biotite and Chlorite. *Environmental Science & Technology,* 49(22)**,** 13139-13148.

Butcher, E. J., Borwick, J., Collier, N. and Williams, S. J. (2012). Long term leachate evolution during flow-through leaching of a vault backfill (NRVB). *Mineralogical Magazine,* 76(8)**,** 3023-3031.

Butler, M. A. and Ginley, D. S. (1978). Prediction of Flatband Potentials at Semiconductor-Electrolyte Interfaces from Atomic Electronegativities. *Journal of The Electrochemical Society,* 125(2)**,** 228-232.

Catalano, J. G. and Brown, G. E. (2004). Analysis of uranyl-bearing phases by EXAFS spectroscopy: Interferences, multiple scattering, accuracy of structural parameters, and spectral differences. *American Mineralogist,* 89(7)**,** 1004-1021.

Cronin, J. and Collier, N. (2012). Corrosion and expansion of grouted Magnox. *Mineralogical Magazine,* 76(8)**,** 2901-2909.

Davis, J. A., Meece, D. E., Kohler, M. and Curtis, G. P. (2004). Approaches to surface complexation modeling of Uranium(VI) adsorption on aquifer sediments. *Geochimica et Cosmochimica Acta,* 68(18)**,** 3621-3641.

DECC. (2010). *Government Response to the House of Lords Science and Technology Committee Report: Radioactive Waste Management: A Further Update*. ST/10-11/40.

DECC. (2015). *Implementing Geological Disposal: Annual Report.* London. URN 15D/361.

Diamond, S., Dolch, W. L. and White, J. L. (1963). Studies on Tobermorite-like Calcium Silicate Hydrates. *Annual Meeting of the Highway Research Board.* Wachington D.C.

Dodge, C. J., Francis, A. J., Gillow, J. B., Halada, G. P., Eng, C. and Clayton, C. R. (2002). Association of Uranium with Iron Oxides Typically Formed on Corroding Steel Surfaces. *Environmental Science & Technology,* 36(16)**,** 3504-3511.

Dow, C. and Glasser, F. P. (2003). Calcium carbonate efflorescence on Portland cement and building materials. *Cement and Concrete Research,* 33(1)**,** 147-154.

Downward, L., Booth, C. H., Lukens, W. W. and Bridges, F. (2007). A variation of the F-Test for determining statistical relevance of particular parameters in EXAFS fits. *In:* Hedman, B. & Painetta, P. (eds.) *X-Ray Absorption Fine Structure-XAFS13.* Melville: American Institute of Physics.

Farges, F., Ponader, C. W., Calas, G. and Brown, G. E. (1992). Structural Environment of Incompatible Elements in Silicate Glass Melt Systems 2. UIV, UV, and UVI. *Geochimica et Cosmochimica Acta,* 56(12)**,** 4205-4220.

Fernández, R., Ruiz, A. I. and Cuevas, J. (2016). Formation of C-A-S-H phases from the interaction between concrete or cement and bentonite. *Clay Minerals,* 51(2)**,** 223-235.

Finch, R. J. and Ewing, R. C. (1997). Clarkeite: New chemical and structural data. *American Mineralogist,* 82(5-6)**,** 607-619.

Froideval, A., Del Nero, M., Barillon, R., Hommet, J. and Mignot, G. (2003). pH dependence of uranyl retention in a quartz/solution system: An XPS study. *Journal of Colloid and Interface Science,* 266(2)**,** 221-235.

Gaona, X., Kulik, D. A., Macé, N. and Wieland, E. (2012). Aqueous–solid solution thermodynamic model of U(VI) uptake in C–S–H phases. *Applied Geochemistry,* 27(1)**,** 81-95.

Gardiner, M. P., Hotlom, G. J. and Swanton, S. W. (1998). Influence of Colloids, Microbes and Other Perturbations on the Near-field Source Term, Paper 3. *RSC/Nirex Symposium: The Chemistry of Deep Disposal of Radioactive Waste.* Loughborough.

Ginderow, D. (1988). Structure cristalline d'un chloro-silico-chromate de plomb, Pb5(CrO4,SiO4)3Cl. *Zeitschrift fur Kristallographie - New Crystal Structures,* 184(3-4)**,** 185-190.

Gorman-Lewis, D., Fein, J. B., Burns, P. C., Szymanowski, J. E. S. and Converse, J. (2008). Solubility measurements of the uranyl oxide hydrate phases metaschoepite, compreignacite, Na-compreignacite, becquerelite, and clarkeite. *Journal of Chemical Thermodynamics,* 40(6)**,** 980-990.

Grenthe, I., Wanner, H. and Forest, I. (1992). *Chemical Thermodynamics of Uranium*. North-Holland.

Grive, M., Duro, L., Domenech, C. and Salas, J. (2009). Model of the Redox conditions in the near field of a cementitious geological disposal facility (GDF).

Grive, M., L., D., Domenech, C. and Salas, J. (2011). Redox Evolution of a Cementitous Geological Disposal Facility. *13th International High-Level Radioactive Waste Management Confenece.* Albuqueque, NM.

Harfouche, M., Wieland, E., Dahn, R., Fujita, T., Tits, J., Kunz, D. and Tsukamoto, M. (2006). EXAFS study of U(VI) uptake by calcium silicate hydrates. *Journal of Colloid and Interface Science,* 303(1)**,** 195-204.

Heberling, F., Brendebach, B. and Bosbach, D. (2008). Neptunium(V) adsorption to calcite. *Journal of Contaminant Hydrology,* 102(3-4)**,** 246-252.

Ilton, E. S., Haiduc, A., Moses, C. O., Heald, S. M., Elbert, D. C. and Veblen, D. R. (2004). Heterogeneous reduction of uranyl by micas: Crystal chemical and solution controls. *Geochimica et Cosmochimica Acta,* 68(11)**,** 2417-2435.

Ilton, E. S., Heald, S. M., Smith, S. C., Elbert, D. and Liu, C. (2006). Reduction of uranyl in the interlayer region of low iron micas under anoxic and aerobic conditions. *Environmental Science & Technology,* 40(16)**,** 5003-5009.

Kerisit, S. and Liu, C. (2014). Molecular Dynamics Simulations of Uranyl and Uranyl Carbonate Adsorption at Aluminosilicate Surfaces. *Environmental Science & Technology,* 48(7)**,** 3899-3907.

Kersting, A. B., Efurd, D. W., Finnegan, D. L., Rokop, D. J., Smith, D. K. and Thompson, J. L. (1999). Migration of plutonium in ground water at the Nevada Test Site. *Nature,* 397**,** 56-59.

King, R. B. (2002). Some Aspects of Structural and Bonding in Binary and Ternary Uranium(VI) Oxides. *Chemistry of Materials,* 14**,** 3628-3635.

Kosmulski, M. (2009). *Surface Charging and Points of Zero Charge* (Vol. 145). Boca Roton: CRC Press.

Kosmulski, M. (2012). IEP as a parameter characterizing the pH-dependent surface charging of materials other than metal oxides. *Advances in Colloid and Interface Science,* 171-172**,** 77-86.

Loopstra, B. O. and Rietveld, H. M. (1969). The Structure of Some Alkaline-Earth Metal Uranates. *Acta Crystallographica,* 25**,** 787-791.

Lowry, G. V., Shaw, S., Kim, C. S., Rytuba, J. J. and Brown Jr, G. E. (2004). Macroscopic and microscopic observations of particle-facilitated mercury transport from New Idria and Sulphur Bank mercury mine tailings. *Environmental Science & Technology,* 38(19)**,** 5101-5111.

Macé, N., Wieland, E., Dähn, R., Tits, J. and Scheinost, A. C. (2013). EXAFS investigation on U(VI) immobilization in hardened cement paste: influence of experimental conditions on speciation. *Radiochimica Acta,* 101(6)**,** 379-389.

Marshall, T. A., Morris, K., Law, G. T., Livens, F. R., Mosselmans, J. F., Bots, P. and Shaw, S. (2014). Incorporation of Uranium into Hematite during crystallization from ferrihydrite. *Environmental Science & Technology,* 48(7)**,** 3724-3731.

Ministry of the Environment Sweden. (2014). *Sweden's implementation of the obligations of the Joint Convention*. Ds 2014:32.

Missana, T., Alonso, Ú., García-Gutiérrez, M. and Mingarro, M. (2008). Role of bentonite colloids on europium and plutonium migration in a granite fracture. *Applied Geochemistry,* 23(6)**,** 1484-1497.

Moroni, L. P. and Glasser, F. P. (1995). Reactions between cement components and U(VI) oxide. *Waste Management,* 15(3)**,** 243-254.

Morris, K., Law, G. T. W. and Bryan, N. D. (2011). Geodisposal of Higher Activity Wastes. *In:* Hester, R. E. & Harrison, R. M. (eds.) *Nuclear Power and the Environment.* Royal Society of Chemistry.

Moyce, E. B. A., Rochelle, C., Morris, K., Milodowski, A. E., Chen, X., Thornton, S., Small, J. S. and Shaw, S. (2014). Rock alteration in alkaline cement waters over 15 years and its relevance to the geological disposal of nuclear waste. *Applied Geochemistry,* 50**,** 91-105.

Moyes, L. N., Parkman, R. H., Charnock, J. M., Vaughan, D. J., Livens, F. R., Hughes, C. R. and Braithwaite, A. (2000). Uranium Uptake from Aqueous Solution by Interaction with Goethite, Lepidocrocite, Muscovite, and Mackinawite: An X-ray Absorption Spectroscopy Study. *Environmental Science & Technology,* 34(6)**,** 1062-1068.

Murphy, W. M. and Shock, E. L. (1999). Environmental aqueous geochemistry of actinides. *Reviews in Mineralogy and Geochemistry,* 38**,** 221-253.

Nakashima, S., Bessho, H., Tomizawa, R., Kirino, Y., Nishiyama, N., Tonoue, R., Yokoyama, T. and Sasamoto, H. (Year). Calcium silicate hydrate formation rates during alkaline alteration of rocks as revealed by infrared spectroscopy. *In:* ISRM International Symposium - 8th Asian Rock Mechanics Symposium, ARMS 2014, 2014. 2002-2009.

NDA. (2010). *Near-field evolution status report*. Harwell. NDA/RWMD/033.

NDA. (2013). *Geological Disposal: How the World is Dealing with its Radioactive Wastes*. Harwell. 978-1-905985-32-6.

NDA. (2014). *Geological Disposal: Generic disposal facility designs*. Harwell. NDA/RWMD/048.

Nebelung, C. and Brendler, V. (2010). U(VI) sorption on granite: Prediction and experiments. *Radiochimica Acta,* 98(9-11)**,** 621-625.

O'Hare, P. A. G., Boerio, J. and Hoekstra, H. R. (1976). Thermochemistry of uranium compounds VIII. Standard enthalpies of formation at 298.15 K of the uranates of calcium (CaUO4) and barium (BaUO4). Thermodynamics of the behavior of barium in nuclear fuels. *The Journal of Chemical Thermodynamics,* 8(9)**,** 845-855.

Olin, M., Puukko, E., Puhakka, E., Lehikoinan, J., Lindberg, A. and Hakanen, M. (2006). *Sorption of Nickel on Biotite*. Helsinki. VTT-R-08046-06.

Pabalan, R. T. and Turner, D. R. (1997). Uranium(6+) sorption on montmorillonite: Experimental and surface complexation modeling study. *Aquatic Geochemistry,* 2(3)**,** 203-226.

Parkhurst, D. L. and Appelo, C. A. J. (2013). *Description of input and examples for PHREEQC version 3—A computer program for speciation, batch-reaction, one-dimensional transport, and inverse geochemical calculations* [Online]. available only at http://pubs.usgs.gov/tm/06/a43/. [Accessed 06/11/2015].

Pitois, A., Abrahamsen, L. G., Ivanov, P. I. and Bryan, N. D. (2008). Humic acid sorption onto a quartz sand surface: A kinetic study and insight into fractionation. *Journal of Colloid and Interface Science,* 325(1)**,** 93-100.

Prikryl, J. D., Jain, A., Turner, D. R. and Pabalan, R. T. (2001). UraniumVI sorption behavior on silicate mineral mixtures. *Journal of Contaminant Hydrology,* 47(2-4)**,** 241-253.

Ravel, B. and Newville, M. (2005). ATHENA, ARTEMIS, HEPHAESTUS: data analysis for X-ray absorption spectroscopy using IFEFFIT. *Journal of Synchrotron Radiation,* 12(Pt 4)**,** 537-541.

Reeder, R. J., Nugent, M., Lamble, G. M., Tait, C. D. and Morris, D. E. (2000). Uranyl incorporation into calcite and aragonite: XAFS and luminescence studies. *Environmental Science & Technology,* 34(4)**,** 638-644.

RWM. (2015). *Geological Disposal: The 2013 Derived Inventory*. Harwell. NDA/RWM/120.

Schaefer, K. W. (1991). Determination of the Ca2+ Sorption Capacity of Quartz Surface Using Ca45 as Tracer - A Column Experiment. *Radiochimica Acta,* 54(1)**,** 47-51.

Scheinost, A. C., Schmeisser, N., Benerjee, D., Rossberg, A., Denecke, M. A., Dardenne, K., Rothe, J. and Daehn, R. (2013). AcXAS An Actinide Reference X-ray Absorption Spectroscopy Database. https://www.hzdr.de/acxas.

Sen, T. K. and Khilar, K. C. (2006). Review on subsurface colloids and colloid-associated contaminant transport in saturated porous media. *Advances in Colloid and Interface Science,* 119(2-3)**,** 71-96.

Singer, D. M., Maher, K. and Brown Jr, G. E. (2009). Uranyl-chlorite sorption/desorption: Evaluation of different U(VI) sequestration processes. *Geochimica et Cosmochimica Acta,* 73(20)**,** 5989-6007.

Skakle, J. M. S., Moroni, L. P. and Glasser, F. P. (1997). X-ray diffraction data for two new calcium uranium (VI) hydrates. *Powder Diffraction,* 12(2)**,** 81-86.

Small, J. S. and Thompson, O. R. (2009). Modelling the spatial and temporal evolution of pH in the cementitious backfill of a geological disposal facility. *In:* Hyatt, N. C., Pickett, D. A. & Rebak, R. B. (eds.) *Scientific Basis for Nuclear Waste Management Xxxii.*

Smith, K. F., Bryan, N. D., Swinburne, A. N., Bots, P., Shaw, S., Natrajan, L. S., Mosselmans, J. F. W., Livens, F. R. and Morris, K. (2015). U(VI) behaviour in hyperalkaline calcite systems. *Geochimica et Cosmochimica Acta,* 148**,** 343-359.

Sylwester, E. R., Hudson, E. A. and Allen, P. G. (2000). The structure of uranium(VI) sorption complexes on silica, alumina, and montmorillonite. *Geochimica et Cosmochimica Acta,* 64(14)**,** 2431-2438.

Takahashi, K., Fujino, T. and Morss, L. R. (1993). Crystal Chemical and Thermodynamic Study on CaUO4-x, (Ca0.5Sr0.5)UO4-x, and α-SrUO4-x (x = 0 ~ 0.5). *Journal of Solid State Chemistry,* 105(1)**,** 234-246.

Tang, W., Takeda, S.-i. and Tari, I. (1995). Reaction behavior of SiO2 in Ca(OH)2 solution (Part 2) - in the case of SiO2 glass and Ca(OH)2 solution. *Journal of the Ceramic Society of Japan. International ed.,* 103(2)**,** 168-172.

Telchadder, R., Smith, K. and Bryan, N. D. (2012). Europium interaction with a vault backfill at high pH. *Mineralogical Magazine,* 76(8)**,** 3083-3093.

Thompson, H. A., Brown, G. E. and Parks, G. A. (1997). XAFS spectroscopic study of uranyl coordination in solids and aqueous solution. *American Mineralogist,* 82(5-6)**,** 483-496.

Tits, J., Fujita, T., Tsukamoto, M. and Wieland, E. (2008). Uranium(VI) Uptake by Synthetic Calcium Silicate Hydrates. *Materials Research Society Symposium Proceedings,* 1107**,** 467-474.

Tits, J., Gaona, X., Laube, A. and Wieland, E. (2014). Influence of the redox state on the neptunium sorption under alkaline conditions: Batch sorption studies on titanium dioxide and calcium silicate hydrates. *Radiochimica Acta,* 102(5)**,** 385-400.

Tits, J., Geipel, G., Macé, N., Eilzer, M. and Wieland, E. (2011). Determination of uranium(VI) sorbed species in calcium silicate hydrate phases: a laser-induced luminescence spectroscopy and batch sorption study. *Journal of Colloid and Interface Science,* 359(1)**,** 248-256.

Utsunomiya, S., Kersting, A. B. and Ewing, R. C. (2009). Groundwater Nanoparticles in the Far-Field at the Nevada Test Site: Mechanism for Radionuclide Transport. *Environmental Science & Technology,* 43**,** 1293-1298.

Uyuşur, B., Li, C., Baveye, P. C. and Darnault, C. J. G. (2014). pH-dependent reactive transport of uranium(VI) in unsaturated sand. *Journal of Soils and Sediments,* 15(3)**,** 634-647.

Viswanathan, K. and Harneit, O. (1986). Refined Crystal-Structure of Beta-Uranophane, $Ca(UO_2)_2(SiO_3OH)2.5H_2O$. *American Mineralogist,* 71(11-12)**,** 1489-1493.

Vochten, R., Van Haverbeke, L. and Sobry, R. (1991). Transformation of schoepite into uranyl oxide hydrates of the bivalent cations Mg2+, Mn2+ and Ni2+. *Journal of Materials Chemistry,* 1(4)**,** 637-642.

Walter, M., Arnold, T., Geipel, G., Scheinost, A. and Bernhard, G. (2005). An EXAFS and TRLFS investigation on uranium(VI) sorption to pristine and leached albite surfaces. *Journal of Colloid and Interface Science,* 282(2)**,** 293-305.

Walther, C. and Denecke, M. A. (2013). Actinide colloids and particles of environmental concern. *Chemical Reviews,* 113(2)**,** 995-1015.

Wang, Y., Frutschi, M., Suvorova, E., Phrommavanh, V., Descostes, M., Osman, A. A. A., Geipel, G. and Bernier-Latmani, R. (2013). Mobile uranium(IV)-bearing colloids in a mining-impacted wetland. *Nature Communications,* 4.

Wieland, E., Macé, N., Dähn, R., Kunz, D. and Tits, J. (2010). Macro- and micro-scale studies on U(VI) immobilization in hardened cement paste. *Journal of Radioanalytical and Nuclear Chemistry,* 286(3)**,** 793-800.

Wieland, E. and Spieler, P. (2001). Colloids in the mortar backfill of a cementitious repository for radioactive waste. *Waste Management,* 21**,** 511-523.

Yamamura, T., Kitamura, A., Fukui, A., Nishikawa, S., Yamamoto, T. and Moriyama, H. (1998). Solubility of U(VI) in highly basic solutions. *Radiochimica Acta,* 83(3)**,** 139-146.

Yoshida, H. (1994). Relation between U-series nuclide migration and microstructural properties of sedimentary rocks. *Applied Geochemistry,* 9(5)**,** 479-490.

Zhao, P., Allen, P. G., Sylwester, E. R. and Viani, B. E. (2000). The partitioning of uranium and neptunium onto hydrothermally altered concrete. *Radiochimica Acta,* 88(9-11)**,** 729.

Supporting Information for: U(VI) Nanoparticle Stability Under Alkaline Conditions in the Presence of Rock Forming Minerals and Cement

Rosemary Hibberd[a, b], Gareth T. W. Law[a, b], Nicholas D. Bryan[a, c], Samuel Shaw[a], Pieter Bots[a, 1], Kurt F. Smith[a, b], Timothy A. Marshall[a, 2], Ryan Telchadder[b], Adam Swinbourne[b], Louise Natrajan[b], Rebecca Beard[d], Steve Williams[d], Katherine Morris[a, b*]

[a]Research Centre for Radwaste Disposal and Williamson Research Centre for Molecular Environmental Science, School of Earth and Environmental Sciences, The University of Manchester, Oxford Road, Manchester, M13 9PL, UK.

[b]Centre for Radiochemistry Research, School of Chemistry, The University of Manchester, Oxford Road, Manchester, M13 9PL, UK.

[c]National Nuclear Laboratory, 5th Floor, Chadwick House, Birchwood Park, Warrington Road, Warrington, WA3 6AE, UK.

[d]Radioactive Waste Management Limited, Harwell, Oxfordshire, OX11 0RH, UK.

[1]Present address: Department of Civil and Environmental Engineering, University of Strathclyde, Glasgow, G1 1XQ, UK.

[2]Present address: Office of Nuclear Regulation, Building 4, Redgrave Court, Bootle, Merseyside, L20 7HS, UK.

*Corresponding author, Tel: +44 (0) 161 275 7541; Email: katherine.morris@manchestester.ac.uk

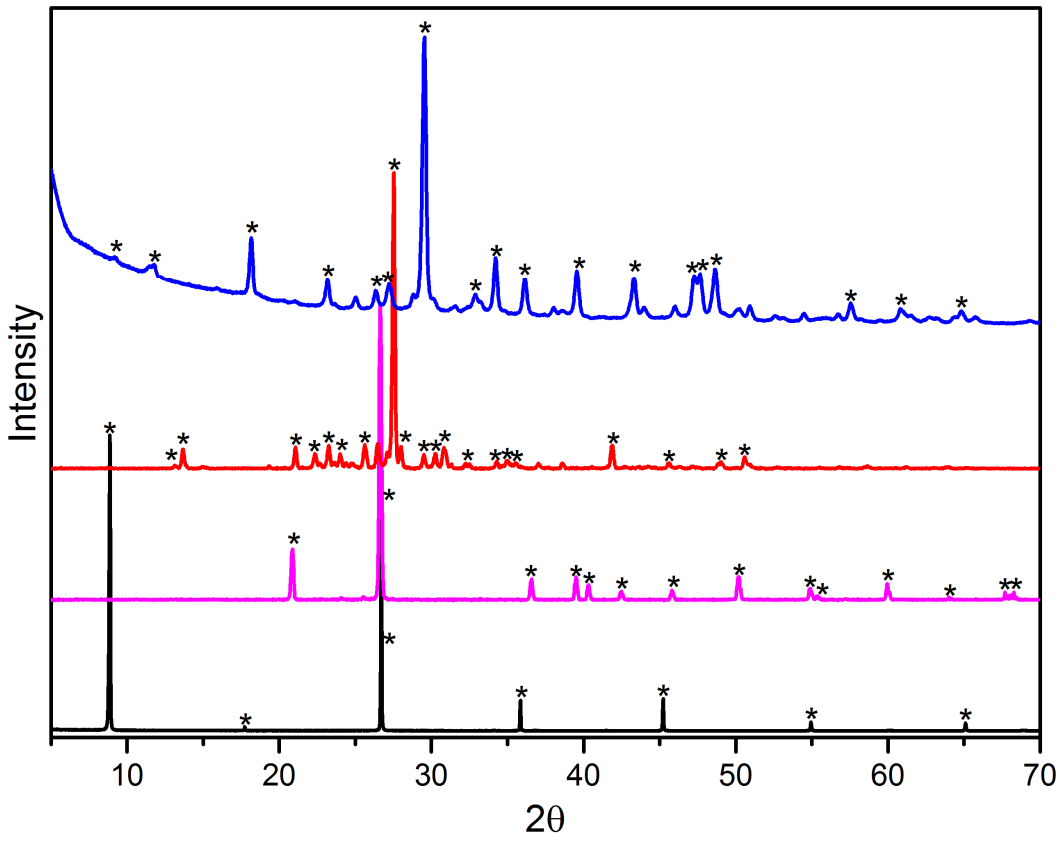

SI Figure 1. XRD of starting minerals, biotite (black), quartz (pink), orthoclase (red), and cement (blue). * denotes identifying peaks.

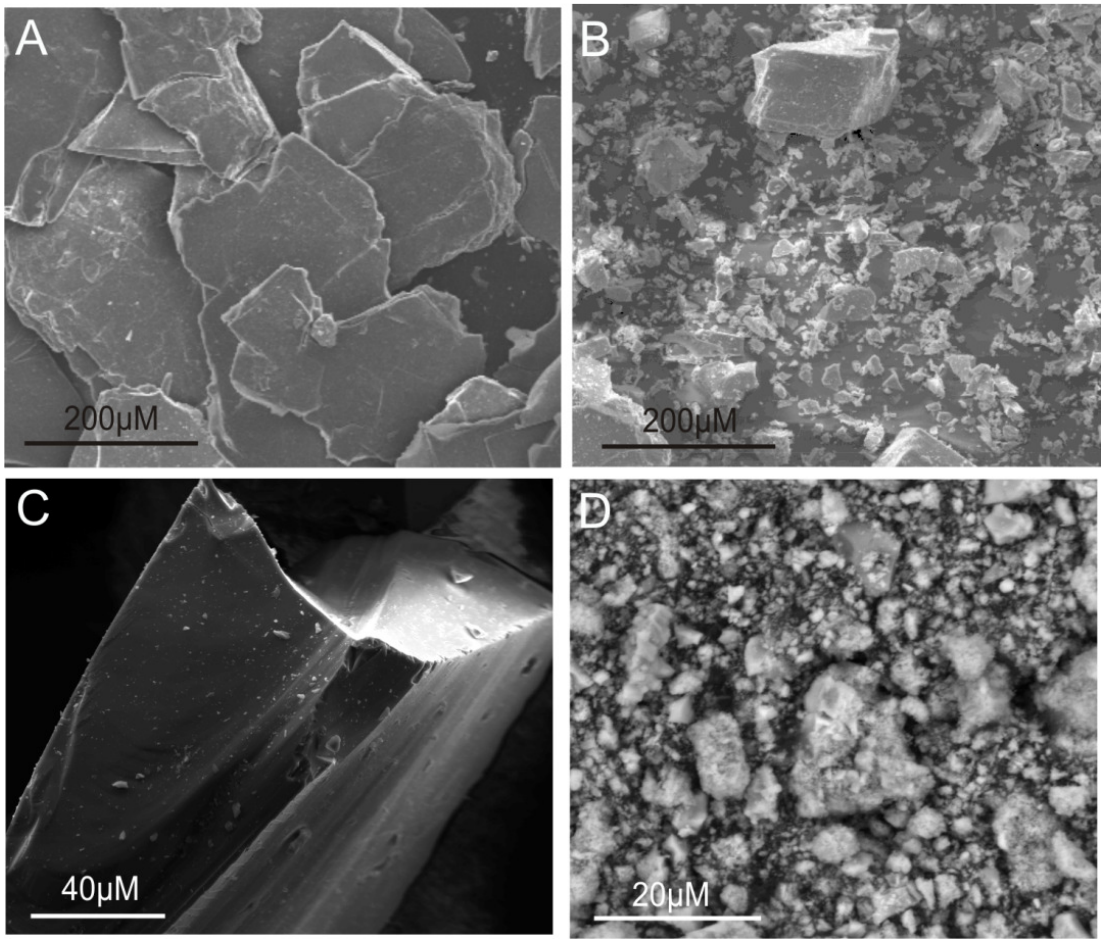

SI Figure 2. SEM images of minerals prior to experimentation. A = biotite, B = orthoclase, C = quartz, D = cement. The plated morphology of biotite, tabular morphology of orthoclase, euhedral morphology of quartz, and the powdered particulate morphology of the cement confirmed the phase identity. The chemical purity of the minerals was confirmed by EDX with only the following elements identified: biotite, Fe, O, K, Mg, F, Si, Al; orthoclase, Si, O, Al, K; quartz, Si, O; and cement, O, Mg, Al, Si, S, K, Ca.

Mineral	Surface area (m^2g^{-1})
Biotite	0.69 ± 0.1
Quartz	0.05 ± 0.002
Orthoclase	0.52 ± 0.02
Cement (< 63 μm)	13.3 ± 0.1
Cement (125 – 251 μm)	14.6

SI Table 1. Surface areas of starting minerals, as determined by BET.

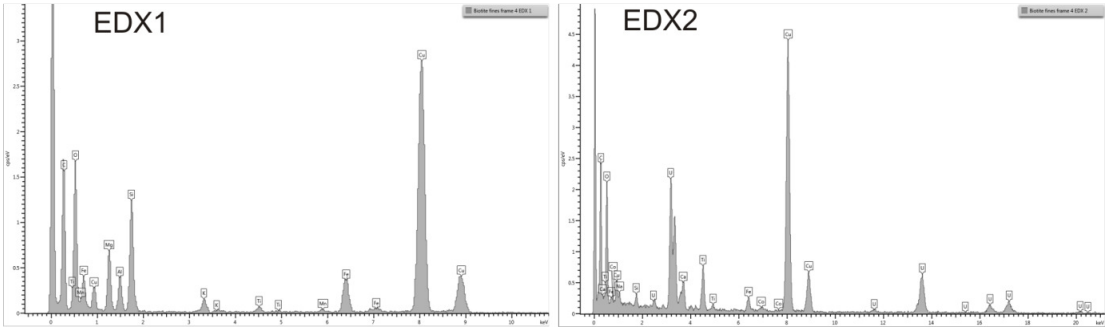

SI Figure 3. EDX spectra of areas of a TEM image (Figure 2) taken of biotite solid after 1 year in contact with young cement leachate containing 42 µM U(VI) colloids.

EDX2 taken of the biotite fine shown in Figure 2 clearly shows the presence of U, co-located with Fe and Ca. Uranium could not be detected in EDX1 which showed the presence of O, Si, Mg, Fe, K, and Al.

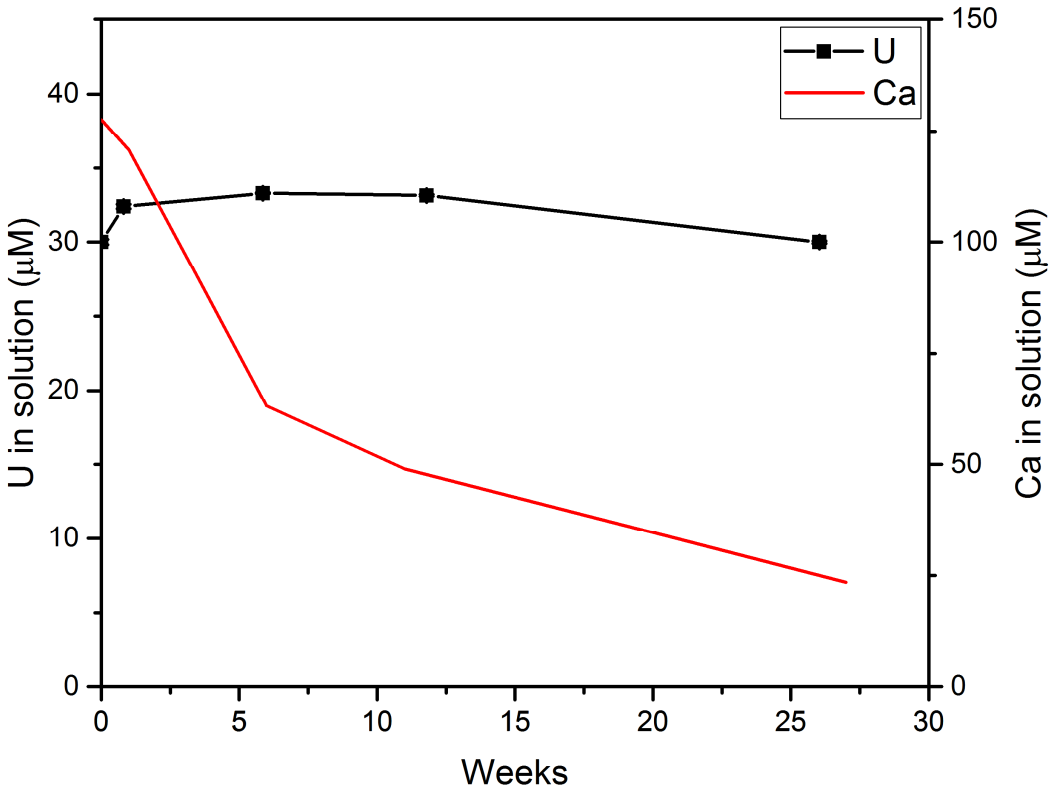

SI Figure 4. Ca and U concentration in < 0.45 µm filtered cement leachate spiked with 42 µM U(VI) colloids and equilibrated with 10 g L^{-1} biotite.

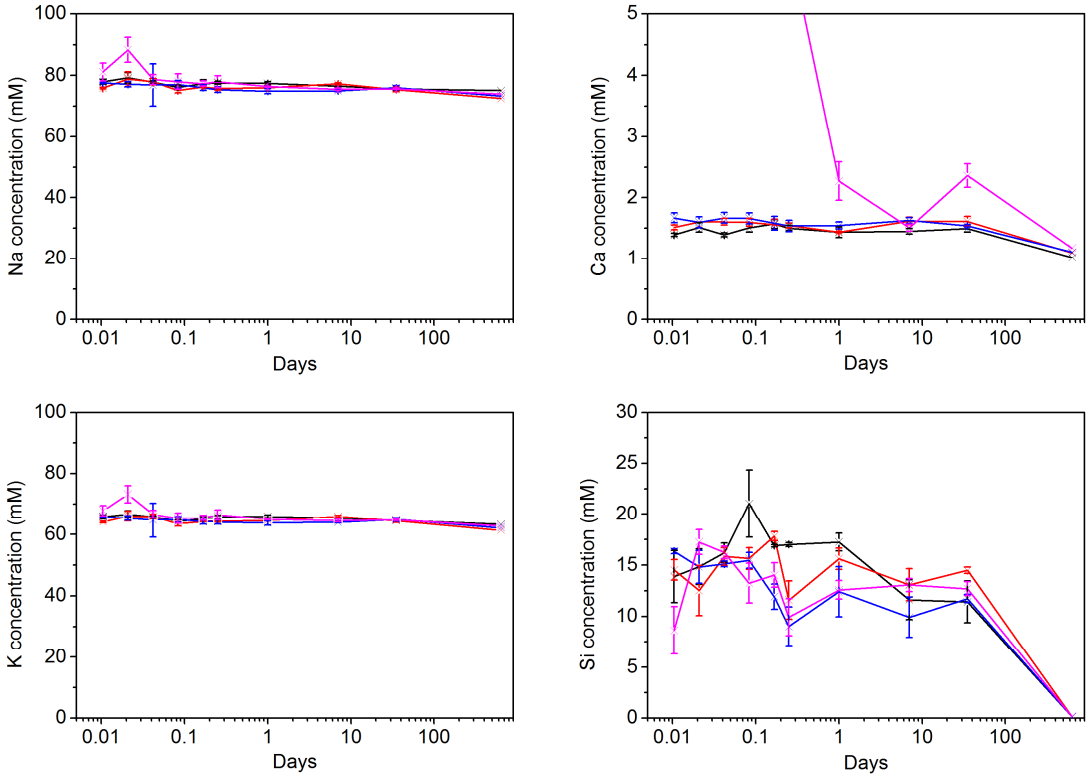

SI Figure 5. Elemental composition of cement leachate containing 42 uM U(VI) after exposure to cement, as determined by ICP-AES. Black = 0.02 µm filter, red = 0.1 µm filter, blue = 0.2 µm filter, pink = unfiltered. Error bars are 1σ from three replicates.

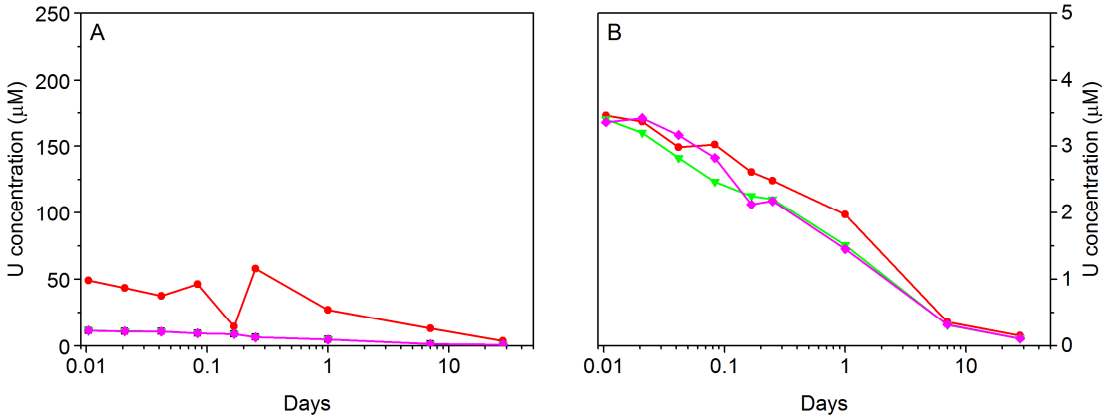

SI Figure 6. Cement leachate equilibrated with A = 252 µM U(VI) and B = 4.2 µM U(VI) and exposed to 10 g L^{-1} cement; ■ = 0.02 µm filtered, ▼ = 0.1 µm filtered, ♦ = 0.22 µm filtered, ● = unfiltered.

Saturation Indices	Spiked to 4.2 µM U(VI)		Spiked to 42 µM U(VI)				Spiked to 252 µM U(VI)	
	Start (4.2 µM U(VI))	End (0.1 µM U(VI))	Start (42 µM U(VI))	10 minutes (27 µM U(VI))	1 month (1.2 µM U(VI))	21 months (1.1 µM U(VI))	Start (252 µM U(VI))	End (1.0 µM U(VI))
Clarkeite	2.54	0.89	3.54	3.71	2.34	1.93	4.32	1.89
$U_2O_7Na_2$	1.29	-	3.29	3.62	0.89	0.07	4.84	-
$CaUO_4$	5.72	5.05	6.72	6.80	5.48	6.09	7.50	6.05
Uranophane	-	-	-	3.77	0.92	-	-	-

SI Table 2. Saturation indices of a selection of uranium containing phases, as determined by thermodynamic modelling, in cement leachate exposed to solid cement at the experimental end point (U concentrations determined by ICP-MS). Where no figure is given the phase is under-saturated.

	Cement leachate	Equilibrated with biotite for 2.5 years	Equilibrated with orthoclase for 5 years	Equilibrated with quartz for 5 years
Clarkeite	2.14	2.03	1.84	1.87
$U_2O_7Na_2$	0.48	0.27	-	-
$CaUO_4$	6.22	4.74	4.35	2.85
Uranophane	-	-	-	-

SI Table 3. Saturation indices of a selection of uranium containing phases in cement leachate containing 42 μM U(VI) equilibrated with single mineral phases as determined by thermodynamic modelling, leachate composition determined by experimentation. Where no figure is given the phase is not supersaturated.

Reaction Time	Structure and backscatterer path	N	R (Å)	σ^2 (Å^2)	ΔE^0 (eV)	S_0^2	R-factor
1 month	**Clarkeite**						
	O_{ax}	2	1.83(1)	0.0040(18)			
	O_{eq}	5	2.26(1)	0.0081(25)			
	Na	2	3.30(3)	0.0131(53)	2.41	1.0	0.0210
	Ca-Uranate						
	O_{ax}	2	1.83(1)	0.0035(6)			
	O_{eq}	4.5	2.25(1)	0.0061(6)			
	Ca	2	3.52(3)	0.0163(48)	2.1	1*	0.0198
21 months	**Clarkeite**						
	O_{ax}	2	1.87(0)	0.0045(6)			
	O_{eq1}	4.5	2.29(1)	0.0064(8)			
	O_{eq2}	1.5	2.50(2)	0.0063(29)			
	Na	2	3.41(2)	0.0084(33)	9.5*	1*	0.0147
	Ca-Uranate						
	O_{ax}	2	1.85(1)	0.0058(9)			
	O_{eq1}	4.5	2.24(1)	0.0055(12)			
	O_{eq2}	1.5	2.41(3)	0.0086(67)			
	Ca	2	3.53(2)	0.0108(30)	2.25*	1*	0.0172

SI Table 4. Alternative EXAFS fit parameters for 42 μM U(VI) equilibrated in young cement leachate and exposed to cement for 1 and 21 months. R = atomic distance; N = coordination number; σ^2 (Å^2) = Debye-Waller factor; ΔE^0 (eV) = energy shift from Fermi level; S_0^2 = amplitude factor; R-factor = normalised least squares residual. Coordination numbers were fixed and multiple scattering paths were included for the axial oxygens in all systems. * Denotes fixed parameter. Errors are presented in parentheses and are 1σ of last decimal.

Reaction time	Model	R-factor		
		Without the Na/Ca/Si shell	Reported fit and confidence (%) of the addition of the Na/Ca/Si shell	Addition or removal of the split equatorial oxygen shell
1 month	**Clarkeite**	0.0335	0.0210 99 %	0.0199
	Ca uranate	0.0327	0.0194 100 %	0.0192$^{\Delta}$
	Uranophane	0.0302	0.0178 99 %	0.0252
21 months	**Clarkeite**	0.0327	0.0147 100 %	0.0483
	Ca uranate	0.0402	0.0172 100 %	0.0290
	Uranophane	0.0415	0.0270 97 %	0.0500

SI Table 5. Comparison of the R-factors of fits to the EXAFS of cement exposed to cement leachate containing 42 μM U(VI). Subsequent fits have either the Ca, Na, or Si shell removed, or the split equatorial oxygen shell added or removed. Confidence was determined using the F-test (Downward et al., 2007). $^{\Delta}$ Fit contained numerous correlations.

References

Downward, L., Booth, C. H., Lukens, W. W. and Bridges, F. (2007). A variation of the F-Test for determining statistical relevance of particular parameters in EXAFS fits. *In:* Hedman, B. & Painetta, P. (eds.) *X-Ray Absorption Fine Structure-XAFS13.* Melville: American Institute of Physics.

Chapter 6. Interaction of U(VI) with Mn minerals: An EXAFS and reversibility study

This chapter is a manuscript prepared for submission in the journal *Environmental Science & Technology*. Supporting Information provided with this manuscript is included following the manuscript.

Interaction of U(VI) with Mn minerals: An EXAFS and reversibility study

Rosemary Hibberd,[1,2] Nicholas D. Bryan,[1,3] Adam J. Fuller,[1] Samuel Shaw,[2] Katherine Morris,[2] Gareth T. W. Law[1]

[1]Centre for Radiochemistry Research, School of Chemistry, The University of Manchester, Oxford Road, Manchester, M13 9PL, UK.

[2]Research Centre for Radwaste Disposal, School of Earth, Atmospheric and Environmental Sciences, The University of Manchester, Oxford Road, Manchester, M13 9PL, UK.

[3]National Nuclear Laboratory, 5th Floor, Chadwick House, Birchwood Park, Warrington Road, Warrington, WA3 6AE, UK.

[*]Corresponding author, Tel: +44 (0) 161 306 0514; Email: gareth.law@manchestester.ac.uk

Keywords: uranium, manganese oxide, rhodochrosite, XAS, reversibility

Abstract

Manganese minerals are ubiquitous and potentially reactive phases that could retard the migration of radionuclides through the geosphere. Here, we investigate the interaction of U(VI) with δ-Mn(IV)O_2, triclinic (Na)-birnessite [$Na_{0.5}Mn(III/IV)_2O_4 \cdot 1.5H_2O$], hausmannite [$Mn(II/III)_3O_4$], and rhodochrosite [$Mn(II)CO_3$] under alkaline to circumneutral pH conditions relevant to the geological disposal of radioactive waste and radioactively contaminated land. Uranium uptake onto all of the Mn oxide minerals was strong (> 84 %) across the whole pH range and at both U(VI) concentrations investigated (5.27×10^{-5} μM and 1 μM). Adsorption to rhodochrosite was slower and less extensive, with 25 ± 0.8 % of the U(VI) remaining in solution. Evidence of partially irreversible sorption, and the formation of edge-sharing bidentate inner-sphere adsorption complexes, were identified by X-ray Absorption Spectroscopy (XAS) and desorption experiments in systems containing δ-MnO_2 and hausmannite. Inner-sphere adsorption complexes were also identified on the surface of rhodochrosite and in triclinic (Na)-birnessite systems after 4 hours of reaction. However, after 720 hours, U(VI) in the triclinic (Na)-birnessite system was found to have migrated into the mineral's interlayer, located in Na^+ sites. Together, these results suggest that Mn minerals will be an important factor controlling U(VI) transport in the geosphere. The identification of irreversible sorption to δ-MnO_2 and hausmannite suggests that these minerals will be particularly important in retarding U(VI) migration.

1. Introduction

Being able to accurately predict the mobility of uranium (U) in the geosphere is crucial to the safe implementation of radioactive waste geological disposal (Morris et al., 2011). Uranium dominates the geodisposal waste inventory (Marshall et al., 2014; RWM, 2015) and given its long half-life (4.5×10^9 years for U-238), it will eventually escape primary containment. Once released into the subsurface, U sorption to minerals and/or co-precipitation reactions could act to lessen its migration (Fox et al., 2006; Chardon et al., 2008; Sherman et al., 2008; Ilton et al., 2012b; Macé et al., 2013; Marshall et al., 2014). However, many repository designs for the geological disposal of intermediate level waste (ILW) use cementitious materials that will weather and create an alkaline, cation rich environment (a so-called Chemically Disturbed Zone (CDZ)) upon ingress of groundwater into the facility (NDA, 2010b; Butcher et al., 2012; Moyce et al., 2014). U(VI) is expected to be relatively stable in the CDZ (Gaona et al., 2012), but cement weathering should encourage hydrolysis of U and precipitation of poorly soluble alkali and alkali-earth uranates (Yamamura et al., 1998; Gorman-Lewis et al., 2008), lessening groundwater transport; however, some U will still be transported out of the repository into the surrounding host rock. Here, the groundwater pH will buffer towards ~ pH 7 with time and distance from the repository. Understanding U migration through this environment will require a detailed assessment of U interaction with common minerals under alkaline to circumneutral ambient pH. This information may also prove useful in predicting U behaviour in shallow aquifers at nuclear contaminated sites (e.g. Sellafield, Savannah River; MacKenzie et al., 1999; Barnett et al., 2000; Bea et al., 2013; Sellafield Ltd., 2014).

The transport of U(VI) in subsurface environments is predominately controlled by reduction to U(IV) (Law et al., 2011; Renshaw et al., 2011), dissolution/precipitation (Giammar and Hering, 2001; Duff et al., 2002), and sorption/desorption reactions (NDA, 2010a; and references therein). Uranium (as U(VI)) has been observed to sorb to a wide

range of mineral surfaces, including clays (Pabalan and Turner, 1997; Sylwester et al., 2000; Missana et al., 2004), silicate minerals (Fox et al., 2006; Wang et al., 2014), cements (Harfouche et al., 2006; Wieland et al., 2010; Tits et al., 2011; Gaona et al., 2012; Macé et al., 2013), and metal oxide and hydroxide minerals (Lenhart and Honeyman, 1999; Moyes et al., 2000; Sherman et al., 2008; Yusan and Akyil, 2008; Sun et al., 2012). Uranium can also be incorporated into a range of neo-forming minerals, for example calcite (Reeder et al., 2000) and iron oxides (Ilton et al., 2012a; Marshall et al., 2014). However, other actinides (e.g. Np and Pu) have also been reported to associate preferentially with Mn minerals in heterogeneous environmental samples (Duff et al., 1999; Powell et al., 2006; Francis and Dodge, 2015). Manganese minerals are common in the environment and will likely pervade both the far-field of a geological disposal facility (GDF) and shallow subsurface and contaminated nuclear sites (Roy, 1981; Dixon et al., 1990; Post, 1999; NDA, 2010a). The interaction of U with Mn minerals therefore presents a potentially significant mechanism for retarding U(VI) subsurface migration, particularly given that analogous iron oxide and hydroxide minerals have been found to be important for U (Lenhart and Honeyman, 1999; Moyes et al., 2000; Sherman et al., 2008; Yusan and Akyil, 2008; Ilton et al., 2012a; Li and Kaplan, 2012; Sun et al., 2012; Marshall et al., 2014).

Mn oxides in natural systems are predominantly formed by bacteria *via* the catalysis of Mn(II) oxidation, which occurs even at low dissolved O_2 concentrations (Tebo, 1991; Clement et al., 2009). These minerals are therefore expected to persist under the mildly reducing conditions such as those expected in the far-field of a GDF. Their formation is also expected where groundwater contains relatively high levels of Mn(II), as has been found at radioactively contaminated sites (Campbell et al., 2011). Mn(IV) and Mn(III) containing Mn oxides can also oxidise immobilised U(IV) to much more soluble U(VI) (Fredrickson et al., 2002; Liu et al., 2002; Chinni et al., 2008), meaning that adsorption and desorption reactions to/from these highly biogeochemically active phases could exert

significant control over U mobility. The removal of U(VI) from solution by birnessite, δ-MnO_2, and birnessite coated sand has been observed above ~ pH 6 under atmospheric conditions (Al-Attar and Dyer, 2002; Zou et al., 2010; Mukherjee et al., 2013). Extensive (> 95 %) adsorption to δ-MnO_2 has been observed in the absence of carbonate at relatively high (50 μM) U(VI) concentrations, with a mixture of surface complexes formed (Wang et al., 2013). While Webb et al. (2006) found that when < 1 μM U(VI) was present during the formation of biogenic MnO_2, the U(VI) adsorbed as a bidentate surface complex. Further, extended X-ray absorption fine structure spectroscopy (EXAFS) has been used to study U associated with hexagonal birnessite and K-birnessite under acidic conditions, with pH dependent edge-sharing bidentate and layer vacancy-capping sorption sites identified (Brennecka et al., 2011; Rihs et al., 2014).

Despite the aforementioned work, U(VI) interactions with Mn minerals are still poorly understood, especially under the alkaline, low carbonate conditions relevant to UK ILW geological disposal. Reflecting this, here we use batch sorption and desorption experiments in conjunction with X-ray absorption spectroscopy techniques to investigate the interaction and degree of reversibility of U(VI) when reacted with a range of environmentally relevant Mn minerals that encompass a range of Mn oxidation states (namely: δ-$Mn(IV)O_2$, triclinic (Na)-birnessite [$Na_{0.5}Mn(III/IV)_2O_4 \cdot 1.5H_2O$], hausmannite [$Mn(II/III)_3O_4$], and rhodochrosite [$MnCO_3$]) across pH range (7.5-10.5).

2. Materials and methods

2.1. Mineral preparation

Rhodochrosite was purchased from Alfa Aesar. δ-MnO_2, triclinic (Na)-birnessite, and hausmannite were synthesised chemically, with the preparation methods detailed below. All chemicals were analytical reagent grade and all water was Milli-Q (18.2 MΩ). Mineral

formation was confirmed using X-ray diffraction (XRD; Bruker D8Advance; Supporting Information Figure 1) prior to use. Scanning electron microscopy (SEM; FEI XL30 ESEM-FEG; Supporting Information Figure 2) was utilised to confirm morphology and energy dispersive X-ray spectroscopy (Supporting Information Figure 3) was performed to confirm mineral purity. SEM samples were prepared on standard 1 cm aluminium stubs with an adhesive carbon pad and carbon coated prior to imaging to limit charging. The surface areas of the δ-MnO_2, triclinic (Na)-birnessite, hausmannite, rhodochrosite were measured using N_2 Brunauer-Emmett-Teller (BET) analysis.

2.1.1. Mn mineral synthesis

The δ-MnO_2 synthesis was adapted from Villalobos et al. (2003). $KMnO_4$ solution (0.2 M, 1.28 L) was added slowly, over 5 minutes, with vigorous stirring, to a solution of $MnCl_2$ (0.3 M, 1.28 L). NaOH (0.5 M, 1.44 L) solution was then added to the mixture slowly over 35 minutes, with vigorous stirring, to form a black precipitate. The suspension was then allowed to settle for 4 hours. The pH of the supernatant was then measured as 7 and the majority of the supernatant was decanted and disposed of. The remaining suspension was then centrifuged (17000 *g*, 20 minutes, 20 °C) and the majority of the supernatant was discarded. The resulting mineral paste was washed 5 times with NaCl (1 M) and then 10 times with water, with centrifuging (17000 *g*, 20 minutes, 20 °C) conducted between washes. The mineral suspension was finally adjusted to pH 8 using NaOH and was then stored below 5 °C in the dark prior to use.

The triclinic (Na)-birnessite synthesis was adapted from Villalobos et al. (2003). $MnCl_2$ (0.16 M, 0.32 L) solution was added slowly, over 40 minutes, to a NaOH (7.6 M, 0.36 L) solution, to form a pink gel like phase. A $KMnO_4$ (0.2 M, 0.32 L) solution was then added to the mixture slowly, over 50 minutes, with vigorous stirring, to form a dark grey

precipitate. The mixture was stirred for a further 2 hours before heating to 55 °C for 24 hours. The supernatant was then discarded and the mineral paste was washed 5 times with NaCl (1 M), followed by washing with Milli-Q (MQ) water until the pH of the suspension reached 9.8, with centrifuging (17000 *g*, 20 minutes, 20 °C) performed between steps. The mineral paste was centrifuged (17000 *g*, 20 minutes, 20 °C) between washing steps and stored in the dark and below 5°C prior to use.

The hausmannite synthesis was adapted from McArdell et al. (1998). All solutions were sparged with N_2 prior to reaction. The synthesis and subsequent manipulations were carried out under N_2 to prevent the conversion of hausmannite to manganite (Kirillov et al., 2009). A solution of $MnSO_4$ (0.06 M, 1.5 L) was heated to 60 °C before the addition of H_2O_2 (8.8 M, 30.75 mL). To this NH_4OH (0.2 M, 0.45 L) solution was added slowly (1 mL per second). The resulting suspension was heated to 95 °C and maintained at this temperature for 6 hours before being allowed to cool overnight. The resulting mineral was washed 10 times with water (with centrifugation between washes; 17000 *g*, 20 minutes, 20 °C), re-suspended, and stored under N_2.

2.2. Uranium spike preparation

^{232}U was separated from its daughters prior to use using a 2 mL UTEVA resin column (Eichrom) that was pre-conditioned with HCl (5 M, 3 x 5 mL). The unseparated $^{232}U(VI)Cl_2$ stock solution (80 kBq mL^{-1}, 2 mL) was adjusted to 5 M HCl and loaded onto the column. $^{228}Th(IV)$ and its daughters were eluted from the column using HCl (5 M). The $^{232}U(VI)$ was then eluted using HCl (0.1 M). A more concentrated depleted uranium (DU) stock solution was made for use in higher concentration experiments by dissolving UO_3 (1 g) in HCl (1 M, 10 mL). In order to keep the volume and acidity of the U spikes used in

subsequent experiments as low as possible, both the purified $^{232}U(VI)$ and DU stock solutions were concentrated and the pH adjusted to 3 using HCl and MQ water.

2.3. Sorption experiments

Batch sorption experiments investigating U(VI) uptake by each of the minerals were carried out under CO_2 controlled conditions. Tracer level experiments were carried out using $^{232}U(VI)$. DU was used in experiments needing higher U concentrations and samples of the mineral phase from these experiments were analysed by XAS to determine the U oxidation state and coordination environment on solids. Experiments containing δ-MnO_2, triclinic (Na)-birnessite, or hausmannite were performed at pH 10.5, 9.0, and 7.5. Due to carbonate equilibria, experiments containing rhodochrosite were performed at pH 9.3. All experiments were performed in triplicate.

2.3.1. $^{232}U(VI)$ tracer sorption experiments

Mineral (0.01 g) was added to 100 mL batch experiments, containing $NaClO_4$ (0.01 M) as background electrolyte. These were adjusted to the appropriate pH using HCl and NaOH, prior to spiking with $^{232}U(VI)$ (40 kBq mL^{-1}) to give a ^{232}U concentration of 10 Bq mL^{-1}. Samples were taken periodically, centrifuged (10 minutes, 15000 *g*), acidified, mixed with liquid scintillation fluid (Scintisafe 3, Fisher Scientific or later, Optiphase Hisafe 3, Perkin Elmer, investigations using U^{232} found these gave comparable results) and analysed using a 1220 QUANTULUS ultra-low level scintillation spectrometer to determine the concentration of ^{232}U remaining in solution. Samples were also taken to monitor the pH.

2.3.2. Higher concentration U(VI) sorption experiments

Mineral (0.1 g) was added to 1 L batch experiments, containing $NaClO_4$ (0.01 M) as background electrolyte. These were adjusted to the appropriate pH using HCl and NaOH, prior to spiking with DU (0.5 mg mL^{-1}) to give a U(VI) concentration of 1 μM. Samples were taken periodically, centrifuged (10 minutes, 15000 *g*), acidified, diluted and analysed by inductively coupled plasma – mass spectrometry (ICP-MS; Agilent 7500cx) to determine U and Mn concentrations in solution. Samples were also taken to monitor the pH, and the solids were collected for XAS (see below). An additional pH 7.5 birnessite experiment was also set up, this was stopped after 4 hours to provide an additional time point for XAS.

2.4. Reversibility experiments

The reversibility of the sorption of both $^{232}U(VI)$ and depleted U(VI) to each of the minerals was investigated at pH 10.5, 9.0, and 7.5. Experiments were performed in triplicate and set up in the same manner as the sorption reactions (described in section 2.3), except that experiments were scaled down to 50 mL. Equilibration prior to desorption was confirmed by determining the solution U concentration. The experiments were then centrifuged (20 minutes, 6000 *g*) and the supernatant was replaced with an identical solution without any added U(VI) before re-suspending the mineral. Samples were taken periodically and analysed, as described above (section 2.3), to determine the pH and U concentration (as well as Mn concentration in experiments containing 1 μM DU).

2.5. X-ray Absorption Spectroscopy (XAS)

Mineral samples labelled with DU were analysed by XAS to examine the speciation and local coordination environment of U on the solids. Analysis was performed at beamline B18 at Diamond Light Source, UK and the MARS beamline at the SOLIEL synchrotron, France on the U-L_{III} absorption edge using a Si(111) monochromator in both cases. Samples were analysed in fluorescence mode using a 36 element (Diamond) or a 12 element (Soleil) Ge detector. Samples were prepared by centrifuging (6000 *g* for 5 minutes) to obtain a mineral paste with a U-loading of > 1000 mg kg^{-1}. The paste was then mounted in a double contained, gas tight XAS sample cell. An yttrium foil reference was used for energy calibration at both beamlines. Background subtraction, data normalization, and fitting to the EXAFS spectra were performed using the Demeter software package (Ravel and Newville, 2005). For EXAFS fitting, FEFF 6 was used to calculate structural models of U sorbed to Mn oxides. All data were fit in R-space (typical range, 1 – 4 Å).

3. Results and discussion

3.1. Sorption experiments

3.1.1. ^{232}U(VI) tracer experiments

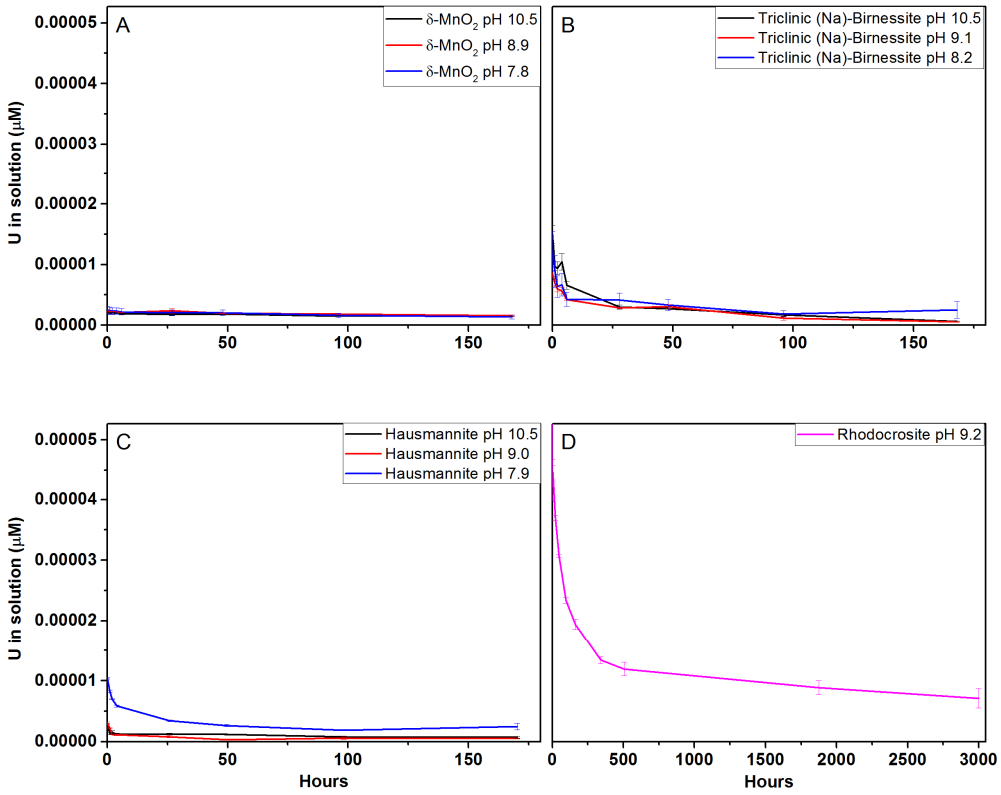

Figure 1. ^{232}U remaining in solution in systems containing 0.1 g L^{-1} (A) = δ-MnO_2, (B) = triclinic (Na)-birnessite, (C) = hausmannite, and (D) = rhodochrosite. Systems contained 0.01 M $NaClO_4$ as background electrolytes and the initial ^{232}U concentration was 5.27 x 10^{-5} μM. Error bars are 1σ. (For pH measurements see Supporting Information Figure 5).

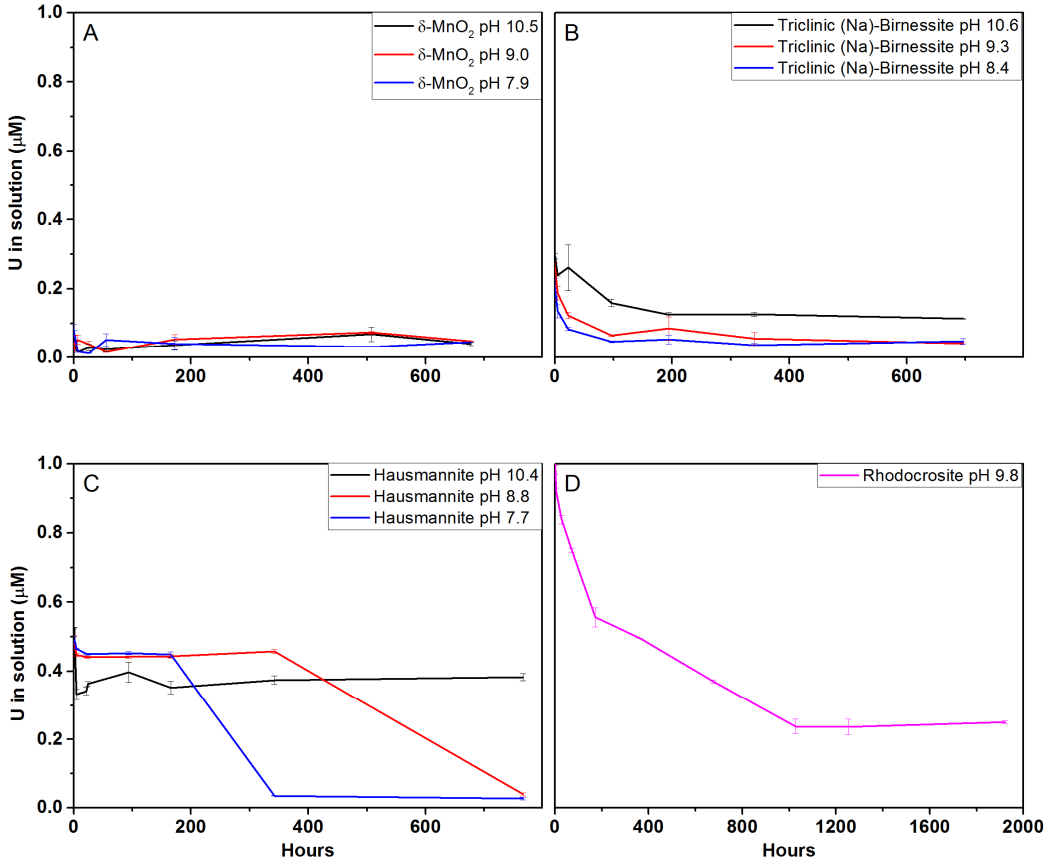

Figure 2. U(VI) remaining in solution in systems containing 0.1 g L^{-1} (A) = δ-MnO_2, (B) = triclinic (Na)-birnessite, (C) = hausmannite, and (D) = rhodochrosite. Systems contained 0.01 M $NaClO_4$ as background electrolytes and the initial U(VI) concentration was 1 μM. Error bars are 1σ. (For pH measurements see Supporting Information Figure 6).

The uptake of U(VI) by a range of Mn minerals (δ-MnO_2, triclinic (Na)-birnessite, hausmannite, and rhodochrosite) was investigated over a circumneutral to alkaline pH range. Following the addition of ^{232}U(VI) to tracer concentration experiments, to give an initial solution concentration of 5.27 x 10^{-5} μM, ^{232}U(VI) was rapidly removed from solution across the whole pH range in all mineral systems (Figure 1). Removal was fastest in the presence of δ-MnO_2, here 96 ± 0.4 % of the added ^{232}U(VI) was removed from solution within 10 minutes (0.167 hours) and equilibrium (3 ± 0.3 % (1.7 x 10^{-6} μM) U(VI) remaining in solution) was attained within 96 hours (Figure 1A). Triclinic (Na)-birnessite

and hausmannite removed at least 71 ± 2 % and 80 ± 0.6 % of the added ^{232}U(VI) from solution, respectively, within the first 10 minutes. Removal then continued over the next 168 and 96 hours, respectively, until equilibrium was reached with < 5 % ^{232}U(VI) remaining in solution in all systems (Figure 1B and 1C). Varying the pH of the δ-MnO_2 and triclinic (Na)-birnessite systems, through circumneutral to alkaline conditions, did not influence either the rate, or the extent of uptake in tracer ^{232}U(VI) experiments (Figure 1A and 1B). However, in the hausmannite systems, while the concentration of ^{232}U(VI) remaining in solution at equilibrium was similar across the pH range (1.4 ± 0.5 % at pH 10.5; 1.0 ± 0.2 % pH 9.0; 4.7 ± 2.2 % at pH 7.9), the rate at which equilibrium was achieved was substantially slower in the pH 7.9 systems. Interestingly, this system took 96 hours to reach equilibrium, as opposed to 4 hours in the pH 9.0 and 10.5 systems (Figure 1C); the reason for this is unclear since it seems to contrast with observations made in more (1 μM) concentrated U(VI) systems (section 3.1.2, Figure 2C).

Reaction of tracer concentrations of ^{232}U(VI) with rhodochrosite was much slower and sorption experiments were halted after 4 months (due to ^{228}Th ingrowth) before equilibrium was attained (Figure 1D). At this time, 13.5 ± 6 % (7.1 μM) of the ^{232}U(VI) still remained in solution (Figure 1D). This could be partially due to the lower surface area of rhodochrosite (8.22 ± 0.04 m^2g^{-1}), which is significantly lower than that of δ-MnO_2, triclinic (Na)-birnessite, and hausmannite (101.5 ± 0.5 m^2 g^{-1}, 84.7 ± 0.8 m^2 g^{-1}, and 48.6 ± 0.4 m^2 g^{-1}, respectively). The reaction of ^{232}U(VI) with rhodochrosite is slower than that observed to the other Mn minerals, with at least 5 times less U(VI) having been removed from solution after 10 minutes (0.167 hours, Figure 1). However, while the surface areas differ by an order of magnitude they remain present in vast excess compared to the low ^{232}U(VI) concentration of 5.27 x 10^{-5} μM ^{232}U(VI). This implies that there is an additional reason for the slow uptake of ^{232}U(VI) by rhodochrosite, suggesting the mechanism of uptake is not simple adsorption to the surface as is likely for the other Mn

minerals. As rhodochrosite is a carbonate mineral the formation of U(VI) carbonate complexes in solution is expected for this system. These are expected to be in rapid equilibrium with aqueous cationic U(VI) species and are therefore only expected to delay sorption momentarily, or to prevent it entirely. Indeed, sorption of U(VI) to calcite ($CaCO_3$, an isostructral carbonate mineral) has been investigated assuming steady state has been reached within a few days (Elzinga et al., 2004; Rihs et al., 2004). This slow uptake of U(VI) by rhodochrosite is consistent with the precipitation, or surface-mediated precipitation, of a U(VI) containing phase (Giammar and Hering, 2001; Smith et al., 2015), or the incorporation of U(VI) into the rhodochrosite structure (Marshall et al., 2014).

3.1.2. Higher concentration sorption experiments

When higher (1 μM) concentrations of U(VI) were used to study the interaction with δ-MnO_2, equilibrium was reached within 10 minutes with < 5 % (< 0.05 μM) U(VI) remaining in solution, and with the extent and rate of U(VI) unaffected by solution pH (Figure 2A). This suggests that δ-MnO_2 has a high affinity for U(VI) and would readily remove it from circumneutral and alkaline solutions upon contact across a range of concentrations. In systems containing triclinic (Na)-birnessite, equilibrium was established within the first 96 hours of reaction, although significant removal (70 – 80 %) was seen during the first 10 minutes (Figure 2B). The kinetics of this reaction were also unaffected by pH. However, equilibrium was reached with 6 ± 0.5 % and 5 ± 0.6 % (0.06 and 0.05 μM), respectively, remaining in solution in systems at pH 9.3 and 8.4. In contrast, at pH 10.6, 16 ± 2 % (0.16 μM) of the added U(VI) remained in solution at equilibrium (Figure 2B). Triclinic (Na)-birnessite has a point of zero charge (PZC) of ~ pH 2 – 3 (McKenzie, 1981; Appelo and Postma, 1999; Yang and Wang, 2001; Tan et al., 2008) and is therefore expected to be negatively charged over the alkaline to circumneutral pH range investigated in this study. Consequently, reaction of cationic U(VI) species with the

surface is expected to occur via the cationic uranyl species UO_2^{2+}. Speciation modelling (Supporting Information Table 1) and Choppin (2006) suggest that the proportion of positively charged uranyl species decreases with increasing pH, and that negatively charged uranyl hydroxide species will dominate U(VI) speciation at pH 10.5. This suggests that observed reduction in the reactivity of U(VI) with triclinic (Na)-birnessite at pH 10.6 (84 ± 2 %, as opposed to > 94 % sorption) is likely due to increased competition from hydroxide ions, meaning that the position of equilibrium is shifted away from U(VI) complexation with the mineral and towards the formation of aqueous U(VI) species at increased pH.

In contact with hausmannite, 50 – 70 % of the 1 μM U(VI) was removed from solution within the first 10 minutes of reaction (Figure 2C). However, the remaining 30 – 50 % of the U(VI) was stable in solution for 168 – 336 hours, after which time the U(VI) concentration in the pH 8.8 and 7.7 systems decreased further to 0.04 and 0.03 μM (4 ± 0.9 and 3 ± 0.7 %), respectively, after 720 hours. In the pH 10.4 systems, 38 ± 2 % of the U(VI) remained stable in solution, in contact with hausmannite, for 720 hours. Hausmannite can oxidise to manganite in the presence of oxygen; however, analysis of the mineral morphology before and after sorption experiments by SEM (Supporting Information Figure 4) confirmed that no appreciable amount of oxidation occurred during the course of the experiment. The PZC of hausmannite is disputed with reported values ranging from < pH 5 to > pH 10 (Backes et al., 1995; Shaughnessy et al., 2003; Wilk et al., 2005). However, similarly to triclinic (Na)-birnessite, it is likely that the supressed sorption of U(VI) to hausmannite at pH 10.4, when compared to pH 8.8 and 7.7, was due the decrease in cationic U(VI) solution species at alkaline pH (Supporting Information Table 1) (Choppin, 2006) and therefore reduced affinity for a negatively charged surface. The decrease in U(VI) uptake at alkaline pH is in contrast to the tracer level hausmannite containing systems, in which removal of U(VI) from solution appeared to be slower in the

lowest pH (7.9) systems (section 3.1.1, Figure 1C). This could suggest that either the sorption capacity has been exceeded in the high 1 µM U(VI) experiments, or that the mechanism of U(VI) uptake was different at different U(VI) concentrations.

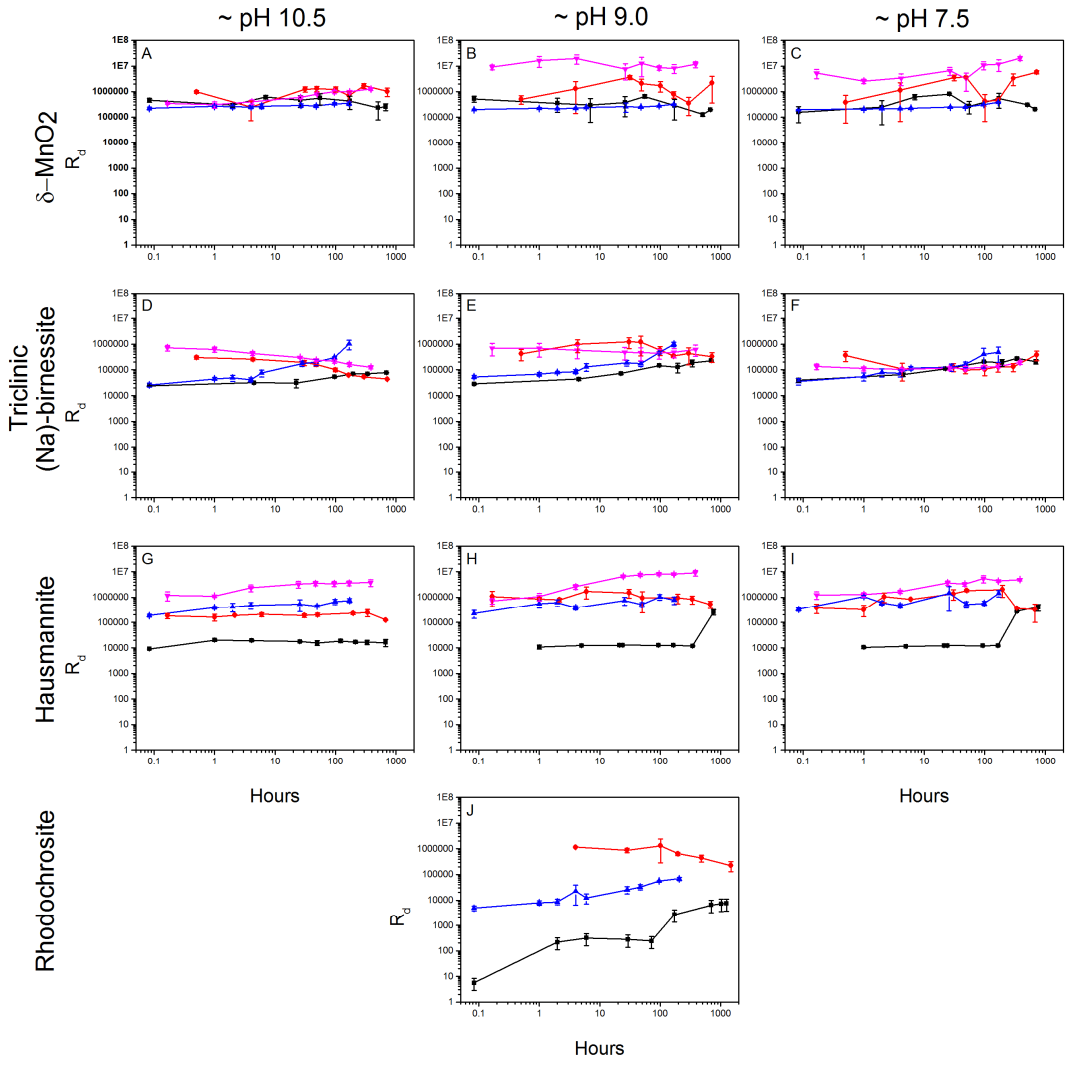

Figure 3. R_d(a) and R_d(d) values for sorption and reversibility experiments investigating the reaction of U(VI) with a range of Mn minerals (0.1 g / L) at circumneutral to alkaline pH. Black = 1 µM sorption; Red = 1 µM desorption; Blue = 5.27 x 10^{-5} µM sorption; Pink = 5.27 x 10^{-5} µM desorption. A = δ-MnO_2 pH 10.5; B = δ-MnO_2 pH 9.2; C = δ-MnO_2 pH 7.8; D = triclinic (Na)-birnessite pH 10.5; E = triclinic (Na)-birnessite pH 9.2; F = triclinic (Na)-birnessite pH 8.1; G = hausmannite pH 10.5; H = hausmannite pH 9.1; I = hausmannite pH 7.8; J = rhodochrosite pH 9.5.

The interaction of 1 µM U(VI) with rhodochrosite (Figure 2D) was much slower and less extensive, with equilibrium taking 42 days to be established and with 25 ± 0.8 % (0.25 µM) U(VI) remaining in solution. Again, the lower surface area of rhodochrosite could be partially responsible for the lower reactivity when compared to the other Mn minerals. The lower surface area of rhodochrosite is more likely to have an effect in the more concentrated 1 µM depleted U(VI) system since the excess of surface sites for sorption will be reduced. However, the kinetics of U(VI) removal from solution are the same at both concentrations (Figure 3J), suggesting the mechanism of uptake is the same, and therefore that the slow sorption kinetics are not purely due to the lower surface area of rhodochrosite.

Overall, the sorption of U(VI) to δ-MnO_2, triclinic (Na)-birnessite, hausmannite, and rhodochrosite was found to be similar to sorption to Fe minerals, which are known to be important in controlling U(VI) migration through the subsurface. This similar sorption was confirmed when comparable R_d(a) values were calculated for sorption experiments (68000 – 75000; section 3.2, Figure 3) (Li and Kaplan, 2012).

3.2. Reversibility experiments

The solution phase was removed from the sorption experiments after they attained equilibrium. It was then replaced by an identical, pH adjusted, U-free solution. The U concentration in the solution was then monitored to determine whether equilibrium was re-established or whether there was an element of irreversibility in the system. R_d values were calculated (Equation 1) for both the adsorption (R_d(a)) and desorption (R_d(d)) reactions at both U(VI) concentrations investigated. The results are summarised in Figure 3.

$$R_d = \frac{concentration\ on\ mineral\ (mol\ kg^{-1})}{concentration\ in\ solution\ (mol\ L^{-1})} \qquad \text{(Equation 1)}$$

Sorption of U(VI) to δ-MnO_2 produced the highest R_d(a) values, showing that, of the four Mn minerals studied, U(VI) sorbed most strongly to δ-MnO_2. The R_d(a) values for adsorption to δ-MnO_2 were comparable at both U(VI) concentrations and across all 3 pHs (Figure 3A-C), suggesting that the mechanism of uptake was the same in all six δ-MnO_2 sorption systems. The R_d(d) values calculated for the desorption of ^{232}U(VI) from δ-MnO_2 across the pH range are ~ 1 – 2 orders of magnitude higher than those in the sorption experiments (Figure 3A-C). This means that equilibrium was not fully re-established, and therefore that the uptake of U(VI) by δ-MnO_2 was at least partially irreversible in the tracer ^{232}U(VI) systems. Therefore, U(VI) must be associated with δ-MnO_2 by at least two different mechanisms, one reversible and one irreversible. In the higher concentration systems irreversibility was only observed in the circumneutral system (Figure 3A-C). Irreversibility can result from processes where the element of interest becomes an intrinsic part of the structure (Fuller et al., 2015), such as incorporation or surface-precipitation, or redox processes (Brookshaw et al., 2015), which are unlikely in the case of U(VI) reacting with δ-Mn(IV)O_2, or the formation of strong adsorption complexes (Pan et al., 2004).

R_d(a) values for U(VI) uptake by hausmannite from the higher (1 μM) concentration sorption experiments were significantly lower (~ 1 order of magnitude; Figure 3G-I) than those calculated for tracer ^{232}U(VI) (16000 ± 5000 versus 750000 ± 100000). This is consistent with qualitative analysis of U(VI) sorption data (section 3.1), and suggests that sorption was stronger in the tracer ^{232}U(VI) systems. R_d(d) values were significantly higher than R_d(a) values across the pH and concentration range investigated (Figure 3G-I), suggesting that like δ-MnO_2, the uptake of U(VI) by hausmannite was partially irreversible. All the hausmannite systems appeared to have reached equilibrium within the first 10 minutes of reaction. However, in some (pH 7.7 and 8.4) of the higher concentration systems further rapid uptake of U(VI) was observed between 168 and 672 hours. It is possible that this was an artefact of the way in which the experiments were conducted, or

due to an external factor, such as the disturbance of the systems or the ingress of oxygen. However, no evidence of the oxidation of hausmannite to manganite was visible in environmental SEM (ESEM) images of reacted hausmannite (Supporting Information Figure 4), suggesting that the observed rapid U(VI) uptake was not due to alteration of the mineral. Interestingly, no additional U(VI) uptake was observed during the course of the 1 month pH 10.5 sorption experiment, and occurred at different time points in the pH 9.0 and 7.5 sorption experiments, as well as occurring in the pH 7.5 desorption experiment. This implies that it was real and could be due to a second, kinetically slow sorption mechanism, the onset of which was likely pH dependent.

At ~ pH 10.5 in systems containing triclinic (Na)-birnessite, U(VI) uptake is weaker in the more concentrated (1 μM U(VI)) experiments (Figures 1B and 2B), an effect which became less pronounced as the pH decreased. Therefore, at ~ pH 10.5, $R_d(a)$ values in the tracer $^{232}U(VI)$ sorption experiments ($10^7 \pm 400000$) were much higher than those in higher concentration systems (78000 ± 1000), indicating stronger uptake at lower U(VI) concentrations. Comparison of $R_d(d)$ values with the corresponding $R_d(a)$ values (Figure 3D-F), shows that in each case either the values were within experimental error, or the $R_d(a) > R_d(d)$. This is typical of a reversible system (Missana et al., 2004) and suggests U(VI) is taken up reversibly by triclinic (Na)-birnessite.

Uptake of U(VI) by rhodochrosite had a larger $R_d(a)$, and was therefore stronger, at the tracer $^{232}U(VI)$ concentration (68000 ± 10000) than at the higher concentration (7400 ± 4000). The desorption of tracer $^{232}U(VI)$ concentrations from rhodochrosite could not be studied due to the long time period required to reach equilibrium and the short window available for analysis prior to the ingrowth of ^{228}Th. At the higher concentration, $R_d(d) > R_d(a)$ at the final time point. However, while equilibrium was not reached in the desorption experiment, it is likely that, given the slow uptake kinetics observed (Figures 1D and 2D), $R_d(d) = R_d(a)$ at equilibrium and that U(VI) uptake would be reversible. This

slow release of U(VI) would be consistent with the U(VI) having become incorporated into rhodochrosite, or reduced to U(IV) and subsequently precipitated out of solution. The incorporation of U into minerals isostructural to rhodochrosite, such as calcite (Sturchio et al., 1998; Kelly et al., 2003) and siderite (O'Loughlin et al., 2010) has been observed. The interaction of U(VI) with siderite and calcite is also sometimes associated with its reduction to U(IV) (Ithurbide et al., 2009; Ithurbide et al., 2010; O'Loughlin et al., 2010), but reduction is not always observed (Reeder et al., 2000; Kelly et al., 2003; Rihs et al., 2004).

3.3. X-ray Absorption Spectroscopy

3.3.1. X-ray Absorption Near Edge Spectroscopy (XANES)

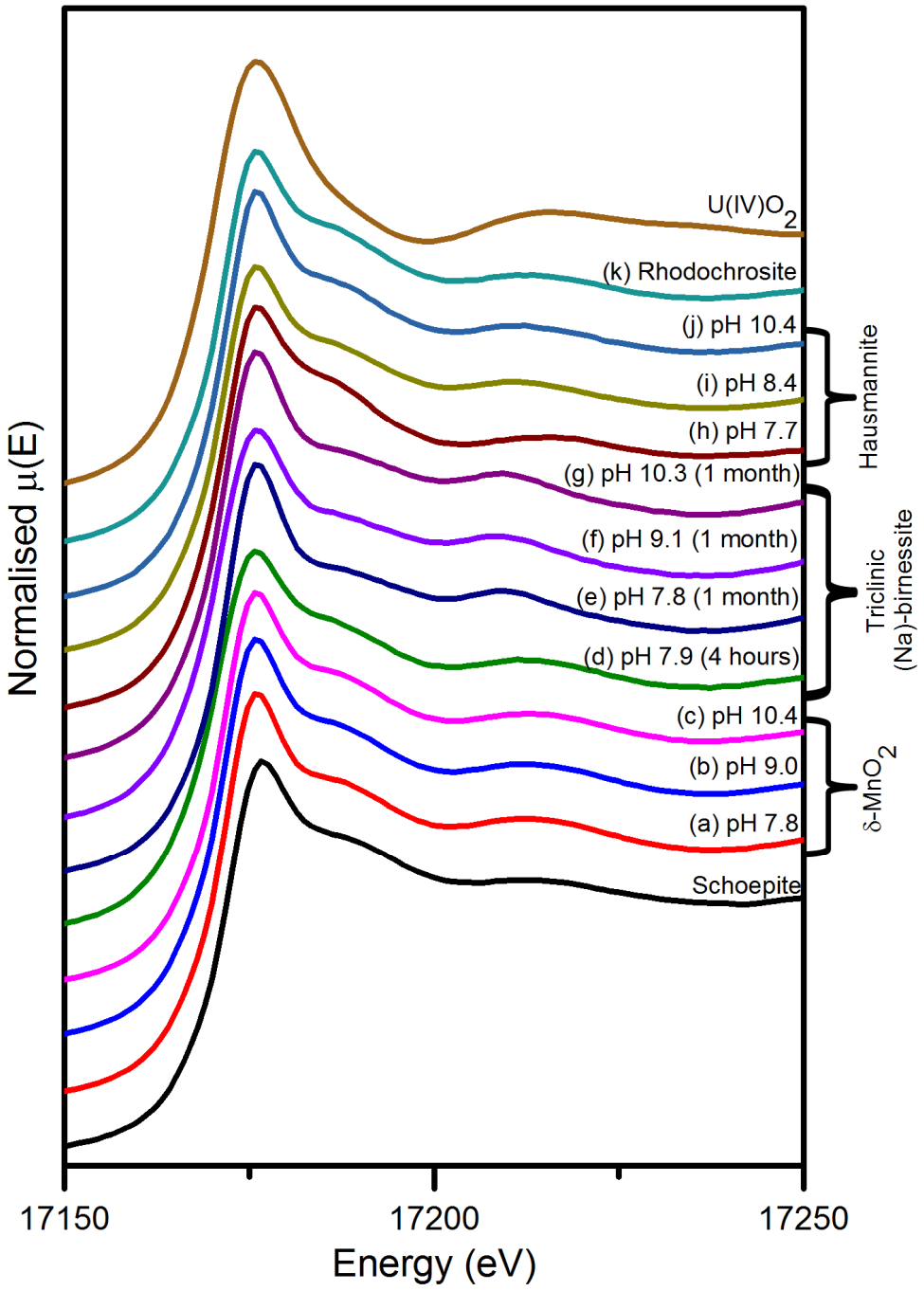

Figure 4. U L_{III}-edge XANES spectra of Mn minerals equilibrated with 1 μM U(VI) compared with reference spectra. Sample descriptions are summarised in Table 1.

XANES data were collected from the U-L_{III} edge of select samples of four minerals exposed to 1 μM U(VI) at a range of pHs from alkaline to circumneutral (Figure 4). The spectra were compared to a UO_2 and schoepite ($UO_3 \cdot 2H_2O$) standard (Opel et al., 2007; Scheinost et al., 2013). The U in all samples was clearly present as U(VI), owing to the uniform presence of the uranyl dioxygenyl multiple scattering resonance feature at ~ 17190 eV (Farges et al., 1992). The edge position of U(VI) in schoepite is 17172 eV (Marshall et al., 2014) while that of U(IV) is 17168 eV (Francis and Dodge, 2008). All edge positions in the experimental samples were within 1.0 eV of the expected U(VI) edge position (Supporting Information Table 2), confirming the presence of U(VI). However, during analysis of the pH 10.4 and 7.7 hausmannite samples it was not possible to collect an inline calibration, while reference foils taken before and analysis showed beam drift.

The XANES data show that no U(VI) reduction took place in the presence of any of the Mn minerals investigated (Figure 4). The abiotic reduction of U(VI) to U(IV) by Fe(II), and the subsequent precipitation of U(IV) hydroxide phases has previously been observed in natural sediments and Fe(II) containing minerals (Regenspurg et al., 2009; Hyun et al., 2012; Latta et al., 2012; Singer et al., 2012; Fox et al., 2013). However, the redox couples for the reduction of U(VI) to U(IV) by hausmannite [$Mn(II/III)_3O_4$] and rhodochrosite [$Mn(II)CO_3$] are not favourable (Atkins, 1998; Fredrickson et al., 2002; Rinklebe et al., 2017), meaning the reduction of U(VI) was not expected in the systems studied here. The lack of U(VI) reduction means that the observed removal of U from solution is due to the sorption of U(VI) on to the mineral surfaces or incorporation into their structures.

3.3.2. EXAFS

3.3.2.1. δ–MnO_2

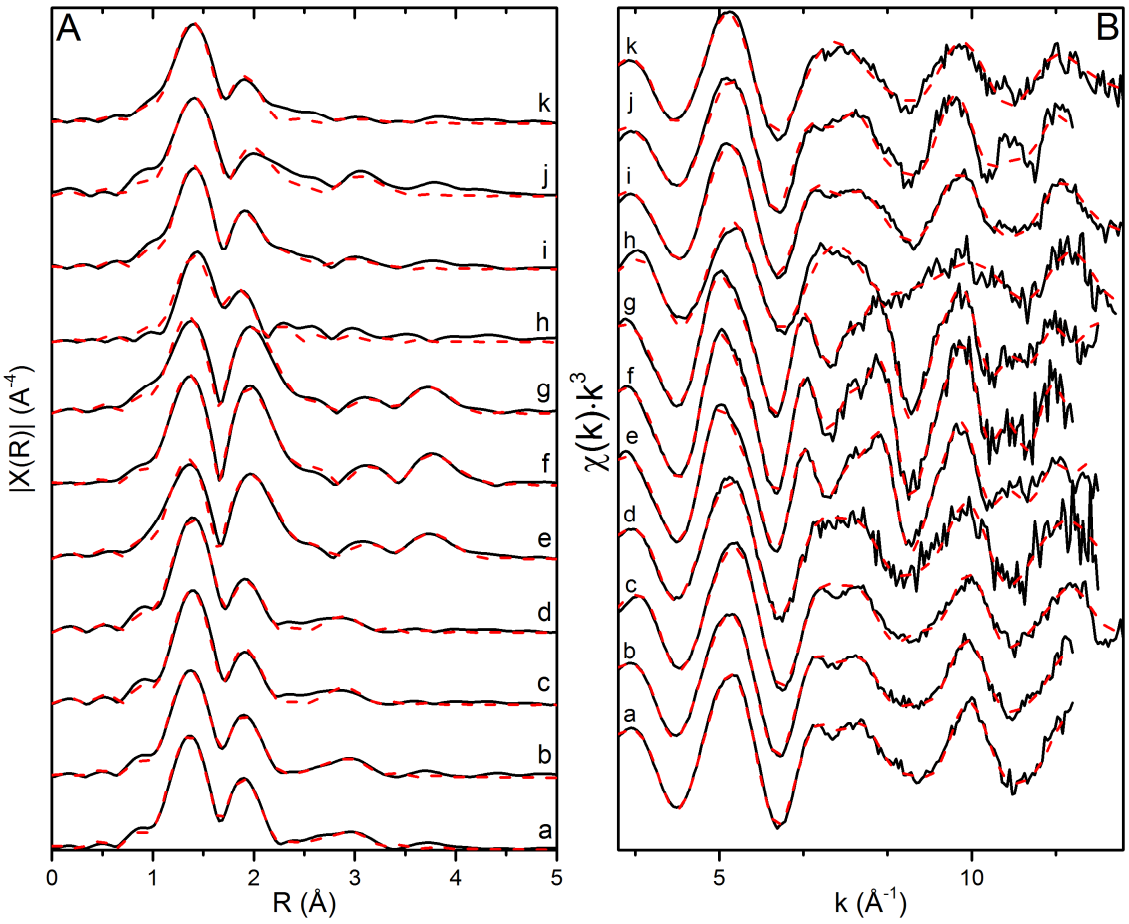

Figure 5. EXAFS of Mn minerals equilibrated with 1 µM U(VI). Sample descriptions are summarised in Table 1.

Sample and backscatter path	N	R (Å)	σ^2 (Å^2)	ΔE^0 (eV)	S_0^2	R-factor
δ-MnO_2 pH 7.8 (1 month) (a)						
O_{ax}	2	1.78(1)	0.0020(6)			
O_{eq1}	2	2.27(3)	0.0046(27)			
O_{eq2}	4	2.40(1)	0.0046(27)			
C	1.2	2.91(3)	0.0032(40)			
Mn	0.8	3.37(2)	0.0048(20)	3.36(1.39)	1.04(6)	0.0036
δ-MnO_2 pH 9.0 (1 month) (b)						
O_{ax}	2	1.78(1)	0.0025(5)			
O_{eq1}	2	2.26(2)	0.0053(24)			
O_{eq2}	4	2.40(1)	0.0053(20)			
C	0.9	2.90(3)	0.0032(38)			
Mn	1.2	3.36(1)	0.0068(14)	3.27(0.97)	1.00(6)	0.0023
δ-MnO_2 pH 10.4 (1 month) (c)						
O_{ax}	2	1.79(1)	0.0026(10)			
O_{eq1}	2	2.24(3)	0.0063(27)			
O_{eq2}	4	2.39(1)	0.0063(27)			
Mn	1.1	3.36(2)	0.0068(24)	6.29(1.27)	1.05(10)	0.0130
Triclinic (Na)-birnessite pH 7.9 (4 hours) (d)						
O_{ax}	2	1.79(1)	0.0018(4)			
O_{eq1}	2	2.23(2)	0.0046(14)			
O_{eq2}	4	2.39(1)	0.0046(14)			
Mn	1	3.34(2)	0.0077(27)	3.80(1.03)	1*	0.0091
Triclinic (Na)-birnessite pH 7.8 (1 month) (e)						
O_{ax}	2	1.78(1)	0.0026(6)			
O_{eq1}	5	2.46(1)	0.0047(7)			
O_{eq2}	2	2.85(2)	0.0031(21)			
Mn_1	2	3.80(3)	0.0058(29)			
Mn_2	3	3.99(2)	0.0057(22)			
Mn_3	1	4.38(5)	0.0054(58)	5.79(1.02)	1*	0.0136
Triclinic (Na)-birnessite pH 9.1 (1 month) (f)						
O_{ax}	2	1.78(1)	0.0020(7)			
O_{eq1}	5	2.45(1)	0.0044(8)			
O_{eq2}	2	2.86(1)	0.0023(15)			
Mn_1	3	3.84(2)	0.0054(23)			
Mn_2	4	4.02(2)	0.0048(22)			
Mn_3	1.5	4.34(4)	0.0070(59)	5.99(0.78)	1.07	0.0059
Triclinic (Na)-birnessite pH 10.3 (1 month) (g)						
O_{ax}	2	1.78(1)	0.0027(6)			
O_{eq1}	4.5	2.46(1)	0.0036(6)			
O_{eq2}	2	2.86(1)	0.0030(20)			
Mn_1	2	3.80(3)	0.0057(29)			
Mn_2	3	4.00(2)	0.0052(21)			
Mn_3	1	4.38(6)	0.0067(74)	5.95(1.00)	1*	0.0131
Hausmannite pH 7.7 (1 month) (h)						
O_{ax}	2	1.80(2)	0.0034(2)			
O_{eq1}	4	2.32(4)	0.0054(34)			
O_{eq2}	2	2.50(8)	0.0054(34)	9.14(3.34)	0.84(15)	0.0320

Table 1 continues overleaf

Hausmannite pH 8.4 (1 month) (i)						
O_{ax}	2	1.81(1)	0.0026(8)			
O_{eq1}	2	2.33(2)	0.0038(29)			
O_{eq2}	3	2.46(1)	0.0038(29)			
C	2.3	2.94(2)	0.0056(33)			
Mn	1	3.44(3)	0.0074(31)	9.38(1.30)	0.98(76)	0.0086
Hausmannite pH 10.4 (1 month) (j)						
O_{ax}	2	1.81(1)	0.0025(8)			
O_{eq1}	1.5	2.26(2)	0.0039(18)			
O_{eq2}	3.5	2.44(1)	0.0039(18)			
C	2.4	2.92(3)	0.004*			
Mn	1.5	3.45(2)	0.0057(27)	7.13*	1*	0.0337
Rhodochrosite pH 9.0 (1 month) (k)						
O_{ax}	2	1.79(2)	0.0029(6)			
O_{eq1}	2	2.22(2)	0.0058(20)			
O_{eq2}	4	2.39(2)	0.0058(20)	3.21(1.52)	1*	0.0237

Table 1. Summary of the EXAFS parameters of fits to Mn minerals exposed to solutions containing 1 μM U(VI). R = atomic distance; N = coordination number; σ^2 ($Å^2$) = Debye-Waller factor; ΔE^0 (eV) = energy shift from Fermi level; S_0^2 = amplitude factor; R-factor = normalised least squares residual. Coordination numbers were fixed and multiple scattering paths were included for the axial oxygens in all systems. * Denotes fixed parameter. Errors are presented in parentheses and are 1σ of last decimal.

The EXAFS of the δ-MnO_2 associated U(VI) was best fit by a split equatorial oxygen shell, indicative of inner-sphere surface complexation, over the circumneutral to alkaline pH range investigated (Table 1 and Figure 5). The addition of a Mn shell at 3.36 – 3.37 Å suggests that the U(VI) was bound to the surface as an edge-sharing, bidentate complex, as observed by Wang et al. (2013). However, the coordination number of this Mn shell range was 1.2 – 0.8, suggesting that this coordination environment may only represent approximately half of the δ-MnO_2 associated U(VI). At alkaline pH, Wang et al. (2013) observed a limited contribution to the EXAFS from Mn backscatterers at both 3.3 – 3.4 Å and 4.0 – 4.4 Å which was attributed to the presence of multiple surface U(VI) complexes. At pH 8.4, in the absence of carbonate and when bound to synthetic δ-MnO_2, the contribution to the EXAFS from Mn backscatterers was dominated by a 4.0 – 4.4 Å shell.

The authors suggested that this resulted from a monodentate, or bidentate bridging, coordination environment. When added to our model this additional 4.0 – 4.4 Å Mn shell did improve the fit across the pH range studied (7.8 – 10.4); however, it was not significant and was therefore omitted from the model (Supporting Information Table 3). The addition of a C backscatterer, with a coordination number of 0.9 – 1.2 at 2.9 Å significantly improved the fit of the pH 7.8 and 9.0 systems. This suggests that despite low carbonate present in these experiments, U(VI) was adsorbed to the mineral surface as a ternary carbonate complex, which have previously been identified on the surface of Mn oxides with birnessite-like and todorokite-like structures (Webb et al., 2006). The U-C bond distance modelled in our δ-MnO_2 systems (2.90 – 2.91 Å) is comparable with that previously found in Mn oxide systems (2.85 – 2.95 Å) (Webb et al., 2006) and that observed in iron oxide systems (~2.89 Å) (Bargar et al., 1999). However, the C coordination number in our systems was significantly lower than the U triscarbonate surface complexes identified on ferrihydrite in the presence of CO_2 (Rossberg et al., 2009). Interestingly, at the highest pH investigated (pH 10.4), where carbonate solubility would be expected to be highest, the addition of a C backscatterer did not significantly improve the fit.

The EXAFS suggest that, under circumneutral to alkaline pH at low carbonate conditions, U(VI) adsorbs to the surface of δ-MnO_2 as a bidentate inner-sphere complex. However, the low coordination number of the Mn backscatterer in the model suggests that multiple sites are involved in adsorption and that there may also be other U(VI) coordination environments present. This is concurrent with observations made in the desorption experiments where evidence of irreversibility was observed across all pHs when ^{232}U(VI) was adsorbed to δ-MnO_2 (section 3.2). The formation of irreversible Zn(II) and Eu(III) bidentate, edge-sharing adsorption complexes have previously been observed on Mn

oxides (Pan et al., 2004; Sheng et al., 2014), while adsorption of Zn(II) in tridentate, corner-sharing complexes was reversible (Li et al., 2004).

3.3.2.2. Triclinic (Na)-birnessite

In order to investigate the mechanism of U(VI) uptake on triclinic (Na)-birnessite, a sample of the mineral reacted at pH 7.9 for 4 hours was initially analysed by XAS. The EXAFS spectra of this sample were best fit by a split equatorial oxygen shell, suggesting inner-sphere adsorption, and a Mn shell at 3.33 Å (Table 1 and Figure 5). This is a similar model to that used to fit spectra collected from U(VI)–amended δ-MnO_2 (section 3.3.2.1), suggesting the same bidentate, edge-sharing adsorption complex is initially formed when U(VI) is reacted with triclinic (Na)-birnessite (Webb et al., 2006; Wang et al., 2013; Rihs et al., 2014).

Further XAS samples were taken from across the circumneutral to alkaline pH range investigated (7.8 – 10.3) after 1 month (720 hours) of reaction. The EXAFS from these samples were best fit by a split equatorial oxygen shell containing 4.5-5 O at 2.45 – 2.46 Å and 2 O at 2.85 – 2.86 Å (Table 1 and Figure 5). Three shells of Mn backscatterers could be added at ~ 3.82, 4.00, and 4.37 Å, with the F-test (Downward et al., 2007) showing that the addition of each of these shells produced a significant improvement in the fit (Supporting Information Table 3). The Mn backscatterers at ~ 3.82 and 4.00 Å can be explained if the $[U(VI)O_2]^{2+}$ ion replaced a Na^+ in the interlayer, as a range of interlayer Na – Mn distances exist in triclinic (Na)-birnessite, including 3.758, 3.806, 3.934, 4.084, 4.128, 4.146 Å (Post et al., 2002). The 2 O backscatterers at 2.85 – 2.86 Å observed in our systems are also predicted by a model of U(VI) located in the Na^+ interlayer sites of triclinic (Na)-birnessite. Na – O distances of 2.46 and 2.74 Å are found as the interlayer Na^+ ions are located slightly (0.28 Å) closer to one sheet than the other, even when no

vacancies are present (Lanson et al., 2002). Further scrutiny of the structure also found Na – O bond distances of 2.88 Å, which could explain the elongation of the average U – O_{eq2} distances to 2.85 – 2.86 Å as observed in our systems. An additional Mn backscatterer was also identified at 4.40 Å, which likely results from the same interlayer site as the previous two Mn shells, since a Mn backscatterer would also be expect at ~ 4.5 Å.

By the time the 4 hour EXAFS sample was taken 87 % of the U(VI) had already been removed from solution. The observed change in the U coordination environment therefore suggests that U(VI) initially adsorbed in an edge-sharing, bidentate complex and then migrated into the interlayer to replace Na^+ over the course of 1 month (720 hours). This implies that U(VI) associated with triclinic (Na)-birnessite is likely to be susceptible to release by cation exchange. This is supported by reversibility experiments (section 3.2, Figure 3) which suggest that after 2 months equilibration the U(VI) was more easily removed from triclinic (Na)-birnessite than from δ-MnO_2 and hausmannite, where an inner-sphere, edge-sharing, bidentate surface complex was observed. This also means the U(VI) cannot be structurally incorporated into the Mn oxide sheets since this would be expected to be less easily reversible than the adsorption complex formed in the δ-MnO_2 and hausmannite systems.

3.3.2.3. Hausmannite

The EXAFS spectra of U(VI) associated with hausmannite were best fit by a split equatorial oxygen shell across circumneutral to alkaline pH, suggesting inner-sphere adsorption (Table 1 and Figure 5). The addition of a C and a Mn shell also significantly improved the fits at pH 10.4 and 8.4, as determined by the F-test (Downward et al., 2007) (Supporting Information Table 3). A further Mn shell at 4.0 – 4.4 Å could be added to

improve the fit; however this was not statistically significant. In the pH 7.7 system neither the addition of a C, nor a Mn shell, produced a significant improvement in the fit.

The presence of a Mn backscatterer at 3.44 – 3.45 Å suggests the formation of bidentate, edge-sharing U(VI) adsorption complexes with a Mn backscatterer at 3.3 – 3.4 Å also having been identified on δ-MnO_2, hexagonal birnessite, and birnessite-like and todorokite-like Mn oxides (Webb et al., 2006; Brennecka et al., 2011; Wang et al., 2013; Rihs et al., 2014). Desorption data (section 3.2), which suggests sorption is partially irreversible, implies that there may be more than one sorption complex present in these systems. This is supported by the improvement in fit observed when a Mn backscatterer at 4.0 – 4.4 Å is added to the model (Supporting Information Table 3), suggesting that a small portion of either monodentate or bridging bidentate coordination complexes may also be formed (Webb et al., 2006; Wang et al., 2013). If the kinetics of formation of these two complexes differ this could explain the 'two-step' sorption behaviour observed in the pH 7.7 and 8.8 1 μM U(VI) systems (Figure 2C), where 50 – 70 % of the U(VI) is removed from solution within the first 10 minutes of reaction. The U(VI) solution concentration is then stable for 168 – 336 hours, before further sorption reduces the U(VI) solution concentration to < 5 %. The formation of irreversible, Zn(II) bidentate, edge-sharing, inner-sphere adsorption complexes, as suggested by the Mn backscatterers at 3.44 and 3.45 Å, have previously been observed on Mn oxides (Pan et al., 2004; Sheng et al., 2014), while partial irreversibility has been attributed to the concurrent formation of reversible Zn(II) tridentate, corner-sharing complexes (Li et al., 2004). Variation in the relative kinetics of formation of different surface complexes with pH could explain the variation in reversibility observed over the circumneutral to alkaline pH range studied.

3.3.2.4. Rhodochrosite

The introduction of a split equatorial oxygen shell to the model of the EXAFS spectra of U(VI) associated with rhodochrosite significantly improved the fit to data (Figure 5, Table 1, Supporting Information Table 3). This is consistent with the adsorption of U(VI) to the mineral surface as an inner-sphere complex. However, the U – O_{eq1} bond length (2.22 ± 0.02 Å) was shorter than that found in U(VI) surface complexes with Mn oxides (this study) (Webb et al., 2006; Brennecka et al., 2011; Wang et al., 2013; Rihs et al., 2014). In addition, the sorption of U(VI) to rhodochrosite was much slower than that to δ-MnO_2 and hausmannite where inner-sphere surface complexes were observed. U(VI) has previously been seen to form both a surface precipitate, and to be incorporated into the structurally analogous $CaCO_3$ mineral calcite (Elzinga et al., 2004; Smith et al., 2015). EXAFS of U(VI) precipitated on the surface of calcite revealed a coordination environment of 2 axial O at 1.81 Å and a split equatorial oxygen shell, with 2.5 O at 2.23 Å and 2.5 O at 2.40 Å (Smith et al., 2015). Structurally incorporated U(VI) has been found with a coordination environment of 2 axial O at 1.78 Å, 2 equatorial O at 2.20 Å, and 4 equatorial O at 2.38 Å (Reeder et al., 2001; Smith et al., 2015). With the exception of the variation in coordination number, which favours an incorporated structure, the U(VI) coordination environment found in our rhodochrosite associated U(VI) system (Table 1 and Figure 5) was within error of U(VI) both incorporated into calcite and precipitated onto the surface. The lack of any U-U backscatterer suggests incorporation is a more likely mechanism, since a U precipitate would be expected to contain U neighbours. Although this could result from a disordered precipitate structure containing a range of U phases with a range of U-U distances which cannot be identified by a bulk technique such as EXAFS. However, the desorption data (Figure 3J) showed that the equilibrium U(VI) solution concentration was re-established at the same slow rate at which sorption occurred (Figure 1D and 2D), supporting an incorporation mechanism which is likely to be rate limited by

the rate of mineral turnover. The inclusion of C or Mn shells in the model did not significantly improve the fit and were therefore discarded.

4. Conclusions

U(VI) has been found to be taken up strongly to a range of Mn minerals (δ-MnO_2, triclinic (Na)-birnessite, hausmannite, and rhodochrosite). R_d(a) values of sorption were found to be comparable to those describing uptake by Fe minerals (Li and Kaplan, 2012). XANES analysis of sorbed U found U(VI) present in all experimental systems and no evidence of reduction was observed.

The uptake of U(VI) by δ-MnO_2 was rapid (< 10 minutes) and extensive (> 95 %) at both 5.27 x 10^{-5} μM and 1 μM U(VI) concentrations, and over the circumneutral to alkaline conditions investigated. Partially irreversible uptake was observed over the whole pH range at the lower (5.27 x 10^{-5} μM) U(VI) concentration and at pH 7.8 in the more concentrated (1 μM) U(VI) systems. EXAFS identified the formation of edge-sharing bidentate inner-sphere adsorption complexes on δ-MnO_2. Uptake of U(VI) by triclinic (Na)-birnessite was also found to be rapid (< 168 hours) at both U(VI) concentrations investigated. At 5.27 x 10^{-5} μM U(VI) uptake was stronger and independent of pH; however, at 1 μM U(VI) uptake was marginally less extensive (84 ± 2 %) at pH 10.4. Sorption of U(VI) to triclinic (Na)-birnessite was found to be reversible at both U(VI) concentrations studied and over the whole circumneutral to alkaline pH range. After 4 hours reaction EXAFS showed U(VI) to be present adsorbed to the triclinic (Na)-birnessite surface as the same edge-sharing bidentate inner-sphere adsorption complex identified in the δ-MnO_2 systems. However, after 720 hours of reaction the U(VI) was found to have migrated into the interlayer of the triclinic (Na)-birnessite and replaced Na^+. At low (5.27 x 10^{-5} μM) U(VI) concentrations, adsorption by hausmannite was also

rapid (> 97 % adsorption within 96 hours) across the circumneutral to alkaline pH range. However, at higher (1 μM) U(VI) concentrations uptake appeared to occur via an initially fast but later slower, 'two-step' adsorption process, which was slower at high pH. Partial irreversibility was observed across all the systems investigated and EXAFS identified the formation the edge-sharing bidentate inner-sphere complex identified in the δ-MnO_2 systems. Uptake of U(VI) by rhodochrosite was found to be slower and less extensive than that observed to the Mn oxide minerals investigated, with equilibrium taking 6 weeks (1008 hours) to be established in systems containing 1 μM U(VI) and 25 ± 0.8 % of the U(VI) remaining in solution. Desorption experiments showed slow kinetics and suggested U(VI) may be being reversibly incorporated into the rhodochrosite structure or forming a surface precipitate.

The strong uptake of U(VI) by Mn minerals observed here suggests they could play an important role in retarding U migration in the geosphere, meaning the transport of U away from a GDF though the host-rock, and through shallow aquifers at contaminated nuclear sites, could be slower. Additionally, the partially irreversible formation of edge-sharing bidentate U(VI) adsorption complexes on δ-MnO_2 and hausmannite implies that these minerals could further reduce the U mobility.

Acknowledgements

Rosemary Hibberd is a Nuclear FiRST DTC student, funded by EPSRC (FIRST EP/G037140/1). We thank Diamond Light Source for access to beamline B18 (SP10163-2 and SP12767) and The SOLEIL synchrotron for access to beamline MARS (20150125) that contributed to the results presented here. This work was supported by the NERC LO-RISE (NE/L000547/1) consortium, which is part of the NERC RATE program (Radioactivity and the Environment) and as part of the NERC BIGRAD consortium

(NE/H007768/1). The RATE programme is co-funded by the Environment Agency and Radioactive Waste Management Ltd. The authors would like to thank Paul Lythgoe and John Waters for geochemical analysis, and XRD and BET, respectively. Pieter Bots is also thanked for helpful discussions.

References

Al-Attar, L. and Dyer, A. (2002). Sorption behaviour of uranium on birnessite, a layered manganese oxide. *Journal of Materials Chemistry,* 12(5)**,** 1381-1386.

Appelo, C. A. J. and Postma, D. (1999). A consistent model for surface complexation on birnessite (-MnO_2) and its application to a column experiment. *Geochimica et Cosmochimica Acta,* 63(19/20)**,** 3039-3033-3048.

Atkins, P. W. (1998). *Physical Chemistry*. Oxford: Oxford University Press.

Backes, C. A., McLaren, R. G., Rate, A. W. and Swift, R. S. (1995). Kinetics of Cadmium and Cobalt Desorption from Iron and Manganese Oxides. *Soil Science Society of America Journal,* 59(3)**,** 778-785.

Bargar, J. R., Reitmeyer, R. and Davis, J. A. (1999). Spectroscopic confirmation of uranium(VI)-carbonato adsorption complexes on hematite. *Environmental Science & Technology,* 33(14)**,** 2481-2484.

Barnett, M. O., Jardine, P. M., Brooks, S. C. and Selim, H. M. (2000). Adsorption and transport of uranium(VI) in subsurface media. *Soil Science Society of America Journal,* 64(3)**,** 908-917.

Bea, S. A., Wainwright, H., Spycher, N., Faybishenko, B., Hubbard, S. S. and Denham, M. E. (2013). Identifying key controls on the behavior of an acidic-U(VI) plume in the Savannah River Site using reactive transport modeling. *Journal of Contaminant Hydrology,* 151**,** 34-54.

Brennecka, G. A., Wasylenki, L. E., Bargar, J. R., Weyer, S. and Anbar, A. D. (2011). Uranium Isotope Fractionation during Adsorption to Mn-Oxyhydroxides. *Environmental Science & Technology,* 45(4)**,** 1370-1375.

Brookshaw, D. R., Pattrick, R. A. D., Bots, P., Law, G. T. W., Lloyd, J. R., Mosselmans, J. F. W., Vaughan, D. J., Dardenne, K. and Morris, K. (2015). Redox Interactions of Tc(VII), U(VI), and Np(V) with Microbially Reduced Biotite and Chlorite. *Environmental Science & Technology,* 49(22)**,** 13139-13148.

Butcher, E. J., Borwick, J., Collier, N. and Williams, S. J. (2012). Long term leachate evolution during flow-through leaching of a vault backfill (NRVB). *Mineralogical Magazine,* 76(8)**,** 3023-3031.

Campbell, K. M., Veeramani, H., Ulrich, K.-U., Blue, L. Y., Giammar, D. E., Bernier-Latmani, R., Stubbs, J. E., Suvorova, E., Yabusaki, S., Lezama-Pacheco, J. S., Mehta, A., Long, P. E. and Bargar, J. R. (2011). Oxidative Dissolution of Biogenic Uraninite in Groundwater at Old Rifle, CO. *Environmental Science & Technology,* 45(20)**,** 8748-8754.

Chardon, E. S., Bosbach, D., Bryan, N. D., Lyon, I. C., Marquardt, C., Römer, J., Schild, D., Vaughan, D. J., Wincott, P. L., Wogelius, R. A. and Livens, F. R. (2008). Reactions of the feldspar surface with metal ions: Sorption of Pb(II), U(VI) and Np(V), and surface analytical studies of reaction with Pb(II) and U(VI). *Geochimica et Cosmochimica Acta,* 72(2)**,** 288-297.

Chinni, S., Anderson, C. R., Ulrich, K.-U., Giammar, D. E. and Tebo, B. M. (2008). Indirect UO2 Oxidation by Mn(II)-oxidizing Spores of Bacillus sp. Strain SG-1 and the Effect of U and Mn Concentrations. *Environmental Science & Technology,* 42(23)**,** 8709-8714.

Choppin, G. R. (2006). Actinide speciation in aquatic systems. *Marine Chemistry,* 99(1-4)**,** 83-92.

Clement, B. G., Luther Iii, G. W. and Tebo, B. M. (2009). Rapid, oxygen-dependent microbial Mn(II) oxidation kinetics at sub-micromolar oxygen concentrations in the Black Sea suboxic zone. *Geochimica et Cosmochimica Acta,* 73(7)**,** 1878-1889.

Dixon, J. B., Golden, D. C., Uzochukwu, G. A. and Chen, C. C. (1990). Soil Manganese Oxides. *In:* De Boodt, M. F., Hayes, M. H. B., Herbillon, A., De Strooper, E. B. A.

& Tuck, J. J. (eds.) *Soil Colloids and Their Associations in Aggregates.* Boston, MA: Springer US.

Downward, L., Booth, C. H., Lukens, W. W. and Bridges, F. (2007). A variation of the F-Test for determining statistical relevance of particular parameters in EXAFS fits. *In:* Hedman, B. & Painetta, P. (eds.) *X-Ray Absorption Fine Structure-XAFS13.* Melville: American Institute of Physics.

Duff, M. C., Hunter, D. B., Triay, I. R., Bertsch, P. M., Reed, D. T., Sutton, S. R., Shea-McCarthy, G., Kitten, J., Eng, P., Chipera, S. J. and Vaniman, D. T. (1999). Mineral Associations and Average Oxidation States of Sorbed Pu on Tuff. *Environmental Science & Technology,* 33**,** 2163-2169.

Duff, M. C., Urbanik, J. and Hunter, D. B. (2002). Uranium co-precipitation with iron oxide minerals. *Geochimica et Cosmochimica Acta,* 66(20)**,** 3533-3547.

Elzinga, E. J., Tait, C. D., Reeder, R. J., Rector, K. D., Donohoe, R. J. and Morris, D. E. (2004). Spectroscopic investigation of U(VI) sorption at the calcite-water interface. *Geochimica et Cosmochimica Acta,* 68(11)**,** 2437-2448.

Farges, F., Ponader, C. W., Calas, G. and Brown, G. E. (1992). Structural Environment of Incompatible Elements in Silicate Glass Melt Systems 2. UIV, UV, and UVI. *Geochimica et Cosmochimica Acta,* 56(12)**,** 4205-4220.

Fox, P. M., Davis, J. A., Kukkadapu, R., Singer, D. M., Bargar, J. and Williams, K. H. (2013). Abiotic U(VI) reduction by sorbed Fe(II) on natural sediments. *Geochimica et Cosmochimica Acta,* 117**,** 266-282.

Fox, P. M., Davis, J. A. and Zachara, J. M. (2006). The effect of calcium on aqueous uranium(VI) speciation and adsorption to ferrihydrite and quartz. *Geochimica et Cosmochimica Acta,* 70(6)**,** 1379-1387.

Francis, A. J. and Dodge, C. J. (2008). Bioreduction of Uranium(VI) Complexed with Citric Acid by *Clostridia* Affects Its Structure and Solubility. *Environmental Science & Technology,* 42**,** 8277-8282.

Francis, A. J. and Dodge, C. J. (2015). Microbial mobilization of plutonium and other actinides from contaminated soil. *Journal of Environmental Radioactivity,* 150**,** 277-285.

Fredrickson, J. K., Zachara, J. M., Kennedy, D. W., Liu, C. X., Duff, M. C., Hunter, D. B. and Dohnalkova, A. (2002). Influence of Mn oxides on the reduction of uranium(VI) by the metal-reducing bacterium Shewanella putrefaciens. *Geochimica et Cosmochimica Acta,* 66(18)**,** 3247-3262.

Fuller, A. J., Shaw, S., Ward, M. B., Haigh, S. J., Mosselmans, J. F. W., Peacock, C. L., Stackhouse, S., Dent, A. J., Trivedi, D. and Burke, I. T. (2015). Caesium incorporation and retention in illite interlayers. *Applied Clay Science,* 108**,** 128-134.

Gaona, X., Kulik, D. A., Macé, N. and Wieland, E. (2012). Aqueous–solid solution thermodynamic model of U(VI) uptake in C–S–H phases. *Applied Geochemistry,* 27(1)**,** 81-95.

Giammar, D. E. and Hering, J. G. (2001). Time scales for sorption-desorption and surface precipitation of uranyl on goethite. *Environmental Science & Technology,* 35(16)**,** 3332-3337.

Gorman-Lewis, D., Fein, J. B., Burns, P. C., Szymanowski, J. E. S. and Converse, J. (2008). Solubility measurements of the uranyl oxide hydrate phases metaschoepite, compreignacite, Na-compreignacite, becquerelite, and clarkeite. *Journal of Chemical Thermodynamics,* 40(6)**,** 980-990.

Harfouche, M., Wieland, E., Dahn, R., Fujita, T., Tits, J., Kunz, D. and Tsukamoto, M. (2006). EXAFS study of U(VI) uptake by calcium silicate hydrates. *Journal of Colloid and Interface Science,* 303(1)**,** 195-204.

Hyun, S. P., Davis, J. A., Sun, K. and Hayes, K. F. (2012). Uranium(VI) Reduction by Iron(II) Monosulfide Mackinawite. *Environmental Science & Technology,* 46(6)**,** 3369-3376.

Ilton, E. S., Pacheco, J. S., Bargar, J. R., Shi, Z., Liu, J., Kovarik, L., Engelhard, M. H. and Felmy, A. R. (2012a). Reduction of U(VI) incorporated in the structure of hematite. *Environmental Science & Technology,* 46(17)**,** 9428-9436.

Ilton, E. S., Wang, Z., Boily, J. F., Qafoku, O., Rosso, K. M. and Smith, S. C. (2012b). The effect of pH and time on the extractability and speciation of uranium(VI) sorbed to SiO 2. *Environmental Science and Technology,* 46(12)**,** 6604-6611.

Ithurbide, A., Peulon, S., Miserque, F., Beaucaire, C. and Chaussé, A. (2009). Interaction between uranium(VI) and siderite (FeCO3) surfaces in carbonate solutions. *Radiochimica Acta,* 97(3)**,** 177-180.

Ithurbide, A., Peulon, S., Miserque, F., Beaucaire, C. and Chaussé, A. (2010). Retention and redox behaviour of uranium(VI) by siderite (FeCO3). *Radiochimica Acta,* 98(9-11)**,** 563-568.

Kelly, S. D., Newville, M. G., Cheng, L., Kemner, K. M., Sutton, S. R., Fenter, P., Sturchio, N. C. and Spötl, C. (2003). Uranyl Incorporation in Natural Calcite. *Environmental Science & Technology,* 37(7)**,** 1284-1287.

Kirillov, S. A., Aleksandrova, V. S., Lisnycha, T. V., Dzanashvili, D. I., Khainakov, S. A., García, J. R., Visloguzova, N. M. and Pendelyuk, O. I. (2009). Oxidation of synthetic hausmannite (Mn3O4) to manganite (MnOOH). *Journal of Molecular Structure,* 928(1-3)**,** 89-94.

Lanson, B., Drits, V. A., Feng, Q. and Manceau, A. (2002). Structure of synthetic Na-birnessite: Evidence for a triclinic one-layer unit cell. *American Mineralogist,* 87(11-12)**,** 1662-1671.

Latta, D. E., Boyanov, M. I., Kemner, K. M., O'Loughlin, E. J. and Scherer, M. M. (2012). Abiotic reduction of uranium by Fe(II) in soil. *Applied Geochemistry,* 27(8)**,** 1512-1524.

Law, G. T. W., Geissler, A., Burke, I. T., Livens, F. R., Lloyd, J. R., McBeth, J. M. and Morris, K. (2011). Uranium Redox Cycling in Sediment and Biomineral Systems. *Geomicrobiology Journal,* 28(5-6)**,** 497-506.

Lenhart, J. J. and Honeyman, B. D. (1999). Uranium(VI) sorption to hematite in the presence of humic acid. *Geochimica et Cosmochimica Acta,* 63(19)**,** 2891-2901.

Li, D. and Kaplan, D. I. (2012). Sorption coefficients and molecular mechanisms of Pu, U, Np, Am and Tc to Fe (hydr)oxides: A review. *Journal of Hazardous Materials,* 243**,** 1-18.

Li, X. L., Pan, G., Qin, Y. W., Hu, T. D., Wu, Z. Y. and Xie, Y. N. (2004). EXAFS studies on adsorption-desorption reversibility at manganese oxide-water interfaces II. Reversible adsorption of zinc on delta-MnO2. *Journal of Colloid and Interface Science,* 271(1)**,** 35-40.

Liu, C., Zachara, J. M., Fredrickson, J. K., Kennedy, D. W. and Dohnalkova, A. (2002). Modeling the Inhibition of the Bacterial Reduction of U(VI) by β-MnO2(s). *Environmental Science & Technology,* 36(7)**,** 1452-1459.

Macé, N., Wieland, E., Dähn, R., Tits, J. and Scheinost, A. C. (2013). EXAFS investigation on U(VI) immobilization in hardened cement paste: influence of experimental conditions on speciation. *Radiochimica Acta,* 101(6)**,** 379-389.

MacKenzie, A. B., Cook, G. T. and McDonald, P. (1999). Radionuclide distributions and particles size associations in Irish Sea surface sediments: implications for actinide dispersion. *Journal of Environmental Radioactivity,* 44**,** 275-296.

Marshall, T. A., Morris, K., Law, G. T., Livens, F. R., Mosselmans, J. F., Bots, P. and Shaw, S. (2014). Incorporation of Uranium into Hematite during crystallization from ferrihydrite. *Environmental Science & Technology,* 48(7)**,** 3724-3731.

McArdell, C. S., Stone, A. T. and Tian, J. (1998). Reaction of EDTA and related aminocarboxylate chelating agents with Co(III)OOH (heterogenite) and Mn(III)OOH (manganite). *Environmental Science & Technology,* 32(19)**,** 2923-2930.

McKenzie, R. M. (1981). The surface charge on manganese dioxide. *Australian Journal of Soil Science Research,* 19**,** 41-50.

Missana, T., Garcia-Gutierrez, M. and Alonso, U. (2004). Kinetics and irreversibility of cesium and uranium sorption onto bentonite colloids in a deep granitic environment. *Applied Clay Science,* 26**,** 137-150.

Morris, K., Law, G. T. W. and Bryan, N. D. (2011). Geodisposal of Higher Activity Wastes. *In:* Hester, R. E. & Harrison, R. M. (eds.) *Nuclear Power and the Environment.* Royal Society of Chemistry.

Moyce, E. B. A., Rochelle, C., Morris, K., Milodowski, A. E., Chen, X., Thornton, S., Small, J. S. and Shaw, S. (2014). Rock alteration in alkaline cement waters over 15 years and its relevance to the geological disposal of nuclear waste. *Applied Geochemistry,* 50**,** 91-105.

Moyes, L. N., Parkman, R. H., Charnock, J. M., Vaughan, D. J., Livens, F. R., Hughes, C. R. and Braithwaite, A. (2000). Uranium Uptake from Aqueous Solution by Interaction with Goethite, Lepidocrocite, Muscovite, and Mackinawite: An X-ray Absorption Spectroscopy Study. *Environmental Science & Technology,* 34(6)**,** 1062-1068.

Mukherjee, J., Ramkumar, J., Chandramouleeswaran, S., Shukla, R. and Tyagi, A. K. (2013). Sorption characteristics of nano manganese oxide: efficient sorbent for removal of metal ions from aqueous streams. *Journal of Radioanalytical and Nuclear Chemistry,* 297(1)**,** 49-57.

NDA. (2010a). *Geological Disposal: Radionuclide behaviour status report.* Harwell. NDA/RWMD/034.

NDA. (2010b). *Geological Disposal: Generic Post-closure Safety Assessment.* Harwell. NDA/RWMD/030.

O'Loughlin, E. J., Kelly, S. D. and Kemner, K. M. (2010). XAFS investigation of the interactions of UVI with secondary mineralization products from the bioreduction of FeIII oxides. *Environmental Science & Technology,* 44(5)**,** 1656-1661.

Opel, K., Weiß, S., Hübener, S., Zänker, H. and Bernhard, G. (2007). Study of the solubility of amorphous and crystalline uranium dioxide by combined spectroscopic methods. *Radiochimica Acta,* 95**,** 143-149.

Pabalan, R. T. and Turner, D. R. (1997). Uranium(6+) sorption on montmorillonite: Experimental and surface complexation modeling study. *Aquatic Geochemistry,* 2(3)**,** 203-226.

Pan, G., Qin, Y., Li, X., Hu, T., Wu, Z. and Xie, Y. (2004). EXAFS studies on adsorption–desorption reversibility at manganese oxides–water interfaces: I. Irreversible adsorption of zinc onto manganite (γ-MnOOH). *Journal of Colloid and Interface Science,* 271(1)**,** 28-34.

Post, J. E. (1999). Manganese oxide minerals: Crystal structures and economic and environmental significance. *Proceedings of the National Academy of Sciences,* 96(7)**,** 3447-3454.

Post, J. E., Heaney, P. J. and Hanson, J. (2002). Rietveld refinement of a triclinic structure for synthetic Na-birnessite using synchrotron powder diffraction data. *Powder Diffraction,* 17(3)**,** 218-221.

Powell, B. A., Duff, M. C., Kaplan, D. I., Fjeld, R. A., Newville, M., Hunter, D. B., Bertsch, P. M., Coates, J. T., Eng, P., Rivers, M. L., Sutton, S. R., Triay, I. R. and Vaniman, D. T. (2006). Plutonium oxidation and subsequent reduction by Mn(IV) minerals in Yucca Mountain tuff. *Environmental Science & Technology,* 40(11)**,** 3508-3514.

Ravel, B. and Newville, M. (2005). ATHENA, ARTEMIS, HEPHAESTUS: data analysis for X-ray absorption spectroscopy using IFEFFIT. *Journal of Synchrotron Radiation,* 12(Pt 4)**,** 537-541.

Reeder, R. J., Nugent, M., Lamble, G. M., Tait, C. D. and Morris, D. E. (2000). Uranyl incorporation into calcite and aragonite: XAFS and luminescence studies. *Environmental Science & Technology,* 34(4)**,** 638-644.

Reeder, R. J., Nugent, M., Tait, C. D., Morris, D. E., Heald, S. M., Beck, K. M., Hess, W. P. and Lanzirotti, A. (2001). Coprecipitation of Uranium(VI) with Calcite: XAFS, micro-XAS, and luminescence characterization. *Geochimica et Cosmochimica Acta,* 65(20)**,** 3491-3503.

Regenspurg, S., Schild, D., Schäfer, T., Huber, F. and Malmström, M. E. (2009). Removal of uranium(VI) from the aqueous phase by iron(II) minerals in presence of bicarbonate. *Applied Geochemistry,* 24(9)**,** 1617-1625.

Renshaw, J. C., Handley-Sidhu, S. and Brookshaw, D. R. (2011). Pathways of Radioactive Substances in the Environment. *In:* Hester, R. E. & Harrison, R. M. (eds.) *Nuclear Power and the Environment.* Royal Society of Chemistry.

Rihs, S., Gaillard, C., Reich, T. and Kohler, S. J. (2014). Uranyl sorption onto birnessite: A surface complexation modeling and EXAFS study. *Chemical Geology,* 373**,** 59-70.

Rihs, S., Sturchio, N. C., Orlandini, K., Cheng, L., Teng, H., Fenter, P. and Bedzyk, M. J. (2004). Interaction of uranyl with calcite in the presence of EDTA. *Environmental Science & Technology,* 38(19)**,** 5078-5086.

Rinklebe, J., Sophia, A. and Paller, M. (2017). *Trace Elements in Waterlogged Soils and Sediments*. Boca Raton: CRC Press.

Rossberg, A., Ulrich, K.-U., Weiss, S., Tsushima, S., Hiemstra, T. and Scheinost, A. C. (2009). Identification of Uranyl Surface Complexes on Ferrihydrite: Advanced EXAFS Data Analysis and CD-MUSIC Modeling. *Environmental Science & Technology,* 43(5)**,** 1400-1406.

Roy, S. (1981). *Manganese Deposits*. London: Academic Press.

RWM. (2015). *Geological Disposal: The 2013 Derived Inventory*. Harwell. NDA/RWM/120.

Scheinost, A. C., Schmeisser, N., Benerjee, D., Rossberg, A., Denecke, M. A., Dardenne, K., Rothe, J. and Daehn, R. (2013). AcXAS An Actinide Reference X-ray Absorption Spectroscopy Database. https://www.hzdr.de/acxas.

Sellafield Ltd. (2014). *Groundwater Monitoring at Sellafield: Annual Data Review 2014* LQTD000080.

Shaughnessy, D. A., Nitsche, H., Booth, C. H., Shuh, D. K., Waychunas, G. A., Wilson, R. E., Gill, H., Cantrell, K. J. and Serne, R. J. (2003). Molecular interfacial reactions between Pu(VI) and manganese oxide minerals manganite and hausmannite. *Environmental Science & Technology,* 37(15)**,** 3367-3374.

Sheng, G. D., Yang, S. T., Li, Y. M., Gao, X., Huang, Y. Y., Hu, J. and Wang, X. K. (2014). Retention mechanisms and microstructure of Eu(III) on manganese dioxide studied by batch and high resolution EXAFS technique. *Radiochimica Acta,* 102(1-2)**,** 155-167.

Sherman, D. M., Peacock, C. L. and Hubbard, C. G. (2008). Surface complexation of U(VI) on goethite (α-FeOOH). *Geochimica et Cosmochimica Acta,* 72(2)**,** 298-310.

Singer, D. M., Chatman, S. M., Ilton, E. S., Rosso, K. M., Banfield, J. F. and Waychunas, G. A. (2012). U(VI) Sorption and Reduction Kinetics on the Magnetite (111) Surface. *Environmental Science & Technology,* 46(7)**,** 3821-3830.

Smith, K. F., Bryan, N. D., Swinburne, A. N., Bots, P., Shaw, S., Natrajan, L. S., Mosselmans, J. F. W., Livens, F. R. and Morris, K. (2015). U(VI) behaviour in hyperalkaline calcite systems. *Geochimica et Cosmochimica Acta,* 148**,** 343-359.

Sturchio, N. C., Antonio, M. R., Soderholm, L., Sutton, S. R. and Brannon, J. C. (1998). Tetravalent Uranium in Calcite. *Science,* 281(5379)**,** 971.

Sun, Y. B., Yang, S., Sheng, G. D., Wang, Q., Guo, Z. Q. and Wang, X. K. (2012). Removal of U(VI) from aqueous solutions by the nano-iron oxyhydroxides. *Radiochimica Acta,* 100(10)**,** 779-784.

Sylwester, E. R., Hudson, E. A. and Allen, P. G. (2000). The structure of uranium(VI) sorption complexes on silica, alumina, and montmorillonite. *Geochimica et Cosmochimica Acta,* 64(14)**,** 2431-2438.

Tan, W.-f., Lu, S.-j., Liu, F., Feng, X.-h., He, J.-z. and Koopal, L. K. (2008). Determination of the Point-Of-Zero Charge of manganese Oxides with Differnet Methods Includingan Improved Salt Titration Method. *Soil Science,* 173(4)**,** 277-286.

Tebo, B. M. (1991). Manganese(II) oxidation in the suboxic zone of the Black Sea. *Deep Sea Research Part A. Oceanographic Research Papers,* 38**,** S883-S905.

Tits, J., Geipel, G., Macé, N., Eilzer, M. and Wieland, E. (2011). Determination of uranium(VI) sorbed species in calcium silicate hydrate phases: a laser-induced luminescence spectroscopy and batch sorption study. *Journal of Colloid and Interface Science,* 359(1)**,** 248-256.

Villalobos, M., Toner, B., Bargar, J. and Sposito, G. (2003). Characterization of the manganese oxide produced by Pseudomonas putida strain MnB1. *Geochimica et Cosmochimica Acta,* 67(14)**,** 2649-2662.

Wang, Z., Lee, S. W., Catalano, J. G., Lezama-Pacheco, J. S., Bargar, J. R., Tebo, B. M. and Giammar, D. E. (2013). Adsorption of uranium(VI) to manganese oxides: X-ray absorption spectroscopy and surface complexation modeling. *Environmental Science & Technology,* 47(2)**,** 850-858.

Wang, Z., Zachara, J. M., Shang, J., Jeon, C., Liu, J. and Liu, C. (2014). Investigation of U(VI) adsorption in quartz-chlorite mineral mixtures. *Environmental Science & Technology,* 48(14)**,** 7766-7773.

Webb, S. M., Fuller, C. C., Tebo, B. M. and Bargar, J. R. (2006). Determination of Uranyl Incoporation into Biogenic Manganese Oxides Using X-ray Absorption Spectroscopy and Scattering. *Environmental Science & Technology,* 40**,** 771-777.

Wieland, E., Macé, N., Dähn, R., Kunz, D. and Tits, J. (2010). Macro- and micro-scale studies on U(VI) immobilization in hardened cement paste. *Journal of Radioanalytical and Nuclear Chemistry,* 286(3)**,** 793-800.

Wilk, P. A., Shaughnessy, D. A., Wilson, R. E. and Nitsche, H. (2005). Interfacial Interactions between Np(V) and Manganese Oxide Minerals Manganite and Hausmannite. *Environmental Science & Technology,* 39**,** 2608-2615.

Yamamura, T., Kitamura, A., Fukui, A., Nishikawa, S., Yamamoto, T. and Moriyama, H. (1998). Solubility of U(VI) in highly basic solutions. *Radiochimica Acta,* 83(3)**,** 139-146.

Yang, D. S. and Wang, M. K. (2001). Syntheses and Characterization of Well-Characterized Birnessite. *Chemistry of Materials,* 13**,** 2589-2594.

Yusan, S. and Akyil, S. (2008). Sorption of uranium(VI) from aqueous solutions by akaganeite. *Journal of Hazardous Materials,* 160(2-3)**,** 388-395.

Zou, W., Zhao, L. and Han, R. (2010). Adsorption characteristics of uranyl ions by manganese oxide coated sand in batch mode. *Journal of Radioanalytical and Nuclear Chemistry,* 288(1)**,** 239-249.

Supporting Information for: Interaction of U(VI) with Mn minerals: An EXAFS and reversibility study

Rosemary Hibberd,[1,2] Nicholas D. Bryan,[1,3] Adam J. Fuller,[1] Samuel Shaw,[2] Katherine Morris,[2] Gareth T. W. Law[1]

[1]Centre for Radiochemistry Research, School of Chemistry, The University of Manchester, Oxford Road, Manchester, M13 9PL, UK.

[2]Research Centre for Radwaste Disposal, School of Earth, Atmospheric and Environmental Sciences, The University of Manchester, Oxford Road, Manchester, M13 9PL, UK.

[3]National Nuclear Laboratory, 5th Floor, Chadwick House, Birchwood Park, Warrington Road, Warrington, WA3 6AE, UK.

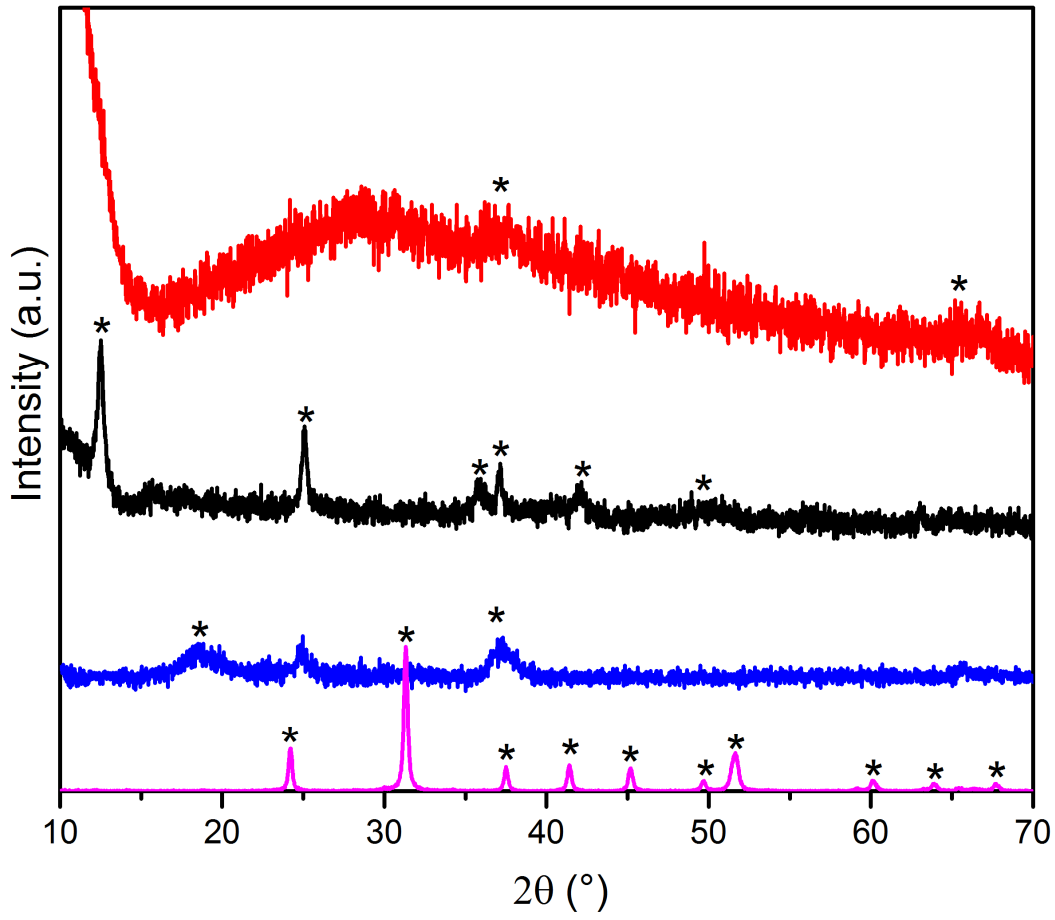

SI Figure 1. XRD of starting materials, red = δ-MnO_2; black = triclinic (Na)-birnessite; blue = hausmannite; pink = rhodochrosite. The characteristic diffraction peaks (*) were compared to those reported in the literature to confirm mineral identity and purity: δ-MnO_2 (Villalobos et al., 2003), triclinic (Na)-birnessite (Villalobos et al., 2003), hausmannite (Park et al., 2015), and rhodochrosite (Graf, 1961).

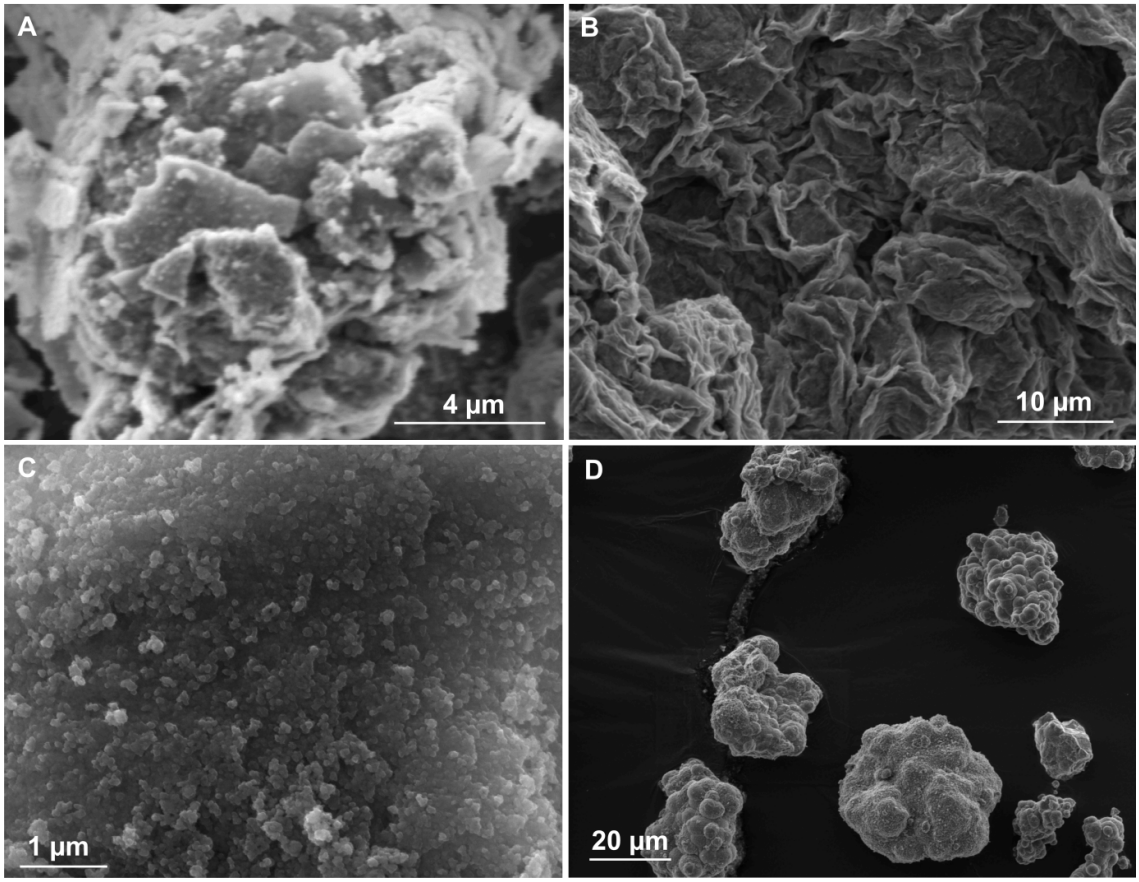

SI Figure 2. SEM images of starting materials, A = δ-MnO_2; B = triclinic (Na)-birnessite; C = hausmannite; D = rhodochrosite.

The starting minerals were analysed by SEM to determine their morphology and compared to previously reported literature (Sternbeck, 1997; Qiu et al., 2011; Rihs et al., 2014). This was particularly important for hausmannite since it can oxidise to manganite, which is difficult to differentiate by XRD. The formation of hausmannite was confirmed by the 'fluffy' spherical particles; the absence of needles indicates absence of manganite (Kirillov et al., 2009). The δ-MnO_2 consisted of characteristically small particles, the triclinic (Na)-birnessite consisted of platelets, and the rhodochrosite formed much larger globules.

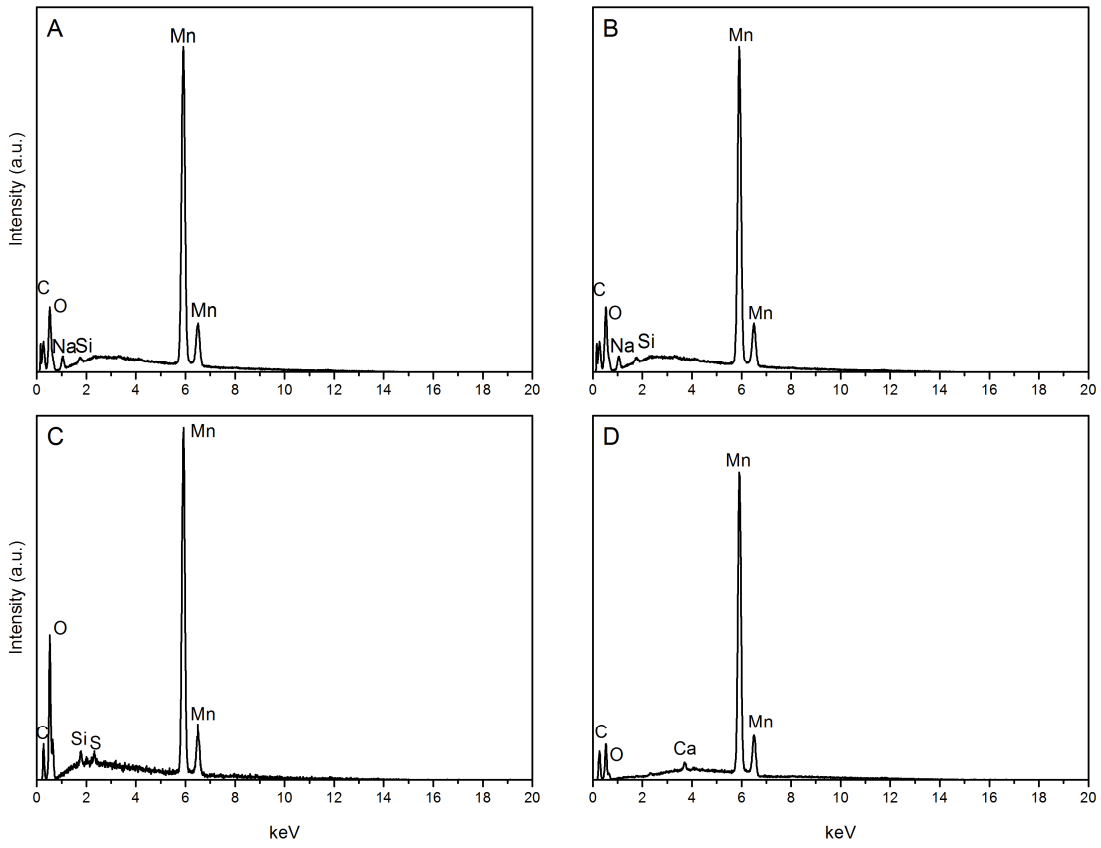

SI Figure 3. Energy dispersive X-ray spectra (EDX) of starting materials A = δ-MnO_2; B = triclinic (Na)-birnessite; C = hausmannite; D = rhodochrosite. EDX spectra were taken from the starting minerals to confirm the absence of common contaminant metals such as Fe.

	1 µM U(VI)			5.27 x 10^{-5} µM U(VI)		
U(VI) species	**pH 7.5 (M)**	**pH 9.0 (M)**	**pH 10.5 (M)**	**pH 7.5 (M)**	**pH 9.0 (M)**	**pH 10.5 (M)**
$UO_2(OH)_2$	9.54E-07	4.20E-07	2.24E-08	5.03E-11	2.22E-11	1.18E-12
$UO_2(OH)_3^-$	4.16E-08	5.79E-07	9.77E-07	2.19E-12	3.05E-11	5.15E-11
UO_2OH^+	4.29E-09	5.98E-11	1.01E-13	2.26E-13	3.15E-15	5.32E-18
$(UO_2)_3(OH)_5^+$	6.84E-11	1.85E-13	8.87E-19	1.00E-23	2.72E-26	1.30E-31
UO_2^{2+}	3.02E-11	1.33E-14	7.13E-19	1.59E-15	7.02E-19	3.76E-23
$(UO_2)_3(OH)_7^-$	2.39E-11	6.46E-11	3.09E-13	3.50E-24	9.47E-24	4.53E-26
$(UO_2)_2(OH)_2^{2+}$	1.38E-12	2.69E-16	7.66E-22	3.84E-21	7.46E-25	2.13E-30
$(UO_2)_4(OH)_7^+$	5.92E-13	7.07E-16	1.80E-22	4.57E-30	5.46E-33	1.39E-39
UO_2Cl^+	3.21E-13	1.42E-16	7.54E-21	1.69E-17	7.46E-21	3.97E-25
$UO_2(OH)_4^{2-}$	2.83E-14	1.25E-11	6.69E-10	1.49E-18	6.59E-16	3.53E-14
$(UO_2)_3(OH)_4^{2+}$	1.38E-14	1.18E-18	1.79E-25	2.02E-27	1.73E-31	2.62E-38
UO_2Cl_2	1.45E-16	6.40E-20	3.40E-24	7.65E-21	3.37E-24	1.79E-28
$(UO_2)_2OH^{3+}$	6.21E-17	3.82E-22	3.46E-29	1.73E-25	1.06E-30	9.62E-38
$UO_2ClO_3^+$	1.06E-32	4.65E-36	2.48E-40	5.56E-37	2.45E-40	0

SI Table 1. U(VI) speciation in 1 and 5.27 x 10-5 µM U(VI) sorption experiments as calculated by PHREEQC using the LLNL database. No supersaturated phases were identified in any of the solutions.

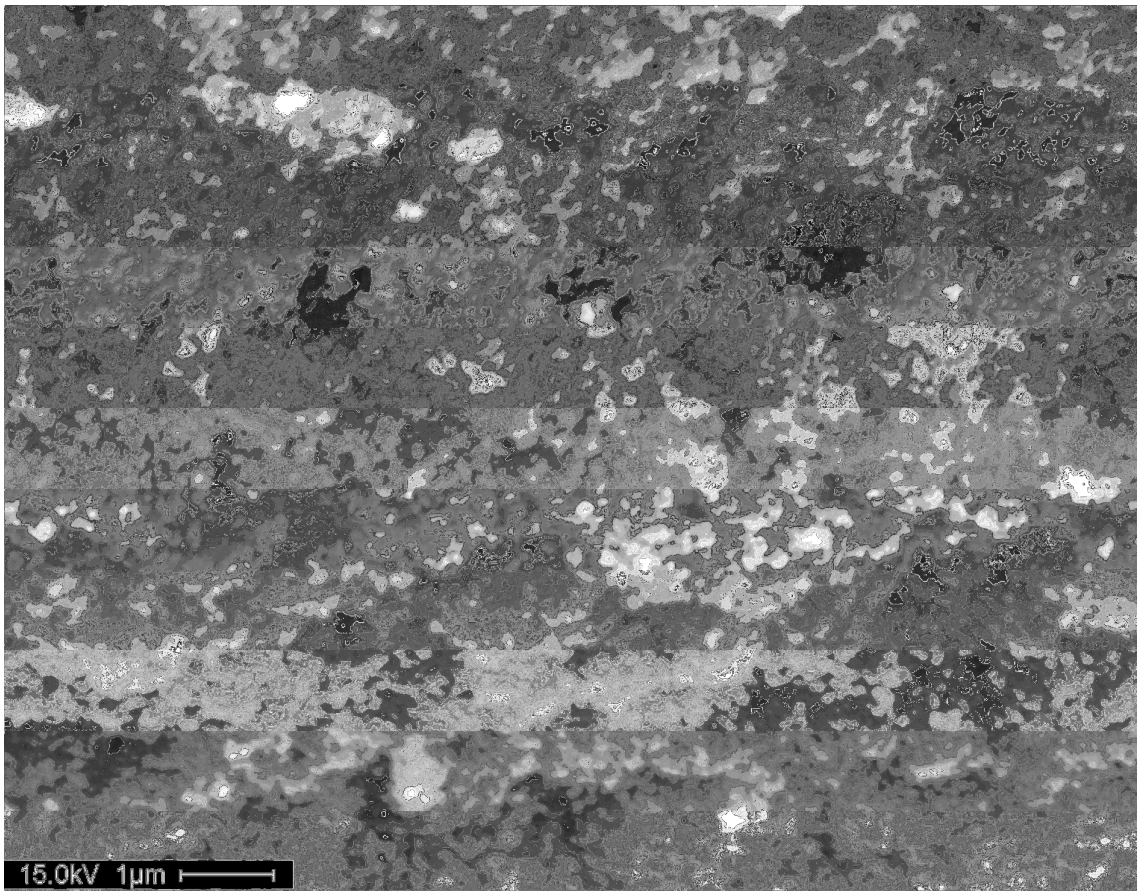

SI Figure 4. ESEM image of hausmannite reacted with 1 µM U(VI) at pH 10.4 for 1 month, confirming no oxidation to manganite had taken place (as indicated by the absence of needles (Kirillov et al., 2009)).

Sample	White line (eV)	E_0 (eV)
δ-MnO_2 pH 7.8 (1 month) (a)	17176.0	17172.3
δ-MnO_2 pH 8.9 (1 month) (b)	17176.0	17172.0
δ-MnO_2 pH 10.4 (1 month) (c)	17176.0	17171.9
Triclinic (Na)-birnessite pH 7.9 (4 hours) (d)	17176.0	17171.0
Triclinic (Na)-birnessite pH 7.8 (1 month) (e)	17176.0	17172.2
Triclinic (Na)-birnessite pH 9.1 (1 month) (f)	17176.0	17171.3
Triclinic (Na)-birnessite pH 10.3 (1 month) (g)	17176.0	17172.0
Hausmannite pH 7.7 (1 month) (h)	17176.0	17172.3
Hausmannite pH 8.4 (1 month) (i)	17176.0	17172.0
Hausmannite pH 10.4 (1 month) (j)	17176.0	17172.5
Rhodochrosite pH 9.0 (1 month) (k)	17176.0	17172.0

SI Table 2. White line and edge position of XANES spectra of U associated with a range of Mn minerals.

		Split O_{eq}	Mn	C	Mn	Mn
δ-MnO_2 pH 7.8 (1 month) (a)	R-factor	0.0168	0.0070	0.0036	0.0024	
	Significance		100 %	98 %	94 %	
δ-MnO_2 pH 9.0 (1 month) (b)	R-factor	0.0193	0.0048	0.0023		
	Significance		100 %	99 %		
δ-MnO_2 pH 10.4 (1 month (c)	R-factor	0.0262	0.0130		0.0122	
	Significance		100 %		67 %	
Triclinic (Na)-birnessite pH 7.9 (4 hours) (d)	R-factor	0.0180	0.0091			
	Significance		100 %			
Triclinic (Na)-birnessite pH 7.8 (1 month) (e)	R-factor	0.0471	0.0362		0.0266	0.0136
	Significance		98 %		98 %	100 %
Triclinic (Na)-birnessite pH 9.1 (1 month) (f)	R-factor	0.0466	0.0284		0.0151	0.0059
	Significance		100 %		100 %	100 %
Triclinic (Na)-birnessite pH 10.3 (1 month) (g)	R-factor	0.0500	0.0368		0.0269	0.0131
	Significance		99 %		98 %	100 %
Hausmannite pH 7.7 (1 month) (h)	R-factor	0.0320	0.0243	0.0256		
	Significance		68.6 %	60.7 %		
Hausmannite pH 8.4 (1 month) (i)	R-factor	0.0329		0.0179	0.0086	0.0065
	Significance			99.6 %	99.5 %	76.6 %
Hausmannite pH 10.4 (1 month) (j)	R-factor	0.0831		0.0564	0.0337	0.0299
	Significance			100 %	99 %	56 %
Rhodochrosite pH 9.0 (1 month) (k)	R-factor	0.0237				
	Significance	98 %				

SI Table 3. Statistical significance of the sequential addition shells to the models fitting EXFAS data as determined by the F-test (Downward et al., 2007). Shells included in the final fit are coloured green. Shells with no data did not improve the fit.

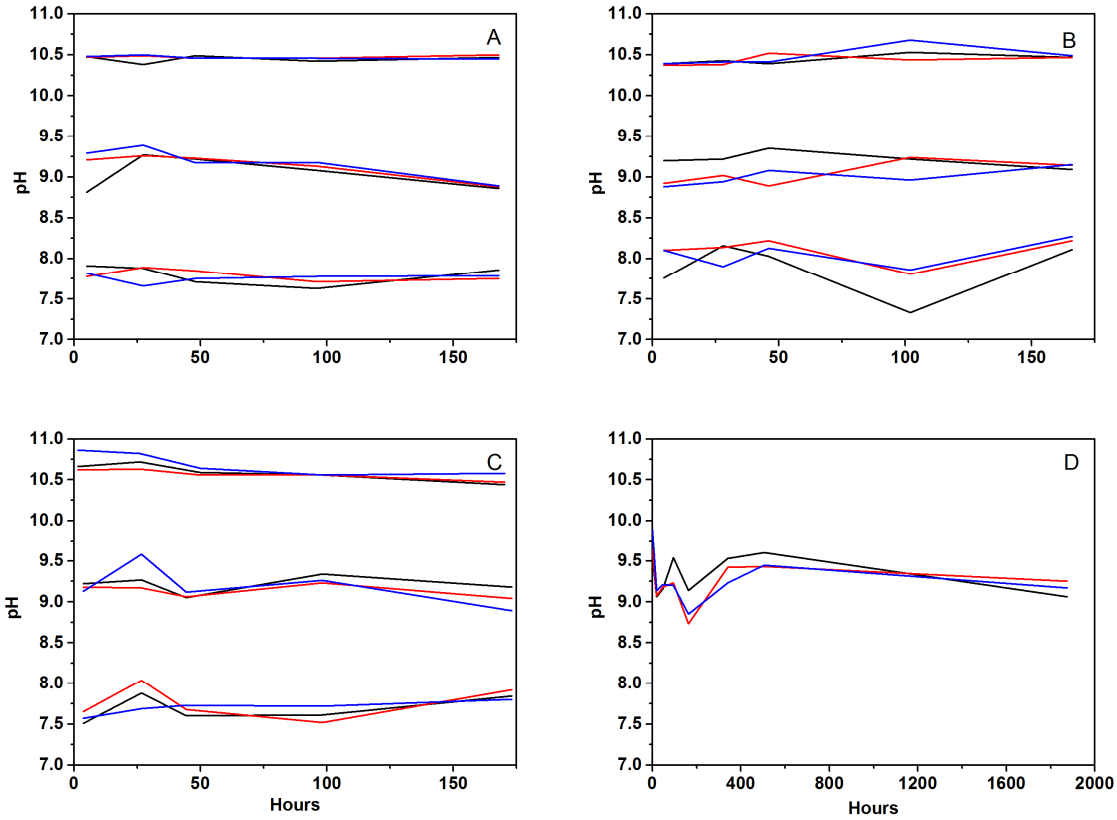

SI Figure 5. pH of U-232 sorption experiments. A = δ-MnO_2; B = triclinic (Na)-birnessite; C = hausmannite; D = rhodochrosite. Black = A; Red = B; Blue = C.

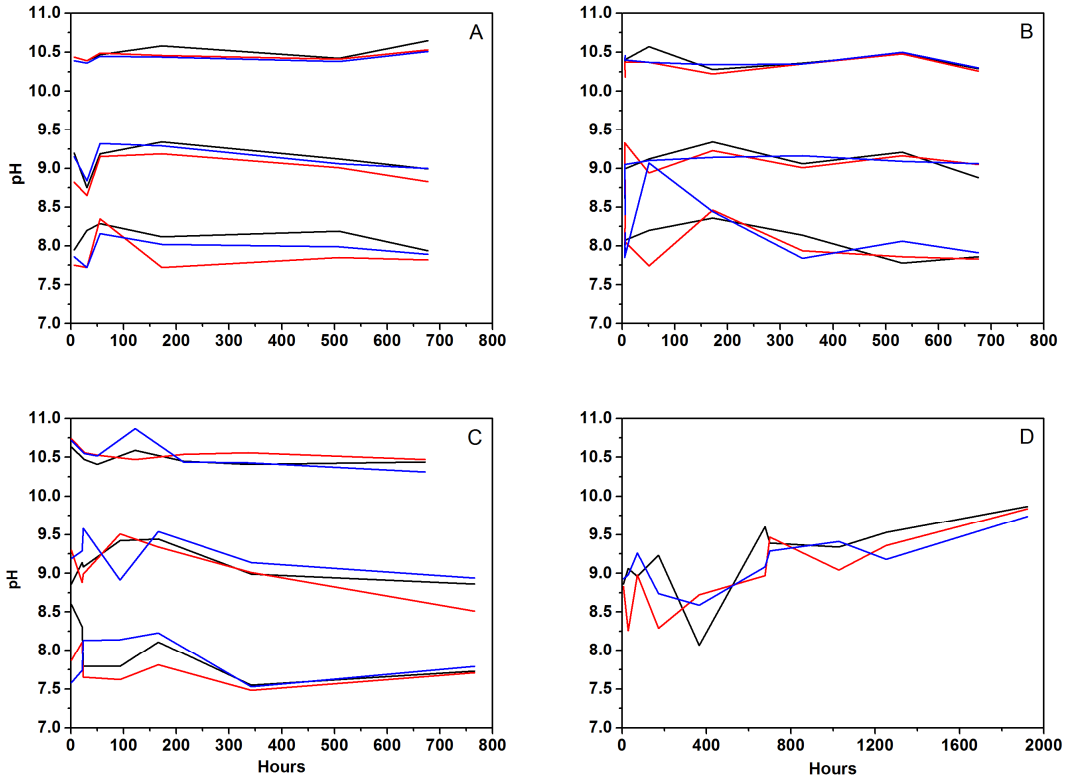

SI Figure 6. pH of NU sorption experiments. A = δ-MnO_2; B = triclinic (Na)-birnessite; C = hausmannite; D = rhodochrosite. Black = A; Red = B; Blue = C.

References

Downward, L., Booth, C. H., Lukens, W. W. and Bridges, F. (2007). A variation of the F-Test for determining statistical relevance of particular parameters in EXAFS fits. *In:* Hedman, B. & Painetta, P. (eds.) *X-Ray Absorption Fine Structure-XAFS13.* Melville: American Institute of Physics.

Graf, D. L. (1961). Crystallographic Tables for the Rhombohedral Carbonates. *American Mineralogist,* 46**,** 1283-1316.

Kirillov, S. A., Aleksandrova, V. S., Lisnycha, T. V., Dzanashvili, D. I., Khainakov, S. A., García, J. R., Visloguzova, N. M. and Pendelyuk, O. I. (2009). Oxidation of synthetic hausmannite (Mn3O4) to manganite (MnOOH). *Journal of Molecular Structure,* 928(1-3)**,** 89-94.

Park, Y., Woo Lee, S., Kim, K. H., Min, B.-K., Kumar Nayak, A., Pradhan, D. and Sohn, Y. (2015). Understanding hydrothermal transformation from Mn2O3 particles to Na0.55Mn2O4·1.5H2O nanosheets, nanobelts, and single crystalline ultra-long Na4Mn9O18 nanowires. *Scientific Reports,* 5**,** 18275.

Qiu, G., Li, Q., Yu, Y., Feng, X., Tan, W. and Liu, F. (2011). Oxidation behavior and kinetics of sulfide by synthesized manganese oxide minerals. *Journal of Soils and Sediments,* 11(8)**,** 1323-1333.

Rihs, S., Gaillard, C., Reich, T. and Kohler, S. J. (2014). Uranyl sorption onto birnessite: A surface complexation modeling and EXAFS study. *Chemical Geology,* 373**,** 59-70.

Sternbeck, J. (1997). Kinetics of rhodochrosite crystal growth at 25°C: The role of surface speciation. *Geochimica et Cosmochimica Acta,* 61(4)**,** 785-793.

Villalobos, M., Toner, B., Bargar, J. and Sposito, G. (2003). Characterization of the manganese oxide produced by Pseudomonas putida strain MnB1. *Geochimica et Cosmochimica Acta,* 67(14)**,** 2649-2662.

Chapter 7. Interaction of Np(V) with Mn minerals

This chapter is a manuscript prepared for submission in the journal *Applied Geochemistry*. Supporting Information provided with this manuscript is included following the manuscript.

Interaction of Np(V) with Mn minerals

Rosemary Hibberd,[1,2] Katherine Morris,[2] Clare L. Thorpe,[2,a] Katie A. Law,[1] Jörg Rothe,[3] Pieter Bots,[2,b] Nicholas D. Bryan,[1,4] Gareth T. W. Law[1*]

[1] Centre for Radiochemistry Research, School of Chemistry, The University of Manchester, Oxford Road, Manchester, M13 9PL, UK.

[2] Research Centre for Radwaste Disposal, School of Earth, Atmospheric and Environmental Sciences, The University of Manchester, Oxford Road, Manchester, M13 9PL, UK.

[3] Institut für Nukleare Entsorgung, Karlsruhe Institute of Technology (KIT-INE), D-76021 Karlsruhe, Germany.

[4] National Nuclear Laboratory, 5th Floor, Chadwick House, Birchwood Park, Warrington Road, Warrington, WA3 6AE, UK.

[b] Present address: Department of Materials Science and Engineering, The University of Sheffield, Sheffield, S1 3JD, UK.

[b] Present address: Department of Civil and Environmental Engineering, University of Strathclyde, Glasgow, G1 1XQ, UK.

* Corresponding author, Tel: +44 (0) 161 306 0514; Email: gareth.law@manchestester.ac.uk

Keywords: neptunium, manganese oxide, rhodochrosite, radioactive waste

Abstract

The long-term behaviour and migration of key risk-driving radionuclides, such as neptunium-237, is of significant concern for the safe management of radioactive wastes. The interaction of Np(V) with a range of Mn minerals has been investigated using batch sorption studies and X-ray Absorption Spectroscopy (XAS), under circumneutral pH conditions relevant to the far-field of a geological disposal facility containing radioactive wastes, or radioactively contaminated land. Strong uptake of Np(V) was observed by δ-MnO_2, triclinic (Na)-birnessite, and rhodochrosite, with > 90 % removal of Np from solution within 1 month for all systems. The interaction of Np(V) with δ-MnO_2 and triclinic (Na)-birnessite was found to be particularly rapid, with 96.4 ± 0.2 % and 95.9 ± 0.7 %, respectively, being removed from solution with the first 10 minutes of reaction. Np-L_{III} edge XAS of δ-MnO_2, triclinic (Na)-birnessite, and rhodochrosite found Np(V) present in the neptunyl moiety. EXAFS of δ-MnO_2 and triclinic (Na)-birnessite found that edge-sharing, bidentate adsorption complexes had been formed. The interaction of Np(V) with hausmannite was also investigated and found to be less extensive than that to the other Mn minerals investigated in some systems, although greater than 55 % sorption was observed in all systems. XANES of the hausmannite amended Np suggested the presence of neptunate or Np(IV), while the EXAFS showed that this was only a small proportion and the majority of the Np was present as Np(V) in inner-sphere, edge-sharing, bidentate adsorption complexes.

1. Introduction

The safe management of radioactive wastes from both the civil nuclear industry and from the production of nuclear weapons is of global public concern, especially given the advent of new nuclear build (Walls, 2011). Neptunium-237 is an alpha-emitting radioactive isotope with a long half-life (2,144,000 years). It contributes significantly to the radioactivity of High Level radioactive Waste (HLW) as ^{237}Np is a radiogenic progeny of ^{241}Am (Ojovan and Lee, 2014). Combined with the high predicted solubility of Np(V) species, this means that ^{237}Np is a key risk-driving radionuclide in radioactive wastes since it could potentially migrate over large distances in the geosphere (Runde et al., 1996; Kaszuba and Runde, 1999; Frohlich, 2015). Understanding neptunium (Np) behaviour in the subsurface is therefore crucial to accurately predict its mobility and migration, which is relevant for the management of radioactivity contaminated land and for the disposal of radioactive waste in a deep geological disposal facility.

The mobility of Np in the geosphere is expected to be predominantly controlled by its redox chemistry. The most environmentally significant oxidation states are Np(IV) and Np(V), whilst Np(VI) may also be stable under certain, strongly oxidising, alkaline conditions (Hennig et al., 2009). Under reducing conditions Np(IV) is expected to dominate (Choppin, 2006). The solubility of Np(IV) in water at circumneutral pH is low ($< 10^{-8}$ M) as a result of hydrolysis and the subsequent precipitation of poorly soluble Np(IV)-hydroxide phases (Kaszuba and Runde, 1999; Yoshida et al., 2011). By contrast, Np(V) is the most stable of the pentavalent actinides and the dioxygenyl NpO_2^+ species is expected to dominate under circumneutral, oxidising conditions (Keeney-Kennicutt and Morse, 1984; Hursthouse et al., 1991; Yamamoto et al., 1991; Kaszuba and Runde, 1999; Morris et al., 2000; Choppin, 2006; Law et al., 2010; Zavarin et al., 2012; Bots et al., 2016). The high solubility of NpO_2^+ (up to 10^{-4} M) is due to its low charge density, meaning that it is less susceptible to hydrolysis (Runde, 2000; Choppin, 2006; Yoshida et

al., 2011). The solubility of Np(V) is also increased by the formation of stable, negatively charged, carbonate species (Clark et al., 1995; Runde et al., 1996; Choppin, 2006).

Interaction with mineral phases and precipitation reactions are also likely to limit NpO_2^+ mobility in the subsurface (Moyes et al., 2002; Law et al., 2010; NDA, 2010; Brookshaw et al., 2015; Scheinost et al., 2016). Sorption to a range of mineral phases has previously been observed, including cement (Tits et al., 2014), clays (Frohlich, 2015; Amayri et al., 2016; Nagasaki et al., 2016), silicates (Brookshaw et al., 2015), carbonates (Zavarin et al., 2005; Heberling et al., 2008a; Heberling et al., 2008b; Scheinost et al., 2016), and metal oxide minerals, including Mn- and Fe- oxyhydroxides (Wilk et al., 2005; Tanaka et al., 2011; Li and Kaplan, 2012; Muller et al., 2015; Yang et al., 2015; Bots et al., 2016; Virtanen et al., 2016; Wylie et al., 2016). Interestingly, Mn-oxides in Yucca Mountain Tuff, have been found to preferentially sorb Pu(V) despite the presence of more abundant Fe oxides (Duff et al., 1999). Neptunium has also been found predominantly associated with Mn (and Fe) oxides in sediment collected from the Ob River (Siberia) (Roy, 1981; Dixon et al., 1990; Post, 1999; Kenna, 2009; NDA, 2010). Further, plutonium (Shaughnessy et al., 2003; Powell et al., 2006; Francis and Dodge, 2015), Eu(III) (Sheng et al., 2014), and U(VI) (Al-Attar and Dyer, 2002; Webb et al., 2006; Zou et al., 2010; See Chapter 6; Brennecka et al., 2011; Mukherjee et al., 2013; Wang et al., 2013; Rihs et al., 2014) have also been found to react readily with Mn oxides. This suggests that Mn-oxides, which are ubiquitous in the subsurface (Roy, 1981; Dixon et al., 1990; Post, 1999; NDA, 2010), may play an important role in determining radionuclide mobility.

The mobility of Np(V) in the subsurface can also be lessened *via* reduction to Np(IV); however reduction mechanisms are somewhat unclear. For example, in axenic cultures and under conditions optimal for growth, neither *Shewanella putrefaciens* or *Citrobacter sp.* alone could remove Np(V) from solution (Lloyd et al., 2000). However when cultured together, *Shewanella putrefaciens* reduced Np(V) to Np(IV) coupled to the oxidation of

H_2, whilst *Citrobacter sp.* facilitated bioprecitation of Np(IV) (Lloyd et al., 2000). Further, *Shewanella oneidensis* (a common metal reducing bacteria, in anexic culture) and *Desulfovibrio* species (in a sulfate-reducing consortium) successfully reduced Np(V) and removed it from solution (Rittmann et al., 2002; Icopini et al., 2007). However, *Geobacter metallireducens* and *Geobacter sulfurreducens* cannot reduce Np(V) (Renshaw et al., 2005; Icopini et al., 2007). In more complex sediment systems, Np(V) reduction was found to be commensurate with microbially mediated Mn and Fe reduction (Law et al., 2010; Thorpe et al., 2015), but Np(V) reduction was also observed in analogue sterile systems that contained biogenic Fe(II) (Law et al., 2010). This implicates Mn and Fe minerals in Np redox cycling; Mn minerals have also previously been identified as important mineral phases in uranium redox cycling (Fredrickson et al., 2002; Liu et al., 2002; Chinni et al., 2008). Finally, abiotic reduction of Np(V) to Np(IV) has also been documented in a range of single mineral systems: mackinawite (Moyes et al., 2002), magnetite (Nakata et al., 2002; Wylie et al., 2016), green rust (Christiansen et al., 2011), and biotite and chlorite (Brookshaw et al., 2015).

There are few studies investigating the interaction of radionuclides with Mn minerals, despite their relative abundance in the subsurface. This is compounded by the radiological challenges associated with studying Np, and as a result the interactions of Np with Mn minerals are poorly understood. In order to accurately predict the migration of Np(V) through the subsurface, it is important to determine the mechanism of any interaction with mineral phases. Therefore, this study uses carefully controlled batch sorption experiments in conjunction with X-ray absorption spectroscopy techniques to investigate the interaction of Np(V) with a range of Mn minerals, namely: δ-Mn(IV)O_2, triclinic (Na)-birnessite [$Na_{0.5}Mn(IV/III)_2O_4 \cdot 1.5H_2O$], hausmannite [$Mn(III/II)_3O_4$], and rhodochrosite [$Mn(II)CO_3$]. These minerals are common in the subsurface and encompass a range of Mn oxidation states. The experiments have been conducted at circumneutral pH and are

relevant to geological disposal over long timescales as well as for the assessment of radioactively contaminated land. In addition, studies such as these provide an important analogue for aiding the prediction of Pu(V) behaviour since Pu(V) and Np(V) posses similar chemical behaviour while Pu is notoriously difficult to work with due to it high radiotoxicity and range of simultaneously available oxidation states.

2. Materials and Methods

Neptunium-237 is an alpha-emitting radioactive isotope with beta/gamma-emitting daughters. Radioisotopes should be handled by suitably qualified and experienced personnel in a properly equipped laboratory, and any work should follow an appropriate risk assessment. The possession and use of radioactive material is subject to statutory controls.

2.1. Mineral preparation

Rhodochrosite was purchased from Alfa Aesar. δ-MnO_2, triclinic (Na)-birnessite, and hausmannite were synthesised chemically, with the preparations detailed below. All chemicals were analytical regent grade and all water was Milli-Q (18.2 MΩ). Prior to reaction with Np(V), mineral formation was confirmed using X-ray diffraction (XRD; Bruker D8Advance; Supporting Information Figure 1) prior to use. Scanning electron microscopy (SEM) samples were prepared on standard aluminium stubs with an adhesive carbon pad and carbon coating was completed prior to imaging to limit sample charging (FEI XL30 ESEM-FEG; Supporting Information Figure 2). SEM was used to confirm morphology and energy dispersive X-ray spectroscopy (EDX; Supporting Information Figure 3) was used to confirm chemical composition. The surface area of the δ-MnO_2, triclinic (Na)-birnessite, hausmannite, rhodochrosite was measured using N_2 B.E.T

analysis (Micromeritics Gemini V, with a Flowprep 060 sample degas system; Supporting Information Table 1).

2.1.1. Mn mineral synthesis

The δ-MnO_2 synthesis was adapted from Villalobos et al. (2003). $KMnO_4$ solution (0.2 M, 1.28 L) was added slowly, over 5 minutes, with vigorous stirring, to a solution of $MnCl_2$ (0.3 M, 1.28 L). NaOH (0.5 M, 1.44 L) solution was then added to the mixture slowly over 35 minutes, with vigorous stirring, to form a black precipitate. The suspension was then allowed to settle for 4 hours. After this time the pH of the supernatant was measured as 7 and the majority of the supernatant was decanted and disposed of. The remaining suspension was centrifuged (17000 *g*, 20 minutes, 20 °C) and thereafter the remaining supernatant was discarded. The resulting mineral paste was washed 5 times with NaCl (1 M) and then 10 times with water, with centrifuging (17000 *g*, 20 minutes, 20 °C) conducted between washes. The mineral suspension was finally adjusted to pH 8 using NaOH and was then stored in the dark at 5 °C prior to use.

The triclinic (Na)-birnessite synthesis was adapted from Villalobos et al. (2003). $MnCl_2$ (0.16 M, 0.32 L) solution was added slowly, over 40 minutes to NaOH (7.6 M, 0.36 L) solution, to form a pink gel like phase. $KMnO_4$ (0.2 M, 0.32 L) solution was then added to the mixture slowly, over 50 minutes, with vigorous stirring, to form a dark grey precipitate. The mixture was stirred for a further 2 hours before heating to 55 °C for 24 hours. The supernatant was then discarded and the mineral paste washed 5 times with NaCl (1 M), followed by washing with MQ water until the pH of the suspension reached 9.8, with centrifuging (17000 *g*, 20 minutes, 20 °C) performed between steps. The mineral paste was centrifuged (17000 *g*, 20 minutes, 20 °C) between washing steps and stored in the dark at 5 °C.

The hausmannite synthesis was adapted from McArdell et al. (1998). All solutions were sparged with N_2 prior to reaction. The synthesis and subsequent manipulations were carried out under N_2 to prevent the conversion of hausmannite to manganite (Kirillov et al., 2009). A solution of $MnSO_4$ (0.06 M, 1.5 L) was heated to 60 °C before the addition of H_2O_2 (8.8 M, 30.75 mL). NH_4OH (0.2 M, 0.45 L) solution was then added slowly (1 mL per second). The resulting suspension was heated to 95 °C and maintained at this temperature for 6 hours before being allowed to cool overnight. The resulting mineral was washed 10 times with water (with centrifugation between washes; 17000 *g*, 20 minutes, 20 °C), re-suspended, and stored under N_2.

2.2. Neptunium spike preparation

A small aliquot of NaOH solution was added to a mixed oxidation state (Np(IV/V)), radiochemically pure, ^{237}Np stock solution (LEA-CERCA, France) to precipitate the radionuclide. The resulting Np precipitate was washed three times with MQ water (18.2 MΩ; with centrifuging carried out in between) and the washed precipitate was then dissolved in HNO_3 (6 M), and heated gently with addition of 2 drops 10 % H_2O_2 to facilitate oxidation to Np(V). After visible colour change (olive green to emerald green, indicative of Np(V)) the Np was again precipitated with NaOH, washed three times in MQ water (as described above), and finally dissolved in HCl (0.1 M). UV-vis-NIR (Schimadzu, UV-1800) spectrum (Supporting Information Figure 4) was used to confirm speciation as Np(V) with diagnostic Np(V) peaks present at 618 and 980 nm and no contribution from peaks at 723 and 960 nm (indicative of Np(IV)).

2.3. Sorption experiments

Batch sorption reactions investigating Np(V) uptake by δ-MnO_2, triclinic (Na)-birnessite, hausmannite, and rhodochrosite were carried out at two $^{237}Np(V)$ concentrations (0.162

and 5.24 μM). Selected, Np-amended samples from the higher Np(V) sorption experiments were analysed by X-ray Absorption Spectroscopy (XAS) to determine the Np oxidation state and coordination environment after reaction with the Mn minerals. In addition, experiments parallel to those with lower (0.162 μM) Np(V) concentrations were also spiked to higher activities to provide solid samples with > 450 mg kg^{-1} Np for analysis by XAS.

PHREEQC (Parkhurst and Appelo, 2013) was used to model the expected thermodynamic speciation of Np(V) in the experimental systems with the Lawrence Livermore National Laboratory (LLNL, V8 R6, April 2015) database.

2.3.1. Lower level (0.162 μM Np(V)) experiments

Mineral (0.3 g) was added to 30 mL of adapted synthetic groundwater recipe (Supporting Information Table 2) without $CaCO_3$ (to avoid calcite precipitation) (Wilkins et al., 2007). The pH was then adjusted to 7 using HCl and NaOH prior to spiking with $^{237}Np(V)$ to give a ^{237}Np concentration of 1 Bq mL^{-1} (0.162 μM). Samples were taken periodically, centrifuged (10 minutes, 15000 *g*), acidified, diluted and analysed by ICP-MS (Agilent 7500cx) to determine Np concentrations in solution. Samples were also taken to monitor the pH. Experiments were performed in triplicate. Experiments containing rhodochrosite were performed at pH 9.3 as the experiment buffered to this pH.

2.3.2. Higher level (5.24 μM Np(V)) experiments

The sorption of 5.24 μM $^{237}Np(V)$ to Mn minerals at pH 7 was investigated in select experiments. Mineral (0.5 g) was added to MQ water (18.2 MΩ, 100 mL), containing $NaClO_4$ (0.01 M) as background electrolyte. The pH was adjusted using HCl and NaOH

prior to spiking with $^{237}Np(V)$ (3.67 kBq mL^{-1}) to give a ^{237}Np concentration of 32.4 Bq mL^{-1} (5.24 μM). Samples were taken periodically, centrifuged (10 minutes, 15000 *g*), acidified, mixed with scintillation cocktail (Optiphase Hisafe 3, Perkin Elmer) and analysed using a 1220 QUANTULUS ultra-low level scintillation spectrometer to determine the concentration of ^{237}Np remaining in solution. Samples were also taken to monitor the pH, and the solids were collected for XAS (see below). Due to carbonate equilibria, experiments containing rhodochrosite were performed at pH 9.3.

2.4. X-ray Absorption Spectroscopy

From higher activity experiments, select reacted samples labelled with Np were analysed by X-ray Absorption Spectroscopy (XAS) to examine the speciation and local coordination environment of Np on the solids. Samples were analysed in fluorescence mode on the Np-L_{III} absorption edge. Analysis was performed at either beamline I20 at Diamond Light Source, UK, using a Si(111) monochromator and a 36 element Ge detector, or at the INE-beamline at ANKA Light Source, Germany, using a Ge(422) monochromator and a 5 element Ge detector. Samples were prepared by centrifuging (6000 *g,* 5 minutes) to obtain a mineral paste with a Np-loading of greater than several hundred ppm. The mineral pastes were then mounted in triple contained, gas tight and approved XAS sample cells. An in-line Zr reference foil was used for energy calibration. Background subtraction, data normalization, and fitting to the extended X-ray absorption fine structure (EXAFS) spectra were performed using the Demeter software package (Ravel and Newville, 2005). For EXAFS fitting, FEFF 8 was used to calculate structural models of Np sorbed to Mn oxides. All data were fit in R-space (typical range, 1 – 4 Å).

3. Results and discussion

3.1. Np(V) sorption experiments

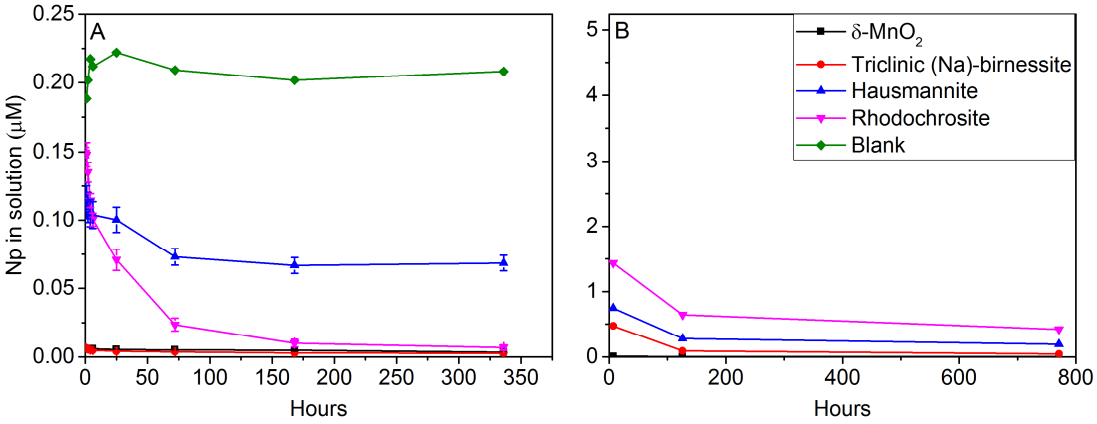

Figure 1. ^{237}Np remaining in solution in contact with Mn minerals. (A) = 0.162 μM Np(V), 10 g L^{-1} Mn mineral, pH 7; (B) = 5.24 μM Np(V), 5 g L^{-1} Mn mineral, pH 7.5. Error bars are 1σ. (For pH measurements see Supporting Information Figure 5).

Following the addition of 0.162 μM Np(V) to synthetic groundwater containing a range of Mn minerals, rapid removal of Np from solution was observed in all systems (Figure 1). Thermodynamic calculations showed that there were no supersaturated Np containing phases in any system (Supporting Information Table 5), meaning that any removal from solution resulted from the presence of the mineral phases. Removal was particularly rapid in systems containing δ-Mn(IV)O_2 and triclinic (Na)-birnessite [$Na_{0.5}Mn(IV/III)_2O_4 \cdot 1.5H_2O$] where only 3.6 ± 0.2 % (0.006 ± 0.0002 μM) and 4.1 ± 0.7 % (0.007 ± 0.001 μM) of the Np(V) remained in solution after 10 minutes, respectively. In experiments containing elevated Np(V) concentrations (5.24 μM Np(V)), rapid Np(V) removal from solution was observed in systems containing δ-MnO_2 (0.16 %, 0.008 μM, remained in solution after 7 hours). However, the removal of Np(V) from solution by triclinic (Na)-birnessite at the elevated Np(V) concentration (5.24 μM Np(V)) was slower

than that by δ-MnO_2 (1.7 %, 0.47 µM remained in solution after 5.25 days), but remained extensive (0.8 %, 0.05 µM Np(V) in solution after 1 month). This is comparable to the reactivity of U(VI) with these minerals in similar systems, where < 5 % of the 5.27 x 10^{-5} µM U(VI) remained in solution after 10 minutes (See Chapter 6). However, when the U(VI) concentration was increased to 1 µM, equilibrium took longer to establish in both systems (1 and 4 days, in the δ-MnO_2 and triclinic (Na)-birnessite systems, respectively; See Chapter 6). This suggests that the reaction of Np(V) with δ-MnO_2 and triclinic (Na)-birnessite is similar to that of U(VI). Extensive uptake of U(VI) by (Na)-birnessite has also been observed at pH 3 (K_d = 10^5) after 0.5 – 8 hours contact, however the kinetics of this reaction were not investigated (Al-Attar and Dyer, 2002). The sorption of Np(V) to birnessite [$(Na_{0.3}Ca_{0.1}K_{0.1})Mn(IV/III)_2O_4 \cdot 1.5H_2O$], cryptomelane [$K_xMn(IV/II)_8O_{16}$], and pyrolusite [$Mn(IV)O_2$] was investigated in the presence of atmospheric carbonate concentrations by Zhao et al. (2005). In this past work, approximately 20 % of the initial 3.4 µM Np(V) was associated with the minerals after 4 weeks, with the majority of this being removed from solution within 1 day, and equilibrium taking ~ 1 month to be established (Zhao et al., 2005). This suggests that it is important to consider the kinetics of sorption over a longer timeframe.

In Chapter 6 the morphology of hausmannite [$Mn(III/II)_3O_4$] reacted with U(VI) under comparable conditions was monitored by SEM and found that this remained unchanged, indicating that oxidation to manganite [Mn(III)O(OH)] had not taken place. In the current work, sorption of Np(V) to hausmannite was slower and less extensive than that to δ-MnO_2 and triclinic (Na)-birnessite (Figure 1). In the more concentrated 5.24 µM Np(V) system, 0.19 µM (3.6 %) Np(V) remained in solution after 1 month. This is consistent with the uptake of U(VI) by hausmannite, which has been found to remove > 95 % of the U(VI) for solution at equilibrium (See Chapter 6). Less extensive (~ 20 – 60 %) sorption of Np(V) to hausmannite has been observed by Wilk et al. (2005). However, these experiments were

halted after 48 hours and our time-resolved sorption data (Figure 1) suggests that equilibrium may not have been reached, since 2 weeks were required to establish equilibrium even in the less concentrated system. Interestingly, a similar proportion (45 %) of U(VI) was observed sorbed to hausmannite after 2 weeks of reaction (See Chapter 6). This system also appeared to be at equilibrium before a further reduction in the U(VI) solution concentration was observed (See Chapter 6), which suggests that there could be two mechanisms of radionuclide uptake by hausmannite, one of which is delayed. This could explain the seemingly greater proportion of Np(V) uptake observed at higher Np(V) concentrations, if the 0.162 μM Np(V) system had reached the same pseudo equilibrium after 2 weeks. Cobalt and Cd have previously been observed to have both fast and slow desorption mechanisms from hausmannite, which also suggests that hausmannite has a slow secondary cation uptake process (Backes et al., 1995).

The sorption of Np(V) to rhodochrosite [$Mn(II)CO_3$] was slower than to the three Mn oxide minerals investigated here, with equilibrium taking 2 weeks to be established and 20 times more Np(V) remaining in solution after 24 hours in the less concentrated rhodochrosite system than the equivalent systems containing δ-MnO_2 and triclinic (Na)-birnessite (Figure 1). However, over 2 weeks, the uptake of Np(V) by Mn(II) bearing rhodochrosite was extensive ($R_d > 10^3$) with the concentration remaining in solution at equilibrium (0.007 ± 0.004 μM, 4.2 ± 2 % Np left in solution) being within error of that observed in systems containing δ-MnO_2 and triclinic (Na)-birnessite. This slow uptake is typical of both incorporation or the formation of a surface precipitate and has previously been observed with U(VI) uptake by rhodochrosite (See Chapter 6). The removal of Np(V) by the analogous Fe(II) bearing mineral siderite, has also been found to be extensive ($R_d > 10^5$) after 7 days interaction, although the Np(V) was found to have been reduced to Np(IV) (Scheinost et al., 2016) likely due to reaction with Fe(II) in siderite.

3.2. X-ray Absorption Spectroscopy

3.2.1. XANES

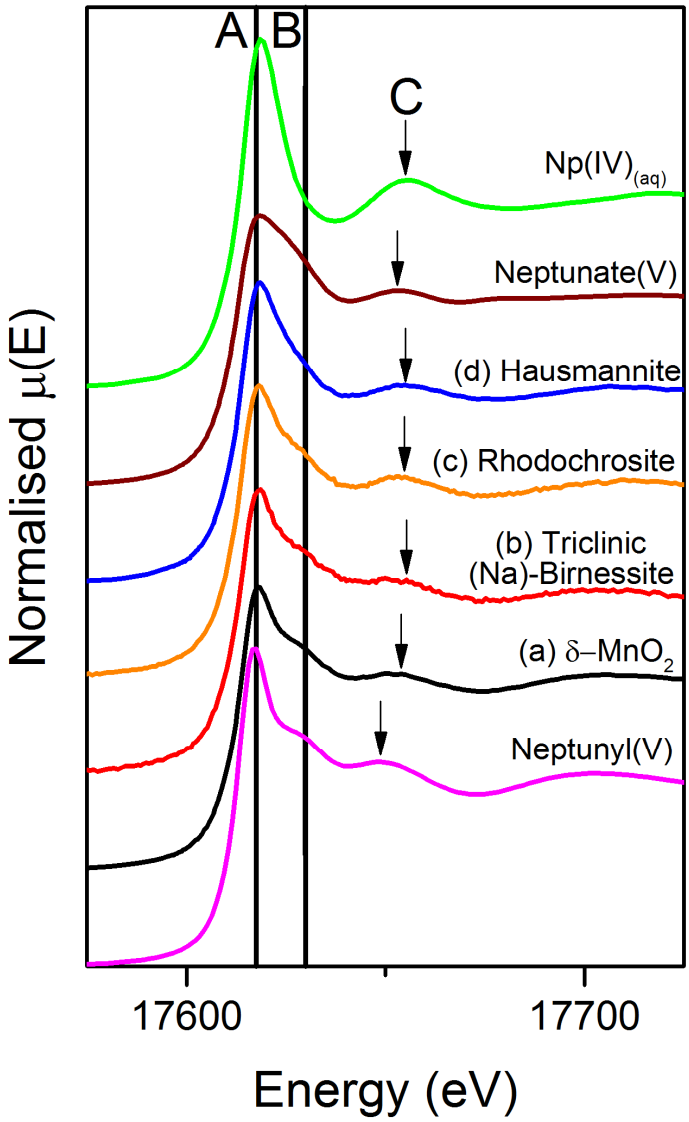

Figure 2. Np L_{III}-edge XANES spectra of Mn minerals equilibrated with Np(V) compared with reference spectra. Black = δ-MnO_2; red = triclinic (Na)-birnessite; orange = rhodochrosite; blue = hausmannite; green = aqueous Np(IV) standard (Hennig et al., 2009); pink = neptunyl(V) standard (Hennig et al., 2009; Scheinost et al., 2013); brown = neptunate(V) standard (Smith et al., 2016). Line A shows the position of the white line in the neptunyl standard. Line B and arrows C show features related to axial and equatorial Np – O bonds, respectively.

The XANES of selected samples of Mn minerals equilibrated with Np(V) were collected from the Np-L_{III} edge (Figure 2). The sample spectra were compared to an aqueous neptunyl ($Np(V)O_2^+$) standard (Hennig et al., 2009; Scheinost et al., 2013), a solid neptunate ($Na_3Np(V)O_4$) standard (Smith et al., 2016), and an aqueous $Np(IV)^{4+}$ standard (Hennig et al., 2009; Scheinost et al., 2013). Comparison with the reference spectra shows that the Np associated with the δ-$Mn(IV)O_2$, triclinic (Na)-birnessite [$Na_{0.5}Mn(IV/III)_2O_4 \cdot 1.5H_2O$], and rhodochrosite [$Mn(II)CO_3$] were similar to the neptunyl standard. Specifically, there was little or no change in either the white line position or the post edge resonance features when compared to the Np(V) neptunyl standard despite the presence of Mn(II) in rhodochrosite and Mn(III) in triclinic (Na)-birnessite confirming reduction had not occurred (Supporting Information Table 3). The neptunyl coordination environment in these samples is confirmed by the presence of two resonance features between 17620–17627 eV and 17652–17659 eV (lines B and arrows C, Figure 2), which result from multiple scattering of the ejected photon along the actinide – axial oxygen (Np-O_{ax}) and actinide – equatorial oxygen (Np-O_{eq}) scattering paths within the linear dioxygenyl neputunyl ions, respectively (Farges et al., 1992; Den Auwer et al., 2003; Den Auwer et al., 2004; Denecke et al., 2005; Lozano et al., 2009; Bots et al., 2016). There is an inverse relationship between the position of these resonance features in the XANES spectra and the lengths of the Np-O bonds, as is observed with U(VI) (Farges et al., 1992; Marshall et al., 2014; Bots et al., 2016). This means that as the lengths of Np-O_{ax} and Np-O_{eq} bonds converge, the resonance features become further apart in energy and appear less pronounced, eventually resulting in a spectrum which reflects a neptunate-like coordination environment (Figure 2).

This is significant since the XANES of the Np(V) reacted hausmannite [$Mn(III/II)_3O_4$] differs from the neptunyl standard and the other mineral samples. Here, most notably the post edge resonance feature between 17620–17627 eV, indicative of the dioxygenyl axial

oxygen, is reduced in intensity. Interestingly, reduction of hausmannite associated Np(V) to Np(IV) during XAS has been reported (Wilk et al., 2005). The authors attributed this reduction to the X-ray beam either as a direct result of interaction with the beam, or due to catalysis, since analysis by optical absorption spectroscopy showed no reduction of Np(V) in solution samples contacted with hausmannite unless samples had been introduced to the X-ray beam in order to perform XAS. In our work the XANES data can be interpreted as intermediate between Np(V) and Np(IV) (Figure 2). It is also interesting that the hausmannite sample has similar features to the Np(V) neptunate standard and reflects the non-diagnostic nature of Np L_{III}-edge XANES (Denecke et al., 2005). Overall, the Np(V) reacted δ-MnO_2, triclinic (Na)-birnessite, and rhodochrosite show a Np(V) neptunyl like XANES standard whilst the hausmannite which contains Mn(II) and Mn(III) shows clear differences consistent with either partial reduction to Np(IV) or a Np(V)-neptunate like coordination environment.

3.2.2. EXAFS

3.2.2.1. δ-MnO_2

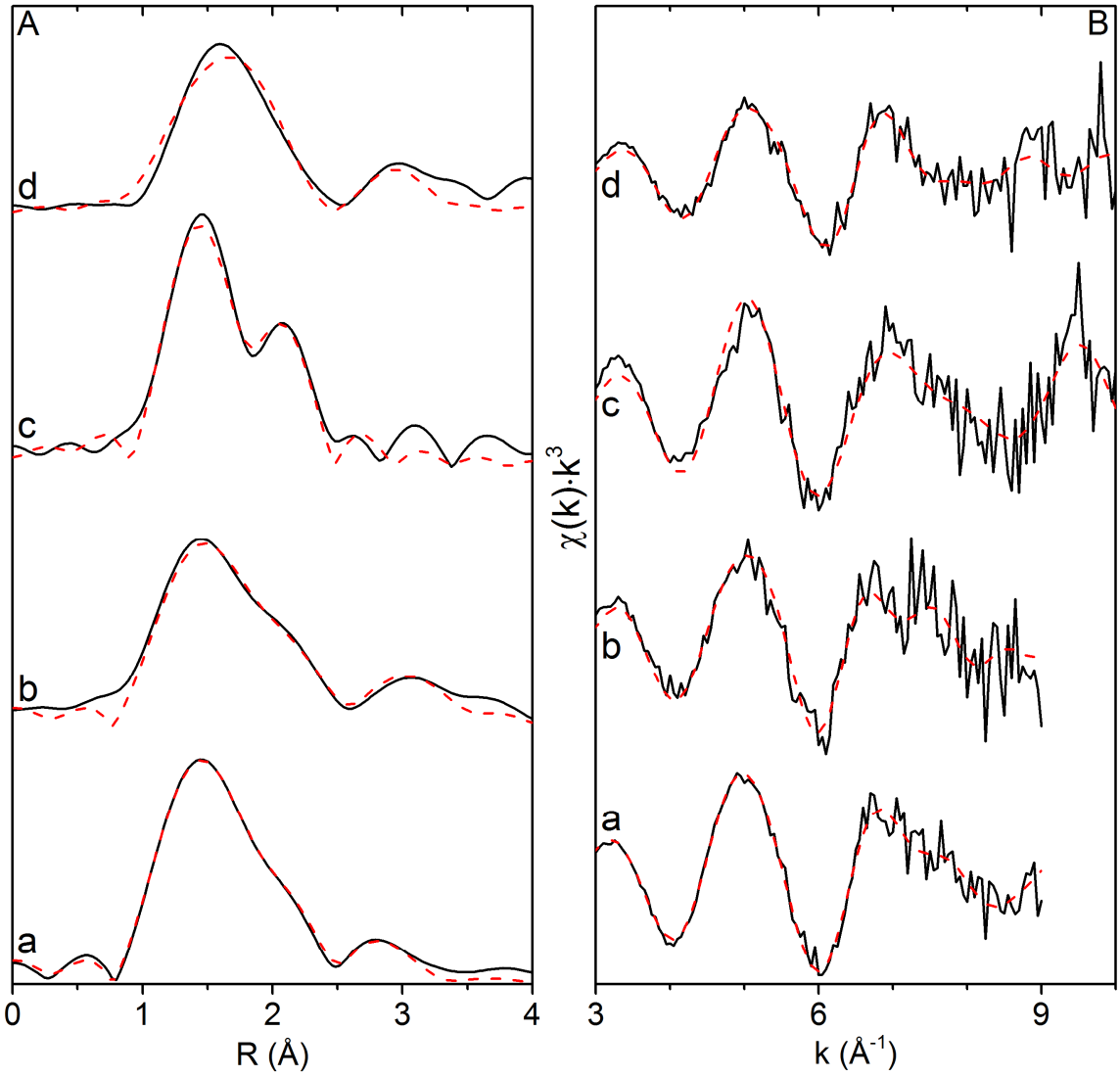

Figure 3. Np L_{III}-edge EXAFS spectra of Mn minerals equilibrated with Np(V). A = R space; B = k space; a = δ-MnO_2; b = triclinic (Na)-birnessite; c = rhodochrosite; d = hausmannite; black = data; red = fit; sample descriptions are summarised in Table 1.

Sample	N	R (Å)	σ^2 (Å^2)	ΔE^0 (eV)	S_0^2	R-factor
δ-MnO_2 pH 7.3 (1 month) (a)						
O_{ax}	2	1.85(1)	0.0033(8)			
O_{eq1}	1.5	2.23(2)	0.0046(14)			
O_{eq2}	4.3	2.43(1)	0.0046(14)			
Mn	1.1	3.41(2)	0.0077(30)	10.8(1.1)	1*	0.0029
Triclinic (Na)-birnessite pH 7.0 (1 month) (b)						
O_{ax}	2	1.86(1)	0.0051(18)			
O_{eq1}	1.5	2.22(4)	0.0067(22)			
O_{eq2}	4.3	2.45(2)	0.0067(22)			
Mn	2	3.49(3)	0.0080(28)	13.3(1.8)	1*	0.0070
Rhodochrosite pH 9.3 (1 month) (c)						
O_{ax}	2	1.85(1)	0.0043(17)			
O_{eq1}	1.7	2.25(4)	0.0055(31)			
O_{eq2}	4.3	2.47(3)	0.0055(31)	12.0(2.4)	1*	0.0310
Hausmannite pH 7.3 (1 month) (d)						
O_{ax}	2	1.86(1)	0.0089(18)			
O_{eq}	5	2.38(2)	0.0104(18)			
Mn	2	3.37(3)	0.0115*	11.1(2.1)	0.8*	0.0292

Table 1. Summary of the EXAFS parameters of fits to Mn minerals exposed to solutions containing Np(V). R = atomic distance; N = coordination number; σ^2 (Å^2) = Debye-Waller factor; ΔE^0 (eV) = energy shift from Fermi level; S_0^2 = amplitude factor; R-factor = normalised least squares residual. Coordination numbers were fixed and multiple scattering paths were included for the axial oxygens in all systems. * Denotes fixed parameter. Errors are presented in parentheses and are 1σ of last decimal.

The EXAFS data collected from the Np-L_{III} edge of δ-MnO_2 reacted with ^{237}Np(V) (Figure 2) was best fit by 2 axial O at 1.85 Å, a split equatorial shell (1.5 O_{eq} at 2.23 Å and 4.3 O_{eq} at 2.43 Å), and a Mn backscatterer at 3.41 Å (Table 1). The axial and equatorial oxygen backscatters at 1.85, 2.23, and 2.41 Å confirm the presence of Np in the neptunyl moiety reinforcing interpretation of the XANES data for this sample (Figures 2 and 3) and comparable to neptunyl sorbed to other metal oxide minerals (Combes et al., 1992; Bots et al., 2016). The split equatorial oxygen shell also suggests that Np(V) formed an inner-sphere adsorption complex on the surface of δ-MnO_2. The fit to Np(V) associated with δ-MnO_2 was significantly improved by the addition of a Mn shell at 3.41 Å (Supporting

Information Table 4). In samples of U(VI) adsorbed to δ-MnO_2 (Wang et al., 2013; See Chapter 6) and other Mn minerals such as hexagonal birnessite, hausmannite, and birnessite-like and todorokite-like Mn oxides (Webb et al., 2006; See Chapter 6; Brennecka et al., 2011; Wang et al., 2013; Rihs et al., 2014), a Mn backscatterer at 3.3 – 3.4 Å has been found to be indicative of edge-sharing, bidentate adsorption complexation. This has also been observed in Np(V) complexation to Fe oxides (Arai et al., 2007; Bots et al., 2016) and corundum (α-Al_2O_3) (Virtanen et al., 2016). Therefore the presence of a Mn shell at 3.41 Å in our spectra of Np(V) associated with δ-MnO_2 suggests that Np(V) is present as an inner-sphere, edge-sharing, bidentate adsorption complex.

3.2.2.2. Triclinic (Na)-birnessite

The Np-L_{III} edge EXAFS spectra of Np(V) associated with triclinic (Na)-birnessite fitted best with 2 axial O at a distance of 1.86 Å (Table 1) and a split equatorial oxygen shell with 1.5 O_{eq} at 2.22 Å and 4.3 O_{eq} at 2.45 Å. The fit was significantly improved by the addition of 2 Mn backscatterers at 3.49 Å. These data again suggest Np(V) is adsorbed to the surface as an inner-sphere complex and the split equatorial shell is consistent with this (Webb et al., 2006; Marshall et al., 2014). The formation of edge-sharing bidentate adsorption complexes on Mn oxide minerals has previously been indicated by the presence of a Mn backscatterer at 3.3 – 3.4 Å (Pan et al., 2004; Webb et al., 2006; Arai et al., 2007; Brennecka et al., 2011; Wang et al., 2013; Marshall et al., 2014; Rihs et al., 2014; Sheng et al., 2014; See Chapter 6; Bots et al., 2016; Virtanen et al., 2016). While the Mn backscatterers observed in this system is at 3.49 Å, this is only slightly longer than those previously seen in edge-sharing bidentate adsorption complexes, and (given the relatively large interatomic distance and the error associated with this) likely results from a similar complex.

3.2.2.3. Rhodochrosite

The Np-L_{III} edge EXAFS from rhodochrosite was best fit by 2 axial O at 1.85 Å, and a split equatorial oxygen shell with 1.7 O_{eq} at 2.25 Å and 4.3 at 2.47 Å (Table 1) confirming the presence of Np(V). A C backscatterer could only be added at an unphysical distance and was therefore excluded from the final fit. A split equatorial oxygen shell suggests the formation of inner-sphere adsorption complexes. However, EXAFS of Np(V) adsorbed to isostructural calcite showed a single equatorial oxygen shell of 5 O at 2.46 Å (Heberling et al., 2008a). Np(V) structurally incorporated into the Ca sites within the calcite structure also showed a single shell of ~ 4 equatorial oxygens at 2.40 Å (Heberling et al., 2008b). A split equatorial O shell with similar distances to those observed here (2.20 – 2.25 Å and 2.38 – 2.45 Å) has been seen when U(VI) was precipitated on a calcite surface (Elzinga et al., 2004; Smith et al., 2015), suggesting a Np(V) containing precipitate may be forming in our system. The formation of a surface precipitate would explain kinetically slow removal of Np(V) from solution (Figure 1). While the U(VI) precipitates were formed in calcite systems containing much higher actinide concentrations, Elzinga et al. (2004) found that precipitate formation began at lower U(VI) concentrations when the solutions were not kept saturated with carbonate. The authors suggest that this reduces the formation of U(VI) tricarbonates in solution and therefore reduces the formation of carbonate adsorption complexes (Elzinga et al., 2004). The absence of all but dissolved carbonate from the equilibrated rhodochrosite in our systems may inhibit the formation of Np(V) carbonate adsorption complexes and lead to the formation of a Np(V) precipitate on the rhodochrosite surface.

3.2.2.4. Hausmannite

The XANES of Np-amended hausmannite was inconsistent with neptunyl speciation and could be explained by either the reduction to Np(IV) or the formation of a distorted Np(V), neptunate like species (Figure 2). However, modelling of the EXAFS required 2 O_{ax} to be fitted at 1.86 Å (Table 1) suggesting neptunyl was dominant in the sample. The best fit to also contained a single equatorial O shell with 5 O at 2.38 Å, and 2 Mn backscatterers at 3.37 Å (Table 1). This model is very similar that used to describe Np(V) adsorbed to the surface of δ-MnO_2 and triclinic (Na)-birnessite as an edge-sharing bidentate complex, except that in these models the equatorial O shell is split. The presence of even a small amount of Np(IV) in a Np(V) sample has previously been shown to obscure the characteristic 'yl' features in the XANES due to the small shift in the edge position associated with the change in Np oxidation state (Denecke et al., 2005). This suggests that the apparent discrepancy between the XANES and the EXAFS could be explained by the reduction of a small proportion of the Np(V) to Np(IV), however, this cannot be reproduced in EXAFS modelling.

4. Conclusions

Neptunium(V) has been found to sorb to a range of Mn minerals at circumneutral pH (δ-MnO_2, triclinic (Na)-birnessite, hausmannite, and rhodochrosite). Sorption to both δ-MnO_2 and triclinic (Na)-birnessite was found to be rapid and extensive with > 95 % removal of Np from solution within the first 10 minutes of reaction in systems containing 0.162 μM Np(V). XAS showed that neptunyl, edge-sharing, bidentate adsorption complexes were formed on the surface of both δ-MnO_2 and triclinic (Na)-birnessite.

The interaction of Np(V) with hausmannite varied between the two initial Np(V) concentrations investigated, with 42 ± 7 % remaining in solution after 14 days in systems

initially containing 0.162 μM Np(V) and 3.6 % remaining in solution after 1 month in systems initially containing 5.24 μM Np(V). This suggests the reaction with hausmannite may take place in two stages, with equilibrium appearing to have been reached between the two. The XANES appear to suggest either partial reduction to Np(IV), or the presence of neptunate. However, the EXAFS suggest that results from a small portion of reduced Np(IV) (Denecke et al., 2005), while Np(V) adsorbed to hausmannite surface as inner-sphere, edge-sharing, bidentate complexes dominates.

Neptunium(V) was removed from solution slowly in the presence of rhodochrosite, with more than 91 % of the Np(V) removed from solution by the final timepoint in both the 0.162 and 5.24 μM Np(V) systems. X-ray absorption spectroscopy suggested that this could be due to the precipitation of a Np(V) containing phase on the rhodochrosite surface.

Together, the rapid uptake of Np(V) by a range of Mn minerals suggests they could play an important role of sequestering Np(V) from groundwater and therefore in controlling its migration through the subsurface. Upon association with δ-MnO_2, triclinic (Na)-birnessite, and hausmannite, XAS suggested Np(V) formed inner-sphere, edge-sharing, bidentate adsorption complexes, which have previously been observed in systems in which irreversible sorption has occurred (Pan et al., 2004; Sheng et al., 2014). This could mean that the uptake on Np(V) by some Mn minerals is partially irreversible and therefore warrants further investigation.

Acknowledgements

Rosemary Hibberd is a Nuclear FiRST DTC student, funded by EPSRC (FIRST EP/G037140/1). We thank Diamond Light Source for access to beamline I20 (SP9621-3) that contributed to the results presented here. This work was supported by the NERC LO RISE (NE/L000547/1) consortium, which is part of the NERC RATE program

(Radioactivity and the Environment) and as part of the NERC BIGRAD consortium (NE/H007768/1). The RATE programme is co-funded by the Environment Agency and Radioactive Waste Management Ltd. The authors would also like to thank Paul Lythgoe for geochemical analysis.

References

Al-Attar, L. and Dyer, A. (2002). Sorption behaviour of uranium on birnessite, a layered manganese oxide. *Journal of Materials Chemistry,* 12(5)**,** 1381-1386.

Amayri, S., Frohlich, D. R., Kaplan, U., Trautmann, N. and Reich, T. (2016). Distribution coefficients for the sorption of Th, U, Np, Pu, and Am on Opalinus Clay. *Radiochimica Acta,* 104(1)**,** 33-40.

Arai, Y., Moran, P. B., Honeyman, B. D. and Davis, J. A. (2007). In situ spectroscopic evidence for neptunium(V)-carbonate inner-sphere and outer-sphere ternary surface complexes on hematite surfaces. *Environmental Science & Technology,* 41(11)**,** 3940-3944.

Backes, C. A., McLaren, R. G., Rate, A. W. and Swift, R. S. (1995). Kinetics of Cadmium and Cobalt Desorption from Iron and Manganese Oxides. *Soil Science Society of America Journal,* 59(3)**,** 778-785.

Bots, P., Shaw, S., Law, G. T. W., Marshall, T. A., Mosselmans, J. F. W. and Morris, K. (2016). Controls on the Fate and Speciation of Np(V) During Iron (Oxyhydr)oxide Crystallization. *Environmental Science & Technology,* 50(7)**,** 3382-3390.

Brennecka, G. A., Wasylenki, L. E., Bargar, J. R., Weyer, S. and Anbar, A. D. (2011). Uranium Isotope Fractionation during Adsorption to Mn-Oxyhydroxides. *Environmental Science & Technology,* 45(4)**,** 1370-1375.

Brookshaw, D. R., Pattrick, R. A. D., Bots, P., Law, G. T. W., Lloyd, J. R., Mosselmans, J. F. W., Vaughan, D. J., Dardenne, K. and Morris, K. (2015). Redox Interactions of Tc(VII), U(VI), and Np(V) with Microbially Reduced Biotite and Chlorite. *Environmental Science & Technology,* 49(22)**,** 13139-13148.

Chinni, S., Anderson, C. R., Ulrich, K.-U., Giammar, D. E. and Tebo, B. M. (2008). Indirect UO2 Oxidation by Mn(II)-oxidizing Spores of Bacillus sp. Strain SG-1 and the Effect of U and Mn Concentrations. *Environmental Science & Technology,* 42(23)**,** 8709-8714.

Choppin, G. R. (2006). Actinide speciation in aquatic systems. *Marine Chemistry,* 99(1-4)**,** 83-92.

Christiansen, B. C., Geckeis, H., Marquardt, C. M., Bauer, A., Römer, J., Wiss, T., Schild, D. and Stipp, S. L. S. (2011). Neptunyl (Np) interaction with green rust. *Geochimica et Cosmochimica Acta,* 75(5)**,** 1216-1226.

Clark, D. L., Hobart, D. E. and Neu, M. P. (1995). Actinide carbonate complexes and their importance in actinide environmental chemistry. *Chemical Reviews,* 95(1)**,** 25-48.

Combes, J. M., Chisholm-Brause, C. J., Brown, G. E., Parks, G. A., Conradson, S. D., Eller, P. G., Triay, I. R., Hobart, D. E. and Miejer, A. (1992). EXAFS spectroscopic study of neptunium(V) sorption at the .alpha.-iron hydroxide oxide (.alpha.-FeOOH)/water interface. *Environmental Science & Technology,* 26(2)**,** 376-382.

Den Auwer, C., Guillaumont, D., Guilbaud, P., Conradson, S. D., Rehr, J. J., Ankudinov, A. and Simoni, E. (2004). Theoretical chemical contribution to the simulation of the LIII X-ray absorption edges of uranyl, neptunyl and osmyl hydrates and hydroxides. *New Journal of Chemistry,* 28(8)**,** 929-939.

Den Auwer, C., Simoni, E., Conradson, S. and Madic, C. (2003). Investigating Actinyl Oxo Cations by X-ray Absorption Spectroscopy. *European Journal of Inorganic Chemistry,* 2003(21)**,** 3843-3859.

Denecke, M. A., Dardenne, K. and Marquardt, C. M. (2005). Np(IV)/Np(V) valence determinations from Np L3 edge XANES/EXAFS. *Talanta,* 65(4)**,** 1008-1014.

Dixon, J. B., Golden, D. C., Uzochukwu, G. A. and Chen, C. C. (1990). Soil Manganese Oxides. *In:* De Boodt, M. F., Hayes, M. H. B., Herbillon, A., De Strooper, E. B. A. & Tuck, J. J. (eds.) *Soil Colloids and Their Associations in Aggregates.* Boston, MA: Springer US.

Duff, M. C., Hunter, D. B., Triay, I. R., Bertsch, P. M., Reed, D. T., Sutton, S. R., Shea-McCarthy, G., Kitten, J., Eng, P., Chipera, S. J. and Vaniman, D. T. (1999). Mineral Associations and Average Oxidation States of Sorbed Pu on Tuff. *Environmental Science & Technology,* 33**,** 2163-2169.

Elzinga, E. J., Tait, C. D., Reeder, R. J., Rector, K. D., Donohoe, R. J. and Morris, D. E. (2004). Spectroscopic investigation of U(VI) sorption at the calcite-water interface. *Geochimica et Cosmochimica Acta,* 68(11)**,** 2437-2448.

Farges, F., Ponader, C. W., Calas, G. and Brown, G. E. (1992). Structural Environment of Incompatible Elements in Silicate Glass Melt Systems 2. UIV, UV, and UVI. *Geochimica et Cosmochimica Acta,* 56(12)**,** 4205-4220.

Francis, A. J. and Dodge, C. J. (2015). Microbial mobilization of plutonium and other actinides from contaminated soil. *Journal of Environmental Radioactivity,* 150**,** 277-285.

Fredrickson, J. K., Zachara, J. M., Kennedy, D. W., Liu, C. X., Duff, M. C., Hunter, D. B. and Dohnalkova, A. (2002). Influence of Mn oxides on the reduction of uranium(VI) by the metal-reducing bacterium Shewanella putrefaciens. *Geochimica et Cosmochimica Acta,* 66(18)**,** 3247-3262.

Frohlich, D. R. (2015). Sorption of Neptunium on Clays and Clay Minerals - A Review. *Clays and Clay Minerals,* 63(3-4)**,** 262-276.

Heberling, F., Brendebach, B. and Bosbach, D. (2008a). Neptunium(V) adsorption to calcite. *Journal of Contaminant Hydrology,* 102(3-4)**,** 246-252.

Heberling, F., Denecke, M. A. and Bosbach, D. (2008b). Neptunium(V) Coprecipitation with Calcite. *Environmental Science & Technology,* 42**,** 471-476.

Hennig, C., Ikeda-Ohno, A., Tsushima, S. and Scheinost, A. C. (2009). The Sulfate Coordination of Np(IV), Np(V), and Np(VI) in Aqueous Solution. *Inorganic Chemistry,* 48(12)**,** 5350-5360.

Hursthouse, A. S., Baxter, M. S., Livens, F. R. and Duncan, H. J. (1991). Transfer of Sellafield-derived Np-237 to and within the Terrestrial Environment. *Journal of Environmental Radioactivity,* 14(2)**,** 147-174.

Icopini, G. A., Boukhalfa, H. and Neu, M. P. (2007). Biological Reduction of Np(V) and Np(V) Citrate by Metal-Reducing Bacteria. *Environmental Science & Technology,* 41(8)**,** 2764-2769.

Kaszuba, J. P. and Runde, W. H. (1999). The Aqueous Geochemistry of Neptunium: Dynamic Control of Soluble Concentrations with Applications to Nuclear Waste Disposal. *Environmental Science & Technology,* 33(24)**,** 4427-4433.

Keeney-Kennicutt, W. L. and Morse, J. W. (1984). The interaction of Np(V)O2+ with common mineral surfaces in dilute aqueous solutions and seawater. *Marine Chemistry,* 15(2)**,** 133-150.

Kenna, T. C. (2009). Using sequential extraction techniques to assess the partitioning of plutonium and neptunium-237 from multiple sources in sediments from the Ob River (Siberia). *Journal of Environmental Radioactivity,* 100(7)**,** 547-557.

Kirillov, S. A., Aleksandrova, V. S., Lisnycha, T. V., Dzanashvili, D. I., Khainakov, S. A., García, J. R., Visloguzova, N. M. and Pendelyuk, O. I. (2009). Oxidation of synthetic hausmannite (Mn3O4) to manganite (MnOOH). *Journal of Molecular Structure,* 928(1-3)**,** 89-94.

Law, G. T. W., Geissler, A., Lloyd, J. R., Livens, F. R., Boothman, C., Begg, J. D. C., Denecke, M. A., Rothe, J., Dardenne, K., Burke, I. T., Charnock, J. M. and Morris, K. (2010). Geomicrobiological Redox Cycling of the Transuranic Element Neptunium. *Environmental Science & Technology,* 44(23)**,** 8924-8929.

Li, D. and Kaplan, D. I. (2012). Sorption coefficients and molecular mechanisms of Pu, U, Np, Am and Tc to Fe (hydr)oxides: A review. *Journal of Hazardous Materials,* 243**,** 1-18.

Liu, C., Zachara, J. M., Fredrickson, J. K., Kennedy, D. W. and Dohnalkova, A. (2002). Modeling the Inhibition of the Bacterial Reduction of U(VI) by β-MnO2(s). *Environmental Science & Technology,* 36(7)**,** 1452-1459.

Lloyd, J. R., Yong, P. and Macaskie, L. E. (2000). Biological Reduction and Removal of Np(V) by Two Microorganisms. *Environmental Science & Technology,* 34(7)**,** 1297-1301.

Lozano, J. M., Clark, D. L., Conradson, S. D., Den Auwer, C., Fillaux, C., Guilaumont, D., Webster Keogh, D., Mustre de Leon, J., Palmer, P. D. and Simoni, E. (2009). Influence of the local atomic structure in the X-ray absorption near edge spectroscopy of neptunium oxo ions. *Physical Chemistry Chemical Physics,* 11(44)**,** 10396-10402.

Marshall, T. A., Morris, K., Law, G. T., Livens, F. R., Mosselmans, J. F., Bots, P. and Shaw, S. (2014). Incorporation of Uranium into Hematite during crystallization from ferrihydrite. *Environmental Science & Technology,* 48(7)**,** 3724-3731.

McArdell, C. S., Stone, A. T. and Tian, J. (1998). Reaction of EDTA and related aminocarboxylate chelating agents with Co(III)OOH (heterogenite) and Mn(III)OOH (manganite). *Environmental Science & Technology,* 32(19)**,** 2923-2930.

Morris, K., Butterworth, J. C. and Livens, F. R. (2000). Evidence for the remobilization of Sellafield waste radionuclides in an intertidal salt marsh, West Cumbria, UK. *Estuarine Coastal and Shelf Science,* 51(5)**,** 613-625.

Moyes, L. N., Jones, M. J., Reed, W. A., Livens, F. R., Charnock, J. M., Mosselmans, J. F. W., Hennig, C., Vaughan, D. J. and Pattrick, R. A. D. (2002). An X-ray Absorption Spectroscopy Study of Neptunium(V) Reactions with Mackinawite (FeS). *Environmental Science & Technology,* 36(2)**,** 179-183.

Mukherjee, J., Ramkumar, J., Chandramouleeswaran, S., Shukla, R. and Tyagi, A. K. (2013). Sorption characteristics of nano manganese oxide: efficient sorbent for removal of metal ions from aqueous streams. *Journal of Radioanalytical and Nuclear Chemistry,* 297(1)**,** 49-57.

Muller, K., Groschel, A., Rossberg, A., Bok, F., Franzen, C., Brendler, V. and Foerstendorf, H. (2015). In situ Spectroscopic Identification of Neptunium(V) Inner-Sphere Complexes on the Hematite-Water Interface. *Environmental Science & Technology,* 49(4)**,** 2560-2567.

Nagasaki, S., Saito, T. and Yang, T. T. (2016). Sorption behavior of Np(V) on illite, shale and MX-80 in high ionic strength solutions. *Journal of Radioanalytical and Nuclear Chemistry,* 308(1)**,** 143-153.

Nakata, K., Nagasaki, S., Tanaka, S., Sakamoto, Y., Tanaka, T. and Ogawa, H. (2002). Sorption and reduction of neptunium(V) on the surface of iron oxides. *Radiochimica Acta,* 90**,** 665-669.

NDA. (2010). *Geological Disposal: Radionuclide behaviour status report.* Harwell. NDA/RWMD/034.

Ojovan, M. I. and Lee, W. E. (2014). *An Introduction to Nuclear Waste Immobilisation* (2nd ed.). Kidlington, Oxford: Elsevier.

Pan, G., Qin, Y., Li, X., Hu, T., Wu, Z. and Xie, Y. (2004). EXAFS studies on adsorption–desorption reversibility at manganese oxides–water interfaces: I. Irreversible adsorption of zinc onto manganite (γ-MnOOH). *Journal of Colloid and Interface Science,* 271(1)**,** 28-34.

Parkhurst, D. L. and Appelo, C. A. J. (2013). *Description of input and examples for PHREEQC version 3—A computer program for speciation, batch-reaction, one-dimensional transport, and inverse geochemical calculations* [Online]. available only at http://pubs.usgs.gov/tm/06/a43/. [Accessed 06/11/2015].

Post, J. E. (1999). Manganese oxide minerals: Crystal structures and economic and environmental significance. *Proceedings of the National Academy of Sciences,* 96(7)**,** 3447-3454.

Powell, B. A., Duff, M. C., Kaplan, D. I., Fjeld, R. A., Newville, M., Hunter, D. B., Bertsch, P. M., Coates, J. T., Eng, P., Rivers, M. L., Sutton, S. R., Triay, I. R. and Vaniman, D. T. (2006). Plutonium oxidation and subsequent reduction by Mn(IV) minerals in Yucca Mountain tuff. *Environmental Science & Technology,* 40(11)**,** 3508-3514.

Ravel, B. and Newville, M. (2005). ATHENA, ARTEMIS, HEPHAESTUS: data analysis for X-ray absorption spectroscopy using IFEFFIT. *Journal of Synchrotron Radiation,* 12(Pt 4)**,** 537-541.

Renshaw, J. C., Butchins, L. J. C., Livens, F. R., May, I., Charnock, J. M. and Lloyd, J. R. (2005). Bioreduction of Uranium: Environmental Implications of a Pentavalent Intermediate. *Environmental Science & Technology,* 39(15)**,** 5657-5660.

Rihs, S., Gaillard, C., Reich, T. and Kohler, S. J. (2014). Uranyl sorption onto birnessite: A surface complexation modeling and EXAFS study. *Chemical Geology,* 373**,** 59-70.

Rittmann, B. E., Banaszak, J. E. and Reed, D. T. (2002). Reduction of Np(V) and precipitation of Np(IV) by an anaerobic microbial consortium. *Biodegradation,* 13(5)**,** 329-342.

Roy, S. (1981). *Manganese Deposits*. London: Academic Press.

Runde, W. (2000). The Chemical Interactions of Actinides in the Environment. *Los Alamos Science.*

Runde, W., Neu, M. P. and Clark, D. L. (1996). Neptunium(V) hydrolysis and carbonate complexation: Experimental and predicted neptunyl solubility in concentrated NaCl using the Pitzer approach. *Geochimica et Cosmochimica Acta,* 60(12)**,** 2065-2073.

Scheinost, A. C., Schmeisser, N., Benerjee, D., Rossberg, A., Denecke, M. A., Dardenne, K., Rothe, J. and Daehn, R. (2013). AcXAS An Actinide Reference X-ray Absorption Spectroscopy Database. https://www.hzdr.de/acxas.

Scheinost, A. C., Steudtner, R., Hubner, R., Weiss, S. and Bok, F. (2016). Neptunium(V) Retention by Siderite under Anoxic Conditions: Precipitation of NpO2-Like Nanoparticles and of Np-IV Pentacarbonate. *Environmental Science & Technology,* 50(19)**,** 10413-10420.

Shaughnessy, D. A., Nitsche, H., Booth, C. H., Shuh, D. K., Waychunas, G. A., Wilson, R. E., Gill, H., Cantrell, K. J. and Serne, R. J. (2003). Molecular interfacial reactions between Pu(VI) and manganese oxide minerals manganite and hausmannite. *Environmental Science & Technology,* 37(15)**,** 3367-3374.

Sheng, G. D., Yang, S. T., Li, Y. M., Gao, X., Huang, Y. Y., Hu, J. and Wang, X. K. (2014). Retention mechanisms and microstructure of Eu(III) on manganese dioxide studied by batch and high resolution EXAFS technique. *Radiochimica Acta,* 102(1-2)**,** 155-167.

Smith, A. L., Martin, P., Prieur, D., Scheinost, A. C., Raison, P. E., Cheetham, A. K. and Konings, R. J. M. (2016). Structural Properties and Charge Distribution of the Sodium Uranium, Neptunium, and Plutonium Ternary Oxides: A Combined X-ray Diffraction and XANES Study. *Inorganic Chemistry,* 55(4)**,** 1569-1579.

Smith, K. F., Bryan, N. D., Swinburne, A. N., Bots, P., Shaw, S., Natrajan, L. S., Mosselmans, J. F. W., Livens, F. R. and Morris, K. (2015). U(VI) behaviour in hyperalkaline calcite systems. *Geochimica et Cosmochimica Acta,* 148**,** 343-359.

Tanaka, K., Tani, Y. and Ohnuki, T. (2011). Specific Sorption Behavior of Actinoids on Biogenic Mn Oxide. *Chemistry Letters,* 40(8)**,** 806-807.

Thorpe, C. L., Morris, K., Lloyd, J. R., Denecke, M. A., Law, K. A., Dardenne, K., Boothman, C., Bots, P. and Law, G. T. W. (2015). Neptunium and manganese biocycling in nuclear legacy sediment systems. *Applied Geochemistry,* 63**,** 303-309.

Tits, J., Gaona, X., Laube, A. and Wieland, E. (2014). Influence of the redox state on the neptunium sorption under alkaline conditions: Batch sorption studies on titanium dioxide and calcium silicate hydrates. *Radiochimica Acta,* 102(5)**,** 385-400.

Villalobos, M., Toner, B., Bargar, J. and Sposito, G. (2003). Characterization of the manganese oxide produced by Pseudomonas putida strain MnB1. *Geochimica et Cosmochimica Acta,* 67(14)**,** 2649-2662.

Virtanen, S., Bok, F., Ikeda-Ohno, A., Rossberg, A., Lutzenkirchen, J., Rabung, T., Lehto, J. and Huittinen, N. (2016). The specific sorption of Np(V) on the corundum (alpha-Al2O3) surface in the presence of trivalent lanthanides Eu(III) and Gd(III): A batch sorption and XAS study. *Journal of Colloid and Interface Science,* 483**,** 334-342.

Walls, J. (2011). Nuclear Power Generation - Past, Present and Future. *In:* Hester, R. E. & Harrison, R. M. (eds.) *Nuclear Power and the Environment.* Royal Society of Chemistry.

Wang, Z., Lee, S. W., Catalano, J. G., Lezama-Pacheco, J. S., Bargar, J. R., Tebo, B. M. and Giammar, D. E. (2013). Adsorption of uranium(VI) to manganese oxides: X-ray absorption spectroscopy and surface complexation modeling. *Environmental Science & Technology,* 47(2)**,** 850-858.

Webb, S. M., Fuller, C. C., Tebo, B. M. and Bargar, J. R. (2006). Determination of Uranyl Incoporation into Biogenic Manganese Oxides Using X-ray Absorption Spectroscopy and Scattering. *Environmental Science & Technology,* 40**,** 771-777.

Wilk, P. A., Shaughnessy, D. A., Wilson, R. E. and Nitsche, H. (2005). Interfacial Interactions between Np(V) and Manganese Oxide Minerals Manganite and Hausmannite. *Environmental Science & Technology,* 39**,** 2608-2615.

Wilkins, M. J., Livens, F. R., Vaughan, D. J., Beadle, I. and Lloyd, J. R. (2007). The influence of microbial redox cycling on radionuclide mobility in the subsurface at a low-level radioactive waste storage site. *Geobiology,* 5(3)**,** 293-301.

Wylie, E. M., Olive, D. T. and Powell, B. A. (2016). Effects of Titanium Doping in Titanomagnetite on Neptunium Sorption and Speciation. *Environmental Science & Technology,* 50(4)**,** 1853-1858.

Yamamoto, M., Yamauchi, Y., Komura, K., Ueno, K. and Assinder, D. J. (1991). Chemical leaching behavior of ^{237}Np from intertidal coastal sediment in the Irish Sea. *Journal of Radioanalytical and Nuclear Chemistry,* 154(5)**,** 299-307.

Yang, C. L., Powell, B. A., Zhang, S. D. and Rao, L. F. (2015). Surface complexation modeling of neptunium(V) sorption to lepidocrocite (gamma-FeOOH). *Radiochimica Acta,* 103(10)**,** 707-717.

Yoshida, Z., Johnson, S. G., Kimura, T. and Krisul, J. R. (2011). Neptunium. *In:* Morss, L. R., Edelstein, N. M. & Fuger, J. (eds.) *The chemistry of the actinide and transactide elements.* 4th ed. Dordrecht: Springer.

Zavarin, M., Powell, B. A., Bourbin, M., Zhao, P. and Kersting, A. B. (2012). Np(V) and Pu(V) Ion Exchange and Surface-Mediated Reduction Mechanisms on Montmorillonite. *Environmental Science & Technology,* 46(5)**,** 2692-2698.

Zavarin, M., Roberts, S. K., Hakem, N., Sawvel, A. M. and Kersting, A. B. (2005). Eu(III), Sm(III), Np(V), Pu(V), and Pu(IV) sokption to calcite. *Radiochimica Acta,* 93(2)**,** 93-102.

Zhao, P., Johnson, M. R., Roberts, S. K. and Zavarin, M. (2005). *Np and Pu Sorption to Manganese Oxide Minerals*. Livermore, California. UCRL-TR-214984.

Zou, W., Zhao, L. and Han, R. (2010). Adsorption characteristics of uranyl ions by manganese oxide coated sand in batch mode. *Journal of Radioanalytical and Nuclear Chemistry,* 288(1)**,** 239-249.

Supporting Information for: Interaction of Np(V) with Mn minerals

Rosemary Hibberd,[1,2] Katherine Morris,[2] Clare L. Thorpe,[2,a] Katie A. Law,[1] Jörg Rothe,[3] Pieter Bots,[2,b] Nicholas D. Bryan,[1,4] Gareth T. W. Law[1*]

[1] Centre for Radiochemistry Research, School of Chemistry, The University of Manchester, Oxford Road, Manchester, M13 9PL, UK.

[2] Research Centre for Radwaste Disposal, School of Earth, Atmospheric and Environmental Sciences, The University of Manchester, Oxford Road, Manchester, M13 9PL, UK.

[3] Institut für Nukleare Entsorgung, Karlsruhe Institute of Technology (KIT-INE), D-76021 Karlsruhe, Germany.

[4] National Nuclear Laboratory, 5th Floor, Chadwick House, Birchwood Park, Warrington Road, Warrington, WA3 6AE, UK.

[b] Present address: Department of Materials Science and Engineering, The University of Sheffield, Sheffield, S1 3JD, UK.

[b] Present address: Department of Civil and Environmental Engineering, University of Strathclyde, Glasgow, G1 1XQ, UK.

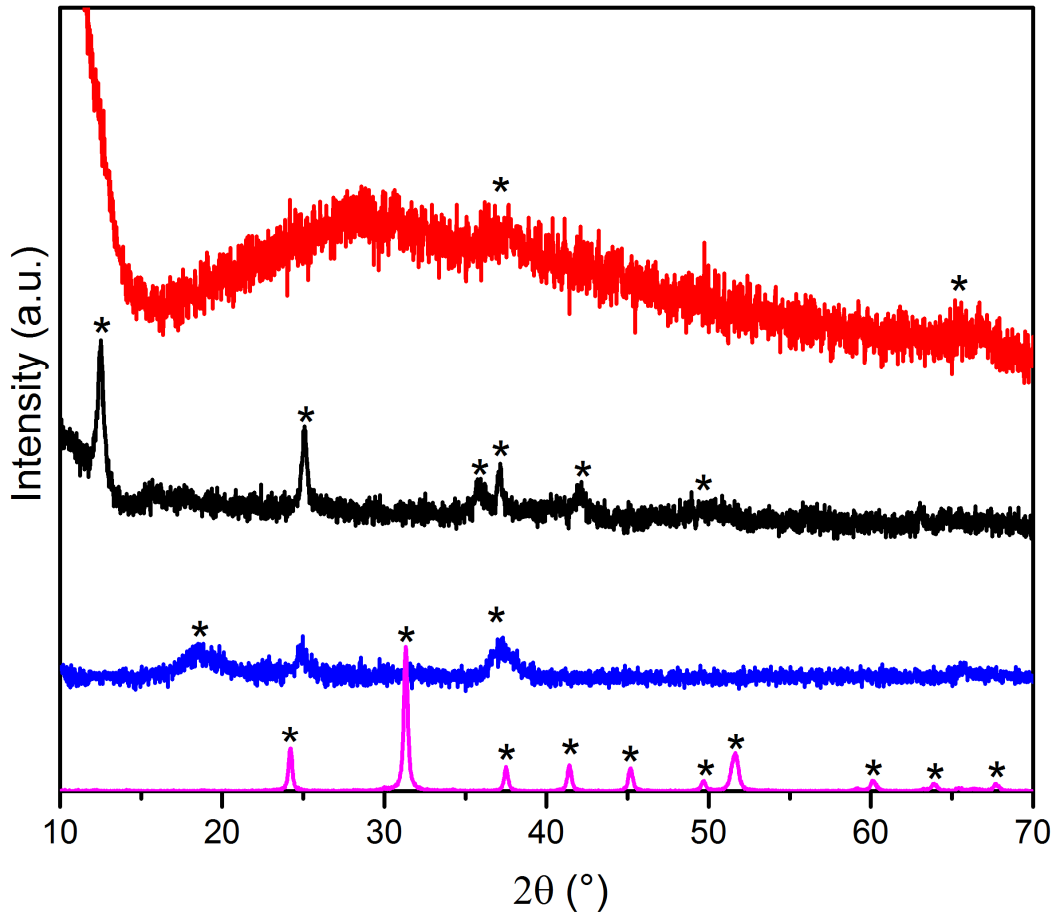

SI Figure 1. XRD of starting materials, red = δ-MnO_2; black = triclinic (Na)-birnessite; blue = hausmannite; pink = rhodochrosite. The characteristic diffraction peaks (*) were compared to those reported in the literature to confirm mineral identity and purity: δ-MnO_2 (Villalobos et al., 2003), triclinic (Na)-birnessite (Villalobos et al., 2003), hausmannite (Park et al., 2015), and rhodochrosite (Graf, 1961).

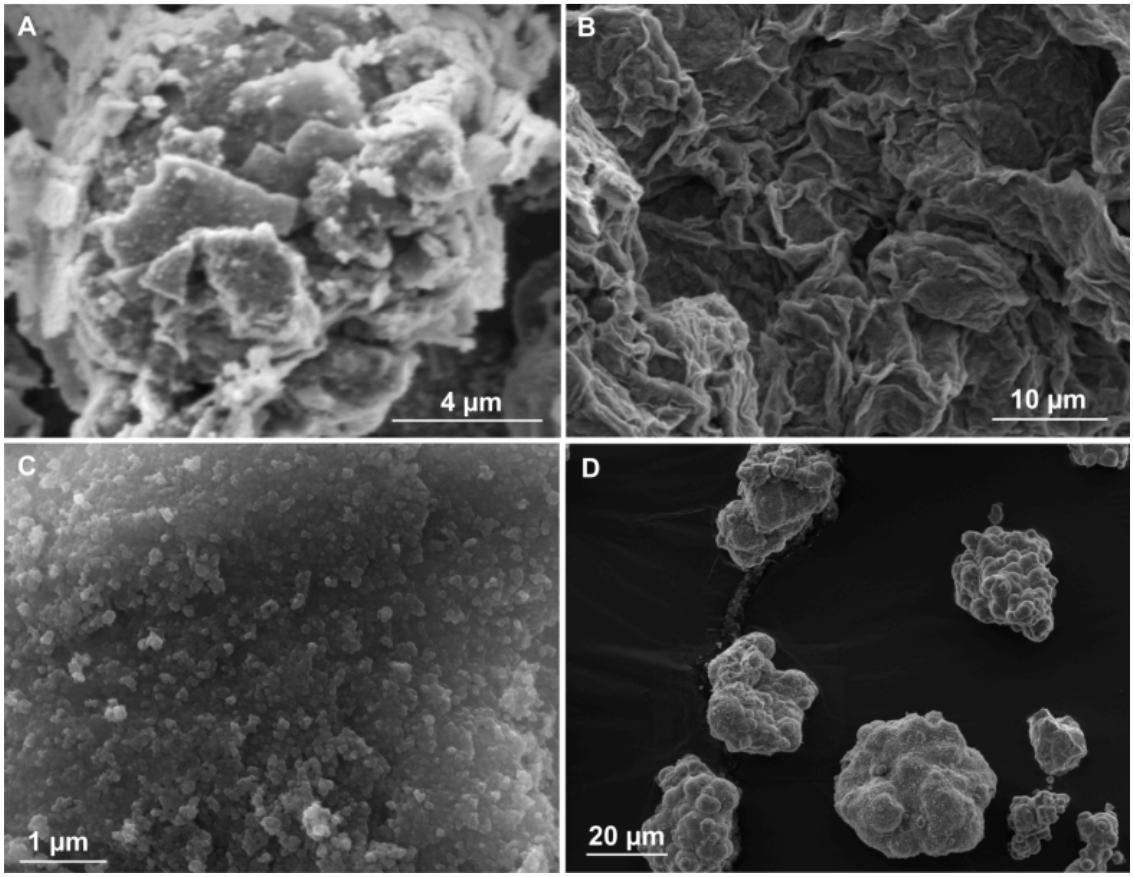

SI Figure 2. SEM images of starting materials, A = δ-MnO_2; B = triclinic (Na)-birnessite; C = hausmannite; D = rhodochrosite. The starting minerals were analysed by SEM to determine their morphology and compared to previously reported literature (Sternbeck, 1997; Qiu et al., 2011; Rihs et al., 2014). This was particularly important for hausmannite since it can oxidise to manganite, which is difficult to differentiate by XRD. The formation of hausmannite was confirmed by the 'fluffy' spherical particles; the absence of needles indicates absence of manganite (Kirillov et al., 2009).

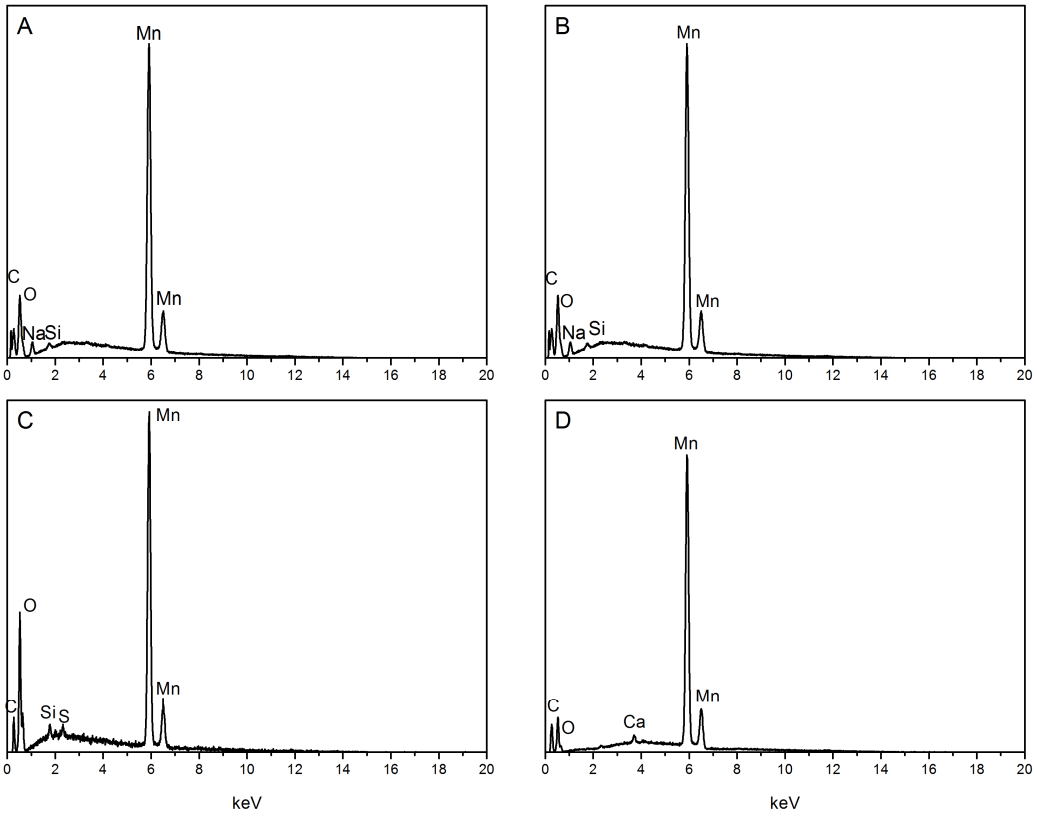

SI Figure 3. EDX of starting materials A = δ-MnO_2; B = triclinic (Na)-birnessite; C = hausmannite; D = rhodochrosite. EDX spectra were taken from the starting minerals to confirm the absence of common contaminant metals such as Fe.

Mineral	Surface area (m^2g^{-1})
δ-MnO_2	100.5
Triclinic (Na)-birnessite	84.7
Hausmannite	2.2
Rhodochrosite	8.2

SI Table 1. Surface areas of starting minerals, as determined by Brunauer-Emmett-Teller (BET).

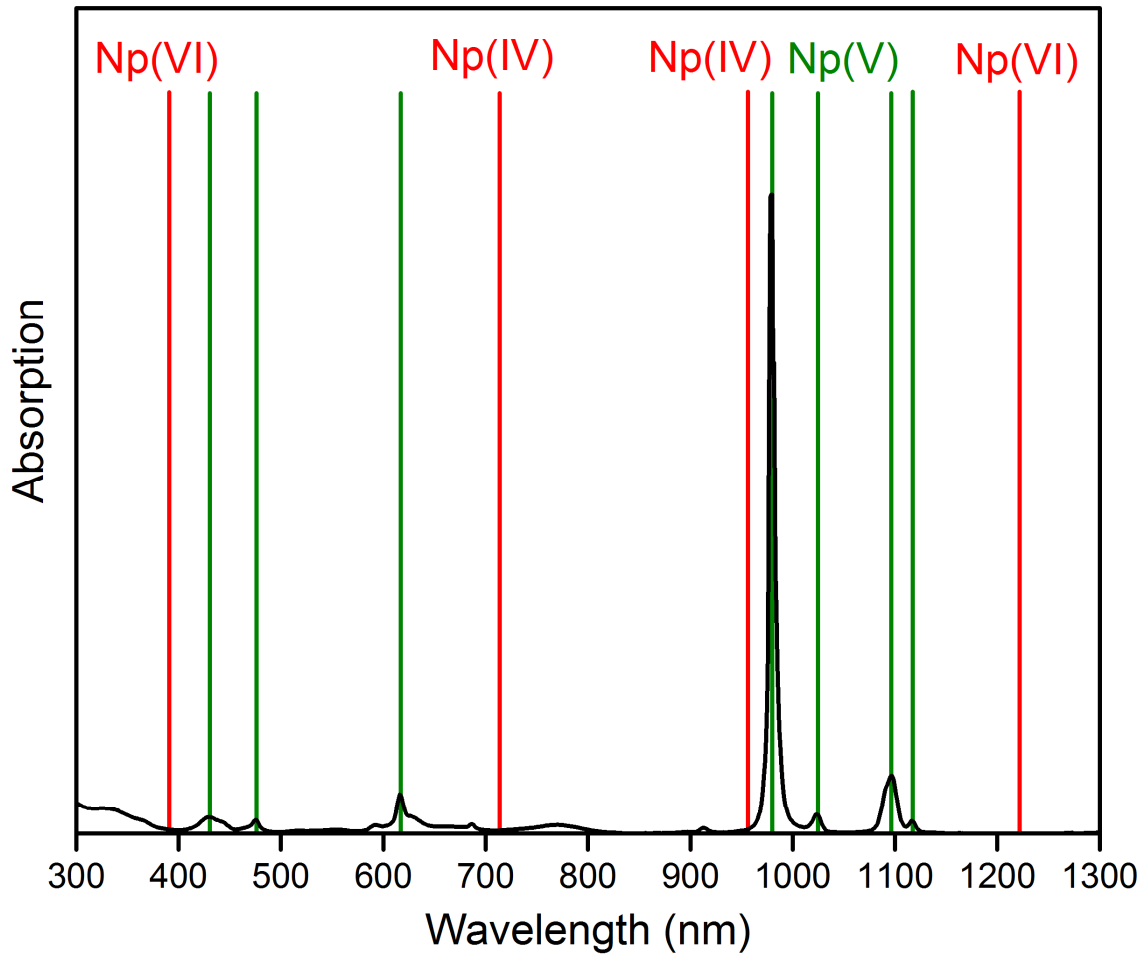

SI Figure 4. UV-Vis-NIR spectra of the Np(V) stock solution used in experiments with characteristic absorption lines for Np(V) (green), Np(IV), and Np(VI) (both red) labelled.

Constituent	g L^{-1} deionised water
KCl	0.0066
$MgSO_4 \cdot 7H_2O$	0.0976
$MgCl_2 \cdot 6H_2O$	0.0810
Na_2SiO_3	0.0829
$NaNO_3$	0.0275
NaCl	0.0094
$NaHCO_3$	0.2424

SI Table 2. Composition of synthetic groundwater used in the lower level 0.162 μM Np(V) sorption experiments, adapted from Wilkins et al. (2007).

Sample	E_0 (eV)	Resonance Feature C (eV)
δ-MnO_2 pH 7.3 (1 month) (a)	17613.1	17654.0
Triclinic (Na)-birnessite pH 7.0 (1 month) (b)	17611.6	17655.3
Rhodochrosite pH 9.3 (1 month) (c)	17611.8	17654.8
Hausmannite pH 7.3 (1 month) (d)	17614.2	17655.1

SI Table 3. Edge positions and position of the second resonance feature (C) in the XANES spectra of Np associated with a range of Mn minerals.

		Single O_{eq}	Split O_{eq}	Mn	Split O_{eq}
δ-MnO_2 pH 7.3 (1 month) (a)	R-factor	0.0247	0.0165	0.0029	
	Significance		96 %	100 %	
Triclinic (Na)-birnessite pH 7.0 (1 month) (b)	R-factor	0.0563		0.0211	0.0070
	Significance			97 %	98 %
Rhodochrosite pH 9.3 (1 month) (c)	R-factor	0.0479	0.0310	0.0241	
	Significance		95 %	80 %	
Hausmannite pH 7.3 (1 month) (d)	R-factor	0.0626		0.0292	
	Significance			99 %	

SI Table 4. Statistical significance of backscattering shells to the models fitting EXFAS data as determined by the F-test (Downward et al., 2007). Shells included in the final fit are coloured green. Shells with no data did not improve the fit.

Np(V) species	pH 7.5, Initial Np(V) = 5.24 µM	pH 7.0, Initial Np(V) = 0.162 µM
NpO_2^+	4.929 x 10^{-6} M	1.434 x 10^{-7} M
NpO_2Cl	2.983 x 10^{-7} M	6.263 x 10^{-11} M
$NpO_2(OH)$	6.855 x 10^{-10} M	3.657 x 10^{-9} M
$NpO_2(OH)_2^-$	2.029 x 10^{-11} M	-
$NpO_2CO_3^-$	-	1.469 x 10^{-8} M
$NpO_2SO_4^-$	-	9.020 x 10^{-11} M
$NpO_2(CO_2)_2^{3-}$	-	1.816 x 10^{-11} M
$NpO_2(CO_2)_3^{5-}$	-	5.513 x 10^{-15} M

SI Table 5. Np(V) speciation in both the higher (5.24 µM) and lower (0.162 µM) Np(V) sorption experiments as calculated by PHREEQC using the LLNL database. No supersaturated Np containing phases were identified in any of the solutions.

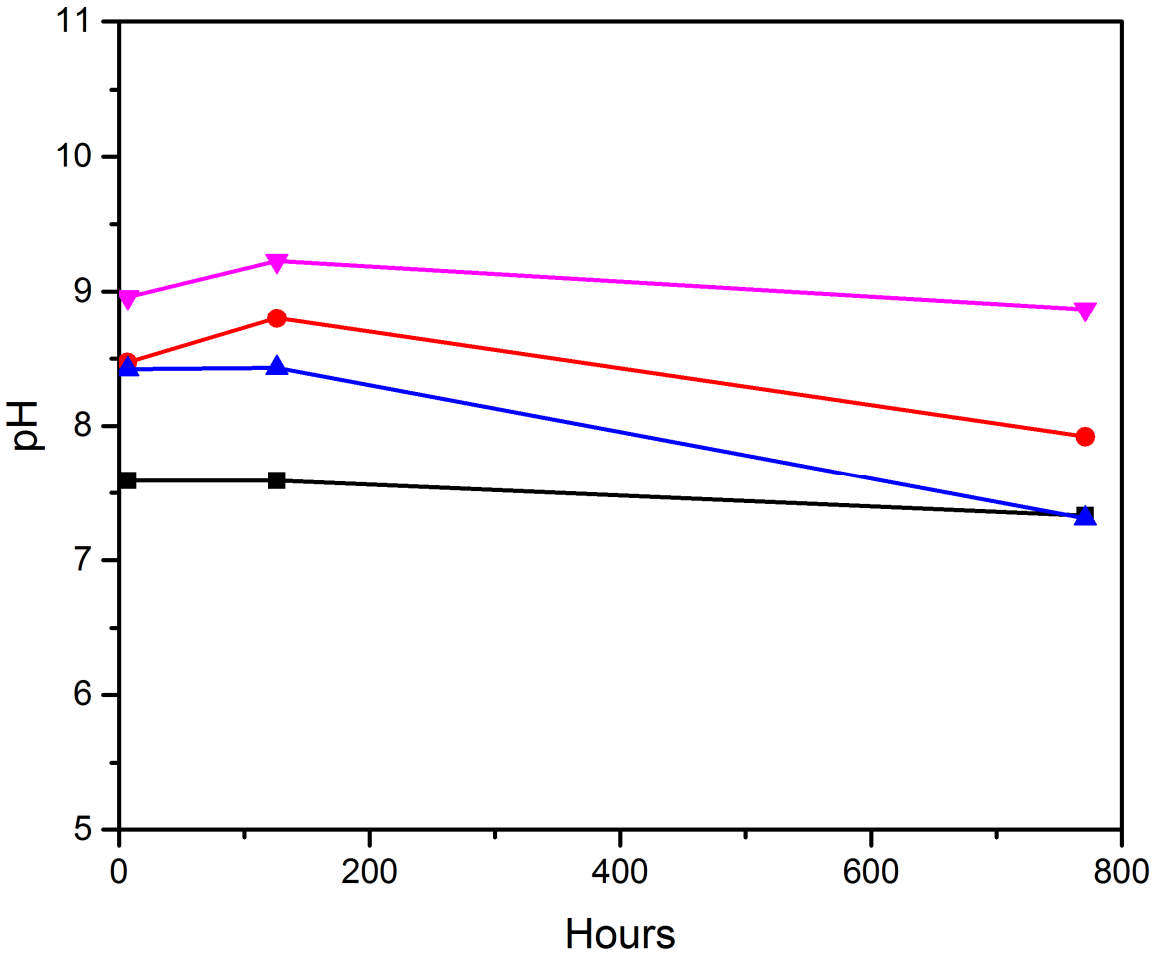

SI Figure 5. pH of 5.24 µM Np(V) sorption experiments. Black = δ-MnO_2; red = triclinic (Na)-birnessite; blue = hausmannite; pink = rhodochrosite.

References

Downward, L., Booth, C. H., Lukens, W. W. and Bridges, F. (2007). A variation of the F-Test for determining statistical relevance of particular parameters in EXAFS fits. *In:* Hedman, B. & Painetta, P. (eds.) *X-Ray Absorption Fine Structure-XAFS13.* Melville: American Institute of Physics.

Graf, D. L. (1961). Crystallographic Tables for the Rhombohedral Carbonates. *American Mineralogist,* 46**,** 1283-1316.

Kirillov, S. A., Aleksandrova, V. S., Lisnycha, T. V., Dzanashvili, D. I., Khainakov, S. A., García, J. R., Visloguzova, N. M. and Pendelyuk, O. I. (2009). Oxidation of synthetic hausmannite (Mn3O4) to manganite (MnOOH). *Journal of Molecular Structure,* 928(1-3)**,** 89-94.

Park, Y., Woo Lee, S., Kim, K. H., Min, B.-K., Kumar Nayak, A., Pradhan, D. and Sohn, Y. (2015). Understanding hydrothermal transformation from Mn2O3 particles to Na0.55Mn2O4·1.5H2O nanosheets, nanobelts, and single crystalline ultra-long Na4Mn9O18 nanowires. *Scientific Reports,* 5**,** 18275.

Qiu, G., Li, Q., Yu, Y., Feng, X., Tan, W. and Liu, F. (2011). Oxidation behavior and kinetics of sulfide by synthesized manganese oxide minerals. *Journal of Soils and Sediments,* 11(8)**,** 1323-1333.

Rihs, S., Gaillard, C., Reich, T. and Kohler, S. J. (2014). Uranyl sorption onto birnessite: A surface complexation modeling and EXAFS study. *Chemical Geology,* 373**,** 59-70.

Sternbeck, J. (1997). Kinetics of rhodochrosite crystal growth at 25°C: The role of surface speciation. *Geochimica et Cosmochimica Acta,* 61(4)**,** 785-793.

Villalobos, M., Toner, B., Bargar, J. and Sposito, G. (2003). Characterization of the manganese oxide produced by Pseudomonas putida strain MnB1. *Geochimica et Cosmochimica Acta,* 67(14)**,** 2649-2662.

Wilkins, M. J., Livens, F. R., Vaughan, D. J., Beadle, I. and Lloyd, J. R. (2007). The influence of microbial redox cycling on radionuclide mobility in the subsurface at a low-level radioactive waste storage site. *Geobiology,* 5(3)**,** 293-301.

8. Conclusions

8.1. Summary and conclusions

This thesis has explored the behaviour of U(VI) and Np(V) in systems representative of the shallow to deep subsurface under conditions relevant to geological disposal and contaminated land. A number of hypotheses were tested (see Chapters 4 – 7) and relevant results are summarised below.

Firstly, **Hypothesis 1** stated that: "*4.2, 42, and 252 μM U(VI) will be removed from solution under high pH conditions representative of geological disposal"*. This hypothesis was proven to be false as in **Chapter 4**, the formation of U(VI) colloids was documented under high pH conditions, and these colloids kept U in solution. Specifically, small colloids (< 2 nm) formed rapidly as identified by TEM and SAXS and then ~ 50 % of the colloids aggregated to form clusters of 60 – 80 nm diameter. TEM and EXAFS indicated that the nanoparticles had crystallised with a clarkeite-type structure within 1 day. The colloids were found to be stable in cement leachate over a period of at least 2.5 years. The presence of U(VI) colloids in high pH solutions provides a potentially new mechanism for U(VI) transport in cementitious environments.

Building on the findings of Chapter 4, **Hypothesis 2** stated that: *"U(VI) nanoparticles formed in high pH cement leachate will be removed from solution by the addition of cement, biotite, quartz, and orthoclase*" and **Hypothesis 3** stated: "*U(VI) is removed from high pH cement leachate by incorporation into the interlayer of the C-S-H phases in cement*". Both hypotheses were tested in **Chapter 5** and both were found to be partially true. Specifically, the colloids were found to remain stable and in solution in the presence of quartz and orthoclase, over a period of at least 18 months. In contrast, limited (~ 20 %) removal of U(VI) (< 0.45 μm filter fraction) was observed in biotite systems but it was unclear whether U(VI) removal resulted from Fe(II) induced reduction of U(VI) to U(IV),

or the precipitation of a Ca, and / or Si U containing phase. Finally, the introduction of cement to the colloid suspension was accompanied by the removal of > 90 % of the U(VI) from solution within 1 month. However, 1.0 µM (2.4 %) of U(VI) remained in the filtered (< 0.02 µm) fraction after 21 months of reaction, suggesting a portion of the clarkeite colloids persist in solution even in the presence of cement. Modelling of EXAFS data collected after 1 month of contact with cement revealed U(VI) was predominantly present in a uranophane-like coordination environment. This was consistent with luminescence spectroscopy and suggested the U(VI) either precipitated out of solution as uranophane or was present in the C-S-H interlayers of the cement phase in a uranyl-silicate-like coordination environment. After 21 months of reaction the XAS showed an increased contribution from a uranate coordination environment, suggesting the precipitation of a uranate phase also occurred, likely due to partial cement dissolution and the subsequent alteration of the solution chemistry. SEM images of the colloid reacted cement phase after 21 months showed discrete uranium rich areas and suggested the co-location of Ca and U, which is consistent with the precipitation of a Ca uranate phase.

Hypothesis 4 stated that: "*U(VI) and Np(V) are removed from solution by sorption to δ-MnO_2, triclinic (Na)-birnessite, hausmannite, and rhodochrosite under circumneutral to high pH conditions relevant to geological disposal"* and **Hypothesis 5** stated that: *"the sorption of U(VI) to δ-MnO_2, triclinic (Na)-birnessite, hausmannite, and rhodochrosite is reversible"*. Hypothesis 4 was found to be true for both U(VI) and Np(V), and Hypothesis 5 was found to be partially true for U(VI). U(VI) interaction with Mn minerals was detailed in **Chapter 6** and here rapid and extensive U(VI) uptake onto δ-MnO_2, triclinic (Na)-birnessite, and hausmannite occurred across the whole pH range, while extensive but kinetically slower uptake was observed by rhodochrosite. Uptake by δ-MnO_2 and hausmannite was found to be only partially reversible, suggesting that these phases could be particularly important in retarding the migration of U(VI). After 1 month of reaction

U(VI) associated with δ-MnO_2 and hausmannite could be identified in an edge-sharing bidentate adsorption complex by EXAFS. This suggests the formation of this surface complex could be responsible for the observed irreversibility, which has previously been suggested in other heavy metal mineral systems (Pan et al., 2004; Sheng et al., 2014). Modelling of EXAFS data collected from rhodochrosite associated U(VI) supported the kinetic data which suggested that U(VI) may have been removed from solution *via* a surface precipitation mechanism. EXAFS data collected after 4 hours reaction of U(VI) with triclinic (Na)-birnessite also showed U(VI) was predominantly sorbed as an edge-sharing, bidentate adsorption complex. Over the course of the first month of reaction changes in the EXAFS data suggested that U(VI) migrated into the interlayer of triclinic (Na)-birnessite and replaced the interlayer Na^+. This could explain the reversibility in the triclinic (Na)-birnessite systems identified by desorption experiments.

Neptunyl reaction with Mn minerals was detailed in **Chapter 7**. Here, rapid (> 95 % within 10 minutes) uptake of Np(V) was apparent for δ-MnO_2 and triclinic (Na)-birnessite. The uptake of Np(V) by rhodochrosite was slower with equilibrium taking longer than 1 week to be established, but was also extensive (> 90 %). The uptake of Np(V) by hausmannite appeared to be extensive (96.4 % removal) at higher (5.24 μM) Np(V) concentrations, while 42 % of the Np(V) remained in solution after 336 hours reaction with 0.162 μM Np(V) and had reached apparent equilibrium. This data suggests that Mn minerals could play an important role in retarding migration in the subsurface. XAS showed that Np(V) adsorbed to δ-MnO_2 and triclinic (Na)-birnessite in a neptunyl moiety as edge-sharing bidentate complexes, and suggested that a Np(V) phase could have precipitated on to the surface of rhodochrosite. EXAFS also identified Np(V) edge-sharing bidentate complexes on hausmannite, which have previously been seen to be irreversible for metals such as Zn^{2+}, Eu^{3+} (Pan et al., 2004; Sheng et al., 2014). XANES from the hausmannite system suggest that some Np(V) may have been reduced to Np(IV).

8.2. Implications

This thesis has important implications for the geological disposal of radioactive wastes and for the management of contaminated land. It has revealed a number of processes which will have both positive and negative impacts on the migration of U(VI) and Np(V) through the subsurface. For example, the formation of U(VI) nanoparticles which are stable in contact with common, rock forming, silicate minerals could significantly increase the migration of U(VI) in cementitious environments. However, further dissolution of cement phases used as buffer and backfill materials may cause the majority of these U(VI) nanoparticles to precipitate out of solution as uranate phases, which may mitigate against the increased U(VI) mobility. However, 1 μM U(VI) remained in solution after 21 months of reaction with cement phases, highlighting the need for experimental data to accurately inform modelling.

In addition, the reaction of U(VI) and Np(V) with Mn minerals may also reduce the mobility of these radionuclides, thereby reducing their migration in the subsurface. Furthermore, the identification of edge-sharing bidentate U(VI) and Np(V) adsorption complexes on the surface of a number of Mn oxide minerals elucidates the mechanism of radionuclide uptake by these minerals. Partially irreversible adsorption of U(VI) to δ-MnO_2 and hausmannite has also been observed, suggesting these minerals could be particularly important in retarding radionuclide migration. This mechanistic understanding is vital for reducing uncertainties in modelling and predicting the subsurface migration of U and Np, and thereby reducing the requirement for conservative assumptions and subsequent costly over-engineering. In particular, the importance of Mn minerals in determining the fate of key, risk-driving radionuclides in contaminated land and within the CDZ of a geological disposal facility is highlighted.

Overall, this thesis has identified and investigated new and important processes which will aid in predicting the subsurface behaviour of radionuclides over the long-term, allowing the risks associated with radionuclide migration to be mitigated.

8.3. Directions for Future Research

The experiments presented in this thesis identify U(VI) colloid formation in a high pH cement leachate. The majority of this U(VI) precipitates out the aqueous phase in the presence of a solid cement phase. However, 1.0 μM U(VI) passed through 0.02 μm filters after 21 months contact with cement, and when in contact with biotite, orthoclase, and quartz this rises to 24.9 ± 0.3, 39.4 ± 0.02, and 40.2 ± 0.2 μM, after 30, 18, and 60 months, respectively. An obvious next step would be to confirm that U(VI) which passed through the 0.02 μm filters remained colloidal in these systems, which could be achieved using ultra-filtration and series of smaller filters (such as 10, 3, and 1 kDa). This work also raises the question of whether other, similar, long-lived radionuclides, such as neptunium and plutonium, form similar intrinsic colloids under high pH conditions.

With regards to the interactions of U(VI) and Np(V) with Mn minerals, the work suggests that Mn minerals could be important in determining radionuclide behaviour in the subsurface. It would therefore be valuable to determine the relative importance of Mn and Fe minerals on radionuclide uptake and to investigate radionuclide partitioning in systems which contained both Fe and Mn minerals. It is also important, now the significant uptake has been observed, to collect data over a wide range of radionuclide concentrations and conditions to allow thermodynamic modelling.

Understanding the uptake of Np(V) in general is important since it is a risk-driving radionuclide, due to its long half-life and mobility in aqueous systems, which is poorly understood. Investigating the reversibility of the interaction of Np(V) with Mn minerals and underpinning our understanding with additional XAS is clearly desirable, as well as

investigating Np(V) behaviour at high pH (although this is less important for Np than for U since this will mostly be HLW and is therefore less likely to be in a cementitious environment). Improved Np XANES standards are also vital to investigate the potential reduction of Np(V) to Np(IV) in the beam in the presence of hausmannite.

The δ-MnO_2 found in the environment is biogenic in nature and, over the geological timescales that the long-lived radionuclides uranium-238 and neptunium-237 are expected to be important, δ-MnO_2 is expected to undergo redox cycling. The fate of U(VI) and Np(V) associated with δ-MnO_2 when this undergoes reduction must be understood to accurately determine the long-term impact of these phases on radionuclide migration in the environment. Further redox cycling could then be used to determine whether any radionuclide incorporation was reversible or whether any recalcitrant phases are formed.

8.4. References

Pan, G., Qin, Y., Li, X., Hu, T., Wu, Z. and Xie, Y. (2004). EXAFS studies on adsorption–desorption reversibility at manganese oxides–water interfaces: I. Irreversible adsorption of zinc onto manganite (γ-MnOOH). *Journal of Colloid and Interface Science,* 271(1)**,** 28-34.

Sheng, G. D., Yang, S. T., Li, Y. M., Gao, X., Huang, Y. Y., Hu, J. and Wang, X. K. (2014). Retention mechanisms and microstructure of Eu(III) on manganese dioxide studied by batch and high resolution EXAFS technique. *Radiochimica Acta,* 102(1-2)**,** 155-167.